

Final Report

Design Synthesis Exercise

Group 15 - Manned Martian Aircraft

June 21, 2023

Javier Alonso Garcia	5228530	Adrian Beňo	5338514
Freek Braspenning	5291526	Joachim Bron	5259754
Pedro Coimbra Dos Santos	4682335	Sebastian Harris	5277418
Timo de Kemp	5310474	Patrick Kostelac	5238676
Thomas van de Pavoordt	5312329	Dominik Stiller	5253969

This page is intentionally left blank.

Final Report

Design Synthesis Exercise

by

Group 15 - Manned Martian Aircraft

June 21, 2023

Javier Alonso Garcia	5228530	Adrian Beňo	5338514
Freek Braspenning	5291526	Joachim Bron	5259754
Pedro Coimbra Dos Santos	4682335	Sebastian Harris	5277418
Timo de Kemp	5310474	Patrick Kostelac	5238676
Thomas van de Pavoordt	5312329	Dominik Stiller	5253969

Version Control			
Version	Date	Author(s)	Description
1.0	21-06-2023	All	First draft
2.0	27-06-2023	All	Final version

Project duration: April 24, 2023 – June 30, 2023

Thesis committee: Dr. A. Sciacchitano, TU Delft, tutor
Dr. S. J. Paardekooper, TU Delft, coach
Dr. ir. J. A. Pascoe, TU Delft, coach

Cover image credit: adapted from NASA/JPL-Caltech, "Daybreak at Gale Crater".

Executive Overview

By Freek Braspenning

Mankind has been exploring Earth for centuries, and as technology advanced, this curiosity extended beyond our planet. The most promising target for making humanity interplanetary is our neighbor Mars. For astronauts going to Mars and exploring the planet in the next decade, rapid transportation between different locations on the surface of Mars is crucial. We aim to fulfill that need and thus our mission statement is the following:

MS: Transport two astronauts with payload quickly over a long range on Mars.

In order to reach a long-range quickly, airborne transport was considered. While a rover-like vehicle is a working proof-of-concept, their maximum speeds are rather low and are limited by terrain accessibility. The scientific gain of increasing the cruise speed and range by means of airborne transport was considered to outweigh the associated possible risks.

There are many ways to achieve airborne transport and is a proven concept for decades on Earth. A high-level selection was made until five concepts were formed, from which a quantitative tradeoff pinpointed the most viable option. This option is the tiltrotor. From the trade-off, conceptual design followed as a proof of concept.

E.1. Areon

The Areon is a tiltrotor aircraft type designed for the transport of two astronauts on Mars. The name is derived from the prefix "areo-", which means "relating to Mars". The Areon is designed as the answer to the previously mentioned mission statement. The capability of Areon to achieve vertical flight makes many places accessible which would have otherwise been unreachable with a rover or a regular fixed wing aircraft. Furthermore, the ability of Areon to fly greatly increases the coverage of a mission, as many locations become reachable within an hour of travel, which would have otherwise taken days to reach.



Figure E.1: Render of Areon on Mars

Areon will be a product with two models available for purchase: the Areon Atlas and the Areon Helios. The Areon Atlas is designed for increased range and the Areon Helios is designed for self-sufficiency, as it is equipped with solar panels capable to recharge the aircraft without any infrastructure needed.

Both models will be able to house two astronauts, having a nominal mass of 80 kg and a spacesuit of 45 kg each, and a payload of 100 kg. The fuselage provides seating for the astronauts and can house the payload in the designated payload bay. The fuselage also has a walkway for easy accessibility to both the cockpit and the payload bay. The internal layout can be seen in Figure E.2

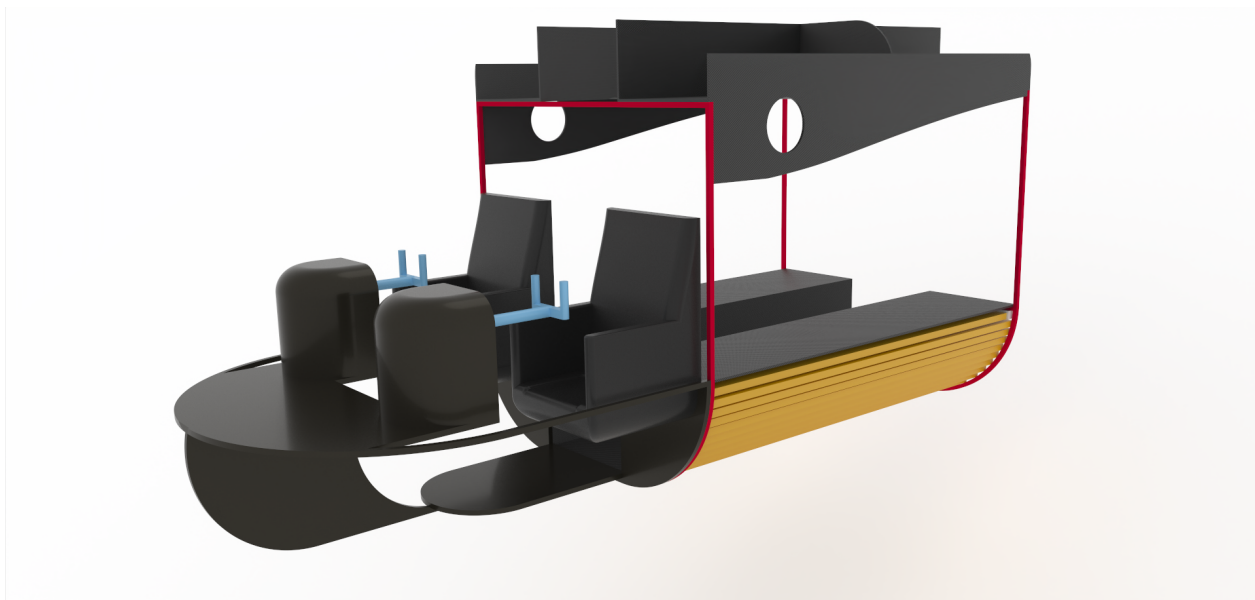


Figure E.2: The internal layout of the fuselage

Areon Atlas

The Areon Atlas is a configuration of the Areon designed for maximizing range. The range is increased by maximizing the weight of the batteries. The added batteries provide enough power to bridge an extra 77 km above the required 1000 km. A render of the Aeron Atlas can be seen in Figure E.3.

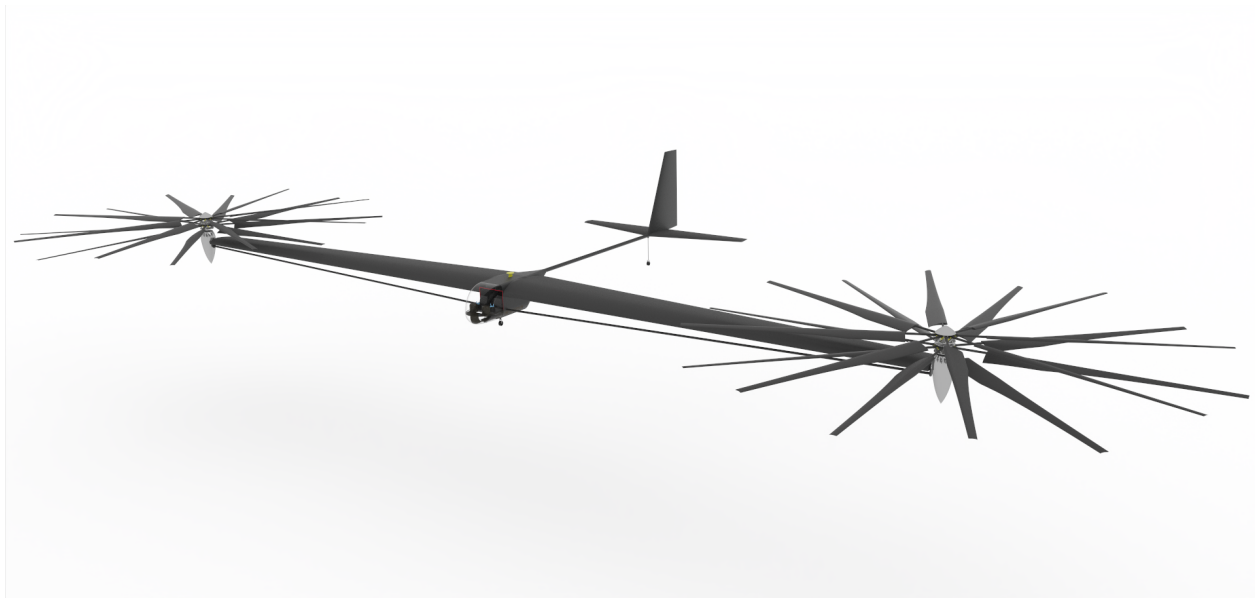


Figure E.3: A 3D render of the Areon Atlas in landing configuration

Areon Helios

The Areon Helios is a tiltrotor equipped with solar panels on the wings. The solar panels allow 100 % in-situ recharging, discarding the need for infrastructure. The addition of solar panels does come at the cost of a reduced range since a small portion of the mass of the batteries was made available for solar panels. A render of the Aeron Helios can be seen in Figure E.4.

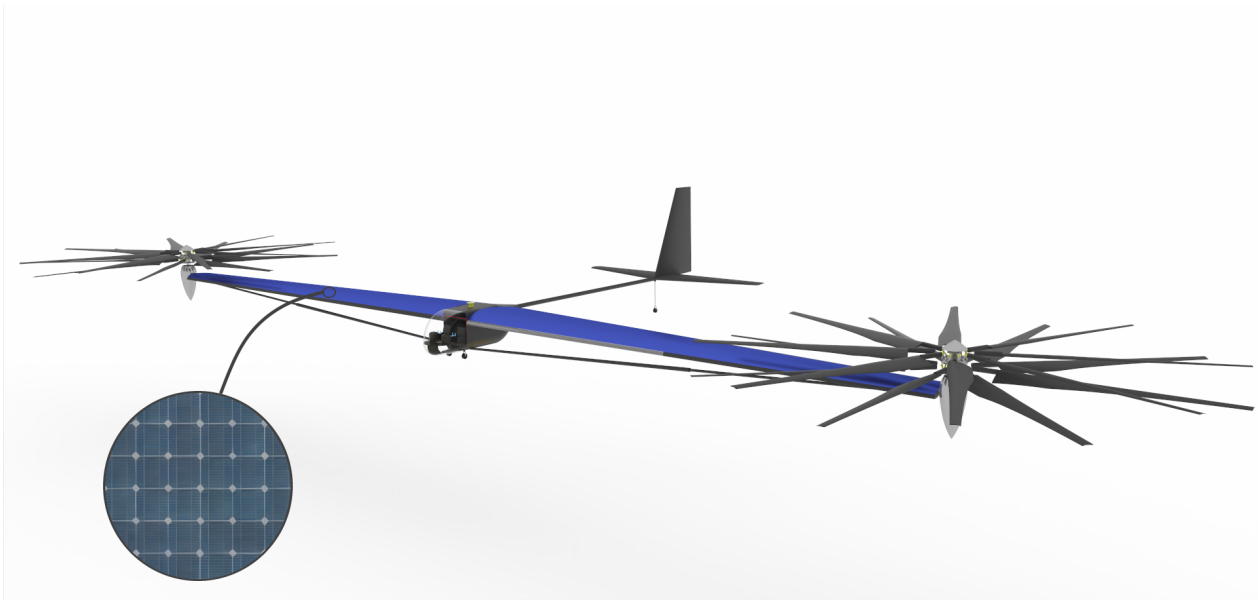


Figure E.4: A 3D render of the Areon Helios in landing configuration

Dimensions

Both the Areon Atlas as well as the Areon Helios have the same design, of which the dimensions are shown in Figure E.5.

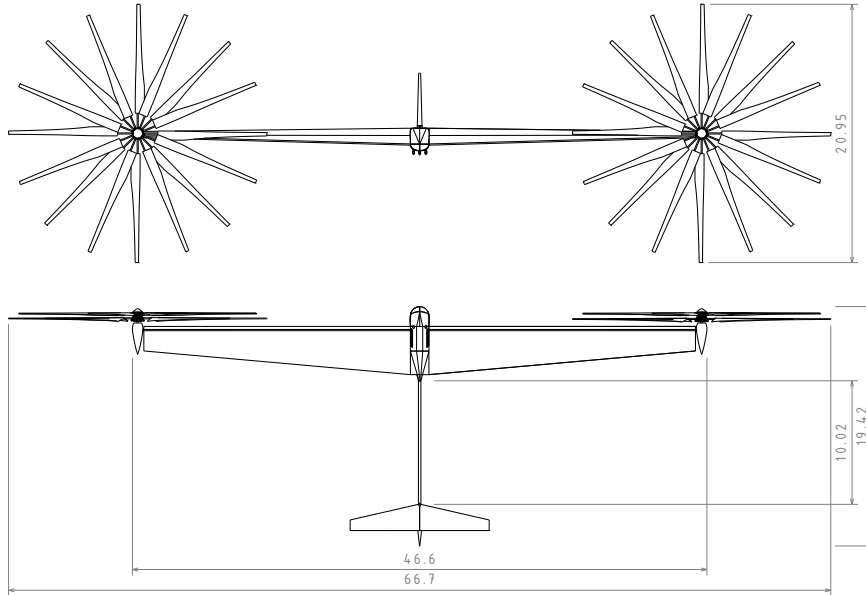


Figure E.5: Front and bottom view of both the Areon

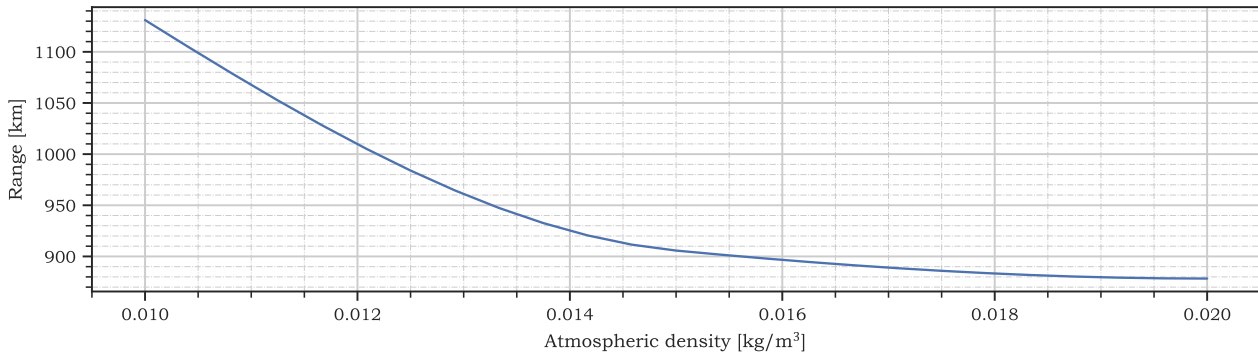
E.2. Aeron Performance

A preliminary analysis of the Aeron performance was conducted. The performance analysis served the purpose of analyzing the capabilities of both the Areon Atlas and the Areon Helios, as well as checking if the aircraft still complied with the requirements set in the baseline report. The most notable performance characteristics are mentioned in Table E.1.

Table E.1: Performance of the Areon Atlas and the Areon Helios

	Areon Atlas	Areon Helios
MTOM	3000 kg	3000 kg
Payload	350 kg	350 kg
Range	1077 km	906 km
Climb rate vertical flight	2 m/s	2 m/s
Cruise speed	403 m/s	403 m/s
Recharge time (grid)	16 hrs	16 hrs
Recharge time (no grid)	-	~ 5 days

The atmosphere of Mars varies greatly throughout the day and location, and since the atmospheric density plays a crucial role in the performance of the Areon, a density power diagram offers insight into the performance through different circumstances. This graph is shown in Figure E.6. Since the aircraft was designed for the worst-case atmospheric density, the power only increases as density increases.

**Figure E.6:** The density power diagram for the Areon Atlas and the Helios Atlas

The performance of the Areon has been verified with the requirements set and is not met in only one instance. The only requirement not met is the range requirement. While the Areon Atlas not only meets but exceeds this range requirement, the Areon Helios does not meet this requirement as the battery mass has been reduced to accommodate for the solar panels. The impact of not meeting the requirement is outweighed by the added benefit of having solar panels. Furthermore, the project has not yet gone into enough detail to verify all of the requirements. This needs to be done in the future project stages.

E.3. Assembly

The Areon was designed for easy assembly on Mars. This came with challenges, as the aircraft has a wingspan greater than that of the Boeing 737. The size of the aircraft forms an issue for transport to Mars as the fairing has a finite size and has to be accounted for. Another consideration was the assembly complexity of the aircraft, as there might not be the needed infrastructure present on Mars. Since the aircraft needs to be transported in a fairing an upper limit of the individual part length was set to 15 m. This constraint was set based on the SpaceX's Starship fairing. Furthermore, mechanical fastening has received priority over any other types of joining, as joining types such as adhesive joining are impossible in the Martian atmosphere. The exploded view of the aircraft assembly is shown in Figure E.7. From the exploded view it can be seen that the main assembly components are the fuselage tail and wings which were separated into the inner and outer parts.

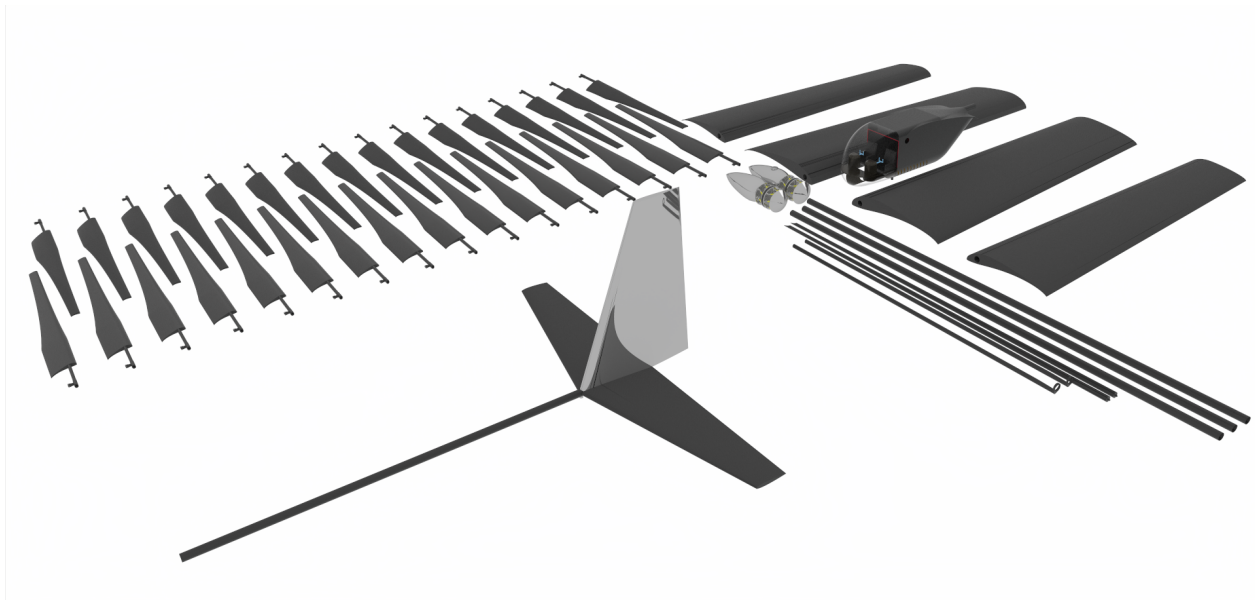


Figure E.7: Exploded view of the Areon

E.4. Market analysis

The Areon is designed to assist future manned Martian missions. The Areon can offer great coverage, and the ability to discover many points of interest in a single mission. A market analysis is performed and found three competitors to the Areon: Hoffman 1997, Morphlab, and Raymer[1, 2]. Hoffman 1997 and Morphlab are both rovers, capable of a range of 500 km and 1000 km respectively. The most similar product currently in development is the Raymer aircraft, an aircraft capable of reaching 482 km at a cruise speed of 278 km/h. The Areon is able to match the range of the best of the competitors and exceeds any of the competitors in terms of mass.

E.5. Cost Breakdown

The cost of the project is divided into two parts: the product costs and the launch costs. The product cost consists of personnel costs, material costs, power system costs, and avionics costs. The total cost breakdown can be seen in Table E.2. The launch costs make up the biggest portion of the project, accounting for over 90 % of the total costs.

Table E.2: Summary of costs

Section	Cost
Personnel	906 300 K USD FY23
Material	147 K USD FY23
Power System	81 K USD FY23
Avionics	828 K USD FY23
Product Total	81 900 K USD FY23
Launch Costs	839 000 K USD FY23
Carbon Offsets	630 K USD FY23
Total Costs	1 021 000 K USD FY23

E.6. Operations and logistics

The flow in Figure E.8 shows what needs to be done to get the aircraft flying on Mars. It also shows the operations on Mars needed for doing the operations, this includes recharging, checkouts, and maintenance. Checkouts will be done with the same equipment that is used to check and assemble the parts shipped to Mars. The system will not be dependent on regular shipments from Earth, only for big fixes or battery life problems leading to limited performance. A nominal mission on Mars would require only the two astronauts and one support person on base. The two astronauts can perform the checkout with the tools used for assembly. The mission can be performed any time of the year in all conditions during which the cross wind and wind gusts are smaller than 15 m/s.

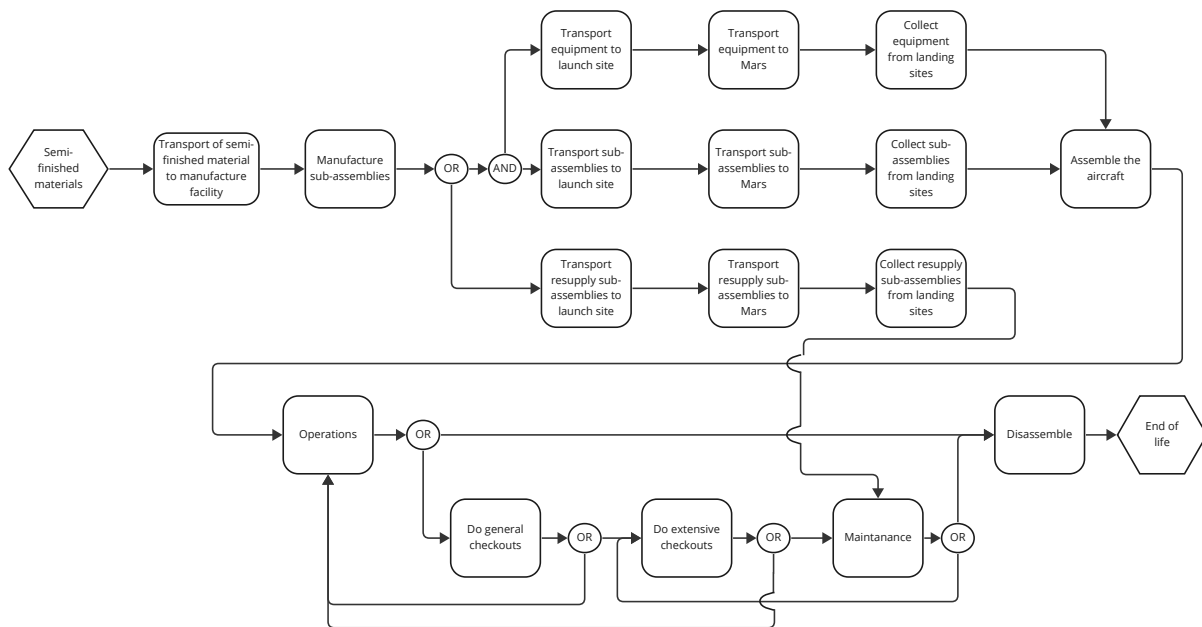


Figure E.8: Operations and logistics flow chart

E.7. Sustainability Development Strategy

Sustainability played a big role in the development of the Areon. The sustainability development strategy considers sustainability in manufacturing and assembly, life cycle assessment, and circular design approach.

The emissions are minimized in various ways during manufacturing. The main material choice of the aircraft is carbon fiber reinforced composites, which in general have a high embodied energy. In order to reduce the embodied energy, they will be recovered with the use of nitric acid. Furthermore, the choice of batteries has a great impact on sustainability. The choice of solid batteries has a relatively positive impact on the environment when compared to other high-performance batteries, such as Lithium-Ion.

A life cycle assessment was performed, which quantifies the environmental impact both on Mars as well as on Earth. Both Mars and Earth were considered as the project impacts both: manufacturing and launch on Earth, and operations and end-of-life on Mars.

The circular design approach limits waste, by reusing degraded items of the Areon. This includes reusing batteries when they have degraded to the point of not providing enough power to sustain flight. Other components of the aircraft can also be utilized after they have reached end-of-life.

E.8. Future of the project

At the end of the Design Synthesis Exercise (DSE), the designs of the Areon Atlas and Areon Helios are given. These follow from the conceptual design stage. After DSE, the project will move into preliminary design and detailed design before manufacturing. The planning for the future of the project can be seen in Figure E.9.

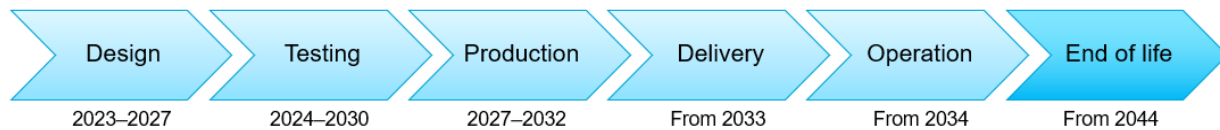


Figure E.9: Timeline of the planning after the DSE

Contents

Executive Overview	i
List of Symbols	xiv
Abbreviations	xv
1 Introduction	1
2 Bird's Eye View	2
2.1 Motivation and Challenges	2
2.2 Mission Statement and Requirements	3
2.3 Trade-off Summary	10
2.4 Concept Introduction	10
2.5 Flow Diagrams	11
2.6 Preliminary Sizing	15
2.7 Budget Management.	15
2.8 Sustainability	16
3 Subsystem Design Methods	19
3.1 N ² chart and iterations.	19
3.2 Wing Sizing Method	21
3.3 Rotor Sizing Method	24
3.4 Stability and Control Method	28
3.5 Undercarriage Sizing Method	33
3.6 Fuselage Sizing Method	34
3.7 Power Sizing Method.	35
3.8 Thermal Management System Sizing Method	37
3.9 Communications Sizing Method	41
3.10 Navigation and Instrumentation Sizing Method.	44
3.11 Life Support Sizing Method	46
3.12 Structural Sizing Method	50
4 Subsystem Design Results	56
4.1 Wing Sizing Results.	56
4.2 Rotor Sizing Results	57
4.3 Control and Stability	61
4.4 Undercarriage Sizing Results	68
4.5 Fuselage.	68
4.6 Power Sizing Results	69
4.7 Electrical block diagram	72
4.8 Thermal Management System Results	72
4.9 Communications Sizing Results.	73
4.10 Navigation and Instrumentation	74
4.11 Life Support System (LSS)	78
4.12 Structures Results	81
5 Verification and Validation	86
5.1 Common Verification and Validation Procedures	86
5.2 Model Verification and Validation and V&V Plan	86
5.3 Compliance Matrix.	94
5.4 Feasibility Analysis	101
6 Final Design	103
6.1 Configuration.	103
6.2 Performance Analysis	104

6.3 Reliability, Availability, Maintainability and Safety.	107
6.4 Sensitivity Analysis	108
7 Technical Risks	110
7.1 Methodology	110
7.2 Risks identified in previous phases	110
7.3 Risks identified in final phase	110
8 Financial Overview	112
8.1 SWOT Analysis	112
8.2 Market Size Estimation	112
8.3 Cost Breakdown	113
8.4 Return on Investment	116
9 Project Future	117
9.1 Project design and development logic	117
9.2 Gantt chart	117
9.3 Operations and logistics	119
9.4 Production plan	120
10 Conclusion	123
Bibliography	124
Miscellaneous	

List of Symbols

E	Energy	J
F_{EOL}	Solar panel degradation due to rotation	1/s
P	Power	W

General

k	Boltzmann constant	$1.38 \times 10^{-23} \text{ J/k}$
-----	--------------------	------------------------------------

Aerodynamics

$\Delta\alpha$	Change in angle of attack	deg
ΔV	Change in true airspeed	m/s
δ	Induced drag factor	—
$\delta_{aileron}$	Deflection of ailerons	deg
λ	Taper ratio	—
ν	Kinematic viscosity	m^2/s
ρ	Atmospheric density	kg/m^3
$\rho_{Mars_{min}}$		kg/m^3
AR	Aspect ratio	—
b	Wingspan	m
C_L	Coefficient of lift	—
C_{D_i}	Coefficient of induced drag	—
CD_f	Fuselage drag coefficient	—
D_f	Fuselage drag force	N
h_f	Fuselage height	m
l_f	Fuselage length	m
M	Mach number	—
MAC	Mean aerodynamic chord	m
r_f	Fuselage shape factor	—
Re	Reynolds number	—
S	Surface area	m^2
S_f	Fuselage wetted area	m^2
S_h/S	Tail area relative to wing area	—
$S_{cylinder}$	Area of the fuselage if it were a perfect cylinder	m^2
S_{ratio}	Area ratio factor	m^2
u	Characteristic flow velocity	m
V_∞	Freestream true airspeed	m/s
V_f	True airspeed	m/s
$V_{rot_{ind}}$	Axial velocity induced by the propellers	m/s

w_f	Fuselage width	m
Stability & control		
ΔF_{tx}	Difference in thrust due to engine failure	N
δ_e	Deflection of the elevator	rad
$\dot{\Omega}$	Angular acceleration	rad/s ²
$\dot{\theta}$	Change in Euler angles	rad/s
\dot{v}	Linear acceleration	m/s ²
$\frac{d\delta_e}{ds_e}$	Change in elevator deflection due to change in elevator area	rad/m ²
$\frac{de}{d\alpha}$	The down wash	—
$\frac{V_h}{V}$	Ratio of the wind speeds at the tail and main wing	—
$\vec{\Omega}$	Angular velocity	rad/s
$\vec{\theta}$	Euler angles	rad
\vec{M}	Moment vector	Nm
\vec{v}	Linear velocity	m/s
c_e	Elevator chord	m
$C_{D_{fus}}$	Drag coefficient of the fuselage	—
C_{Ftx}	Thrust force coefficient	—
$C_{h\delta}$	Change in elevator hinge moment due to a elevator deflection	—
$C_{l\alpha_h}$	Change in lift coefficient of the horizontal tail due to a change in angle of attack	—
$C_{l\alpha_w}$	Change in lift coefficient of the main wing due to a change in angle of attack	—
C_{L_h}	Lift coefficient of the horizontal tail	—
$C_{L_{A-h}}$	Lift coefficient of a tail-less aircraft	—
C_{m0}	Moment at zero elevator deflection	—
$C_{m\alpha}$	Change in moment due to change in angle of attack	—
$C_{m\delta_e}$	Change in the moment due to elevator deflection	—
$C_{m_{ac}}$	Moment coefficient of the aerodynamic center	—
C_{mac}	Mean aerodynamic chord of main wing	—
$C_{N\alpha}$	Normal force gradient of the main wing	—
$C_{Nha_{free}}$	Normal force gradient of the tail in stick free configuration	—
C_{Nha}	Normal force gradient of the tail in stick fixed configuration	—
C_N	Normal force coefficient	—
C_t	Tangential force coefficient	—
$C_{ydeflect}$	Side force coefficient generated by the rudder deflection	—
C_{yside}	Side force coefficient due to sideslip	—
dt		time increments
F_e	Elevator control force	N
F_{net}	Net force	N
I	moment of inertia matrix	—

l_h	Distance from the main wing to the horizontal tail	m
S	Wing area	m^2
S_{fus}	Side area of fuselage	m^2
$S_{minengine}$	Minimum vertical tail area due to one engine out condition	m^2
$S_{minside}$	Minimum vertical tail area due to cross wind	m^2
SF		safetyfactor
V_{cross}	Cross wind	m^2
W	Weight of the aircraft	N
X_{ac}	X location of the aerodynamic center of the main wing	m
X_{cg}	X location of the center of gravity	m
X_n	Neutral point	—
Y_e	Distance of the engine to the center of gravity in y direction	m

Rotor

\hat{r}	Normalized radius	—
Ω	Rotational velocity of the propellers	rad/s
ϕ	Angle between the flow and the normal to the rotor disk	rad
σ	Solidity factor	—
τ		
θ	Blade twist	rad
\tilde{F}	Reference force	N
a	The slope of the $C_L - \alpha$ curve	$1/\text{rad}$
b	Number of blades	—
c	Local chord length	m
C_Q	Coefficient of torque	—
C_T	Coefficient of thrust	—
C_u	Wall jet growth constant	—
C_{Q_0}	Coefficient of profile torque	—
C_{Q_i}	Coefficient of induced torque	—
f_θ	Tangential force per unit radius	N/m
f_x	Axial force per unit radius	N/m
K_T	Terrain erosion factor	—
P	Power	W
$P_{i,rotation}$		
$P_{i,thrust}$		
q_f	Dynamic pressure	Pa
R	Radius of propellers	m
r	Local radial position	m
R_C	Gust cloud radius	m

T	Thrust	N
U_m	Mean momentum velocity of the rotor slipstream	m/s
u_m	Radial velocity in the wall jet	m/s
V_{i_θ}	Tangential induced velocity	m/s
$V_{i_{axial}}$	Axial induced velocity	m/s
$V_{i_{climb}}$	Downwash velocity in climb	m/s
$V_{i_{hover}}$	Downwash velocity in hover	m/s

Structures

ω	Angular velocity	rad/s
σ	Stress	Pa
B	Boom area	m^2
E	Young's modulus	Pa
$F_{centrifugal}$	Centrifugal force	N
I_{xx}	Moment of Inertia around x-axis	m^4
I_{xz}	Product of Inertia	m^4
I_{zz}	Moment of Inertia around z-axis	m^4
q	Shear flow	N/m
r_j	The distance from the center of rotation	m

Communications

λ	Wavelength	m
E_b	Energy per bit	J/bit
F	Noise figure	– or dB
G_{rx}	Receiver antenna gain	– or dBi
G_{tx}	Transmitter antenna gain	– or dBi
L_e	Environment path loss	– or dB
L_s	Free-space path loss	– or dB
$L_{l,rx}$	Antenna-to-receiver line loss	– or dB
$L_{l,tx}$	Transmitter-to-antenna line loss	– or dB
$L_{p,rx}$	Receiver antenna pointing loss	– or dB
$L_{p,tx}$	Transmitter antenna pointing loss	– or dB
N_0	Noise power spectral density	W/Hz
P_{tx}	Transmitter power	W
R	Data rate	bit/s
T_0	Reference noise temperature	290 K
T_s	System noise temperature	K
T_{ant}	Antenna noise temperature	K

Thermal management

α	Absorptivity	—
\dot{Q}_{albedo}	Albedo heat flux	W
\dot{Q}_{conv}	Convection heat flux	W
\dot{Q}_{in}^{ext}	External heat flux in	W
\dot{Q}_{in}^{int}	Internal heat flux in	W
\dot{Q}_{IR}	Infrared heat flux	W
\dot{Q}_{out}	Thermal heat flux out	W
\dot{Q}_{sun}	Solar radiation heat flux	W
κ_f	Fluid conductivity	W/m/K
μ	Dynamic viscosity	Pas
ε	Emissivity	—
b	Albedo fraction	—
C_p	Heat capacity	J/kg/K
$F_{s/v}$	View factor	—
h	Convection coefficient	W/m ² /K
I_s	Solar intensity	W/m ²
Nu	Nusselt number	—
Pr	Prandtl number	—
T_{amb}	Ambient air temperature	K
T_{sub}	Subsystem temperature	K

Life support

ρ	Density	kg/m ³
σ	Stress	MPa
σ_y	Material yield stress	MPa
c_{max}	Max crack length	m
d	Diameter	m
K_{1c}	Material fracture toughness	MPa · m ^{1/2}
l/d	Fineness ratio	—
m	Mass	kg
p	Internal tank pressure	MPa
r	Radius	m
T	Temperature	K
t_{cyl}	Thickness cylindrical	m
t_{sph}	Thickness spherical	m
V	Volume	m ³

Abbreviations

- ADIRS** Air Data Inertial Reference System.
- AOA** angle of attack.
- AR** Aspect Ratio.
- CF/Cy** Carbon Fiber Reinforced Cyanate Ester.
- CF/PEEK** Carbon Fiber Reinforced Polyetheretherketon.
- CG** center of gravity.
- CL** Lift coefficient.
- COPV** composite overwrapped pressure vessel.
- DSE** Design Synthesis Exercise.
- EOL** End of life.
- EVA** Extra Vehicular Activity.
- FAA** Federal Aviation Administration.
- FBD** free body diagram.
- FBS** Functional breakdown structure.
- FEM** Finite Element Method.
- FFD** Functional flow diagram.
- GNSS** global navigation satellite system.
- HF** High Frequency.
- ISS** international space station.
- LAMS** Light Aircraft Maintenance Schedule.
- LDPC** Low-Density Parity Check.
- LRV** lunar roving vehicle.
- LSB** laminar separation bubble.
- LSS** life support system.
- MAC** mean aerodynamic chord.
- NASA** National Aeronautics and Space Administration.
- NVIS** near-vertical incidence skywave.
- OEW** Operational Empty Weight.
- OOP** Object Oriented Programming.
- PID** proportional-integral-derivative.
- REMS** Rover Environmental Monitoring Station.
- ROC** Rate of Climb.
- TCS** thermal control system.
- TMS** thermal management system.
- UHF** Ultra High Frequency.
- VHF** Very High Frequency.
- VTOL** Vertical Take-Off and Landing.

Introduction

By Thomas van de Pavoordt, Adrian Beňo, Timo de Kemp

Modern scientific advances have created possibilities to make humanity a multi-planetary species. Specifically, scientific interest in Mars exploration has increased and Mars is currently being explored in-situ by Ingenuity drone and Curiosity rover. However, these are all unmanned missions. The next step of Mars exploration are hence manned missions with scientists on board, who will explore wide regions of the red planet.

Currently, no feasible solution exists for human transportation on Mars over vast ranges and in a fast manner. While surface rovers may be adapted for human transportation, only airborne transportation will be able to meet the need of mobility, especially to places where land transportation is impossible, too dangerous or too slow. This final report is the fourth in a series of reports to describe the conceptual design of a two-astronaut manned Martian aircraft.

Previously, the project plan showed the organizational aspects of this project, including task division and scheduling. The baseline report represented the first technical report of the project. It outlined the functional description of the system that should fulfill the mission and inventoried all the requirements. Most recently, trade-off was performed in the midterm report between the most promising design options. The winner of this trade-off was a tiltrotor-craft, which was later named Areon. This report focuses on the conceptual design of this aircraft and it gives a detailed outlook into the future of this design project.

Areon is an electric tiltrotor which is designed to fly in the thin Martian atmosphere for 1000 km. The design consists, as shown in a render in Figure 1.1, of two giant propellers, a wing, fuselage, and tail. The huge propellers are able to rotate around the wing's axis which allows the aircraft to take-off and land vertically. This ensures the aircraft is able to reach all kind of interesting science locations.



Figure 1.1: Render of Areon flying in the Martian atmosphere

This report is structured as follows. Firstly, a "bird's eye view" offers the motivation behind the project and defines the structure of the project in terms of scheduling and general outlook, chapter 2. Secondly, the details of the methodology behind the design process of the different subsystems are given chapter 3. The results of the design process are given in chapter 4, which defines the final design. Verification and validation of the design methodology and obtained results is provided in chapter 5. A high level summary of the results is given in chapter 6. The technical risks associated with the results are given in chapter 7. The associated financial aspect of the whole mission is analyzed in chapter 8 and lastly, the future of the project is outlined in chapter 9.

The source code can be found at <https://github.com/DominikStiller/tudelft-dse>.

Bird's Eye View

2.1. Motivation and Challenges

Ever since humans set foot on the surface of the Moon, our eye has turned to the next target, Mars. With contemporary advances of private space organizations, mainly SpaceX, the realization of a human presence on Mars is now within grasp. It is not just a matter of accomplishment to reach Mars, but the planet could also provide massive scientific insight on many topics. As ESA puts it beautifully:

The scientific reasons for going to Mars can be summarized by the search for life, understanding the surface and the planet's evolution, and preparing for future human exploration.¹

Mars can not only provide a vast amount of scientific insight into extraterrestrial life but also provide insight into the formation of our solar system. The National Aeronautics and Space Administration (NASA) has also already published a map of potential zones for human exploration², as can be seen in Figure 2.1, colors in this map indicate the altitude where blue is low and red high.

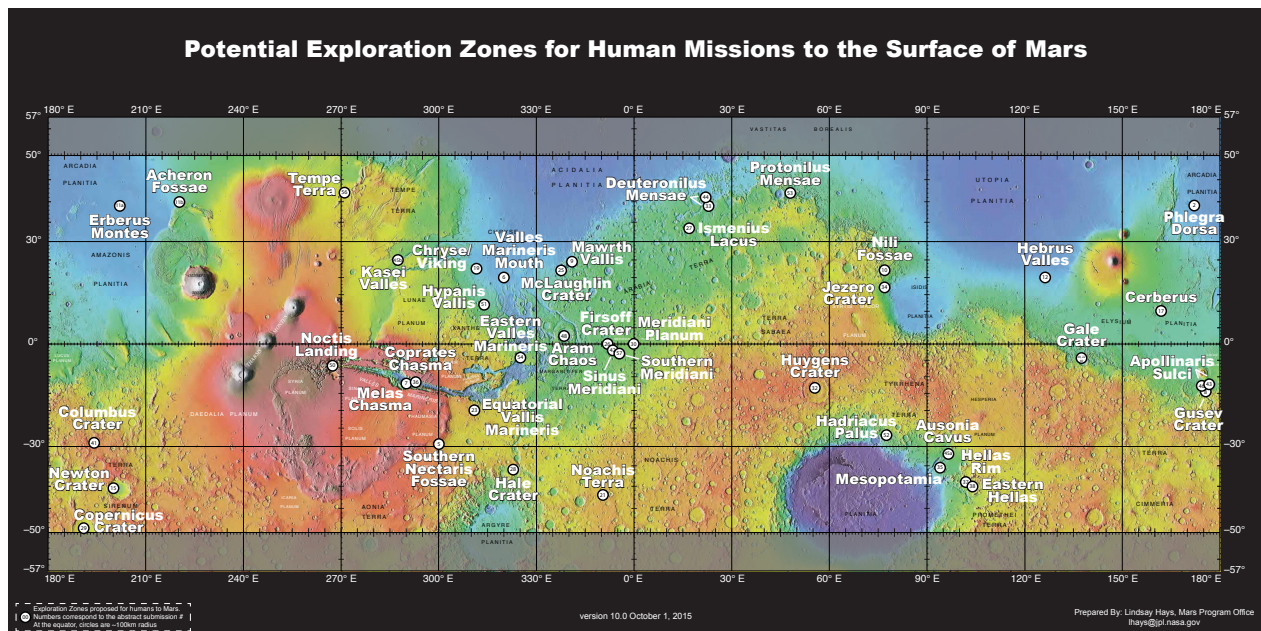


Figure 2.1: Map of potential exploration zones. At the equator, 1000 km corresponds to 17° (half of a square).

However, these zones are not particularly close together, considering that one side of a square in Figure 2.1 compares to 2000 km of actual distance. Adding in the fact that Perseverance, NASA's most recent and most sophisticated rover, has only driven a little under 19 km in 853 Earth days³, the outlook of exploration on the Martian surface is not looking very bright. Therefore, it is highly relevant to design a vehicle that is able to cover large distances on Mars at a rapid pace. This vehicle should be able to land in remote, desert-like places and provide cargo space for scientific research, such as ground samples.

However, the fact that no large aircraft are currently flying on Mars proves it is not as easily done as said. The biggest challenge to overcome on Mars is the incredibly low atmospheric density, over 60 times lower than Earth's density. This results in way less lift generated by wing surfaces and difficulties with flow attachment. On the other hand, the lower density also results in lower amounts of drag, which reduces

¹URL: https://www.esa.int/Science_Exploration/Human_and_Robotic_Exploration/Exploration/Why_go_to_Mars [cited 2023-06-02]

²URL: <https://www.nasa.gov/sites/default/files/atoms/files/exploration-zone-map-v10.pdf> [cited 2023-06-01]

³URL: <https://mars.nasa.gov/mars2020/mission/where-is-the-rover/> [cited 2023-06-21]

the amount of thrust required to propel a vehicle forward. This in combination with the lower gravity, about 3 times lower than Earth's gravity, slightly alleviates the major problems caused by the low density. Another issue on Mars is the rugged terrain, consisting of irregular patterns of sand dunes, rocks and regolith. This causes problems for vehicles utilizing conventional horizontal take-off and landing, since no clear runways exist and finding a suitable landing location may prove difficult. Furthermore, the Martian atmosphere almost solely consists of carbon dioxide or CO₂, which excludes the use of conventional combustion engines as used by aircraft on Earth, which run on oxygen. Finally, Mars does not have natural atmospheric protection from solar radiation and cosmic radiation, like Earth does with its magnetic field.

All in all, transportation over ground on Mars is slow, damage-prone due to rocks and not able to cover large distances. Transportation through the Martian atmosphere can provide significant advantages, such as range, amount of payload and a wide range of landing locations. However, challenges such as the low density, oxygen-deprived atmosphere and rugged terrain have to be overcome for an aircraft to be successful. This design project tackled these challenges and provide a worked-out solution for an aircraft on Mars through an extensive design process.

2.2. Mission Statement and Requirements

By Thomas van de Pavoordt The project can be defined through a mission statement and a project objective statement. These two statements summarize the mission's goal and impose requirements and constraints on the mission. The mission statement (MS) and the project objective statement (POS) are:

MS: Transport two astronauts with payload quickly over a long range on Mars.

POS: With 10 people in 10 weeks, design an aerial vehicle that is capable of transporting two astronauts for at least 1000 km on Mars.

The design process starts with requirement discovery. In this discovery process all requirements are derived from top-level requirements to stakeholder requirements to system and subsystem requirements. Several stakeholders and their needs were found and are tabulated in Table 2.1:

Table 2.1: Overview of the stakeholders and their needs

(a) Needs of the astronauts

ID	Astronauts	ID	Astronauts
1	Safety	6	Able to see their surroundings
2	Able to manually control the aircraft	7	Able to travel from one place to another
3	Simple to use	8	Easy and quick ingression and egression
4	Basic level of comfort	9	Simple assembly process
5	Able to transport payload	10	Simple maintenance and repairs

(b) Needs of the space agencies

ID	Space agencies	(c) Needs of the tutors/customers
11	No interference with concurrent missions	
12	Re-usability of the system by different missions	
13	Long lifetime of the system	
14	Compatibility of the system with already existing infrastructure	
15	Ability of the system to be transported by an already existing launcher	

(d) Needs of the manufacturers

ID	Manufacturers	(e) Needs of the scientific community	(f) Needs of the launch provider
21	Materials employed are not toxic	23 No damage is done to collected payload	26 System components are attached to the launcher
22	Manufacturing is profitable	24 No damage is done to scientific instruments	27 System fits within the payload bay
		25 Provide access to scientifically interesting areas	28 System can withstand prescribed loads

From the stakeholder needs and a thorough system requirement discovery was performed in the baseline report, the following requirements were determined, for which the vehicle is to be designed:

Table 2.2: Requirements

Identifier	Description
<i>Top-level user requirements</i>	
REQ-USER-PERF-01	The system shall have a range of at least 1000 [km].
REQ-USER-PERF-02	The system shall have a cruise speed of at least 400 [km/h].
REQ-USER-SARE-01	The system shall be able to perform all its functions in the Mars atmosphere.
REQ-USER-SARE-02	The system shall be able to take-off and land on Mars soil.
REQ-USER-SUST-01	The system shall be able to use in-situ resources to function.
REQ-USER-ENGB-01	The system shall have a Maximum Take-Off Mass (MTOM) of less than 3000 [kg].
REQ-USER-ENGB-02	The system shall be able to transport 2 astronauts with a maximum mass of 250 [kg].
REQ-USER-ENGB-03	The system shall be able to carry a payload of at least 100 [kg].

Table 2.2 continued from previous page

Identifier	Description
REQ-USER-OTHR-01	The system shall be able to be assembled on Mars.
<i>Astronaut requirements</i>	
REQ-ASTR-SAFE-01	Astronauts shall be transported safely by the system.
REQ-ASTR-SAFE-02	The system shall not produce more than 2.5 positive [g] in any direction.
REQ-ASTR-SAFE-03	The system not produce more than -1 negative [g] in any direction.
REQ-ASTR-SAFE-04	In a crash situation, the system shall not induce more than 35 [g] over 0.5 [s] in spineward direction.
REQ-ASTR-SAFE-06	In a crash situation, the system shall not induce more than 35 [g] over 0.5 [s] in tailward direction.
REQ-ASTR-SAFE-10	Astronauts shall be able to exit the aircraft in under 30 [s].
REQ-ASTR-CNTRL-01	Astronauts shall be able to control the system manually.
REQ-ASTR-CNTRL-03	Astronauts shall have an upward field of view of 30 [deg].
REQ-ASTR-CNTRL-04	Astronauts shall have a downward field of view of 45 [deg].
REQ-ASTR-CNTRL-05	Astronauts shall have a lateral field of view of 150 [deg].
REQ-ASTR-CMFRT-02	The system seat shall be within 0.75 [m] of all controls.
REQ-ASTR-CMFRT-03	The astronauts shall be able to enter the aircraft in under 60 [s].
<i>Manufacturer requirements</i>	
REQ-MNFCT-COST-01	The cost of manufacturing and materials should be less than 10 % of the development cost.
REQ-MNFCT-TXIC-01	The system shall not utilize toxic materials, unable to be handled by protected employees.
REQ-MNFCT-TXIC-02	The system shall not utilize materials comprised of toxic raw ingredients, unable to be handled by protected employees.
<i>Scientific community requirements</i>	
REQ-SCNCE-PAYL-01	The integrity of the collected scientific payload shall be preserved.
<i>Space agencies requirements</i>	
REQ-SAG-INT-01	The system shall not interfere with current missions.
REQ-SAG-INT-02	The system shall not utilize the same transmission frequency as current missions.
REQ-SAG-INT-03	The system shall not impede other missions' operations.
REQ-SAG-REUS-03	The system's assembly process shall be repeatable.
REQ-SAG-COMP-01	The system shall be compatible with already existing infrastructure.
REQ-SAG-COMP-02	The system shall be able to communicate with already existing spacecraft.
REQ-SAG-COMP-03	The system shall be able to utilize already existing forms of recharging/refueling.
REQ-SAG-LIFE-01	The system shall have an operational life of 10 years.
REQ-SAG-OPE-02	The system shall be operated independently of the season.
REQ-SAG-OPE-03	The system shall be operated independently of the day-night cycle.
REQ-SAG-OPE-04	The system shall be operational during sand storms.
REQ-SAG-OPE-05	The system shall be operational in all parts of the planet.
REQ-SAG-OPE-06	The system shall not need runways to take-off and land.
<i>Launch provider requirements</i>	
REQ-LAU-01	The system components shall remain attached to the launcher during launch.
REQ-LAU-02	The system components shall be able to fit in the selected launcher.
REQ-LAU-03	The system components shall be able to withstand the loads specified.
REQ-LAU-04	The system shall comply with all requirements set by the manual of the chosen launcher vehicle.
<i>Customer requirements</i>	
REQ-CUST-FAST-01	The conceptual design shall be finished within 3600 working hours.
REQ-CUST-INNO-02	The design shall improve upon state of the art.
REQ-CUST-COST-01	The project cost shall be minimized.
REQ-CUST-COST-02	The design cost shall be at most 6.6 bil. FY2023 USD.
REQ-CUST-COST-03	The manufacturing cost shall be at most 6.0 mil. FY2023 USD per vehicle.
<i>Launch, coasting and descent requirements</i>	

Table 2.2 continued from previous page

Identifier	Description
REQ-LCD-LVEH-SIZE-01	The system, in launch configuration, shall have a volume of less than 150 [m^3].
REQ-LCD-LVEH-SIZE-02	The system, in launch configuration, shall have a height of less than 15 [m].
REQ-LCD-LVEH-SIZE-03	The system, in launch configuration, shall have a width of less than 8 [m].
REQ-LCD-LVEH-SIZE-04	The system, in launch configuration, shall have a depth of less than 8 [m].
REQ-LCD-LNCH-LOAD-01	The system shall be able to withstand longitudinal loads of 6 [g].
<i>Ground operations requirements</i>	
REQ-GOPS-ACT-ASS-01	The system shall be able to be assembled by at least 2 astronauts.
REQ-GOPS-ACT-ASS-02	The assembly process shall only use tools available in-situ.
REQ-GOPS-ACT-ASS-03	The assembly process shall not use more than 24 hours.
REQ-GOPS-ACT-MAINT-02	The system shall allow for system diagnostic checks every flight.
REQ-GOPS-ACT-MAINT-03	The system shall allow for Non-Destructive Testing every 2 flights.
<i>Avionics requirements</i>	
REQ-AVNC-GNRL-01	The system shall have an avionics subsystem.
REQ-AVNC-IFC-01	The avionics subsystem shall include all instruments needed for IFC navigation.
REQ-AVNC-IFC-02	The avionics subsystem shall include an airspeed indicator.
REQ-AVNC-IFC-03	The avionics subsystem shall include an altimeter indicator.
REQ-AVNC-IFC-07	The avionics subsystem shall include a gyroscopic rate-of-turn indicator.
REQ-AVNC-IFC-08	The avionics subsystem shall include a slip-skid indicator.
REQ-AVNC-IFC-09	The avionics subsystem shall include an attitude indicator.
REQ-AVNC-IFC-10	The avionics subsystem shall include a heading indicator.
REQ-AVNC-IFC-11	The avionics subsystem shall gather measurements on total atmosphere pressure.
REQ-AVNC-IFC-12	The avionics subsystem shall gather measurements on static atmosphere pressure.
REQ-AVNC-IFC-13	The avionics subsystem shall gather measurements on inertial acceleration.
REQ-AVNC-IFC-14	The avionics subsystem shall gather measurements on global system position.
REQ-AVNC-NAV-01	The avionics subsystem shall have navigation instruments.
REQ-AVNC-NAV-02	The avionics subsystem shall include a Radar.
REQ-AVNC-NAV-03	The avionics subsystem shall include a Short-Wave Infrared sensor.
REQ-AVNC-NAV-04	The avionics subsystem shall include a Terrain Awareness and Warning System.
REQ-AVNC-NAV-05	The avionics subsystem shall include a Heads Up Display.
REQ-AVNC-NAV-07	The avionics subsystem shall include a Night Vision System.
REQ-AVNC-ICE-01	The avionics subsystem shall include a de-icing system.
<i>Aerodynamics requirements</i>	
REQ-AERO-LFT-02	The aerodynamic system shall produce more than 11130 [N] of lift.
REQ-AERO-LFT-03	The aerodynamic system shall have a maximum lift coefficient of 2.2.
REQ-AERO-LFT-04	The system shall have an induced drag coefficient of no more than 0.1.
REQ-AERO-LFT-05	The aerodynamic system shall have a stall angle larger than 15 [deg].
REQ-AERO-LFT-06	The aerodynamic system shall have a stall speed lower than 85 [m/s].
REQ-AERO-LFT-07	The aerodynamic system shall have a maximum speed of 140 [m/s].
<i>Thermal requirements</i>	
REQ-THRM-01	The system shall have a thermal control system.
REQ-THRM-INS-02	The system shall have an overall emissivity lower or equal to 0.8.
REQ-THRM-INS-03	The system shall have an overall absorptivity lower or equal to 0.2.
REQ-THRM-HTCL-03	The system shall be able to exhaust 60000 [W] of heat.
REQ-THRM-HTCL-04	The system shall be able to distribute heat within the vehicle.
REQ-THRM-DTCT-01	The system shall be able to detect the temperature of different parts of the vehicle with an accuracy of 1 [K].
<i>Storage requirements</i>	

Table 2.2 continued from previous page

Identifier	Description
REQ-STG-PAY-01	The system shall be able to store payload.
REQ-STG-PAY-02	The system shall be able to hold at least 100 [kg] of payload.
REQ-STG-PAY-03	The payload bay shall have a minimum volume of 0.1 [m^3].
REQ-STG-PAY-04	The payload bay shall be airtight.
REQ-STG-PAY-05	The payload bay shall be able to maintain a minimum temperature of 275 [K].
REQ-STG-PAY-06	The payload bay shall be able to maintain a maximum temperature of 390 [K].
<i>Life support requirements</i>	
REQ-LFSP-01	The system shall include life support capabilities.
REQ-LFSP-AIR-01	The system shall provide breathable air to the astronaut.
REQ-LFSP-AIR-03	The system shall store 2.5 [kg] of O ₂ .
REQ-LFSP-WTR-01	The system shall store 8 [kg] of drinkable water.
<i>Structures requirements</i>	
REQ-STR-LD-01	The system shall sustain a maximum load factor of 2 for the MTOM configuration.
REQ-STR-LD-02	The system shall sustain a minimum load factor of -1 for the MTOM configuration.
REQ-STR-LD-03	The system shall ensure damping of all vibrational loads.
REQ-STR-ENV-01	The system shall be suitable for the Martian environment.
REQ-STR-ENV-04	The system shall sustain impacts of objects with an energy of at most 800 [J/m^2].
REQ-STR-THR-01	The system's structure shall be viable in the temperature range found on Mars.
REQ-STR-THR-02	The system shall satisfy all other requirements at an external temperature between 183 [K] and 271 [K].
REQ-STR-THR-03	The system shall sustain thermal loads induced by a temperature change of 90 [K].
REQ-STR-FTG-01	The system shall have a fatigue life of 2500 flights.
<i>Control and stability requirements</i>	
REQ-CS-01	The aircraft shall have control mechanisms that are capable of satisfying the maneuver requirements.
REQ-CS-02	The aircraft shall have a fault-tolerant (fail-safe) control mechanism.
REQ-CS-03	The aircraft shall be statically stable in the lateral directions.
REQ-CS-04	The aircraft shall be statically stable in the longitudinal direction.
REQ-CS-05	The aircraft shall be dynamically stable in the lateral direction.
REQ-CS-06	The aircraft shall be dynamically stable in the longitudinal direction.
REQ-CS-09	The aircraft maximum stick force shall not exceed 100 [N].
REQ-CS-10	The aircraft shall have a positive stick force curve.
<i>Guidance navigation and control requirements</i>	
REQ-GNC-APS-01	The autopilot system shall be operable in low visibility conditions.
REQ-GNC-DGP-01	The communication system shall transmit position data.
REQ-GNC-DGP-02	The communication system shall receive position data.
REQ-GNC-DGP-03	The communication system shall send current position data every 0.1 [s].
REQ-GNC-DGP-04	The guidance system shall be able to determine location based on a non-GPS way.
REQ-GNC-DV-01	The velocity shall be determined with error less than 1 [m/s].
REQ-GNC-DV-02	The velocity shall be determined in at least 2 independent ways.
REQ-GNC-DA-01	The attitude shall be determined with error less than 0.1 [deg].
REQ-GNC-DA-02	The attitude shall be determined in at least 2 independent ways.
REQ-GNC-DDH-01	Local flight plan shall be adjusted to avoid locally detected terrain.
REQ-GNC-DDH-03	The state-space data shall be communicated to autopilot and PFD.
<i>Command and data handling requirements</i>	
REQ-CDH-DAT-01	The C&DH subsystem shall be able to manage all the systems data.
REQ-CDH-DAT-02	The C&DH subsystem shall be able to manage a minimum data throughput of 0.18 [MB/s].
REQ-CDH-DAT-03	The C&DH subsystem shall be able to manage the flight computer data.
REQ-CDH-DAT-04	The C&DH subsystem shall be able to manage the payload data.

Table 2.2 continued from previous page

Identifier	Description
REQ-CDH-DAT-05	The C&DH subsystem shall be able to manage the astronaut health data.
REQ-CDH-DAT-06	The C&DH subsystem shall be able to manage the aircraft subsystems status data.
REQ-CDH-DAT-08	The C&DH subsystem shall be able to manage the data from any external communications.
REQ-CDH-DAT-09	The C&DH subsystem shall be able to manage the data from internal communications.
REQ-CDH-DAT-10	The C&DH subsystem shall be able to manage the data from the GNC subsystem.
REQ-CDH-DAT-11	The C&DH subsystem shall manage the data transmission between different subsystems.
REQ-CDH-PRO-02	The C&DH subsystem shall use a peak power of less than 100 [W].
REQ-CDH-PRO-03	The C&DH subsystem shall have a mass less than 30 [kg].
REQ-CDH-PRO-04	The C&DH subsystem combined hardware shall fit in a volume of 0.5 [m^3].
REQ-CDH-CMD-01	The C&DH subsystem shall manage commands.
REQ-CDH-CMD-02	The C&DH subsystem shall autonomously manage any problems or anomalies that occur in any subsystems based on the data received.
REQ-CDH-CMD-03	The C&DH subsystem shall manage astronaut commands.
REQ-CDH-CMD-04	The C&DH subsystem shall manage external communication commands.
REQ-CDH-CMD-05	The C&DH subsystem shall manage the power usage.
<i>Telecommunications requirements</i>	
REQ-TTC-01	The system shall provide a TTC subsystem.
REQ-TTC-INT-02	The astronauts shall be able to communicate with their suits on.
REQ-TTC-EXT-02	The TTC subsystem shall communicate with the Mars ground segment.
REQ-TTC-EXT-03	The TTC subsystem shall communicate with the space segment.
REQ-TTC-EXT-04	The TTC subsystem shall communicate with other aerial vehicles.
REQ-TTC-EXT-05	The TTC subsystem shall communicate with other ground vehicles.
REQ-TTC-EXT-06	The TTC subsystem shall operate on the UHF frequencies.
REQ-TTC-EXT-07	The TTC subsystem shall have bandwidth of 100 [kHz].
REQ-TTC-EXT-08	The TTC subsystem shall have a maximum bit error rate of 1×10^{-6} .
REQ-TTC-EXT-09	The TTC subsystem shall be able to detect incoming signals with a minimum of 120 [dBm].
REQ-TTC-EXT-10	The TTC subsystem shall operate at a weather availability of 95%.
REQ-TTC-PRO-02	The TTC subsystem shall have a mass less than 30 [kg].
REQ-TTC-PRO-04	The TTC subsystem combined hardware shall fit in a volume of 0.5 [m^3].
<i>Thrust requirements</i>	
REQ-THR-01	The system shall provide 50 [kW] of excess power for take-off.
REQ-THR-02	The system shall provide 50 [kW] of excess power to climb.
REQ-THR-03	The system shall provide 600 [N] of thrust to cancel out drag during cruise.
REQ-THR-04	The system shall allow for throttling as low as 1% of nominal thrust for ground operation.
REQ-THR-05	The system shall ensure thrust direction is optimal.
REQ-THR-07	The system shall have a thrust margin of 1000 [N] for emergency maneuvers.
<i>Power requirements</i>	
REQ-PWR-01	There shall be 357 [kW] of power available to power all essential systems.
REQ-PWR-ELEC-01	There shall be 50 [W] of power available for thermal management.
REQ-PWR-ELEC-01	There shall be 90 [W] of power available for data handling.
REQ-PWR-ELEC-01	There shall be 1275 [W] of power available for avionics.
REQ-PWR-ELEC-01	There shall be 270 [W] of power available for GNC.
REQ-PWR-ELEC-01	There shall be 0 [W] of power for life support.
REQ-PWR-02	There shall be 20% of excess power available for flight maneuvers.
REQ-PWR-04	There shall be a power storage unit providing 288 [W] of power for 2.5 hours.
<i>End-of-Life requirements</i>	
REQ-EOL-TRANSP-01	The system shall be able to be transported to the base at EOL.

Table 2.2 continued from previous page

Identifier	Description
REQ-EOL-DISS-01	The structural components of the system shall be able to be disassembled with tools available in-situ.
REQ-EOL-DISS-02	The electrical components of the system shall be able to be disassembled with tools available in-situ.
REQ-EOL-DISS-03	The propulsion system components of the system shall be able to be disassembled with tools available in-situ.
REQ-EOL-DISS-04	The life support system components of the system shall be able to be disassembled with tools available in-situ.
REQ-EOL-DISS-05	The payload components of the system shall be able to be disassembled with tools available in-situ.
<i>Safety requirements</i>	
REQ-SAF-EMR-01	The system shall provide an emergency abort option.
REQ-SAF-EMR-02	The system shall be designed for crashworthiness.
REQ-SAF-ENV-01	The system shall protect the inside from radiation.
REQ-SAF-ENV-02	The system shall provide breathable air for 24 [hr].
REQ-SAF-ENV-03	The system shall provide an air pressure of 5 [atm].
<i>Ethics requirements</i>	
REQ-ETHC-01	The system shall not be weaponizable.
REQ-ETHC-02	The system shall not pollute the Martian environment.
REQ-ETHC-03	The system shall not harm any potential indigenous Martian species.
<i>Pre- and post-flight requirements</i>	
REQ-PPFO-EMB-01	The system shall provide accessibility for astronauts to embark from the outside.
REQ-PPFO-EMB-02	The system shall provide accessibility for astronauts to disembark from the inside.
REQ-PPFO-LND-01	The system shall receive terrain data with a resolution of 8 [MP].
REQ-PPFO-LND-02	The system shall provide a landing location with rocks no bigger than 0.2 [m].
REQ-PPFO-LND-03	The system shall provide a landing location with a softness above 178 [kPa].
REQ-PPFO-LND-05	The system shall provide a landing location that has a slope of less than 5 [deg].
REQ-PPFO-MNT-01	The system shall be accessible for maintenance purposes.
REQ-PPFO-MNT-02	The system shall have tooling available for maintenance.
REQ-PPFO-MNT-03	The system shall provide sufficient power for maintenance tooling.
REQ-PPFO-FRD-01	The system shall be easily accessible for inspection.
REQ-PPFO-FRD-02	The system shall be inspectable without dust contamination.
REQ-PPFO-FRD-03	The system shall have inspection tooling present.
REQ-PPFO-FRD-04	The system shall provide safety during inspection.
REQ-PPFO-FRD-05	The system shall provide sufficient power for inspection tooling.
REQ-PPFO-ENS-01	The system shall provide full energy replenishment within 16 [hr].
<i>Take-off requirements</i>	
REQ-TOFF-PPS-01	Engines shall provide self-start possibility without external power supply.
REQ-TOFF-PPS-02	Engines shall be able to monitor their functioning.
REQ-TOFF-PPS-03	Aircraft shall be able to provide remaining energy information.
REQ-TOFF-CMCH-01	Aircraft shall be able to detect icing.
REQ-TOFF-CMCH-02	Aircraft shall provide de-icing system.
REQ-TOFF-TOM-01	Aircraft shall provide take-off aiding mechanism.
REQ-TOFF-CTOFF-02	The aircraft shall be able to take-off in low-visibility conditions.
REQ-TOFF-CTOFF-03	The propulsion system shall be able to exert its full thrust capability during take-off.
<i>Climb requirements</i>	
REQ-CLMB-01	The climb rate at take-off altitude shall be at least 2 [m/s].
REQ-CLMB-04	The climb angle at take-off altitude shall be at most 90 [deg].
REQ-CLMB-05	The landing system shall be retracted once a steady climb is achieved.
<i>Maneuver requirements</i>	

Table 2.2 continued from previous page

Identifier	Description
REQ-MAN-01	The aircraft shall be able to perform a horizontal turn in the Martian atmosphere at the rate of 5 [deg/sec].
REQ-MAN-02	The aircraft shall be able to glide in the Martian atmosphere at a glide angle of -5 [deg].
REQ-MAN-03	The aircraft shall not stall in the Martian atmosphere before the angle of attack of 10 [deg].
REQ-MAN-04	The aircraft shall not exceed the load factor of 2.2 [g] during maneuvers.
REQ-MAN-05	The aircraft shall be able to fly with a sideslip angle of 7.7 [deg].
REQ-MAN-06	The aircraft shall be able to perform an emergency landing on Martian soil.
REQ-MAN-07	The aircraft shall be able to withstand gust loads of 15 [m/s] from any direction.
REQ-MAN-08	The aircraft shall not be damaged by local dust storms.
REQ-MAN-09	The aircraft shall be able to fly through the dust storm with maximum winds of 15 [m/s].
REQ-MAN-10	The aircraft shall be able to avoid dust storms with maximum winds of more than 15 [m/s].
REQ-MAN-11	The aircraft shall be able to withstand extreme temperature changes of up to 10 [K/h].
<i>Cruise requirements</i>	
REQ-CRUS-04	The system shall continuously cruise at the optimal speed.
REQ-CRUS-05	The nominal cruise speed shall be at least 111 [m/s].
REQ-CRUS-06	The cruise speed shall not be less than 111 [m/s].
REQ-CRUS-07	The cruise speed shall not exceed 138 [m/s].
REQ-CRUS-08	The cruise Mach number shall not exceed 0.7.
REQ-CRUS-09	The system shall have a service ceiling of at least 1000 [m].
<i>Descent requirements</i>	
REQ-DSCT-03	The descent path angle shall be at most 90 [deg].
<i>Landing requirements</i>	
REQ-LDG-FAPP-01	The system shall be able to scan the ground and detect rocks larger than 0.2 [m] diameter.
REQ-LDG-FAPP-02	Autopilot shall provide automatic landing mode.
REQ-LDG-FAPP-03	The aircraft shall be able to land in low-visibility conditions.
REQ-LDG-TDWN-01	Use of ground effect shall be made to ensure soft landing.
REQ-LDG-TDWN-02	The aircraft shall not exert more than 150 [kPa] pressure on ground during touchdown.
REQ-LDG-TDWN-03	Structural integrity shall be ensured up to 1 [g] during touchdown impact.
REQ-LDG-TDWN-04	The aircraft shall provide pilot and equipment safety during landing.
REQ-LDG-DLRT-02	The aircraft shall decelerate with at least 3 [m/s^2].
REQ-LDG-DLRT-04	The aircraft shall provide steering capability on the ground.

2.3. Trade-off Summary

By Dominik Stiller

The mission can be fulfilled by a range of design with different methods for lift generation, power and propulsion. After brainstorming all possible design concepts and eliminating the infeasible ones, five promising options remained (Figure 2.2).

Preliminary sizing of these options provided the basis for a quantitative trade-off (Table 2.3). The criteria were selected based on customer requirements and distinguishing aspects. All criteria had the same weights. The tiltrotor design scored the highest and was therefore selected. This decision was robust under a sensitivity analysis with respect to sizing assumptions and criteria weights [3].

2.4. Concept Introduction

By Javier Alonso García

The tiltrotor aircraft is a very novel design of which only a handful exist, the most famous one being the Bell-Boeing V-22 Osprey. It differs from normal propeller-powered aircraft in the sense that it is able to

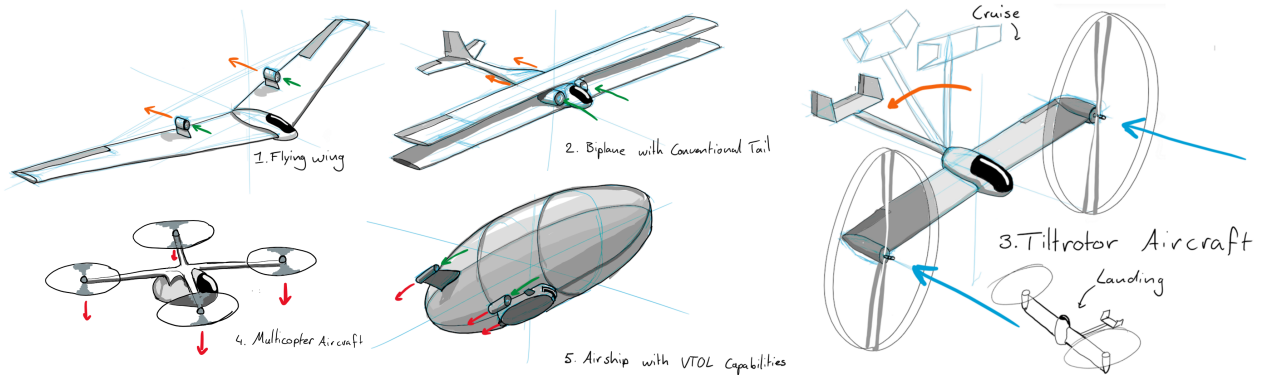


Figure 2.2: The five concepts considered for the trade-off.

Table 2.3: Trade-off summary including criteria values and scores. The total score in the last column indicates the overall goodness of the design. The tiltrotor design has the highest score and is selected.

	Range at 350 kg payload [km]	Landing/take-off distance [m]	Feasibility	Sustainability	Score	
Blended wing	1779	GREAT	ACCEPTABLE	Min. TRL of 4 (Power) and <1000 existing designs ACCEPTABLE	Emits carbon, and the energy source is not renewable GOOD	44
Biplane aircraft	2157	EXCEPTIONAL	ACCEPTABLE	Min. TRL of 4 (Power) and >1000 existing designs GOOD	Emits carbon, and the energy source is not renewable GOOD	56
✓ Tiltrotor	1885	GREAT	0 EXCEPTIONAL	Min. TRL of 6 (Control) GREAT	Rotor blades are not recyclable, but uses batteries GREAT	81
Multicopter	1270	GREAT	0 EXCEPTIONAL	Min. TRL of 4 (Power) and <1000 existing designs ACCEPTABLE	The energy source is not renewable, and rotor blades are not recyclable GOOD	62
Airship	480	UNACCEPTABLE	0 EXCEPTIONAL	Min. TRL of 4 (Power) and <1000 existing designs ACCEPTABLE	Emits carbon and hydrogen, and the energy source is not renewable ACCEPTABLE	38

rotate the propellers with respect to its main body in order to combine the Vertical Take-Off and Landing (VTOL) capabilities of a helicopter with the efficiency in cruise of a propeller aircraft. Another advantage of this design as opposed to more traditional designs is the possibility of using an electrical engine, which is currently the only possibility for an aircraft engine on Mars.

This design concept, however, also has a number of challenges that need to be overcome. Firstly, the transition between helicopter-mode and aircraft-mode is a very complicated maneuver which introduces a number of risks for the crew. Furthermore, the take-off process is naturally unstable and will thus require an on-board computer and extensive training of the pilots in order to perform it.

2.5. Flow Diagrams

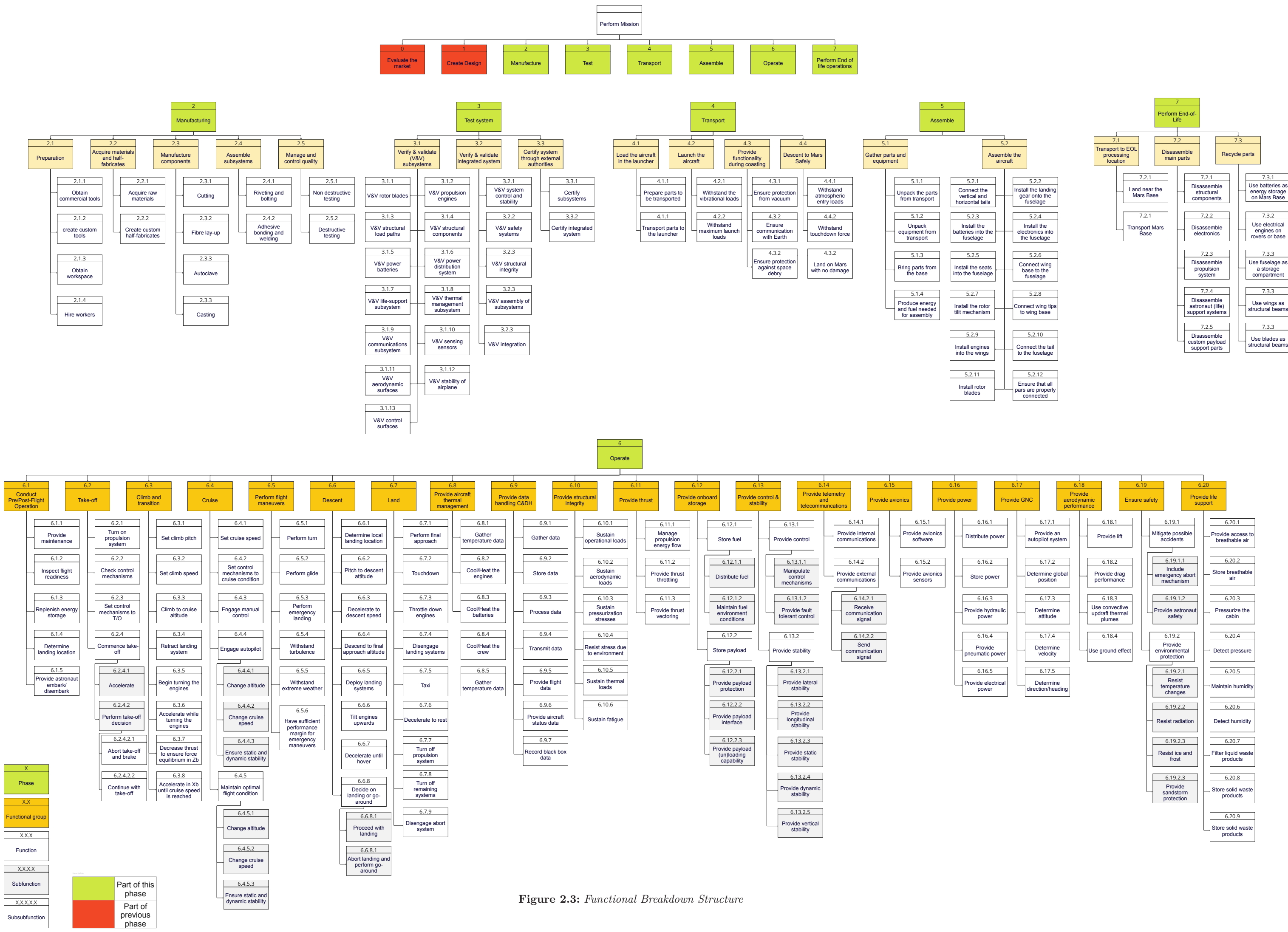
2.5.1. Functional breakdown structure

By Patrick Kostelac The Functional breakdown structure (FBS) provides a hierarchical view of the functions to be performed by the system in the form of an AND tree. This means that any block is made up of the sum of the blocks under it. The advantage of the FBS is that it can display functions that are difficult to include in the FBS, since these are inherently in some kind of chronological order, i.e. in a "flow". The FBS thus allows to showcase functions that are time-independent or that need to be fulfilled at all times, such as providing power or ensuring structural integrity. The FBS does not provide information on the flow of functions, which is done by the Functional flow diagram (FFD). The FBS is shown in Figure 2.3. Each function is given a unique ID for identification. The mission is comprised out of seven parts: Evaluating the market, Creating the design, Manufacturing, Testing, Transporting, Assembly, Operation and End of life (EOL) operations. At this stage of the process the first two parts have already passed and are thus not shown in the FBS which focuses on the future of the project. The functional breakdown structure

can be used as tool to check what tasks have been completed and what tasks need to be completed for successful operation of the aircraft. Due to the FBS not being ordered, it will only be used as a checklist rather than an actual guide of what needs to be performed at what times.

2.5.2. Functional flow diagram

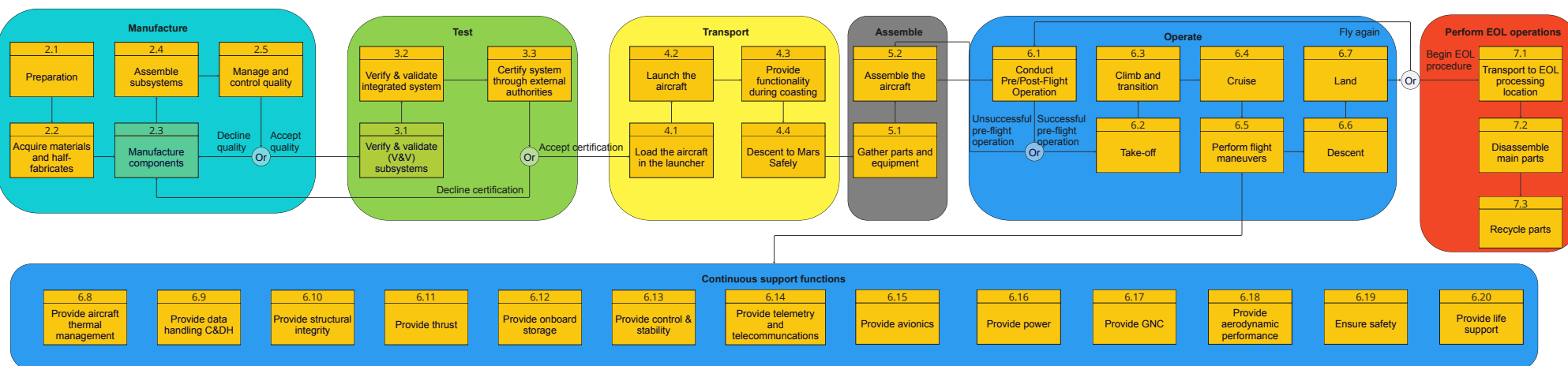
By Patrick Kostelac, Freek Braspennincx, The FFD shows the logical flow of the functions of the system/mission. Contrary to the FBS, the steps in which the functions are performed matter. Functions can be in series, in parallel using AND gates, or optional based on a certain criterion using an OR gate. Each function is given a unique ID, related to the functions in the FBS. Some functions are split up into lower-level functions; this is done for up to a maximum of 5 levels deep, but on average functions are detailed up to 3 levels deep. The FFD is shown in Figure 2.4. The functions followed from the brainstorming sessions on what the system should perform. It consists of pre-launching phases such as manufacturing and testing, mission phases, during which the system should fulfill its mission, and the end-of-life phase. The mission phase is subdivided into functions before arrival on Mars, assembly on Mars, and the flight profile. It is important to note that the functions that were time-independent and easily shown in the FBS are also here. These continuous functions are grouped into the "Continues support functions" block and are shown in parallel to other functions in the FFD, to display the fact that these functions are performed at all times. The FFD will be used throughout the future stages of the project as a guide. The FFD shows step by step the actions that need to be taken to design, manufacture, transport and perform the mission. When it comes to production and transportation a Gantt chart is used as it contains all the information as the FFD with the addition of the time taken for each action. FFD however will be used during the mission itself, it contains the nominal mission and once the astronauts are on Mars they will follow the FFD to execute the mission.



Level 1:



Level 2:



Level 3:

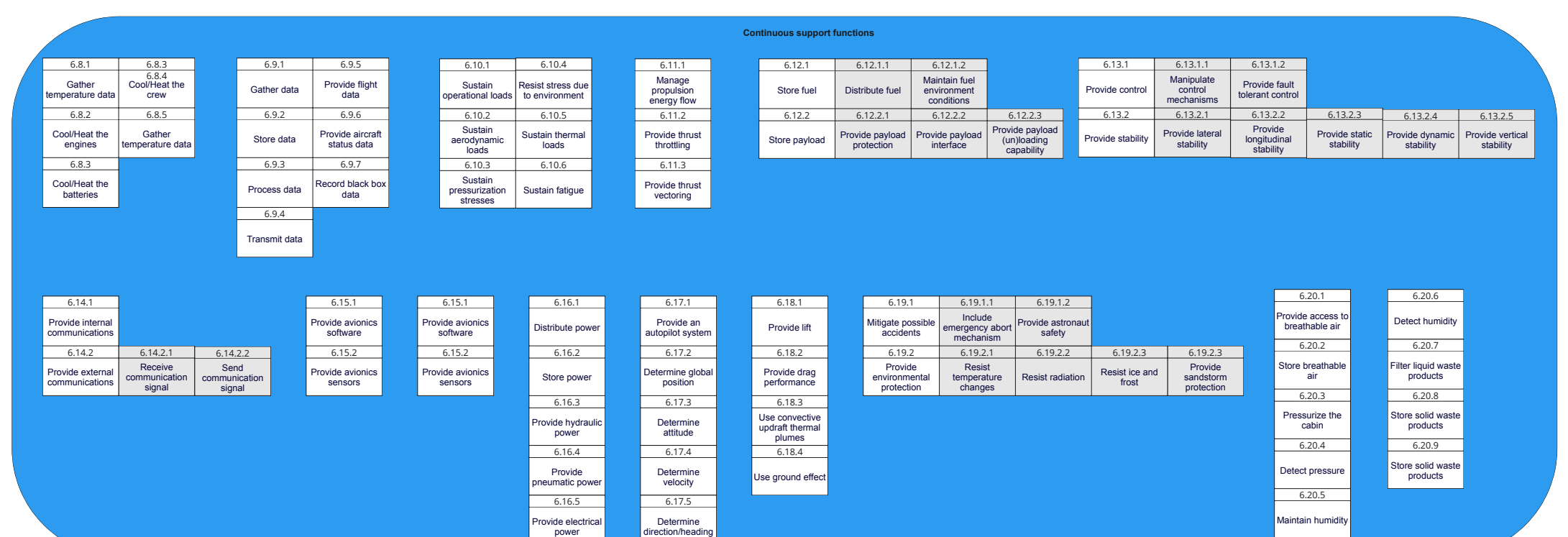
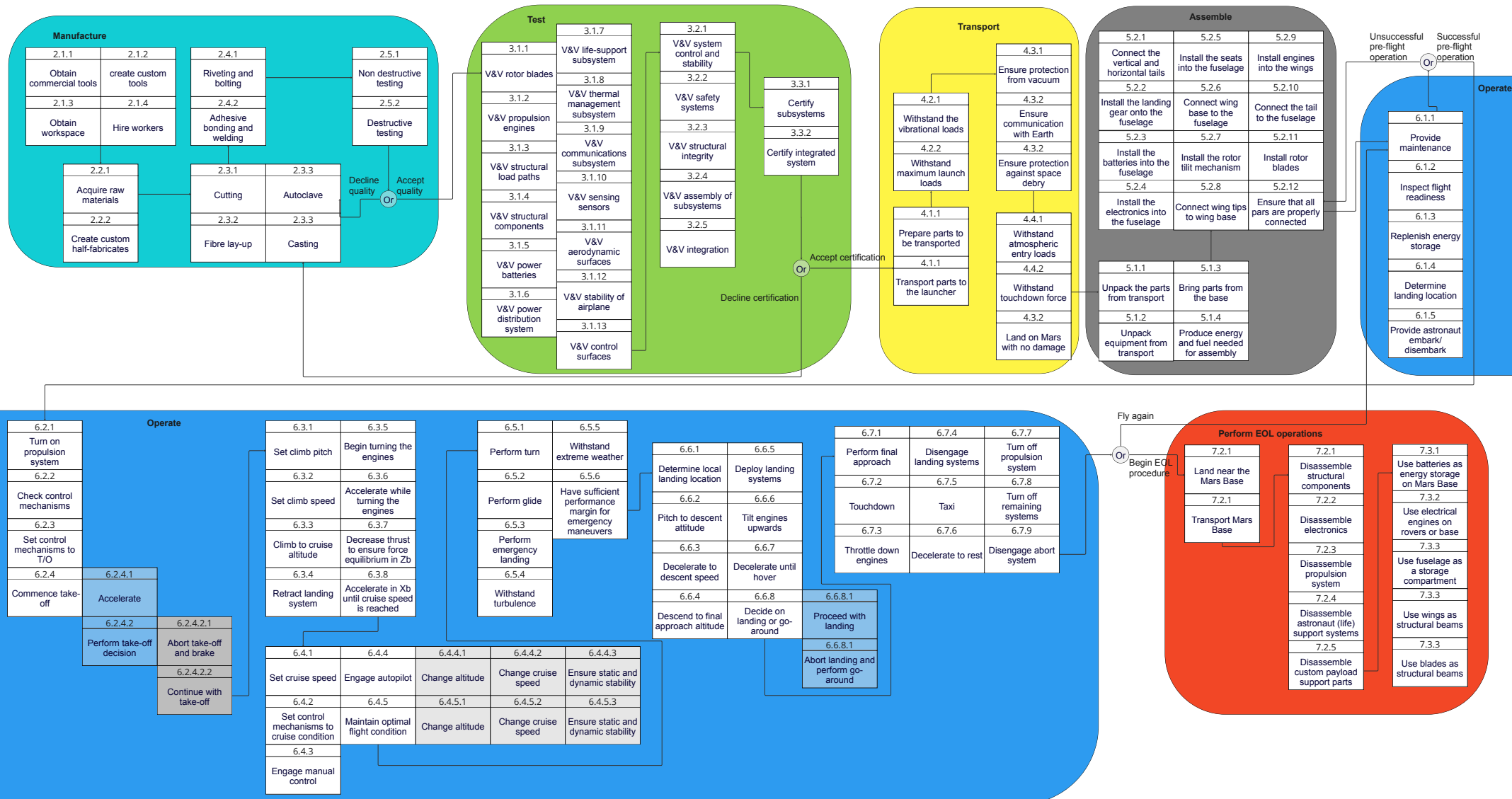


Figure 2.4: Functional Flow Diagram

2.6. Preliminary Sizing

By Javier Alonso García

Some preliminary values were obtained for the tiltrotor aircraft which were used in the trade-off and as starting point for this design phase.

Firstly, the rotor blades were sized, which yielded a total of 24 blades distributed between 2 sets of 2 counter-rotating rotors. Each of these rotors were 10.4 m in radius, require a power of 56.52 kW and produce a maximum thrust of 2.789 kN. Due to time constraints, the interaction between the rotors was not analyzed in detail, but was rather analyzed statistically by stating that 2 counter-rotating rotors produce 88% of the thrust that both rotors would produce on their own. The overall mass budget of the propulsion subsystem can be seen in Table 2.4.

Secondly, the wings were sized. In order to obtain enough lift to sustain the aircraft during cruise with the C_L of the S1223 airfoil at 6 deg angle of attack, a total area of 112.7 m² were required. Adding the constraints that the span needed to be at least 3 times the rotor radius and that the Aspect Ratio (AR) needed to be at least 10, the calculated wingspan and chord were 33.57 m and 3.357 m. Due to time constraints, no taper or sweep was considered, making the wing planform a simple rectangle. The weight of the wings was estimated using relationships from Torenbeek [4], resulting in the values seen in Table 2.4.

The power subsystem was then sized. This was done by calculating the drag of the wings and estimating the drag of the body, again using relationships from Torenbeek [4]. The total drag was then calculated to be 739.5 N. Knowing this and the take-off thrust, it was calculated that the aircraft would need to provide 226.1 kW of power during cruise, consuming a total energy of 18.84 kWh during take-off and a power of 82.16 kW during cruise, consuming a total energy of 205.4 kWh. Batteries with a power and energy density of 1317 W/kg and 437 Wh/kg respectively were found on literature and chosen for the design, resulting in a total battery mass of 878 kg after applying a margin of 30% to account for degradation. Additionally, half of the wing area was covered in space-grade solar panels, adding an extra 99.17 kg to the design.

After these three subsystems were sized, statistical relationships from Torenbeek [4] were used to obtain the preliminary mass of the tail group and fuselage group, which yielded 31.48 kg and 196.4 kg respectively.

Table 2.4: Preliminary mass budget

Subsystem	Propulsion	Power	Wing	Tail	Fuselage	Total
Mass [kg]	1062	977.2	111.5	31.48	196.4	2382

Finally, regarding the performance of the aircraft, the rate of climb in take-off was 2.3 m/s, while in cruise was 62.5 m/s. Furthermore, the range of the aircraft at 350 kg of payload was 1850 km, and the maximum payload was 430 kg, with a range of 1700 km.

2.7. Budget Management

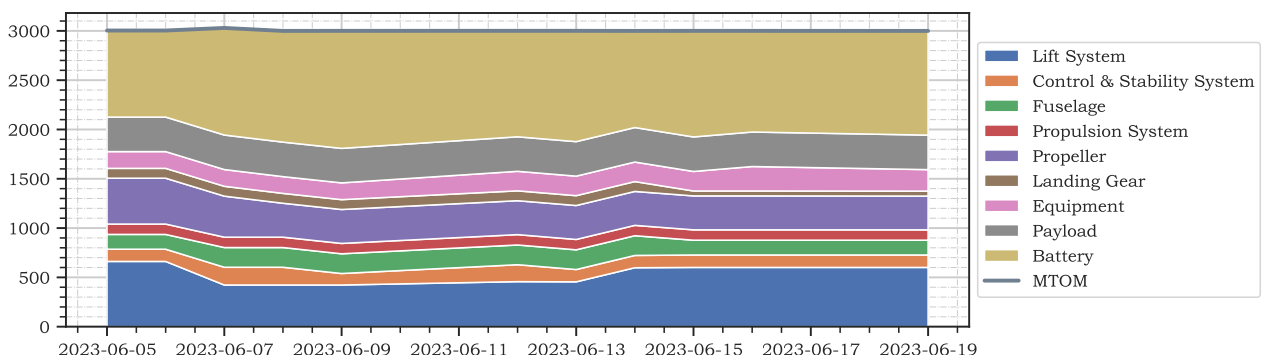
By Freek Braspenning

At the end of the baseline report, the first estimate for the budget breakdown was established. In this first estimate, the design concept was not yet pinned down, many of the subsystems were generalized to not constrain the final design. This led to large deviations from the next iteration of the mass budget, which was made at the end of the midterm report, as shown in Table 2.5. The most notable deviation in the mass budget is for the propulsion system due to the large rotors needed to sustain hover and vertical climb. Furthermore, the choice of electric propulsion has led to the mass budget for fuel to transfer to the mass budget of the power system.

Table 2.5: Mass budget from the baseline report and the midterm report

Aircraft System	Baseline Report Mass [kg]	Midterm Report Mass [kg]
Lift System	755	111.5
Control & Stability System	12	31.48
Fuselage	213	196.4
Propulsion System	281	1062
Landing Gear	61	-
Equipment	198	-
Power System	60	977.2
OEM	1580	2379
Payload	350	350
Propellant	770	-
MTOM	2700	2729

From the midterm, the mass has been updated daily to make sure each subsystem stayed within limits. This evolution of the mass budget throughout the final phase of preliminary design is presented in Figure 2.5.

**Figure 2.5:** The evolution of the mass budgets throughout the final phase of the preliminary design

Besides a mass budget, a power budget was set up as well. While a preliminary mass budget was made after the midterm in order for all subsystems to stay within bounds, the power budget was a result of each subsystem requiring a certain amount of power. The power budget became a result of the power subsystem sizing and can be seen in Section 4.6.

2.8. Sustainability

By Patrick Kostelac

This section highlights the sustainability considerations that influenced the design decisions during the final concept development. Since sustainability is a very broad term, first a definition of sustainability was agreed upon. We define sustainability after Brundtland [5]:

"Meeting the needs of the present without compromising the ability of future generations to meet their own needs."

Since the future of humanity may be multi-planetary, we need to consider the needs of future generations on both Earth and Mars. This means that both the development, design, and manufacturing of the system

on Earth and the operations of the system on Mars should be sustainable. During the midterm phase of the project, the sustainability goals for the final design have been set to be:

- Use in-situ, renewable fuels
- Use non-toxic, abundant, recyclable materials
- Evaluate manufacturing processes and their impact on Earth
- Evaluate assembly process and its impact on both Earth and Mars
- Evaluate the impact of transportation on Earth atmosphere
- Evaluate the impact of pollution on the Martian atmosphere and potential life on Mars
- Evaluate re-usability of system
- Evaluate end-of-life plan

These sustainability goals can be summarized in a larger sustainability framework consisting of multiple parts. First the manufacturing and assembly processes are considered, second the life cycle assessment is performed identifying all emissions and resources used during operations. Lastly, the circular design approach which looks at the end-of-life plan and the re-usability of the system is implemented.

2.8.1. Manufacturing and assembly

The material choice as well as the manufacturing method have a large consequence on the sustainability of the product. Due to the very high required performance of the aircraft, the materials that can be used are highly limited leaving us with only carbon fiber composites. Carbon fiber composites have a high embodied energy at $(183 - 286) \text{ MJ/kg}$ ^[6]. In order to decrease the embodied energy recycled carbon fibers with improved physical properties recovered by using Nitric acid are used during on Earth manufacturing ^[7]. Another large factor impacting the materials are the batteries used for the design. The aircraft uses solid state batteries, which have reduced environmental impact when compared to other high performance batteries such as Lithium-Ion batteries ^[8].

In order to make the manufacturing process as sustainable as possible, the manufacturing process will be optimized in order to minimize energy consumption. Energy efficient equipment with incorporated heat recovery systems will be used for the autoclave. Additionally, renewable energy sources will be used for manufacturing. The production shall also employ lean manufacturing method which aims to minimize all waste. Lastly, the sustainability will be improved by closely collaborating with the supply chain and ensuring that minimum emissions are created during transport.

Finally when it comes to assembly on Mars, the assembly on Mars shall emphasize local resource utilization wherever possible and shall minimize the transport of materials from Earth, reducing the energy requirements. The use of renewable energy sources for assembly are vital, thus electric tools powered by solar power shall be used for assembly. Additionally only common tools shall be used for assembly and those tools will then later be used for everyday operations on Mars

2.8.2. Life cycle assessment

The life cycle assessment quantifies the envirometal impact of the product. The impact will be assessed both on Earth due to the transportation and on Mars due to the operation of the vehicle. Once the aircraft is created, it will need to be transported to the launch site and launched to Mars. In order to minimize the transportation to the launch site, the aircraft will be built on the launch site itself, which is a common practice in the space industry. The launch will produce 538 metric tonnes of CO_2 assuming a Starship transport vehicle.⁴. In order to compensate for the amount of CO_2 that will be produced, 630,000\$ worth of carbon credits will be purchased which will completely offset the pollution caused by the rocket launch.

Once the aircraft reaches Mars, the operational phase begins, where the emissions and energy consumption of the aircraft are considered. As an electric aircraft, the power provided will come directly from the Sun making it fully renewable and utilizing of in-situ resources. In order to make the aircraft as sustainable as possible, maximizing energy efficiency will be crucial during the operational phase. This will

⁴<https://everydayastronaut.com/rocket-pollution/>

reduce the amount of batteries needed and greatly help the sustainability efforts. Other than just increasing the efficiency of the aircraft, mission planning and optimization will be employed. By optimizing flight paths and mission duration, the energy consumption will be minimized. This can be done using advanced modeling techniques to take into account the Martian atmospheric conditions. Sustainable operations involve efficient maintenance and repair procedures. Making the design modular will not only make it easier to transport but it will also make it easier to maintain and repair. Lastly, increasing the lifetime of the mission increases sustainability as it reduces the need for additional missions. The lifetime will be increased by conducting regular maintenance and making sure that the design is robust, such that it can withstand harsh Martian conditions.

2.8.3. Circular design approach

The goal of the circular design approach is an important concept that maximizes resource utilization and minimizes waste generation by creating a closed loop system. This involves creating a product such that its components can be repurposed or recycled at the end of the operational life. For example the degraded batteries can be repurposed for base energy storage. They can be used to store the energy generated by solar panels or wind turbines. The engines can be repurposed to power a rover or serve an on-base purpose, reducing the need to send extra engines on future trips. The body of the aircraft can be repurposed as a shed or a storage system. The wings and blades can be repurposed as structural beams which are used for construction on the Mars base as they don't deteriorate significantly due to fatigue. Their lightweight and durable nature makes them perfect for supporting infrastructure on buildings. By re-purposing various components the circular design approach ensures that the resources are conserve and potential waste is removed. Other parts of the aircraft such as electronics, sensors, or some smaller components can also be salvaged and repurposed withing the Martian base serving different functional needs.

Subsystem Design Methods

The successful design of a Martian aircraft relies on a multidisciplinary and iterative approach that takes into account factors such as aerodynamics, power systems, propulsion, communication, stability and control and many others. Each subsystem plays a vital role in ensuring the aircraft's functionality, safety, and overall mission success. Throughout this chapter, the methods and techniques used to design these crucial subsystem will be explored. Each subsystem is designed according to the requirements set in Chapter 2. All of the formulas used in order to achieve the final result are documented allowing for easy implementation of our design methodology in future projects.

3.1. N² chart and iterations

By Patrick Kostelac

This section describes the iterative design process and its importance in the development of the Martian aircraft. It describes the steps taken in order to facilitate easy iteration at each step, such as making the design modular ensuring that adjustments can be made efficiently. This was done by modifying the code used for the design process and making it easy to change input values. Additionally, an N^2 chart is utilized to visualize and analyze the interdependencies of different subsystems. Clear communication channels are established between different subsystems design teams, enabling seamless coordination and integration. This approach fosters effective feedback loops where insights from one subsystem can be used in other subsystems, such process is key to an effective design of the Martian aircraft.

3.1.1. Iterative design

The iterative design process is a cyclical approach to design. It is applied to the aircraft development, where the design steps are continuously repeated in order to refine and improve the results. This methodology transforms the aircraft design into a dynamic and ongoing project, allowing for regular changes and improvements to the design instead of a one-time completion. The iterative design process eliminates possible errors due to the lack of communication and well as increases the overall quality of the design.

During the final design phase, the iterative design has been employed both on a system and subsystem level. The first design iteration created was the concept made for the mid term report which was then continuously updated and improved. The iterative design process is necessary due to the chronological nature of individual subsystem design. During the first iteration steps, the majority of the design has not yet been defined which is why assumptions needed to be used. As the design progressed these values were continuously updated and made more accurate. In order to make this iteration as efficient as possible, it was decided to use Object Oriented Programming (OOP) which allows for easy changes of input values, speeding up the iteration process. As a general rule, the values were changed until the difference between the new and the old values were less than 1%. In order to perform the iterative design on system level, weekly team meetings were held. During the meetings, each subsystem would present the new updated results found through the week and discuss any challenges, improvements, or modifications that arose during the iteration. This collaborative approach ensured that the entire team had visibility into the progress of each subsystem and could provide input and suggestions for further refinement. The iterative design process on a system level also facilitated the identification and resolution of any conflicts or dependencies between subsystems. By regularly reviewing and integrating the updated results from each subsystem, potential issues or inconsistencies were detected early on, allowing for prompt adjustments and coordination between teams. In order to identify all of the interdependencies and ensure smooth communication a N^2 chart was used.

3.1.2. N² chart

The N^2 chart serves as a powerful tool for visualizing and analyzing the interdependencies among system elements during the design phase. Represented as a matrix, the N^2 chart depicts the functional and physical interfaces between various subsystems. By plotting the outputs of each system along the horizontal axis and the inputs along the vertical axis, the chart highlights the connections and interactions between different subsystems. The N^2 chart is particularly valuable for identifying key subsystems that have a significant influence on multiple other subsystems. In the case of the Martian aircraft, those subsystems were: sensing, stability and control and the structures. By pinpointing these key subsystems, extra resources were allocated in order to ensure the accuracy of the information and the integration engineer paid special attention that all of the newest information was available to and from these subsystems. Furthermore, the N^2 chart is used to determine which subsystem couples are highly dependent on each other. The subsystem combinations identified were power and propulsion, stability and control and aerodynamics, sensing and communications. These subsystem combinations are highly dependent on each other and it was made sure that the communication between the two is constant and that the responsible engineers work together when necessary.

The N^2 chart also helps in identifying design constraints. Subsystems that are highly dependent on numerous other subsystems can face significant design constraints. Modifications or improvements in these subsystems may require coordination with and adjustments in multiple other subsystems. Structures and thermal control were identified as highly dependent. This meant that during the design of those subsystems, careful consideration had to be given to the interdependencies and potential trade-offs with other subsystems. For instance, in the case of structures, changes in material selection or design modifications could have implications for weight distribution, aerodynamics, and overall system integrity. Similarly, in the thermal control subsystem, alterations to heat dissipation methods or insulation materials could impact power consumption, component temperatures, and overall thermal management. Therefore, close collaboration and coordination between the structures, thermal control, and other relevant subsystem teams were essential to ensure that design changes in one subsystem were effectively communicated and accommodated by the interconnected systems. This iterative and collaborative approach enabled the identification and resolution of design constraints, leading to a more integrated and harmonious Martian aircraft design.

	- Flight path - Incoming communications with satellites/base	- External temperature -Airspeed -Current location						-State of the external structure		
Communications		-Required mission			-Required power for communications				-Outgoing communications with satellites/base -Periodic status reports to base	
-Possible failure report -Current state	Sensing	-Attitude -Velocity -Need to transition between T/O and cruise configuration		-Need to transition between T/O and cruise configuration -Incoming airspeed -Speed of sound	-Required power from sensors -Solar irradiance	-Required temperature change of the batteries, payload and engines -External temperature	-	-Required aluminum tail for transmission of signals		
-required state data	-Current attitude	Stability and control	-Required pitch rate -Required yaw rate -Required roll rate	- Required thrust - Required thrust vectoring	- Required power to move control surfaces -Required power to tilt the rotors		-Control surfaces movement -Size and Location of the tail			
		-desired Cl for cruise	Aerodynamics	Drag during cruise			-Wing loading	-Maximum skin roughness		
	-Rotor's rotational speed -Rotor's orientation	-Maximum achievable thrust	-Propellant wing interaction -Rotor radius -Optimum thrust	Propulsion	- Required rotor power for T/O, cruise and manoeuvring -Required energy capacity	-Optimum engine temperatures	-Rotor-induced vibrational loads, axial loads and moments			
-power allocated for communications	-Battery levels -Expected remaining range -Expected recharge time -power allocated for sensors	-power allocated for actuators		-Maximum available power	Power	-Optimum battery temperatures -Maximum available power	-Battery size and mass			
	-Current temperature of the batteries, payload and engines				-Required power for heating/cooling	Thermal control	-Induced thermal loads -Opening/closing of vents for cooling/heating	-Emissivity and absorptivity requirements		
	-Structural integrity -Current fatigue levels	-Mass moment of inertia -CG location	-Maximum wing span			-placement of the engines and batteries	Structures	-Geometry -Loads	-Need to do repairs/maintenance	
			-Skin friction	Weight of the aircraft		-Insulation capabilities	Materials	-Minimum allowable thicknesses -Allowable stresses		

Figure 3.1: The N^2 chart

3.2. Wing Sizing Method

By Adrian Bení, Pedro Santos

The sizing of the main wings is an iterative process. It is initialized with a first estimate based on best performing design parameters as described in the literature. This first design is then customized to the needs of this project mainly due to the dependencies among wing design, power budget, controllability/stability and structural considerations, as defined in the N^2 diagram.

3.2.1. Airfoil selection

Martian atmosphere has density which is approximately 80 times lower than the atmosphere on Earth and this poses driving requirements on the airfoil selection and consequently the whole wing design. The lowest atmospheric density found on Mars is equal to $\rho_{Mars,min} = 0.01 \text{ [kg/m}^3]$ [9, 10] and this is the value for which the aircraft was designed. Airfoil selection also requires knowledge on the operating Reynolds number. This was chosen to correspond to the cruise condition because the wings do not generate lift during the take-off maneuver. The baseline phase revealed that the initial estimate of the mean aerodynamic chord (MAC) was $MAC = 3 \text{ [m]}$. The operating point Reynolds number is then given in Equation 3.1,

$$Re = \frac{u \cdot MAC}{\nu} = \frac{111 \cdot 3}{5.17 \cdot 10^{-4}} \approx 650'000 \quad (3.1)$$

where u is the cruise velocity, and ν is the kinematic viscosity of Martian atmosphere. This results in need for high lift low Reynolds number airfoil. Several airfoils suggested in [11] were considered and the final choice of S1223 airfoil was the result of a trade-off between lift performance and the pitch-down moment an airfoil creates. This was due to stability/controllability constraints.

The lift-drag characteristics of the airfoil were then simulated in XFLR5. Ref. [11] also provides inviscid-theory-based velocity distribution over the airfoil, but because of its very high camber, this was also qualitatively validated via fluorescent oil flow visualization in the open-jet subsonic M-wind tunnel at TU Delft. Similarly, the lift-drag polars generated by XFLR5 were validated in the same wind tunnel.

3.2.2. Overall wing design

There were several wing plan-forms and unconventional overall wing designs considered, mainly due to the power constraints resulting in driving requirements on low drag. [12] provide a study on the induced drag C_{D_i} as function of several unconventional wing designs. This can be seen in Figure 3.2, where the numbers are the induced drag factor, as defined in Equation 3.2,

$$C_{D_i} = \frac{C_L^2}{\pi AR} (1 + \delta) \quad (3.2)$$

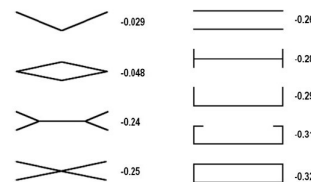


Figure 3.2: Negative induced drag factor δ for unconventional wings [12]

where C_L is the cruise lift coefficient, AR is the aspect ratio and δ is the induced drag factor. The best performing design is the box wing design with $\delta = -0.32$, but later analysis in XFLR5 revealed that the box wing design does not generate better performance than a high aspect ratio conventional single wing configuration, meanwhile adding unnecessary assembly and manufacturing complexity. Especially in low Reynolds number flow, [13] confirm that no benefit can be gained from the unconventional wings. Hence, single wing configuration was selected. This results in higher wingspan, but poses no structural constraints, as, for example, the minimum wing skin thickness for this single wing configuration is dictated by the minimum manufacturable skin thickness, rather than the structural loads. Other drag de-

creasing design options, such as winglets, cannot be used due to the positioning of the engines at the end of the wings.

At the same time, the positioning of the engines creates induced axial and tangential velocity (with respect to the rotation axis of the blades), which locally increases lift and drag in the wake of the propeller blades. Discussion with Dr. Sinnige (TU Delft) revealed that the coaxial counter-rotating propellers of the two engines (per one side) induce negligible tangential velocity, and hence this contribution of the engines was disregarded. The induced axial velocity is also small (as determined in section 3.3), but is taken into account. This creates the need for an iterative wing sizing process which is initialized by lift distribution over the wings in the absence of the induced axial velocity (simulation was done in XFLR5). The lift distribution is adjusted for the presence of the induced axial velocity, which increases the lift of the wing and consequently lower wing installation angle suffices. At this angle the lift distribution must be re-simulated again, resulting in an iterative process. This iterative process was done in a linear fashion. This means that the flow induced by the propellers was superimposed on the flow over the wing in the absence of propellers. This assumption was also validated by Dr. Sinnige. Any non-linear effects of the propeller-wake-wing interaction are advised for further research, but are expected to have negligible effect as the induced axial velocity by the propellers is $V_{rot,ind} = 1$ [m/s], which is less than 1% of the incoming flow velocity $V_\infty = 111$ [m/s].

Moreover, one of the problems encountered in low Reynolds number flight is early flow separation. This was confirmed by the wind tunnel flow visualization conducted during validation. One of the design options which could help mitigate this phenomenon is staggered wing design [14], as shown in Figure 3.3. But none of the currently available flow analysis tools (within the scope of this project) allow investigation of this design and hence further research is advised on this topic.



Figure 3.3: Staggered wing design helps to direct the flow, which would have otherwise separated, according to the shape of the wings staggered behind the first wing. [own work]

3.2.3. Detailed wing parameters

This section justifies the selection of sweep, dihedral, twist, taper ratio, aspect ratio, surface area and wingspan.

According to the experimental and theoretical work presented in Traub et al. [15] performed at $Re = 100'000$, the taper ratio does not affect the lift curve, but higher airfoil efficiency can be achieved with taper ratio $\lambda = 1$. At the same time, Reference [12] provides reporting that taper ratio of $\lambda = 0.4$ is most beneficial independently of the Reynold's number. Hence, value of $\lambda = 0.5$ was chosen as a compromise between the two papers and the simulations done in XFLR5, which are suggestive of lower taper ratio as more effective.

An aspect ratio higher than 10 suffices to reach the saturation part of the range and endurance curves for most low Reynolds' number airfoils [16], hence this value is assumed. According to Gross and Traub [17], the ground effect does not provide any additional noticeable lift. Even worse, ground proximity increases drag. Hence, we assume that the aircraft will not make use of the ground effect. No sweep is needed for the wing because the flight regime is subsonic at Mach number $M = 0.46$. The wing surface area follows directly from the requirement on lift. The cruise condition coefficient of lift was picked to optimize the trade-off between drag performance, small angle of attack and wing span. Small angle of attack is needed for resilience to wind gusts and minimizing drag, while higher angle of attack is needed for acceptable wingspan. Because high wingspan posed no structural constraints, lower cruise C_L was preferred.

A negative tilt is usually applied to the wing tips of conventional aircraft, so that the control surfaces

located near wing tips enter stall later than the middle section of wings and provide controllability during stall. This twist is not needed because of the presence of tilting engines mounted at wing tips. Effectively, these allow for flow vectoring. Moreover, the induced angle of attack at the wing tips compensates for the lack of negative wing twist.

The dihedral angle is set to zero because of natural stability of high wing configuration. The surface area is defined simply as the consequence of the required lift and operational coefficient of lift, as given from Equation 3.3,

$$S = \frac{L}{C_L \frac{1}{2} \rho V^2} \quad (3.3)$$

where S is the required surface area, L is the required lift, equal to aircraft weight during the cruise condition, C_L is the operational coefficient of lift, ρ is the air density and V is the true airspeed. The wingspan b comes as a consequence of the aspect ratio AR and wing surface area S , as given by Equation 3.4.

$$b = \sqrt{S \cdot AR} \quad (3.4)$$

Lastly, it must be mentioned that global optimization of the wing design parameters was attempted using XFLR5-python linux ubuntu-based interface - xflrpy¹. Unfortunately, this was unsuccessful due to missing implementation of several functionalities in the package. To conclude, it is advised to perform such analysis once the missing functionalities are implemented, which is planned to be done until September 2023. This information comes from the written communication with the package's authors.

3.2.4. Wind and wind gusts effects

Another governing factor influencing the wing design is the magnitude of the martian winds and wind-gusts. According to [18], martian winds follow Weibull probability density function with shape parameter $k = 1.73$ and scale parameter $c = 6.87$ [m/s]. This can be seen in Figure 3.4. This distribution corresponds to the magnitude of the wind speed. Even in the very unlikely event of sudden increase in wind speed by $\Delta V_{wind} = 20$ [m/s], the induced angle of attack is $\Delta\alpha_{wind} = 10$ [deg]. Flight can be sustained in this condition because it falls within the linear region of the lift polar of the wing, shown in Figure 5.2b, as the cruise angle of attack of the wing is $\alpha_{wing} = 1$ [deg]. More importantly, these winds do not occur suddenly and can be adjusted for during the nominal cruise condition.

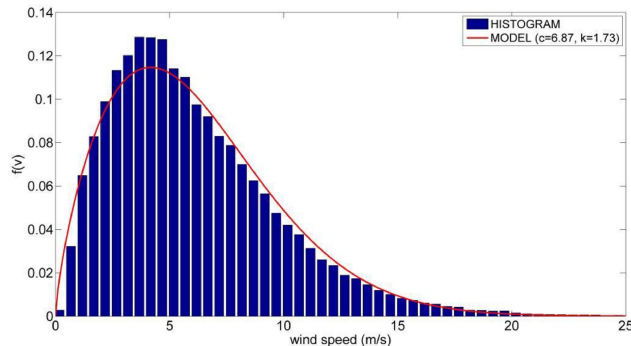


Figure 3.4: The best-fit Weibull probability density function (red line) of the full Rover Environmental Monitoring Station (REMS) wind dataset (blue histogram) [18].

The wind gusts pose even lower constraints. The maximum wind speed of wind gusts measured within the Jezero crater (diameter of 1200 [km]) is $\Delta V_{gusts} = 15$ [m/s], as reported in [19]. This results in the induced angle of attack is $\Delta\alpha_{gusts} = 7.7$ [deg].

¹URL: <https://github.com/nikhil-sethi/xflrpy> [cited 2023-06-20]

3.2.5. Control surfaces - ailerons

Aileron surfaces were sized in accordance to the requirements stipulated by the controllability. These are the minimum required roll moments generated by the ailerons. The aileron deflection angle was limited to $\delta_{\text{ailerons}} = 20$ [deg], which allows to exceed the minimum roll requirements three fold at aileron span equal to half the wingspan. This was done as a safety measure to mitigate any risks associated with lowered ability to roll due to wind gusts or constant winds.

3.3. Rotor Sizing Method

By Sebastian Harris

The sizing of the rotors is a process that follows a set of steps in order to ensure the correct influences are used. To begin, some assumptions are made to allow for adequate detail given the available time-frame.

3.3.1. Upper Rotor

The Windward rotor is the rotor that is the most upstream. In the helicopter configuration, it is the upper rotor. The sizing of this rotor was made according to the Combined Momentum and Blade Element Theory by Prouty [20]. This sizing process determines the blade's performance in hover and allows to create a baseline from which other performances of the blade can be determined.

The process begins by delimiting the rotor into equal sections, over which its performance will be assumed constant. Similarly, the chord at each of these delimitations is calculated along with the Mach number and the slope of the lift curve. This is done with the following equations:

$$M_{\text{local}} = \left(\frac{r}{R} \right) \left(\frac{\Omega R}{V_{\text{sound}}} \right) [20] \quad a_{\text{local}} = \frac{a}{\sqrt{1 - M_{\text{local}}^2}} [20]$$

Where M is the Mach number, r is the local radius, R is the total blade radius, V_{sound} is the speed of sound on Mars, namely 220 m/s and a is the slope of the $C_L - \alpha$ curve.

Next, the inflow of the rotor is calculated. This velocity is defined as follows:

$$v_1 = \frac{-\left(\frac{\Omega}{2}acb + 4\pi V_C\right) + \sqrt{\left(\frac{\Omega}{2}acb + 4\pi V_C\right)^2 + 8\pi b\Omega^2 acr \left(\theta - \frac{V_C}{\Omega r}\right)}}{8\pi} [20] \quad (3.5)$$

Where Ω is the rotational velocity of the rotor in rad/s , a is the slope of the $C_L - \alpha$ curve, c is the local chord, b is the number of blades, V_C is the freestream velocity perpendicular to the rotor disk area and θ is the twist of the blade. In the case of the upper blade in hover, the freestream velocity V_C is null.

From the inflow, the twist is optimized in order to achieve an equal angle of attack on the entirety of the blade. This process is done via the package *scipy* using the *fsolve* function, which solves Equation 3.6 for θ .

$$\alpha - \left(\theta - \arctan \frac{v_1 + V_C}{\Omega r + V_{\text{tangential}}} \right) = 0 \quad (3.6)$$

Where α is the local angle of attack, θ is the blade twist, v_1 is the inflow, V_C is the freestream velocity perpendicular to the disk area, and $V_{\text{tangential}}$ is the tangential component of the freestream velocity. For the first rotor in hover, the last two are null.

Once the twist is optimized, the angle of attack is calculated, and the lift and drag coefficients are determined for the section. A set of performance derivatives can now be calculated to determine the total performance of the rotor. First, the thrust coefficient, C_T can be calculated.

$$\frac{dC_T}{d\frac{r}{R}} = \frac{b\left(\frac{r}{R}\right)^2 \frac{c}{R} C_L}{2\pi} [20] \quad (3.7) \quad C_{T_{\text{lossless}}} = \int_{x_0}^1 \frac{dC_T}{d\frac{r}{R}} d\frac{r}{R} [20] \quad (3.8)$$

Where b is the number of blades, r is the local radius, R is the total radius, c is the local chord, and C_L is the lift coefficient. As the tip of the blade is exposed to vortices, a correction factor is required; this is determined by the portion of the blade that is exposed to the tip vortex, written as B . The calculation of

this portion and the final thrust coefficient follows from:

$$B = 1 - \frac{\sqrt{2.27 \cdot C_{T_{lossless}} - 0.01}}{b} [20] \quad (3.9) \quad C_T = C_{T_{lossless}} - \int_B^1 \frac{dC_T}{d\frac{r}{R}} d\frac{r}{R} [20] \quad (3.10)$$

Leading finally to the total thrust of the blade defined as:

$$T = \rho R^2 \pi (\Omega R)^2 C_T [20] \quad (3.11)$$

Where ρ is the air density. Next, the torque acting on the blade can be calculated, with the contributions stemming from the profile torque, C_{Q_0} , induced torque C_{Q_i} , and wake rotation ΔC_{Q_i} . These three values are calculated by determining their derivatives, similar to the thrust coefficient.

$$\frac{dC_{Q_0}}{d\frac{r}{R}} = \frac{b(\frac{r}{R})^3 \frac{c}{R} C_D}{2\pi} [20] \quad (3.12) \quad C_{Q_0} = \int_{x_0}^1 \frac{dC_{Q_0}}{d\frac{r}{R}} d\frac{r}{R} [20] \quad (3.13)$$

$$\frac{dC_{Q_i}}{d\frac{r}{R}} = \frac{b(\frac{r}{R})^3 \frac{c}{R} C_L \frac{v_1 + V_C}{\Omega r + V_{tangential}}}{2\pi} [20] \quad (3.14) \quad C_{Q_i} = \int_{x_0}^B \frac{dC_{Q_i}}{d\frac{r}{R}} d\frac{r}{R} [20] \quad (3.15)$$

$$\frac{P_{i_{rotation}}}{P_{i_{thrust}}} = \frac{1}{C_T} \int_{\sqrt{2C_T}}^1 \left(\frac{r}{R} \right)^3 \left[1 - \sqrt{1 - \frac{2C_T}{(\frac{r}{R})^2}} \right]^2 d\frac{r}{R} [20] \quad \Delta C_{Q_i} = \frac{P_{i_{rotation}}}{P_{i_{thrust}}} C_{Q_i} [20] \quad (3.17)$$

From here, the torque and power can be calculated through the total torque coefficient as:

$$C_Q = (C_{Q_0} + C_{Q_i} + \Delta C_{Q_i}) \quad (3.18) \quad \tau = \rho R^2 \pi (\Omega R)^2 C_Q [20] \quad (3.19) \quad P = \rho R^2 \pi (\Omega R)^3 C_Q [20] \quad (3.20)$$

From here, the downwash of this rotor can be calculated. This method computes both axial and tangential velocities based on the loading distributions. First, the normalized radius is calculated as follows.

$$\hat{r} = \frac{r - r_{in}}{R - r_{in}} [21] \quad (3.21)$$

Where r is the local radius and r_{in} is the cutout radius. Next, the reference force is calculated.

$$\tilde{F} = \frac{T}{(R - r_{in}) \int_0^1 \hat{r} (1 - \hat{r})^{0.2} d\hat{r}} [21] \quad (3.22)$$

Where T is the thrust produced by the rotor. The axial force per unit radius, f_x , and the tangential force per unit radius, f_θ , can be calculated using this reference force.

$$f_x = \tilde{F} \hat{r} (1 - \hat{r})^0 \cdot 2 [21] \quad (3.23) \quad f_\theta = f_x \tan \theta [21] \quad (3.24)$$

Where θ is the blade twist. These forces' axial and tangential-induced velocities can be determined as follows.

$$V_{i_{axial}} = \sqrt{\frac{V_\infty^2}{4} + \frac{f_x}{4\rho\pi r}} - \frac{V_\infty}{2} [21] \quad (3.25) \quad V_{i_\theta} = \frac{f_\theta}{2\pi r \rho (V_\infty + V_{i_{axial}})} [21] \quad (3.26)$$

When a rotor is in climb, it requires more power due to the change in potential energy. This additional required power depends on the thrust being produced and the climb velocity. From the thrust, the downwash in hover and in the climb can be calculated as follows:

$$v_{i_{hover}} = \sqrt{\frac{T_{hover}}{2\rho\pi R^2}} [20] \quad (3.27) \quad v_{i_{climb}} = -\frac{V_C}{2} + \sqrt{\frac{V_C^2}{2} + v_{i_{hover}}^2} [20] \quad (3.28)$$

Where T_{hover} is the thrust required per rotor in hover, and V_C is the climb speed. From here, the additional required power depends on the aircraft's mass following the relation of Equation 3.29.

$$\Delta P = mg \left(\frac{V_C}{2} + \sqrt{\frac{V_C^2}{2} + v_{i_{hover}}^2} - v_{i_{hover}} \right) [20] \quad (3.29)$$

3.3.2. Lower Rotor

The sizing of the second rotor follows a similar process to that of the upper rotor. The main difference lies in the additional performance after the first rotor. Instead of prescribing a rotative rate, this is calculated

as a function of the wake of the upper rotor. Using the values found in Equation 3.25 and Equation 3.26, the maximum rotative rate is calculated based on the maximum allowed tip speed as follows:

$$V_{tip} - \sqrt{V_{axial}^2 + (\Omega R + V_{tangential})^2} = 0 \quad (3.30)$$

Given this rotative rate, all the other steps present above can be conducted, leading to the performance of the second rotor in the wake of the upper rotor in hover and vertical climb.

The iterative and design process of these two rotors requires the variation of airfoil, chord, radius, and taper, until an ideal performance is achieved.

3.3.3. Transition

The transition of the aircraft consists of the switch from a vertical flight, where the lift is produced solely by the rotors, to horizontal flight, where the wing produces the lift. This conversion process is complex and, as such, has been simplified to allow for first estimates of the performance in these configurations.

The thrust produced by a rotor disk when the flow is at an angle can be calculated with

$$T = \frac{b}{2\pi} \int_0^{2\pi} \int_0^R \left(\Omega R \left(\frac{r}{R} + \mu \sin \phi^2 \right) \right) \frac{\rho C_L \frac{c}{R}}{2} dr d\phi [20] \quad (3.31)$$

Where b is the number of blades, ϕ the angle between the flow and the normal to the rotor disk, Ω is the rotative speed of the rotor, r is the local radius, c is the local chord and μ is calculated as $\mu = \frac{V}{\Omega R} \cos \phi$.

This thrust can be combined with the angle of tilt and the lift originating from the wing to determine the aircraft's total lift. This ensures the transition phase can be modeled in detail. Although the thrust is calculated, the actual dynamics of the transition will be further discussed in subsection 4.3.6

3.3.4. Cruise

In cruise, two main variables can be modified to determine the rotors' ideal performance: the rotative rate Ω and the collective angle θ_1 . As the twist of the blade has been set by the hover conditions, it is now only possible to rotate the entirety of the blade. The performance of the rotor is calculated with the same process as subsection 3.3.1 although the following modifications are made. The angle of attack of each section is calculated through the blade twist and the collective angle as:

$$\theta = \theta_0 + \theta_1 - \alpha_0 \quad (3.32)$$

$$\alpha = \theta - \arctan \frac{v_1 + V_{cruise}}{\Omega r} \quad (3.33)$$

Where θ_0 is the blade twist, α_0 is the zero lift angle of attack, v_1 is the inflow over the blade section, and V_{cruise} is the aircraft's cruise speed. To determine the ideal performance of the aircraft, the rotative rate and collective angles are modified for both the upper and lower rotor until the minimum power required for the given cruise thrust is determined. Similarly, the maximum thrust given the total power available for the aircraft is determined.

Due to the variety in angles and rotative rates, the calculated angles of attack went beyond the selected airfoil's stall angle of attack. This led to using an estimate for both the lift and drag coefficients in these angles where the lift is proportional to the cosine of the angle and the drag to the sine. The maximum for the lift was determined to be 0.5 while the maximum for the drag is that of a flat plate, 1.28 [22].

3.3.5. Rotor Downwash

When taking off, hovering, or landing vertically, the rotor's downwash will put in suspension particles and create dust clouds. Furthermore, the downwash will dislodge larger particles. The size of these particles is dependent on certain assumptions. One such assumption is that the particles are spherical in shape, homogeneous, and have a drag coefficient of 1. These assumptions are the same as those used in studies conducted by the Department of Defense [23], from which the formulas stem.

First, the maximum radius of a particle can be calculated as:

$$r_{particle} = \frac{V_i^2 \frac{1}{2} \rho C_D}{\rho_{rock} g_{mars}} [23] \quad (3.34)$$

Where V_i is the downwash velocity, C_D is the drag coefficient of the particle, ρ is the air density, ρ_{rock} is the particle density, and g_{mars} is the gravity on Mars. The velocity at which the particle is moving can be calculated with two intermediate parameters, the dynamic pressure q_f and β , which is calculated as follows:

$$\beta = \frac{RC_D \rho 4\pi r_{particle}^2}{\frac{4}{3} r_{particle}^3 \pi \rho_{rock}} [23] \quad (3.35)$$

Finally, the velocity of the particle is calculated as:

$$V_{particle} = \sqrt{\frac{q_f}{\rho}} \left(1 - \frac{1}{\sqrt{\beta} + 1} \right) [23] \quad (3.36)$$

Although this applies to the larger particles, it is also important to look into the particulate cloud created by the rotors. This process requires the use of US customary units to ensure proper results.

$$\frac{u_m}{U_m} = C_u \frac{r}{R}^{-1.143} [23] \quad (3.37)$$

Where u_m is the radial velocity in the wall jet, U_m is the mean momentum velocity of the rotor slipstream, C_u is the wall jet growth constant. From here, the distance at which the dust cloud ends, R_C can be calculated.

$$R_C = R \left(\frac{\sqrt{K_T}}{2.2 \frac{1}{2} \rho U_m^2 C_u^2} \right)^{-0.437} [23] \quad (3.38)$$

Where R is the rotor radius, K_T is the terrain erosion factor, assumed to be 0.025 for loose sand, U_m being the wall jet velocity.

Next, the dust cloud is assumed to begin at a distance $R_V = 0.785 R_C$, and the vortex center is at a height of $Z_V = 0.329 R_C$. Next, the cloud rollup, caused by the vortex at the height calculated beforehand, can be estimated by the following relation:

$$l_V = \exp \left(\frac{2}{\pi} \ln \frac{Z_V}{R_C - R_V} \right) [23] \quad (3.39)$$

3.3.6. Unpowered Rotation

Autorotation is a property of rotorcraft that allows the aircraft to land safely despite a lack of onboard power. This occurs due to the air going over the blades in descent, creating torque on the aircraft and thus keeping the blades rotating at an equilibrium speed. As a first estimate, the autorotative equation is:

$$\bar{V}_D - \bar{v}_1 = \frac{\frac{3}{2} \sqrt{3}}{\sqrt{\sigma} \frac{c_l}{c_d}} \quad (3.40)$$

Where \bar{V}_D is the non-dimensional descent rate, \bar{v}_1 is the non-dimensional induced velocity, σ is the solidity factor, and c_l and c_d are the airfoil lift and drag coefficient respectively. There is a relation between induced velocity, thrust, and rate of descent, which leads to an expression by which the induced velocity in hover relates to the descent speed. For most cases on Earth, this ratio is around 2, and this value is used as a rule of thumb for most cases.

3.4. Stability and Control Method

Stability and control is a vital part of each vehicle. Each vehicle has to be stable and controllable in some way. Especially for helicopter-type vehicles, it is often the case that the vehicle is statically stable but dynamically unstable². Therefore, it is of paramount importance that the system has both controllability for dynamically unstable situations and system inherent static stability. This section will outline the approach taken with respect to static and dynamic stability and the measures taken to be controllable.

3.4.1. Static stability

By Patrick Kostelac

Static stability of an aircraft is its tendency to return to its previous state. In order to achieve static stability, the sum of moments around center of gravity (CG) should be zero and if a disturbance is present, a restoring moment is created. During the design of an aircraft the static stability is generally achieved by positioning and sizing the main wing and the tail, as well as positioning the CG of the aircraft.

The CG is important as the main wings and the tail are positioned with respect to it in order to achieve static stability. The possible CG range of an aircraft is determined through the loading diagram. The loading diagrams takes as input the position and mass of the Operational Empty Weight (OEW), the payload and the astronauts. In order to calculate the new locations of the CG once the payload and astronauts are on board the equation Equation (3.41) is used:

$$x_{CG_{new}} = \frac{m_{old} \cdot x_{CG_{old}} + m_{item} \cdot x_{CG_{item}}}{m_{old} + m_{item}} \quad (3.41)$$

The output of the loading diagram are the most forward and the most aft locations of the CG with respect to the main wing chord.

In order to continue with the stability analysis a preliminary free body diagram (FBD) of the aircraft needs to be constructed. The FBD can be seen in Figure 3.5

Where x is positive to the left and z is positive downwards (body axis system). Th, a.c.w, cg, np and a.c.h indicate the locations of thrust, aerodynamic center of the wing, center of gravity, neutral point and the aerodynamic center of the tail respectively. Their respective longitudinal position, measured from the nose of the aircraft is indicated with Xt, Xw, Xcg, Xnp and Xh with Lh indicating the distance between the wing and the tail. The vertical locations of thrust, and the aerodynamic centers are expressed with respect to cg as Zt, Zw and Zh. The velocity vector is present as V and the change in angle of attack (AOA) is presented as $\Delta\alpha$. Ftx is the thrust force, W is the weight of the aircraft. Ma.c.w and Ma.c.h are the moments around the aerodynamic center of the wing and tail. Tw and Th are the tangential forces and Nw and Nh are the normal forces of wing and tail respectively. Change in the normal forces due to change in angle of attack is represented as ΔNw and ΔNh which per definition act at the neutral point but is also shown at the force location, these are the same force shown in two places. AOA is assumed small meaning that $C_L \approx C_N$.

By using the FBD, the stability requirement on the minimum tail area required can be derived. This is expressed in terms of S_h/S , which is a function of the CG location and can be seen in Equation (3.42)

$$\frac{Sh}{S} = \frac{x_{CG}}{\frac{C_{L\alpha_h}}{C_{L\alpha_w}} \cdot (1 - \frac{de}{d\alpha}) \cdot \frac{l_h}{c} \cdot (\frac{V_h}{V})^2} - \frac{X_{ac} - SM}{\frac{C_{L\alpha_h}}{C_{L\alpha_w}} \cdot (1 - \frac{de}{d\alpha}) \cdot \frac{l_h}{c} \cdot (\frac{V_h}{V})^2} \quad (3.42)$$

Where $C_{L\alpha_h}$ and $C_{L\alpha_w}$ are the lift curve slopes of the tail and wing. $\frac{de}{d\alpha}$ is the downwash, c is the main wing chord and $\frac{V_h}{V}$ is the ratio of the velocities at the tail and wing, with the other symbols explained previously. This relationship produces the stability line which indicates the minimum S_h/S for every CG.

²URL: <http://helicopterblog.com/?p=986> [cited 2023-06-15]

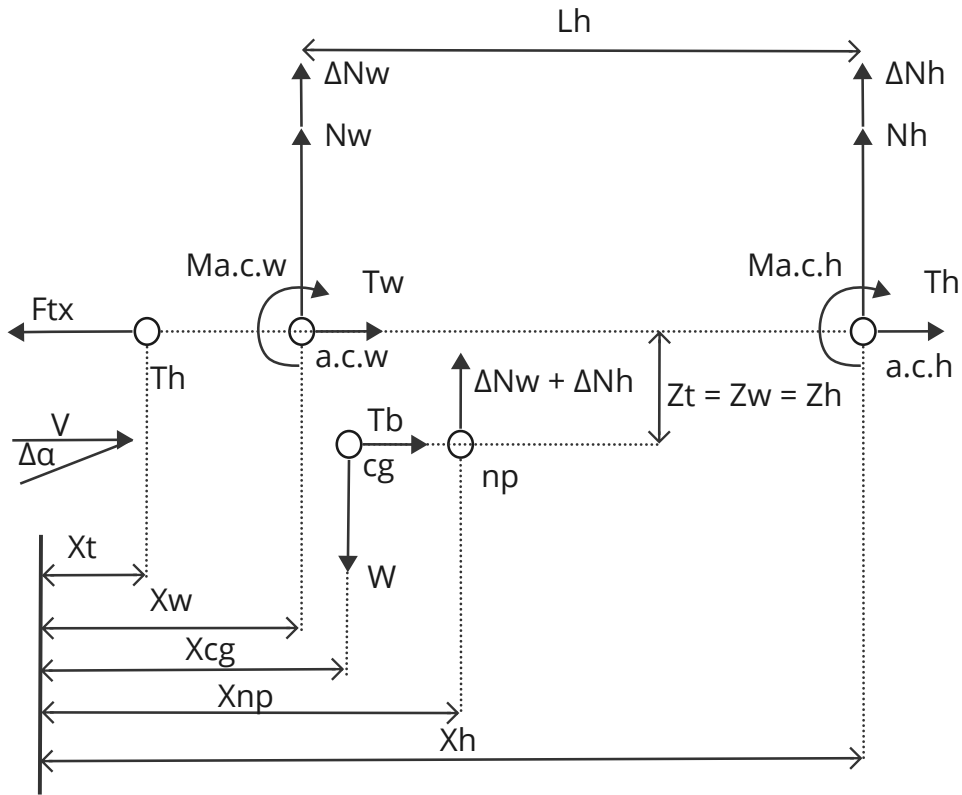


Figure 3.5: Free body diagram of the aircraft

The controllability requirement on the S_h/S concerns the trim condition ($C_m = 0$). The FBD can be used calculate the sum of moments around the CG from which the following equation is derived:

$$\frac{S_h}{S} = \frac{1}{\frac{C_{L_h}}{C_{L_{A-h}}} \frac{l_h}{c} \left(\frac{V_h}{V}\right)^2} \bar{x}_{cg} + \frac{\frac{C_{mac}}{C_{L_{A-h}}} - \bar{x}_{ac}}{\frac{C_{L_h}}{C_{L_{A-h}}} \frac{l_h}{c} \left(\frac{V_h}{V}\right)^2} \quad (3.43)$$

Where C_{mac} is the moment coefficient of the aerodynamic center of the main wing and the rest of the symbols were previously explained. This relationship produces the controllability line which indicates the minimum S_h/S for every CG. The stability and controllability lines are connected to create the scissor plot. The scissor plot shows which criteria is critical; the stability or controllability and thus gives the final value of S_h/S

Once the minimum size of the tail has been derived for a given L_h , the moment equilibrium equations are used to determine the trim condition. The main wing has been sized such that the optimum Lift coefficient (CL) for cruise was found leaving the FBD with four unknowns: F_{tx} , N_h , Th and L_h . The new value for L_h will then be used for new S_h/S beginning the iteration process. Th can be expressed through N_h as was found in xflr5. F_{tx} will be found through the sum of forces in x direction. For simplicity and legibility all of the following equations will be made dimensionless, meaning that ($C_{Ftx} = F_{tx}/qS$) with q the dynamic pressure and S the area of the main wings, this is done for all forces in FBD

$$\sum F_x = C_{Ftx} - C_{Tw} + C_{Tb} \cdot (Sb/S) + C_{Th} \cdot (Sh/S) \cdot (Vh/V)^2 \quad (3.44)$$

Where Sb/S is the body surface area divided by the main wing surface area with other coefficients previously explained. C_{Nh} can be found through sum of forces in z direction:

$$\sum F_z = C_{Nw} + C_{Nh} \cdot (Sh/S) \cdot (Vh/V)^2 - \frac{W}{0.5 \cdot \rho \cdot S \cdot V^2} \quad (3.45)$$

Lastly L_h required for moment equilibrium is calculated through the sum of moments around the CG.

$Lh = x_h - x_w$ with x_w known from the loading diagram, x_h can thus be found:

$$\begin{aligned} \sum M = & C_{m_{acw}} + C_{N_w} \frac{x_{c.g.} - x_w}{\bar{c}} - C_{T_w} \frac{z_w}{\bar{c}} + C_{Ftx} \frac{z_t}{\bar{c}} \\ & + C_{m_{ach}} \left(\frac{V_h}{V} \right)^2 \frac{S_h}{S} \frac{\bar{c}_h}{\bar{c}} + C_{N_h} \left(\frac{V_h}{V} \right)^2 \frac{S_h}{S} \frac{x_{c.g.} - x_h}{\bar{c}} - C_{T_h} \left(\frac{V_h}{V} \right)^2 \frac{S_h}{S} \frac{z_h}{\bar{c}} \end{aligned} \quad (3.46)$$

With the new value of x_h and thus Lh the scissor plot is reconstructed and S_h/S recalculated. The iterative process is continued until the change in both values is less than 1 %. Once the aircraft is trimmed, the change in the moment due to the change in angle of attack ($C_{m\alpha}$) is investigated. This is done with Equation (3.46). The change in normal and tangential force due to change of AOA is found through xflr5. Equation (3.46) is calculated for different angles of attack giving $C_{m\alpha}$. For static stability it is required that $C_{m\alpha} < 0$.

Afterwards, the location of the neutral points is calculated. They indicate the most aft allowable positions of the CG. There are two neutral points, the sick free neutral point which allows for the movement of the elevator and the stick fixed neutral point which has the elevator at a fixed position. If the CG moves behind of the neutral points aircraft becomes statically longitudinally unstable. Therefore, it needs to be ensured that the locations of the neutral points are behind the aft most CG location. The stick free neutral point can be calculated with the following formula derived from FBD:

$$X_{nfree} = \frac{C_{Nh\alpha_{free}}}{C_{N\alpha}} \cdot \left(1 - \frac{d\epsilon}{d\alpha} \right) \cdot \left(\frac{Vh}{V} \right)^2 \frac{S_h \cdot l_h}{S \cdot \bar{c}} + x_w \quad (3.47)$$

Where $C_{Nh\alpha_{free}}$ is the normal force gradient of the tail in stick free configuration, $C_{N\alpha}$ is the normal force gradient of the wing and x_w is expressed in terms of the main wing chord. The stick fixed neutral point can be calculated with the following formula:

$$X_{nfix} = \frac{C_{Nh\alpha}}{C_{N\alpha}} \cdot \left(1 - \frac{d\epsilon}{d\alpha} \right) \cdot \left(\frac{Vh}{V} \right)^2 \frac{S_h \cdot l_h}{S \cdot \bar{c}} + x_w \quad (3.48)$$

Where $C_{Nh\alpha}$ is the normal force gradient of the tail in stick fixed configuration. As long as both of the neutral points are behind the cg, the aircraft is stable and the design can proceed. If one of the neutral points is in front, a design change is required. This will be done by changing the tail airfoil as it affects $C_{Nh\alpha}$ and $C_{Nh\alpha_{free}}$ which can then be increased to achieve stability without negatively impacting the rest of the design.

With the neutral points known, the elevator trim curve is constructed. The elevator trim curve shows the required elevator deflection as a function of the velocity and is calculated according to the following formula:

$$\delta_e = \frac{-1}{C_{m_{\delta_e}}} \cdot \left(C_{m_0} + \frac{C_{m_\alpha}}{C_{N_\alpha}} \cdot \frac{W}{0.5 \cdot \rho \cdot V^2 \cdot S} \right) \quad (3.49)$$

Where δ_e is the elevator deflection, C_{m_0} the moment at zero elevator deflection, $C_{m_{\delta_e}}$ the change in moment due to the elevator deflection, $C_{m\alpha}$ the change in moment due to change in AOA and $C_{N\alpha}$ the change in normal force due to a change in AOA with the other symbols previously explained. In addition to the elevator trim curve, a elevator control force curve can be constructed. The elevator control force curve shows the required control force as a function of velocity. In order for the aircraft to have elevator control force stability, we require $\left(\frac{dF_e}{dV} \right)_{Fe=0} > 0$. The elevator force as a function of velocity can be calculated with the following equation:

$$F_e = \frac{d\delta_e}{ds_e} S_e \bar{c}_e \left(\frac{V_h}{V} \right)^2 \left[\frac{W}{S} \frac{C_{h_\delta}}{C_{m_{\delta_e}}} \frac{x_{c.g.} - x_{n_{free}}}{\bar{c}} - \frac{1}{2} \rho V^2 C_{h_{\delta_t}} (\delta_{t_e} - \delta_{t_{e0}}) \right] \quad (3.50)$$

With F_e the required control force, $\frac{d\delta_e}{ds_e}$ the change in elevator deflection due to a change in elevator area, c_e the elevator chord, C_{h_δ} is the change in elevator hinge moment due to a elevator deflection, $C_{h_{\delta_t}}$ is the change in the elevator hinge moment due to a trim tab deflection.

3.4.2. Vertical Tail Sizing

By Patrick Kostelac

With the final location of the tail known, the vertical tail sizing can begin. The tail is sized according to two requirements, sideslip and one engine out. The sideslip requirement sets the maximum cross wind velocity at $V_{cross} = 15 \text{ m/s}$. With this the minimum vertical tail area can be calculated to be:

$$S_{minside} = \frac{0.5 \cdot \rho \cdot S_{fus} \cdot C_{Dfus} \cdot V_{cross}^2 \cdot SF}{0.5 \cdot \rho \cdot V_{cruise}^2 \cdot (C_{Ydeflect} - C_{Yside})} \quad (3.51)$$

Where S_{fus} and C_{Dfus} are the side area and drag coefficient of fuselage, SF the safety factor and V_{cruise} the cruise speed. The $C_{Ydeflect} = C_{Y\delta r} \cdot \delta r$ is the side force generated by the rudder deflection, $C_{Y\delta r}$ is the change in side force due to a rudder deflection and δr is the maximum rudder deflection. $C_{Yside} = \beta \cdot C_{Y\beta}$ is the side force generated due to the cross wind with β the sideslip angle and $C_{Y\beta}$ the change in side force due to a change in the sideslip angle. The one engine out minimum area can be calculated with the following formula:

$$S_{minengine} = \frac{\Delta Ftx \cdot Y_e \cdot SF}{(X_T - X_{cg}) \cdot 0.5 \cdot \rho \cdot V_{cruise}^2 \cdot C_{Ydeflect}} \quad (3.52)$$

Where ΔFtx is the difference in thrust due to the engine failure and Y_e the distance of the engine to the CG in the y direction. The larger of the two areas will then be taken as the tail area.

3.4.3. Dynamic stability

By Thomas van de Pavoordt

The dynamic stability of an aircraft determines the behavior of an aircraft when disturbed. An aircraft could be statically stable in the sense that it will return to its equilibrium position, but should the motion of the aircraft overshoot the equilibrium position in an oscillating way, it can be dynamically unstable. If an aircraft is dynamically stable, it will always be statically stable as well.

Dynamic stability is often split into two parts; longitudinal and lateral dynamic stability. Both types of dynamic stability will be analysed using 5 typical aircraft eigenmotions. These are the short period motion and phugoid for longitudinal dynamic stability and the a-periodic roll, Dutch roll and spiral for lateral dynamic stability. Dynamic stability analysis is generally analysed through the eigenvalues of a state-space model. For example, for longitudinal or symmetric eigenmotions, one would look at Equation (3.53), which is an aircraft specific derivative of Newton's second law, for symmetrical flight.

$$\begin{bmatrix} C_{X_u} - 2\mu_c D_c & C_{X_\alpha} & C_{Z_0} & 0 \\ C_{Z_u} & C_{Z_\alpha} + (C_{Z_\alpha} - 2\mu_c) D_c & -C_{X_0} & C_{Z_q} + 2\mu_c \\ 0 & 0 & -D_c & 1 \\ C_{m_u} & C_{m_\alpha} + C_{m_\alpha} D_c & 0 & C_{m_q} - 2\mu_c K_{yy}^2 D_c \end{bmatrix} \begin{pmatrix} \hat{u} \\ \alpha \\ \theta \\ \frac{q\bar{c}}{V} \end{pmatrix} = \begin{pmatrix} -C_{X_{\delta_e}} \\ -C_{Z_{\delta_e}} \\ 0 \\ -C_{m_{\delta_e}} \end{pmatrix} \delta_e \quad (3.53)$$

Naturally, to be able to solve this, a significant number of coefficients has to be known, which is not the case for the tiltrotor design. Literature on state-space models of tiltrotor designs, such as the V-22 Osprey, is limited to non-existent and therefore the coefficients are, within the time constraints of the DSE, not determinable. A different approach was thus chosen.

XFLR5 was used to model the wing-elevator-rudder combination along with the desired CG location and masses. A stability analysis can then be performed inside XFLR5, which will utilize the available flaps, elevator and rudder, to calculate the state-space coefficients, eigenvalues of all modes and it can even animate the aircraft's response. These eigenvalues are then reported to determine whether the aircraft is dynamically stable, during cruise, for all eigenmodes.

3.4.4. Cruise control

By Adrian Beňo, Patrick Kostelac

Other than ensuring that the aircraft is controllable via the scissor plot, the control will be demonstrated by creating a flight computer capable of controlling the attitude and velocity of the aircraft. The first step of creating the flight computer consists of deriving the equations of motion for the specific aircraft geometry. The aircraft geometry and aerodynamic behavior are already known from static stability analysis. Given a certain state consisting of the attitude expressed in Euler angles and the linear and angular velocity expressed in the body system, it is possible to calculate the sum of forces and moments around the center of gravity using Equation (3.44), Equation (3.45) and Equation (3.46). Given the sum of forces, the linear acceleration can be calculated through the following formula [24]:

$$\dot{\vec{v}} \Big|_b = \frac{\vec{F}_{net}}{m} \Big|_b - \vec{\Omega} \Big|_b \times \vec{v} \Big|_b \quad (3.54)$$

Where $\dot{\vec{v}}$ is the linear acceleration, \vec{F}_{net} is the sum of forces, m is the mass, $\vec{\Omega}$ is the angular velocity and \vec{v} is the linear velocity. The angular acceleration can be calculated by using the following formula:

$$\dot{\vec{\Omega}} = I^{-1}(\vec{M} - \vec{\Omega} \times I \cdot \vec{\Omega}) \quad (3.55)$$

Where $\dot{\vec{\Omega}}$ is the angular acceleration, I is the moment of inertia matrix and \vec{M} is the moment vector with other symbols previously explained. Once the accelerations are known, the state can be updated to the new values. The linear and angular velocity can be updated by simply multiplying the accelerations by the time increment as can be seen below:

$$\vec{v} = \vec{v}_{prev} + \dot{\vec{v}} \cdot dt \quad \vec{\Omega} = \vec{\Omega}_{prev} + \dot{\vec{\Omega}} \cdot dt \quad (3.56)$$

With dt being the time increment. In order to accurately update the attitude, the change of the body axis system has to be considered. This is done by using a transformation matrix as shown below:

$$\dot{\vec{\theta}} = \begin{bmatrix} \dot{\theta}_1 \\ \dot{\theta}_2 \\ \dot{\theta}_3 \end{bmatrix} = \frac{1}{\cos\theta_2} \begin{bmatrix} \cos\theta_2 & \sin\theta_1 \sin\theta_2 & \cos\theta_1 \sin\theta_2 \\ 0 & \cos\theta_1 \cos\theta_2 & -\sin\theta_1 \cos\theta_2 \\ 0 & \sin\theta_1 & \cos\theta_1 \end{bmatrix} \begin{bmatrix} \omega_1 \\ \omega_2 \\ \omega_3 \end{bmatrix} \quad (3.57)$$

$$\vec{\theta} = \vec{\theta}_{prev} + \dot{\vec{\theta}} \cdot dt \quad (3.58)$$

Here $\vec{\theta} = [\theta_1, \theta_2, \theta_3]^T$ are the Euler angles, $\dot{\vec{\theta}}$ the change in the Euler angles which accounts for the change of the axis system, $\vec{\Omega} = [\omega_1, \omega_2, \omega_3]^T$ and the middle matrix, the transformation matrix from the body axis system in the previous state to the current body axis system. This allows for the state to be updated from the previous values to the new ones, creating the simulation.

In order to control the aircraft during this simulation proportional-integral-derivative (PID) controllers are used. The controllers control the thrust and control surface forces. The method of achieving these forces is determined later. These forces are included in the moment and net force equations used to update the state, allowing for the control of state.

To control the aircraft, a reference state is used. During cruise that is $v_{cruise} = 111 m/s$ with all Euler angles being zero. Force and moment equilibrium are ensured with the use of wing and tail installation angles. With the reference state and the current state, the difference between the two (error) is calculated. Error is used as input for PID controller which apply a correction to their force based on proportional, integral and derivative terms. The controllers were tuned by first increasing the proportional gain until a desired response time was achieved, then by increasing the derivative gain to damp the motion and lastly by increasing the proportional gain to get rid of residual error. Lastly a limitation was set on the maximum force that each controller can exert. During cruise four controllers are used. First controller changes the thrust and takes linear velocity as error, second controller changes the elevator force and takes pitch error, third controller changes rudder force and takes yaw error, fourth controller changes the aileron force and takes roll as error. The PID controllers are individually tuned to get the desired response time. This is done by first changing the proportional gain, then derivative gain and lastly integral gain. The final result is a flight computer capable of controlling the aircraft in cruise while accounting for disturbances.

3.4.5. Take-off, landing and transition control

By Thomas van de Pacoordt

During take-off, landing and the transition-to-cruise phase, the tiltrotor behaves like a helicopter instead of a conventional airplane. It is generally known that a helicopter is dynamically unstable, except for weathervane stability in forward flight, and therefore it was decided to straightforwardly design a PID-controller for these phases, to keep the tiltrotor controllable. The first step is again to determine the correct equations of motion first.

For take-off and landing, the thrust points directly upwards, since the rotors are tilted at 90°. This also means that the wing and elevator are not creating any lift, but are actually assumed to act as flat plates in the flow. This implies their C_d is 1.28, regardless of Reynolds number. Furthermore, the airfoils do not create a constant moment around their aerodynamic center anymore. The sum of forces, thus, essentially reduces to thrust upwards and drag downwards, and their respective created moments due to distance to the CG. Then, Equation (3.54) until Equation (3.58) can be used to determine the state of the system at each time increment.

In order to control the aircraft during take-off and landing, a PID-controller is employed again. The controller, in this case, only controls the thrust. Its reference state will be a constant velocity equal to the maximum rate-of-climb of the aircraft. That is because, at maximum rate of climb, the take-off and landing maneuvers consume the least amount of energy. It is also able to slightly tilt the engines to be able to achieve moment equilibrium with small amounts of thrust in the forward or backward direction. The PID-controller is tuned with proportional, derivative, and integral gain to attain the desired state within a to-be-determined response time.

During transition, controlling the aircraft is much more difficult and it should be noted that very little literature exists on controlling tiltrotor vehicles such as a V-22 Osprey. In theory, the following should happen. The thrust will start slightly tilting forward, creating forward velocity and thus creating a flow over the wing. At first, the forward velocity will not be high enough to create any meaningful lift and the thrust should thus still maintain the required amount to keep the tiltrotor in hover. While increasing the forward speed, the wing will start to create increasing amounts of lift and thus allow the engines to tilt forward more, increasing the forward velocity once more. This cycle will continue until the engines are fully horizontal and the thrust thus points forward, and the wing produces enough lift to keep the aircraft aloft.

In practice, this process will be controlled by the flight computer, or in our case, simulated by PID-controllers. Essentially, in this phase, there is still only one controller, one which controls the thrust. It is assumed that control surfaces such as ailerons or the elevator cannot, yet, provide meaningful control during transition. The PID-controller will control upward thrust to maintain hover in combination with the lift over the wing, and it will allocate any remaining available thrust to obtain forward speed. Its reference state will be 400 km/h in forward speed, 0 km/h in upward speed and 0° in any of the Euler angles. Proportional, derivative and integral gain are once again tuned to achieve the optimal response time.

3.5. Undercarriage Sizing Method

The sizing of the undercarriage is a straightforward process that requires few formulas. The first step is to determine the wheels to be used. For this, each surface has maximum allowable pressure. In the case of Mars, the rocky surface is covered by a layer of dust, which could be considered similar to soft, loose desert sand. This means the maximum allowable pressure for this surface is 170 kPa[4].

Furthermore, the rugged terrain of Mars will require ingenious solutions for tires. The degradation of wheels and environmental damage has been an ongoing issue when considering land rovers. For an aircraft, these problems will only be more important; as such, durable materials that can resist the impacts while inflated will be required.

Regarding the location in the longitudinal direction, a tail dragger configuration was selected due to the

small size of the fuselage relative to the tail. The most important angles in this configuration are the scrape and propeller clearance angles. Due to the size of the propellers, the latter was ignored, as the aircraft was not required to take off with propellers aligned to the wing. From these constraints, the location of the main landing gear and tail landing gear can be calculated while recalling that the tail landing gear must carry at least 8% of the weight for proper steering of the aircraft[4].

Next, the width of the landing gear is calculated by looking at the tip-over angle. This angle must be less than 55° in order to prevent tip-over. This leads to the following expression:

$$y_{mlg} = \frac{l_n + l_m}{\sqrt{\frac{l_n^2 \tan \psi^2}{z^2} - 1}} [4] \quad (3.59)$$

Where l_n is the distance between the center of gravity and the tail wheel, l_m is the distance between the center of gravity and the main landing gear, z is the height of the center of gravity and ψ is the tip over angle which must be less than 55°. It is also necessary to ensure the wing tip has enough clearance in case of a tipping of the aircraft. In this case, a tipping angle is chosen, leading to the expression where the width of the landing gear is also selected:

$$y_{mlg} \geq \frac{b}{2} - \frac{z_t}{\tan \phi} [4] \quad (3.60)$$

Where b is the aircraft's wingspan, z_t is the height of the wing tip, and ϕ is the angle between the landing gear and the tip of the wing.

3.5.1. Crash Landing

In the event of engine failure, the aircraft will enter a state of autorotation, leading to a terminal velocity. From this velocity, the kinetic energy can be calculated as:

$$KE = \frac{1}{2} m V^2 \quad (3.61)$$

This energy must be dissipated by the shock absorbers of the landing gear, for which the energy can be calculated as:

$$E = FS - mgS \quad (3.62)$$

Where F is the force applied, S is the absorber stroke, and mg is the aircraft's weight in Newtons.

3.6. Fuselage Sizing Method

By Pedro Santos

The fuselage design came as a result of structural considerations, the objective to minimize drag, and internal layout requirements such as having optimal space for astronauts, payload, batteries, wingbox, landing gear, and life support. The Cessna 172's interior configuration was used as initial inspiration before margins were added to ensure a larger volume for higher comfort and mobility while using space suits, and dimensions optimized to the larger cockpit and cabin [4].

The fuselage drag calculations were performed using principles outlined in Torenbeek's book, where a C_D is estimated, then multiplied by a correction factor based on the fuselage's geometry. The formulas used can be seen below[4]:

$$CD_f = 0.0031 \cdot r_f \cdot l_f \cdot (w_f + h_f) \cdot \frac{S_{ratio}}{S_{cylinder}} \quad (3.63)$$

Where CD_f is the drag coefficient, r_f is the fuselage's shape factor with value 1.15, S_{ratio} is a factor detailed in Equation 3.64, and $S_{cylinder}$ is the area of the fuselage if it were a perfect cylinder, seen in Equation 3.65. Furthermore, l_f , h_f , and w_f are the fuselage's length, height and width respectively.

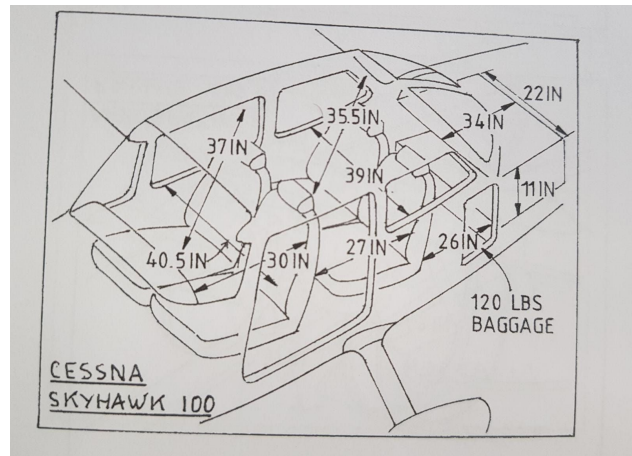


Figure 3.6: Cessna Skyhawk 100-series cockpit layout[4].

$$S_{ratio} = \frac{\pi}{2} \cdot l_f \cdot \frac{h_f + w_f}{2} \quad (3.64)$$

$$S_{cylinder} = 2\pi \cdot \frac{w_f + h_f}{4} \cdot \left(\frac{w_f + h_f}{4} + l_f \right) \quad (3.65)$$

With these formulas, the CD can be obtained, which allows for drag force calculations using the more main stream Equation 3.66.

$$D_f = CD_f \cdot \frac{1}{2} \rho V^2 \cdot S_f \quad (3.66)$$

Where D_f is the fuselage's drag, ρ the air density which is assumed to be 0.01 kg/m^3 , V the true airspeed, and S_f the fuselage's wetted area.

3.7. Power Sizing Method

By Timo de Kemp

This section describes the sizing method of the internal power subsystem, including the engine, gearbox, battery, and solar panel sizing. Off aircraft power generation and charging will be discussed in Chapter 9.

3.7.1. Engine & gearbox sizing

From Section 3.3 the required powers for the rotors were gathered, this required power was different for the upper and lower blade as well as during take-off and cruise. The rotational speeds of the rotors were also gathered from Section 3.3, which also differs in the same way as the power.

The sizing was based on having an engine and gearbox for each rotor, as the power requirements and rotational speeds of the blades were found to be significantly different. The sizing for the engine and gearbox will be described for a single engine, gearbox, rotor group.

Take-off

First the engine is sized for take-off as this will be the most limiting power-wise. The required power is not effected by the gear ratio just by the gear efficiency, which is taken to be 98% for each gear connection [25]. Therefore the engine power, P_{engine} will be the required power from the rotor, P_{rotor} divided by the gearbox efficiency. The gearbox consists of n_{gear} number of gear connections and has an efficiency of

gear efficiency of one gear connection, η_{gear} to the power of n_{gear} as shown in Equation (3.67)

$$P_{engine} = \frac{P_{rotor}}{(\eta_{gear})^{n_{gear}}} \quad (3.67)$$

The engine should be able to provide an continuous power which is higher than the engine power calculated in Equation (3.67). From the technical data of the engine and the power the required rotational speed of the engine was determined. As this was different from the rotational speed of the blades a gear ratio was introduced. The gear ratio was used to reduce the rotational speed of the engine, therefore increasing the torque.

The increase in torque for the engine was needed to overcome the drag and inertia of the blades. The required torque of the rotor was derived from the power and rotational speed, from this and the gear ratio the torque the engine should provide is calculated. The final torque is checked against the maximum continuous torque the engine is able to provide, if the engine cannot sustain this torque a more powerful engine should be selected.

With the engine's rotational speed and torque the efficiency of the engine can be determined from the efficiency map given in its technical data sheet. The efficiencies were given as contours and the lowest efficiency was chosen if in between contours.

Cruise

A similar approach to the take-off is taken for the cruise, however with the engine already selected this step is skipped. The required power was still calculated and from this the engine setting was determined. Together with the rotational speed of the rotor in cruise the cruise gear ratio is determined. It was found that this ratio was always higher than the take-off one. Therefore requiring some kind of adjustable gear ratio, a gearbox. The torque the engine has to provide due to the rotor and gear ratio was calculated as in the take-off case and checked to the torque limits of the engine. Finally the efficiency is determined using the explained approach.

Due to the magnitudes seen in gear ratios the gearbox was designed to get an idea of the size required. To achieve the gear ratio required for take off while keeping the size and mass of the gearbox small 2 sequential gears were used. To be able to change the gear ratio, on the right side of the gearbox shown in Figure 3.7 a single one-to-one gear is used, to increase the gear ratio for cruise another gear ratio is introduced. Letting the shaft that drives the blades grip to the take-off or cruise gear will make sure the right setting is achieved.

3.7.2. Battery sizing

The required power by the engines, taking care of the engine efficiency, as well as the required power for all other systems are gathered. The powers of all subsystems are multiplied by their respective use time during worst case operations. Where E_{bat} is the energy the battery should store and P_i and t_i are the power and time used for each subsystem respectively.

$$E_{bat} = \sum_{i=0}^n P_i t_i \quad (3.68)$$

Consequently the battery mass was sized by using the gravimetric density of batteries. Taking into account also the battery degradation over its life cycle. The sizing for the energy was done as the power density of the state of the art batteries was found to always be higher than the energy density. With the power density of the batteries the maximum power output of the batteries was found, this is checked against the power requirements at different moments in the mission. For the volume a similar argument can be made and is therefore also checked afterwards.

3.7.3. Solar panels

Solar panels on the wing of the Helios variant are applied to extend the range of the aircraft and provide a on-site recharging capabilities. To gather as much sunlight as possible, the largest possible surface area will be used. This will be based on the maximum available wing surface area, meaning wing planform

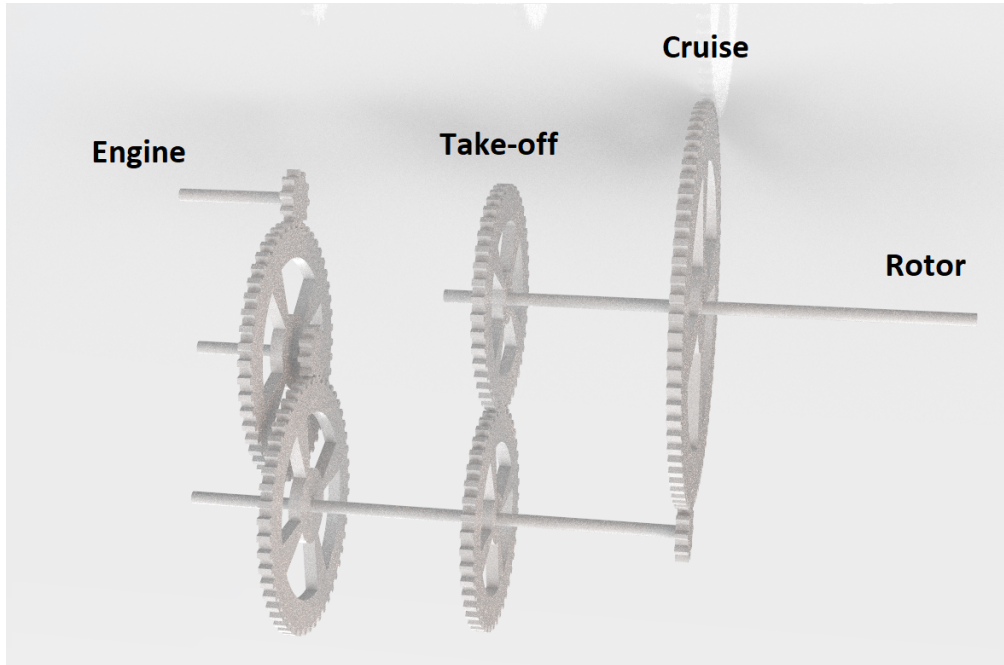


Figure 3.7: The general lay-out of the gearbox with gears for take-off and cruise

area excluding the ailerons and the maximum available mass. To determine the power the solar panels will provide Equation (3.69) is used. In this equation P_{panel} is the power that the panel generates, this consist of the power received from the sun per area, S_{mars} , is multiplied with the panel surface area, A_{cell} . This is further multiplied with the solar cell efficiency, η_{cell} , also the degradation of this efficiency due to radiation over life time is taken into account in F_{EOL} . Finally the incidence angle the solar rays make with the surface, ϕ is taken into account in the formula.

$$P_{panel} = F_{EOL}\eta_{cell}A_{panel}S_{mars}\cos\phi \quad (3.69)$$

To estimate the mass of the solar panels both the photovoltaic cell mass and the protection from the environment need to be taken into account. In Equation (3.70) the mass per unit area of the photovoltaic cell and glass protection, m_{cell} and m_{glass} respectively, have to be added and multiplied with the panel area, A_{panel} .

$$m_{panel} = (m_{cell} + m_{glass}) A_{panel} \quad (3.70)$$

3.8. Thermal Management System Sizing Method

By Joachim Bron

The thermal management system (TMS) is the aircraft subsystem ensuring other subsystems have the necessary temperature range to function properly. This subsystem is needed to keep the other hot subsystems cool, or heat subsystems which are too cold. Colozza et al. (2003) [26] identified the TMS for electric engines on Mars as a critical subsystem, as cooling on Mars is more difficult than on Earth due to the thin atmosphere and thus limited convective heat dissipation. In this section, the method behind the preliminary sizing of the TMS will be explained. Since this is only a preliminary sizing phase, future recommendations are then given on how to improve the analysis and design a more detailed TMS.

3.8.1. Thermal environment and main assumptions

Before starting on sizing the TMS, it is important to have some knowledge about both the internal and external thermal environment the vehicle will be operating in. Quattrocchi et al (2022) [27] performed a case study on the thermal control system (TCS) of NASA's Mars Curiosity rover. According to this study, the rover had to operate within a temperature range of -80 to 5 °C, and a pressure range of 700 to 950 Pa. Our vehicle will operate in similar external conditions, and its TMS will thus be sized for these conditions.

In order to size the TMS, it is important to identify the different external and internal heat sources playing a role in the thermal balance of our vehicle. First of all, heat coming in due to external sources includes direct radiation from the Sun, albedo radiation due to the reflection of Sun radiation on the Martian surface, and infrared radiation (also known as thermal radiation) from Mars directly. Then, heat fluxes going out of the vehicle include convection due to the Martian air flowing around the vehicle and carrying heat away, and thermal radiation from the vehicle itself.

Based on preliminary estimates on the heat generated by different subsystems, it was found that most of the internal heat is generated by two subsystems: the engines and the batteries. Their generated heat is in the order of 40-60 kW and 15-20 kW respectively, compared to less than 1 kW for the other subsystems, rendering these negligible in comparison to the engines and batteries. Although these other subsystems (such as electronics and hydraulics) also require thermal control, the engines and batteries are the most critical based on their heat generated, and thus the preliminary TMS will be sized for these two subsystems only. The batteries and engines are required to be kept in a temperature range between 0 - 60 °C and < 120 °C, respectively.

Initially, the TMS was sized assuming the heat of these two subsystems is perfectly distributed over the whole aircraft. In hindsight, this is quite an unrealistic and optimistic assumption, since the heat will be rather isolated at the location of the batteries (located inside the fuselage) and the engines (located at the wing tips). Also, the wings would initially be used for cooling due to their large surface area and thus large potential for heat dissipation through radiation and convection. However, a lot of internal components would have to be added over this area such as pipes and a pump to ensure proper heat transfer between the TMS and the poor thermal conducting CFRP wings, making the TMS unnecessarily heavy. Therefore, it made more sense to look at both subsystems and their cooling/heating in an isolated way. The TMS was therefore sized for the isolated batteries and engines separately, and radiators for each were sized to ensure proper thermal control, explained in the Section 3.8.2.

Note that in this preliminary phase, the TMS was sized for take-off and cruise only, which are the steady-state worst case hot and worst case cold scenario's, respectively. Take-off is the worst case hot scenario since heat dissipation due to convection is minimal and heat generation due to internal components such as the batteries and engines is maximum. On the other hand, cruise during dusk and cold temperatures was taken as the worst case cold scenario, as then there is no incoming heat due to radiation, the heat dissipation due to convection is maximal (since the air speed is maximal) and the heat generated internally is at its operating minimum.

The TMS was not sized for when it is on the ground and taking off, since this would be a transient and not a steady-state period, complicating the analysis and requiring the need for numerical simulation tools. Furthermore, more details would be needed about the landing gear, which will only be available in future iterations, and about the dust cloud that would form around the vehicle, since it would affect the thermal transfers at play. Also, periods of inactivity, such as when the vehicle is idle and not in operation, were not sized for. In these situations, the batteries might need some heating if the external temperatures are too cold. To size for this situation, however, more information would be needed about the batteries. In order to keep them at the right temperature in this situation, a potential idea would be to discharge and recharge 10% of the battery's energy continuously, but a more detailed analysis is needed to determine if this is feasible or if external heating is required. Since only in-flight scenario's were taken into account for this preliminary TMS sizing, conduction with the ground was not considered.

3.8.2. Sizing method

The following subsection lays out the method behind the preliminary sizing of the TMS, and follows the method by Quattrocchi et al (2022) [27]. From a global point of view, first all the incoming and outgoing heat fluxes are gathered. Then a thermal balance is set up, which is then solved for the equilibrium temperature. This equilibrium temperature needs to be within the acceptable operating range for the specific subsystem. If it is not, a radiator or heater of a certain size is added to cool or heat the subsystem until the new equilibrium temperature is within the acceptable range. Once again, the following analysis

was performed for both the engines and batteries to find equilibrium temperatures and size the TMS for each subsystem separately. In the following paragraphs, subsystem stands for the batteries and engines if not stated otherwise.

The process starts with setting up a thermal balance for the subsystem being analyzed using Equation (3.71).

$$\dot{Q}_{in}^{ext} + \dot{Q}_{in}^{int} - \dot{Q}_{conv} = \dot{Q}_{out} \quad (3.71)$$

where \dot{Q}_{in}^{ext} and \dot{Q}_{in}^{int} are the heat flux coming in to the subsystem due to external and internal heat sources, respectively. \dot{Q}_{conv} is the heat flux due to Martian air convection, and \dot{Q}_{out} is the heat flux out due to thermal radiation of the subsystem.

As explained earlier, the heat flux coming in due to external heat sources $\dot{Q}_{in}^{ext} = \dot{Q}_{sun} + \dot{Q}_{albedo} + \dot{Q}_{thermal}$ consists of direct radiation due to the Sun, albedo radiation, and thermal radiation from Mars. First, the direct solar radiation term is given by Equation (3.72)

$$\dot{Q}_{sun} = \alpha I_s A_{solar} F_{s/v} \quad (3.72)$$

where α is the absorptivity, A_{solar} is the area on which the sunlight is incident, and $F_{s/v}$ is a view factor between the Sun's incident radiation and the surface of the vehicle. The solar intensity is given by $I_s = P/4\pi d^2$, where P is the total power emitted by the Sun and d is the distance to Mars. Then, the albedo radiation term is given by Equation (3.73).

$$\dot{Q}_{albedo} = b \dot{Q}_{sun} = b \alpha I_s A_{solar} F_{s/v} \quad (3.73)$$

where b is the albedo fraction, and for our design purposes can be assumed to be 0.29 [27]. Finally, the (infrared) thermal radiation due to Mars is given by Equation (3.74).

$$\dot{Q}_{IR} = J_p A_{planetary} \quad (3.74)$$

where $A_{planetary}$ is the subsystem area absorbing the infrared heat. $J_p = \epsilon_{pl} \sigma T_{eff}^4$ is the power intensity of Mars' infrared radiation, with $\epsilon_{pl} = 0.71 = (1 - b)$ the planet emissivity, $\sigma = 5.67 \times 10^{-8} \text{ W}/(\text{m}^2 \text{ K})$ the Stefan-Boltzmann constant, and T_{eff} the effective planet temperature.

Two terms in the heat balance allow heat to leave the subsystem: the heat flux due to convection and the heat flux due to thermal radiation of the subsystem. These are important as they can be used to cool the subsystem down. The heat flux due to convection can be approximated by Newton's law given by Equation (3.75).

$$\dot{Q}_{conv} = h (T_{sub} - T_{amb}) A_{conv} \quad (3.75)$$

where A_{conv} is the subsystem area experiencing convection, and T_{sub} and T_{amb} are the temperatures of the subsystem and the ambient air, respectively. h is the convection coefficient, which is hard to calculate accurately as it depends on many factors, but an estimation is performed in Section 3.8.3. Then, the heat flux due to radiation out of the subsystem is given by Equation (3.76), where ϵ_{sub} is the emissivity of the subsystem and A_{out} is the area of the subsystem emitting thermal radiation.

$$\dot{Q}_{out} = \sigma \epsilon_{sub} (T_{sub}^4 - T_{amb}^4) A_{out} \quad (3.76)$$

Finally, the internal heat generated \dot{Q}_{in}^{int} consists of the internal heat generated by the subsystem and equals either \dot{Q}_{eng} or \dot{Q}_{bat} depending on the subsystem being analyzed. Based on all of the previous terms, Equation (3.71) can be solved for the only unknown, which is the subsystem's equilibrium temperature T_{sub} .

3.8.3. Estimation of the heat transfer convection coefficient h

The convection coefficient is difficult to estimate as it depends on many factors: air density, temperature, air speed, etc. The most important reason why it is difficult to estimate however, is that it also depends on the geometry being analyzed, which can be of non-trivial shape. These real-life shapes often cannot be solved analytically, and literature usually resorts to numerical methods to estimate h . In this subsection, we follow a method laid out by Soria-Salinas et al. (2015) [28] and estimate a value for h using semi-analytical expressions given in this paper. Note that in this section, all of the analysis is performed for air in Mars' atmosphere, consisting almost entirely of CO₂.

In order to estimate h , first three dimensionless numbers describing the fluid are needed. The first one is the Prandtl number, given by Equation (3.77), where $C_p(T)$ is the temperature dependent heat capacity, $\kappa_f(T)$ is the temperature dependent fluid conductivity, and μ is the dynamic viscosity. This number describes the relation between the fluids viscous and thermal diffusion effects. Then, the Reynolds number is given by Equation (3.78) and relates the fluids inertial to viscous forces. Here ρ is the density of the flow, v is its speed, and L is a characteristic length. The last dimensionless number needed is the Nusselt number, given by Equation (3.79), which relates the fluids' convective and conductive heat transfer. Here, h is the convection coefficient, which is the variable trying to be estimated.

$$Pr = \frac{C_p(T)\mu}{\kappa_f(T)} \quad (3.77) \qquad Re = \frac{\rho v L}{\mu} \quad (3.78) \qquad Nu = \frac{hL}{\kappa_f(T)} \quad (3.79)$$

In order to find values for h , an experimental expression for the Nusselt number of a cylinder exposed to a normal fluid current is used, given by Equation (3.80). Although our geometry is quite different, it is a good first approximation since both the engines and batteries roughly have a cylindrical shape. This expression is valid for $Pr \cdot Re > 0.2$.

$$Nu = 0.3 + \frac{0.62Re^{1/2}Pr^{1/3}}{\left[1 + (0.4/Pr)^{2/3}\right]^{1/4}} \left[1 + \left(\frac{Re}{282000}\right)^{5/8}\right]^{4/5} \quad (3.80)$$

The heat capacity $C_p(T)$ and conductivity $\kappa_f(T)$ are approximated using temperature dependent polynomials [28] given by Equation (3.81) and Equation (3.82), respectively. Note these are valid for a certain range of temperatures and pressures only, but the present analysis is well within these boundaries, and thus are valid for the conditions considered.

$$C_p(T) = 4.45 \times 10^2 + 1.70 \cdot T - 1.35 \times 10^{-3} \cdot T^2 + 4.65 \times 10^{-7} \cdot T^3 - 2.71 \times 10^{-11} \cdot T^4 \quad (3.81)$$

$$\kappa_f(T) = -7.22 \times 10^{-3} + 8.02 \times 10^{-5} \cdot T + 5.48 \times 10^{-9} \cdot T^2 - 1.05 \times 10^{-11} \cdot T^3 \quad (3.82)$$

The dynamic viscosity is taken as a constant $\mu = 9.82 \times 10^{-6}$ Pas, as given by Bardera et al. [29]. Based on these equations, an estimate for the heat transfer coefficient can be found by solving for h .

3.8.4. Limitations and Future Recommendations

The present analysis was performed in a preliminary way, and improvements can be made in the future to design a more detailed and complete TMS. First of all, only the batteries and engines were analyzed since these are currently the most critical subsystems. A more detailed analysis could be performed by including all other subsystems such as the electronics and hydraulics.

Then, the batteries and engines were assumed to be perfectly insulated from the rest of the aircraft. Although it is a good first approximation, this is in reality not the case, as some heat conduction will occur between the engines and the wings, and between the batteries and the fuselage. In the future, it would be interesting to look at these subsystems and the vehicle as a whole, instead of just looking at the isolated subsystems. This would also include the locations of the heat sources and the thermal transfer inside the structure of the vehicle.

Also, only the in-flight steady-state scenario's were considered (take-off and cruise). In further iterations, it would be beneficial to set up a tool that can analyze the transient situations as well, such as landing

and engine shut-off or turn-on, or other situations, such as periods during which the vehicle is idle. This would allow the visualization of how the temperatures of different subsystems or different locations of the vehicle change over time.

Based on this more detailed knowledge of the whole vehicle's thermal behavior, a more complete and integrated TMS could be sized using a combination of pumps, pipes, radiators, and potentially heaters. An innovative architecture could also be designed in which heat from one subsystem that needs to be cooled is transferred to a subsystem that needs to be heated, or one in which smart use is made of the structure, such as using the wings for cooling.

3.9. Communications Sizing Method

By Dominik Stiller

The communications subsystem enables the astronauts onboard the aircraft to exchange information with the base in real time. Specifically, the (non-)functions are:

- Two-way communication with base through voice radiotelephony and text messages
- Transmit telemetry and astronaut biomedical information to base
- Not: Transmit science data (due to limited bandwidth, no real-time requirement)
- Not: Interplanetary communication with Earth (done by base)
- Not: Internal pilot-to-pilot (direct link through suits)

Note that all communication is near-planet since the latency between Earth and Mars prohibits any useful interplanetary exchange of time-critical information for flights. This relaxes power requirements for the subsystem. If any data needs to be sent to Earth in-flight or post-flight, the base acts as relay.

This section describes the communications concept and link budgeting approach. This includes uplink (vehicle to base) and downlink (base to vehicle)

3.9.1. Communications concept

On Earth, aircraft primarily use Very High Frequency (VHF) radio when in line of sight of air traffic control, but High Frequency (HF) radio is often used in remote areas [30]. In case of HF/VHF radio failure, satellite communication is also used. Over all channels, voice and data/text communication is possible. On Mars, landers and rovers communicate with Earth primarily through a Ultra High Frequency (UHF) link via Mars orbiters, which act as relay [31]. While some surface assets are also equipped with steerable X-band antenna for direct-to-Earth communication, the achievable data rates are low. The only existing Martian aircraft, Ingenuity, uses UHF to its host rover up to a distance of 1000 m [32].

For our aircraft, the base will not be in line of sight. This precludes a direct link via short-wavelength VHF/UHF, so a relay would be necessary at these frequencies. Six Mars science orbiters acting as relay are already in operation, and a dedicated relay network is actively being considered [31]. While different relay architectures are possible, we assume here the one deemed promising by NASA: three satellites, spread uniformly in an equatorial circular orbit at 6000 km altitude [33]. This orbit would ensure visibility at latitudes up to $\pm 60^\circ$, which includes most zones that are relevant for human exploration (within 50° deg of equator, see Figure 2.1). However, such a network may not be in place yet by the time of arrival, or it may not be visible from the latitudes of our base and aircraft [31]. Fortunately, HF radiation can propagate beyond line of sight through reflection and refraction by the ionosphere. No additional infrastructure is needed. Such "skywave" propagation is commonly used for trans-horizon communication on Earth, but is also possible on Mars [34]. The radio performance depends on ionosphere height and stability, which vary diurnally (skywave is likely unusable at nighttime) and with solar activity (a solar maximum is beneficial). Dust storms improve skywave propagation.

Higher frequencies such as S-band, X-band and K-band via a relay orbiter were not considered. These have a higher free-space loss and environmental attenuation [35], which are usually managed by a high gain antenna with a narrow beamwidth. However, this entails stringent pointing requirements [36].

Pointing is not desirable for our mission since it may limit dynamic flight maneuvers and accurate knowledge of the relative relay position would be necessary, which may not be available (see Section 3.10).

Table 3.1: Two complementary modes of communication increase availability. UHF is independent of the environment, but depends on the existence and coverage of relay orbiters.

	UHF via relay	HF via skywave
How it works	A network of orbiters at 6000 km above surface relays data	Short-wavelength radiation is reflected and refracted by the ionosphere
Frequency	300 MHz to 3 GHz	3 to 30 MHz
Benefits	<ul style="list-style-type: none"> • Independent of environment • Used by existing Mars surface assets • Wide bandwidth 	<ul style="list-style-type: none"> • No infrastructure required • Low latency • Global coverage
Limitations	<ul style="list-style-type: none"> • Depends on relay orbiters • Large free-space loss • Limited geographical coverage 	<ul style="list-style-type: none"> • Depends on time of day and solar activity • Large antenna due to long wavelength • Narrow bandwidth

Based on the previously described common communication modes and the limitations of other modes, we select two complementary link types: UHF via a network of relay orbiters, and HF via skywave propagation. They are summarized in Table 3.1. The HF mode will work even if no infrastructure is in place or in regions not covered by the relay orbiters, but will likely be unavailable at night. The UHF mode is more reliable and is the preferred long-term option, but has limited geographical coverage and will take some time to be established. Therefore, the two modes complement each other in terms of spatial and temporal coverage.

The required data rates differ slightly for uplink and downlink but are around 35 kb/s. For uplink, we consider voice (8 kb/s [37]), astronaut biomedical status (0.2 kb/s, 50 floating-point numbers at 1 Hz), and vehicle telemetry (8 kb/s, 200 floating-point numbers at 10 Hz). For downlink, we consider voice (8 kb/s) and mission information (10 kb/s). For both, we apply a factor of two.

3.9.2. Link budget calculation

The link budget describes all contributions between the transmitter power and the received power. The link performance is usually evaluated in terms of the ratio E_b/N_0 , where E_b is the energy per bit [J/bit] and N_0 the noise power spectral density [W/Hz]. This ratio is commonly used as normalized alternative to the signal-to-noise ratio since it is independent of the modulation scheme. A link is considered closed if the received E_b/N_0 exceeds the required E_b/N_0 by a certain margin. We require a margin of at least 3 dB, which is typically used [38].

Received E_b/N_0 The form of the link budget equation to determine the received E_b/N_0 varies, but is generally written as in Equation (3.83) (e.g., [36]).

$$\frac{E_b}{N_0} = \frac{(P_{tx}L_{l,tx}G_{tx}L_{p,tx})(L_sL_e)(L_{p,rx}G_{rx}L_{l,rx})}{kT_sR} \quad (3.83)$$

The numerator contains the transmitter power P_{tx} , the transmitter-to-antenna line loss $L_{l,tx}$, the transmitter antenna gain G_{tx} , the transmitter antenna pointing loss $L_{p,tx}$, the free-space path loss L_s , the environment path loss L_e , the receiver antenna pointing loss $L_{p,rx}$, the receiver antenna gain G_{rx} , and the antenna-to-receiver line loss $L_{l,rx}$. The denominator contains the Boltzmann constant $k = 1.38 \times 10^{-23}$ J/K, the system noise temperature T_s , and the data rate R . Note that the link budget is commonly evaluated in logarithmic dB instead of linear units. We follow this convention for the results in Section 4.9.

Signal power The term $(P_{tx}L_{l,tx}G_{tx}L_{p,tx})$ describes the power radiated by the transmitter. The term $(L_{p,rx}G_{rx}L_{l,rx})$ describes the gains and losses on the receiver side. The transmitter power P_{tx} is an important design parameter. Line losses are taken to be $L_{l,tx} = L_{l,rx} = -1\text{ dB}$ (e.g., from [39, 40]). The gains G and pointing losses L_p depend on the antenna radiation pattern, which describes the gain as a function of receiver direction. This radiation pattern is determined by the antenna geometry and closed-form solutions exist for simple types. However, for this preliminary sizing, we take gain and pointing losses from the antenna data sheets. Note that different antennas are used for different frequencies (longer wavelengths require larger antennas).

In between the transmitter and receiver, losses occur along the transmission path. The free-space path loss in Equation (3.84) depends on the receiver-transmitter distance d and wavelength λ .

$$L_s = \left(\frac{\lambda}{4\pi d} \right)^2 \quad (3.84)$$

The environmental losses are taken from Ho et al. [34] and have a strong frequency dependency. At HF and UHF, environmental attenuation due to atmospheric gases and clouds is negligible. This is in stark contrast to Earth, where water vapor, oxygen, and rain dominate absorption. On Mars, dust and ionosphere absorption are the most relevant. Dust absorption increases with frequency, but is small (0.1 dB at VHF during dust storms). This also means that communication should be stable in case of brownout during landing and take-off. Ionosphere absorption is small for high frequencies (0.5 dB at VHF), but highly disruptive for HF propagation at small zenith angles (around 40 dB at 4.0 MHz [41]).

Noise power The noise power is characterized by the system noise temperature T_s . This temperature is not physical but rather a convenient representation. The system noise is composed of noise originating ahead of the antenna (such as galactic noise and Martian thermal noise), receiver transmission line noise, and receiver amplifier noise. The temperature follows Equation (3.85) [36].

$$T_s = T_{ant} + \frac{T_0(1 - L_{l,rx})}{L_{l,rx}} + \frac{T_0(F - 1)}{L_{l,rx}} \quad (3.85)$$

Noise originating ahead of the antenna is characterized by the antenna temperature T_{ant} , which we take from Ho et al. [35]. A downward-looking antenna (here, just the relay orbiter acting as receiver) has higher antenna noise due to upwelling surface thermal radiation. Receiver noise is characterized by the receiver line loss $L_{l,rx}$, receiver noise figure F and a reference temperature $T_0 = 290\text{ K}$. The noise power spectral density is then found as $N_0 = kT_s$.

Protocol and required E_b/N_0 The required E_b/N_0 depends on the coding and modulation scheme. We use the Proximity-1 Space Link Protocol, which prescribes these schemes. Proximity-1 is the default for current proximity links between orbiters, landers and rovers. This protocol is also one of the options selected by a consortium of space agencies for the Mars communications architecture [31]. Proximity-1 uses biphasic modulation [42] and supports multiple codings [43]. We select the Low-Density Parity Check (LDPC) coding at rate $1/2$, which approaches the theoretical channel performance limit and is the preferred coding scheme for the future [31]. Given the coding and modulation scheme, the required ratio can then be found in literature for a given bit error rate (e.g., [44]). We design for a bit error rate of 1×10^{-6} , although lower rates are easily achievable due to the asymptotic behavior. The required E_b/N_0 for link closure is then 1 dB plus the margin of 3 dB .

Bandwidth The selection of modulation and coding scheme is mainly a matter power efficiency versus spectral efficiency. Since bandwidth is not an issue at high frequencies, UHF is power-limited. Low-order modulation with low-rate coding, such as LDPC at rate $1/2$ over biphasic modulation as used by Proximity-1, is therefore unsurprisingly a power-efficient choice. However, using this combination for the bandwidth-limited HF may lead to spectrum congestion. This is discussed further in Section 3.9.4.

3.9.3. Sizing considerations for UHF relay link

Proximity-1 is designed for UHF and prescribes the specific frequency bands. We select channel 1, corresponding to 401.6 MHz for uplink and 437.1 MHz for downlink. We will use a hemispherical antenna similarly to those used for aircraft satellite communication on Earth (e.g., [45]). These combine a vertical monopole for low-angle coverage with a turnstile antenna for high-angle coverage. The high-angle gain is somewhat larger (around 6 dB), which is acceptable since the relay orbiters will have an elevation of at least 60°. Relay gain properties are based on the Mars Reconnaissance Orbiter [46].

Compared to the skywave link, the relay-based link works over large distances. For relay orbiters in our assumed constellation, the maximum distance to a surface asset is 8240 km. This occurs when two of the three orbiters are equally close. The longer distance means that the free-space loss for UHF is larger than for HF, despite the shorter wavelength. However, the environment attenuation is very low at UHF.

We only size the link from the vehicle to the relay orbiter, not between the relay and the base. However, we assume the distances to be the same for latency calculations. Note that the latencies do not account for onboard processing delay (which is not necessary with certain relay models like bent-pipe [31]) and relay-to-relay forwarding (given the 1000 km range of our aircraft, the same relay orbiter is visible from both vehicle and base).

3.9.4. Sizing considerations for HF skywave link

The maximum usable frequency for skywave communication is governed by the ionosphere electron content and the angle of incidence. Above this frequency, radio waves are not reflected but pass through the ionosphere. The ionosphere electron content decreases at night and during a solar minimum, which limits the availability of skylink communication. For average solar activity during the day, the maximum usable frequency is $4.0 \text{ MHz} / \cos \theta_0$ where θ_0 is the launch/incidence angle. Skywave links with $\theta_0 \approx 0^\circ$ are also known as near-vertical incidence skywave (NVIS).

The hop distance is the surface distance covered by skywave at a certain incidence angle and ionosphere height. Usually, the ionosphere height is 130 km, which increases by up to 30 km during global dust storms. Larger heights are detrimental due to larger free-space loss and a lower usable frequency due to more vertical incidence. At the worst case height of 160 km and a hop distance of 1000 km, the incidence angle would be 72°, which gives a maximum usable frequency of 13 MHz. However, we will use 4.0 MHz (for NVIS) at all times, independent of the actual incidence angle. The ionosphere attenuation at these low frequencies is significant (up to 40 dB [41]), but the free-space loss is smaller than for UHF.

Antennas are typically sized according to the quarter-wavelength, which is 19 m at 4.0 MHz. This is prohibitively large for our vehicle, which necessitates a smaller antenna in combination with a tuner [47]. The most common type of HF antenna in modern aircraft is a shunt antenna mounted on the vertical tail. This type of antenna uses the vertical tail as capacitor by replacing the leading edge with an antenna element [48]. The tail will therefore be made out of a conductive material (see Section 3.12.5).

The HF link was noted to be bandwidth-limited. Based on the spectral efficiency of $2 \text{ Hz}/(\text{kb/s})$ [44] for LDPC at rate 1/2 over biphase modulation, the required bandwidth for uplink is 64.8 kHz. This is pushing the limits of HF channels, which are standardized for 3 kHz to 24 kHz. Bandwidths of 80 kHz are theoretically possible [49], but may lead to spectral congestion if the number of HF users on Mars increases. In that case, a more spectrally efficient coding could be used. For example, LDPC at rate 7/8 over quadrature phase shift keying would only need 19.4 kHz instead of 64.8 kHz for the same data rate.

3.10. Navigation and Instrumentation Sizing Method

By Dominik Stiller

The navigation and instrumentation subsystem supplies astronauts and control systems with all flight-relevant data. Specifically, the (non-)functions are:

- Determine position, velocity and attitude during flight
- Provide landing guidance

- Not: Prevent collision with other Martian aircraft (the risk is low)
 - Not: Collect science or mission-specific data (these sensors are considered part of the payload)
- Particular care is taken to fulfill the functions even in case of dust storms and brownout.

This section describes the navigation and flight instrumentation concept. First, an autonomous navigation concept is presented. Then, supplementary instrumentation is discussed.

3.10.1. Navigation

On Earth, aircraft have historically used VHF omnidirectional range and non-directional beacons for navigation [30]. An instrument landing system uses additional components. More recently, aircraft have also been equipped with global navigation satellite system (GNSS). On Mars, the Ingenuity helicopter navigates using accelerometers, an inclinometer, a lidar altimeter, and a grayscale camera [32]. The Perseverance rover determines its position and pose from stereoscopic color images [50].

For our aircraft, navigation based on surface infrastructure is infeasible since the vehicle is designed to land in remote areas. GNSS navigation may become possible in the future, but at least six satellites would be needed for useful positioning [51], while only three are considered for early relay networks [31]. The relay orbiters may still provide useful ranging and Doppler tracking, but is inadequate as primary means of navigation. Therefore, an autonomous navigation concept is needed.

Autonomous navigation includes inertial, celestial and visual methods, described by Liu [52]. Inertial methods integrate information from accelerometers and gyroscopes to obtain the position, velocity and attitude state. Sensors are not affected by the environment, but errors accumulate. Celestial methods include star sensors, which are infeasible on the surface of Mars due to reduced sky visibility. Visual methods include cameras and lidars with computational algorithms for mapping and state estimation. Two or more methods can be integrated for improved accuracy and redundancy.

We select a visual–inertial navigation approach for our aircraft. Visual navigation can provide a definitive vehicle state, while inertial navigation has a high update rate necessary for control systems. If available, visual–inertial information can be fused with ranging and tracking data from the relay orbiter. During cruise, an omnidirectional field of view aligned with the horizontal plane is desirable to locate the vehicle based on landmarks, observe changes in attitude, and determine the velocity from optical flow. During landing and take-off, nadir vision with depth information is important to avoid ground obstacles and estimate the altitude. Different cameras are needed for these purposes.

For navigation during cruise, visible-wavelength cameras will be used, similarly to the Perseverance rover. The cameras should provide color information to distinguish dust and soil from rocks [50]. A stereoscopic or depth camera is not necessary since depth information can be recovered from monoscopic cameras when moving [53]. Also, the terrain will be at a distance so that stereoscopic vision would not provide useful depth information. The cameras should provide omnidirectional vision within the horizontal plane. Therefore, we select three color monoscopic cameras with a horizontal field of view of 120°. The camera images can be processed using algorithms for optical flow, feature tracking, and map building [54].

For landing and take-off, accurate knowledge of ground geometry and distance is necessary for safe operation. Lidars can provide such information based on distances from laser time-of-flight ranging. The aircraft will be engulfed by dust when hovering close to ground, which disturbs lidar vision [55]. However, dust-penetrating sensors are being developed [56, 57]. Our aircraft will be equipped with a dust-penetrating lidar³ with a maximum range of 5000 m. Therefore, it can also be used during low-altitude cruise. This lidar has proven to provide vision during helicopter brownout on Earth [57].

The cameras and lidar should also be protected from the environment, particularly dust and radiation. Perseverance has covers for the downward-facing cameras, while the uppermost cameras has no cover⁴. We will be able to cover the cameras and lidar on the ground, and regularly clean it as part of the pre-flight

³URL: https://asc3d.com/gsfl_16ks/ [cited 2023-06-20]

⁴URL: <https://www.techbriefs.com/component/content/article/tb/stories/blog/37300> [cited 2023-06-21]

procedure. The rover's camera sensors were commercial sensors without radiation hardening, but they were tested for the acceptable radiation dose.

3.10.2. Instrumentation

In addition to navigation equipment, the aircraft also needs sensors for other flight-relevant environment quantities and computers to process these. In the United States, the Federal Aviation Administration (FAA) mandates certain instruments [58]. There are no regulations for tiltrotor aircraft, so we assume that both Part 23 (Normal Category Airplanes) and Part 27 (Normal Category Rotorcraft) hold. The instrumentation requirements should be adapted to electric aircraft. For example, battery charge should be indicated instead of fuel tank levels. Most instrument requirements pertain to cockpit displays. In this subsection, we focus on sensors to collect the required environment data.

From the FAA requirements, we need the following quantities: airspeed, vertical speed, altitude, heading, pitch angle, and roll angle, external temperature, and rate of turn. In addition, our control system also needs angle of attack, sideslip angle, linear accelerations, and rotational rates. Integrated sensor/processing units exist to outsource the data collection to a single unit containing a pitot-static system. Our aircraft will use the Aventech ARIM320⁵. For redundancy, the Honeywell Air Data Inertial Reference System (ADIRS)⁶ will also be used to measure accelerations and rotational rates. Finally, an inclinometer will help with attitude determination.

Two more components are needed to complete the navigation and instrumentation subsystem. The first is a computer for data fusion and vision processing. This computer should be equipped with graphics hardware specialized on vision, such as the NVIDIA Jetson⁷. The second is a communications management unit, which links the flight computers to the antenna transceiver⁸. No radiation hardening for these components is necessary since commercial-grade processors are adequate for operation on the Mars surface [59].

3.11. Life Support Sizing Method

By Joachim Bron

The life support system (LSS) is a subsystem that provides the functions and resources (water, oxygen, carbon dioxide removal, etc.) necessary to the astronauts' life, health and proper functioning. On a typical mission, astronauts will be equipped with space suits which will provide them with all necessary LSS functions. These functions are fully integrated in their suits, and it is reasonable to assume that once astronauts arrive on Mars, these suits will be ready to be used. If however, the astronauts need to land somewhere and perform extra tasks, or a mission uses up the resources such as breathing and water faster than expected, an auxiliary LSS should be available to allow the astronauts to recharge these resources in their spacesuit through a connection to the aircraft LSS. In this section, some considerations are given regarding the LSS in Section 3.11.1, and the procedure for sizing is given in Section 3.11.2.

3.11.1. Main assumptions and general considerations

Early on, it was decided not to go for a pressurized cabin since this would require too much extra mass. Extra mass would be needed around the cabin to hold the pressurization loads, contain air leakages, as well as to have a cabin pre-pressurization space. At this stage of the design, the LSS will only consist of oxygen and water tanks; the sizing method is given in Section 3.11.2.

It was assumed that the astronauts remain in their suits for the entirety of the mission. It is assumed that this suit contains the necessary functions such as CO₂ removal, and that the LSS sized here just

⁵URL: <https://aventech.com/products/arim320.html> [cited 2023-06-16]

⁶URL: <https://aerospace.honeywell.com/us/en/products-and-services/product/hardware-and-systems/sensors/air-data-inertial-reference-system> [cited 2023-06-16]

⁷URL: <https://www.arrow.com/en/products/945-13730-0055-000/nvidia> [cited 2023-06-20]

⁸URL: <https://www.collinsaerospace.com/what-we-do/industries/commercial-aviation/flight-deck/communications/data-link-services/cmu-900-communication-management-unit> [cited 2023-06-15]

complements the already existing resources and functions of the space suit. The oxygen and water tanks allow for a short extension of the mission, and provide emergency water and oxygen in case the vehicle has problems. Since the nominal mission consists of only a couple of hours, it was decided that the LSS would carry an extra 36 hours of oxygen and an extra 24 hours of oxygen on top of what was already available in the suit. This would allow enough time in case of a problem for a search and rescue operation of the stranded astronauts using another vehicle (we assume that there will not be only a single vehicle present on Mars for a long time). This relatively short duration for missions further justified the decision to not have food on board during a mission. In the future, in case longer mission are planned out, adding food should be investigated. A potential idea would be to add food in the form of a gel to the already carried on board water, but this requires further investigation.

Furthermore some considerations are given regarding astronauts' exposure to radiation. During a mission, it is reasonable to assume that the astronaut suit will provide some radiation protection for a couple of hours, similar to that of an Extra Vehicular Activity (EVA), also known as space walk, on the international space station (ISS). Note that a typical mission on Mars will take approximately the same amount of time as an ISS EVA (couple of hours). Regarding exposure, NASA stipulates a radiation exposure limit of 1000 mSv/year for astronauts in low-Earth orbit [60]. In the worst case scenario, astronaut crews aboard the ISS receive about 160 mSv of radiation per 6 months [60], or 320 mSv/year. On average, radiation on the surface of Mars is 300 mSv/year in the worst case scenario, within acceptable NASA limits [61]. The problem would thus be the duration of the missions and not the intensity of the radiation, as the astronauts have no option to quickly return to Earth but most likely will need to stay for at least 18 months on the surface[60]. The fact that astronauts are on Mars will mean that measures will have been taken to protect them as much as possible from radiation, and performing flights in the vehicle would not lead to much higher levels of radiation than if the astronauts were performing operations on the Martian surface. Furthermore, astronauts should limit or even avoid performing flights or operations on the Martian surface during periods of large solar flares. In the future, an extra layer of polymer could be sized and added to the cockpit to provide the astronauts with some more protection to radiation⁹, even though the radiation levels without this extra layer still fall within acceptable limits. More research into the protection of astronauts from radiation is recommended.

3.11.2. Tank sizing

Before sizing the tanks, it is necessary to know how much oxygen and water needs to be carried. A technical report by ESA [62] states that 840 g of oxygen and 4 L of water are needed per astronaut per day. We assume 36 hours are needed of oxygen and 24 hours of water, leading to a need of 2.64 kg of oxygen and slightly less than 8 kg of water. Based on these required masses, the tanks can be sized with the goal of minimizing mass.

Composite overwrapped pressure vessel (COPVs) are frequently used in space applications due to their low mass and high pressure carrying capabilities. COPVs are made up of an internal metal liner used to contain the fluid and contain leaking, and a composite outside wrapping which mostly carries the loads due to pressurization. Although COPVs were looked into, it was decided to go for classical metal tanks in this first iteration since the failure modes of COPVs are difficult to estimate using preliminary techniques, while metal tanks are easier to size and provide similar performance albeit at a slight increase in mass.

Tank sizing process To size the tanks, multiple assumptions were made. The tanks were assumed to have a cylindrical shape with half-spherical end-caps. The tanks have a length l , a diameter d , a cylindrical section thickness t_{cyl} and a spherical section thickness t , as shown in Figure 3.8.

The pressure vessel has to sustain various stresses. These stresses are the spherical hoop stress, the cylindrical hoop stress and the cylindrical axial stress, given respectively by Equation (3.86), Equation (3.87) and Equation (3.88). Note that in these equations $r = d/2$ stands for the radius of the tank. In the last

⁹URL: <https://www.nasa.gov/feature/goddard/real-martians-how-to-protect-astronauts-from-space-radiation-on-mars> [cited 2023-06-27]

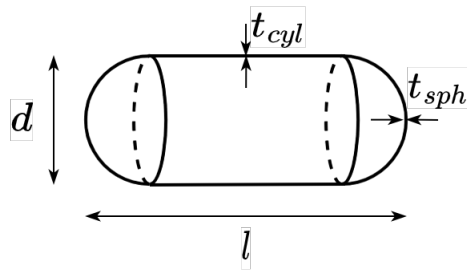


Figure 3.8: Tank shape and dimensions

part of each of these equations, the thickness for the spherical part t_{sph} is renamed to t for simplicity (used instead of t_{sph} from now on), and the cylindrical part thickness t_{cyl} is replaced by $2t$, since this is required for compatibility of the stresses between the cylindrical and spherical part.

$$\sigma_{\theta,sph} = \frac{pr}{2t_{sph}} = \frac{pd}{4t} \quad (3.86) \quad \sigma_{\theta,cyl} = \frac{pr}{t_{cyl}} = \frac{pd}{4t} \quad (3.87) \quad \sigma_{z,cyl} = \frac{pr}{2t_{cyl}} = \frac{pd}{8t} \quad (3.88)$$

The internal volume of the tank is given by Equation (3.89), where the first part of the equation refers to the volume of the spherical endcaps, and the second part to the volume of the cylindrical middle part.

$$V_{tank} = \frac{1}{6}\pi d^3 + \frac{1}{4}\pi d^2(l - d) = \frac{1}{4}\pi d^3\left(\frac{l}{d} - \frac{1}{3}\right) \quad (3.89)$$

The material volume of the tank V_{wall} (i.e. the volume of its skin) is given by Equation (3.90), which contains contributions from the spherical and cylindrical parts:

$$V_{wall} = \pi d^2 t_{sph} + \pi d(l - d) t_{cyl} = 2\pi d^2 t\left(\frac{l}{d} - \frac{1}{2}\right) \quad (3.90)$$

The empty mass of the pressure vessel is estimated using Equation (3.91).

$$m_{wall} = V_{wall}\rho_{wall} = 2\pi d^2 t\left(\frac{l}{d} - \frac{1}{2}\right)\rho_{wall} \quad (3.91)$$

where ρ_{wall} is the density of the tank material. The mass of oxygen in the tank can be written as given by Equation (3.92).

$$m_{O_2} = \rho_{O_2} V_{tank} \quad (3.92)$$

Furthermore, from the ideal gas law $p = \rho RT$, the density of oxygen in the tank ρ_{O_2} is given by Equation (3.93).

$$\rho_{O_2} = \frac{p}{RT_{O_2}} \quad (3.93)$$

where p is the pressure in the tank, R is the gas constant of oxygen, and T_{O_2} is the temperature of the oxygen gas. Equation (3.89) and Equation (3.93) can be substituted into Equation (3.92), which can subsequently be rearranged to express the pressure in the tank solely as a function of d , l/d , T_{O_2} and m_{O_2} . Since the latter three are fixed, the pressure depends solely on the tank diameter d . This expression is given by Equation (3.94).

$$p = \frac{m_{O_2}RT_{O_2}}{\frac{1}{4}\pi d^3\left(\frac{l}{d} - \frac{1}{3}\right)} \quad (3.94)$$

In order for the pressure vessel walls not to yield due to the pressure inside, the pressure inside in combination with the dimensions should satisfy Equation (3.95), where σ_y is the yield stress of the tank wall material.

$$\sigma = \frac{pr}{t} < \sigma_y \implies \frac{pr}{\sigma_y} < t \implies t_{min} = \frac{pr}{\sigma_y} \quad (3.95)$$

Finally, for safety we require the pressure vessels to leak before fracturing. This means that in case the pressure is too high and the tank will break in a violent rupture, it first starts leaking to relieve the pressure and avoid a violent explosion. For this we require the maximum crack length before rupture, given by Equation (3.96), to be larger than the tank thickness, i.e. $c_{max} > t$.

$$c_{max} \leq \frac{1}{Y^2 \pi} \left(\frac{K_{1c}}{\sigma_y} \right)^2 \quad (3.96)$$

where Y is a factor related to the part geometry (assumed to be 1) and K_{1c} is the material fracture toughness.

Tank dimensions optimization Based on the previous sizing considerations, the tank dimensions can be optimized for mass. The fineness ratio was set as $l/d = 3$ based on typical ratios found for other tanks (typical values range between $2.5 < l/d < 4$). The maximum pressure for typical scuba diving tanks was found to be 21 MPa. This can however easily be changed once more is known about the design and another fineness ratio turns out to be more advantageous.

Various combinations of diameter d and tank thickness t can be found to hold the internal pressure of the oxygen. However, the minimum mass is probably somewhere in the middle. To ensure the tank is thin-walled and the previous equations hold, we require Equation (3.97) to be true.

$$\frac{d}{t} \geq 20 \quad (3.97)$$

Furthermore, for the tank to contain the pressure and not yield, the diameter needs to be larger than some minimum value at a certain t . Thus we require Equation (3.98) to be true, which is obtained by combining Equation (3.94) and Equation (3.95).

$$d \geq \left(\frac{m_{O_2} RT}{\sigma_y} \frac{1}{\pi \left(\frac{l}{d} - \frac{1}{3} \right)} \frac{1}{t} \right)^{\frac{1}{2}} \quad (3.98)$$

This leads to the optimization problem given by Equation (3.99):

$$\begin{aligned} \min_{d,t} \quad & m_{wall}(d, t) = \pi d^2 t \left(2 \frac{l}{d} - 1 \right) \rho_{wall} \\ \text{s.t.} \quad & d_{min} < d < d_{max} \\ & t_{min} = \frac{pr}{2\sigma_y} < t \\ & \frac{d}{t} < 20 \\ & d \geq \left(\frac{m_{O_2} RT}{\sigma_y} \frac{1}{\pi \left(\frac{l}{d} - \frac{1}{3} \right)} \frac{1}{t} \right)^{\frac{1}{2}} \end{aligned} \quad (3.99)$$

Here, d_{min} and d_{max} are chosen based on additional constraints such that the tanks are still easy to carry. A summary (in the style of a class diagram) of all variables and structure of the code to size the LSS is given in Figure 3.9.

Usability When sizing the tanks, multiple aspects regarding the usability and interfacing with the astronauts need to be kept in mind. When sizing, it was kept in mind that each tank needed to fit in the fuselage, but also fit through the opening by which it was brought into the fuselage. Furthermore, each tank must not be too heavy, to be able to be easily carried by a single astronaut. Each tank also needs to be easily replaceable, achieved through a special connection to the fuselage, and rechargeable, achieved through an external connection to the fuselage to recharge the oxygen or water. These things were not

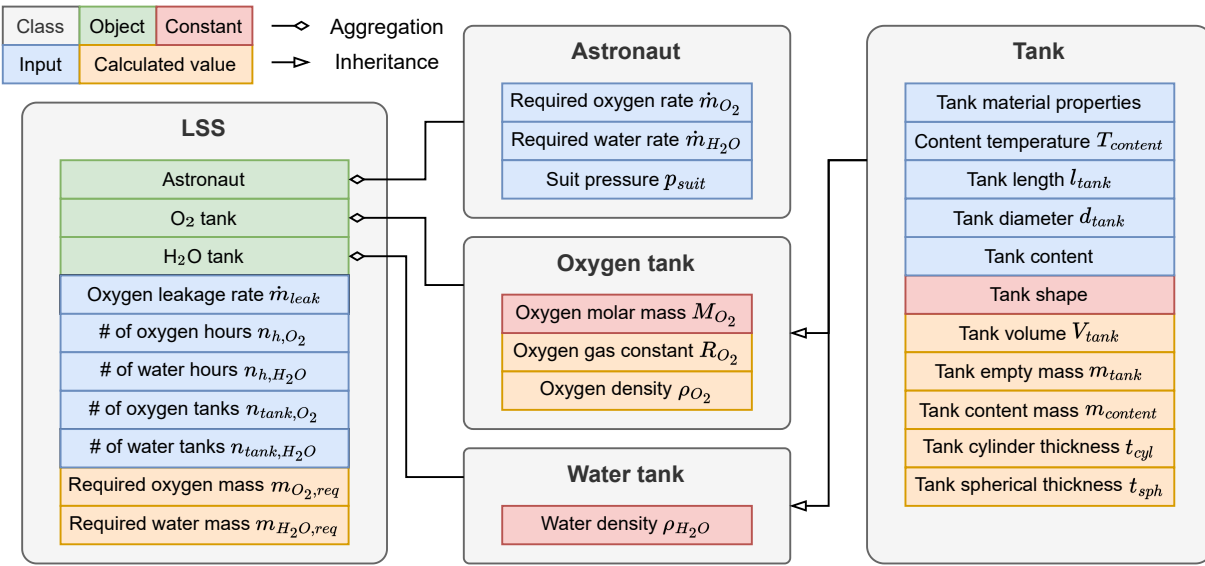


Figure 3.9: LSS sizing code structure

sized for at this stage, but are all things to be kept in mind for future, more detailed iterations of the LSS design.

The tanks also consists of various valves, inspired by NASA's portable LSS¹⁰. For safety, a relief valve is used. In case the pressure becomes too high in the tank, these valves release some of the pressure by actively allowing leakage. Then, pressure regulators are also present to acquire data on the pressure in the tanks. Finally, a special valve for refilling the tanks (a fill fitting) is also present.

The astronauts are able to connect to the water and oxygen supply using "umbilical" cord style connections, present on the inside and outside of the fuselage. The tanks do not use pumps but only use the pressurization inside the tank to blow-down the air into the suits using a regulator valve that limits the pressure so as to be within limits of the suit.

3.12. Structural Sizing Method

By Javier Alonso García and Freek Braspenning

A basic Finite Element Method (FEM) tool was developed in order to evaluate the loading and stresses in the structure. Firstly, the assumptions made in the methodologies will be explained, then the loading cases for all structural components will be explained. The equations used to translate those loads into stresses will then be explained, as well as the possible failure modes considered in this analysis. Finally, the materials considered for the different parts of the structure will be listed and the limitations of this report will be explained.

3.12.1. Structures Idealizations

The aircraft was split into different structural components, for which a structural analysis was performed. Each part of the aircraft was classed as either one of two structural idealizations: a beam or a two-force member. The components and their respected idealizations are listed in Table 3.2.

Table 3.2: Structural components and their idealizations

Structure	Wing	Rotor blade	Brace	Tail beam	Horizontal tail	Vertical tail
Idealization	Beam	Beam	2-force member	Beam	Beam	Beam

¹⁰URL: https://history.nasa.gov/alsj/LM15_Portable_Life_Support_System_ppP1-5.pdf [cited 2023-06-21]

The beams were considered to be a simple boom structure. In a boom structure, the area of the cross-section is lumped into booms united by a skin with a thickness of zero. It is assumed that the booms only carry axial loads, and the sheets only carry shear flows.

The two-force member, on the other hand, is assumed to only be able to withstand axial loads, in line with the element.

3.12.2. Applied Loads

The applied loads on a hybrid design such as the tiltrotor are formed by a particular combination of load cases, namely, the loads from vertical take-off and the loads from the cruise flight, as seen in Figure 3.10 for the wing in the y-z plane. Note how the root of the wing is considered a pinned connection that resists no moments (this was done in order for the system to be statically determinate), therefore, moment equilibrium around the root must be ensured by the force induced by the brace (F_{brace}). Furthermore, the magnitude of the lift load that will be considered is the one in the "ailerons down" configuration, which produces the necessary lift to satisfy the turn constraint. This lift is a factor of 2.2 greater than the nominal cruise lift.

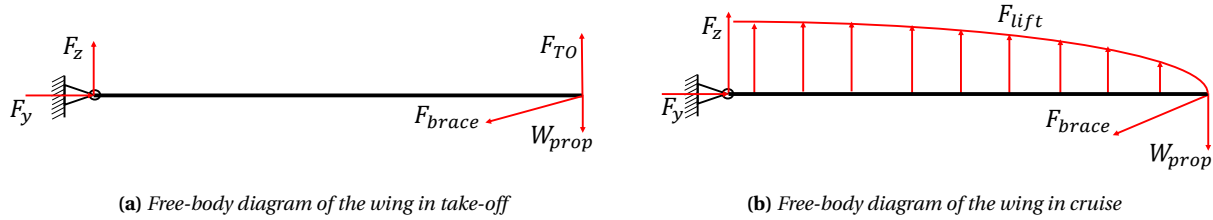


Figure 3.10: Wing's free body diagram in take-off and cruise configuration

For the rotors, a uniformly distributed thrust and drag will be present along its span, together with the axial load due to rotation of the blades follow from Equation (3.100):

$$F_{centrifugal,i} = \sum_{j=0}^i m_j \omega^2 r_j \quad (3.100)$$

where m_j is the mass of the j^{th} section, ω is the angular velocity, and r_j the distance from the center of rotation. In case of the rotors, the root will be considered clamped, therefore the moment will be non-zero at that point.

From the applied loads, the internal loads on the structure were computed. This was done numerically following Equation (3.101).

$$\vec{M}_i = \sum_{j=0}^i \vec{F}_j \times (\vec{r}_i - \vec{r}_j) \quad (3.101)$$

where \vec{M}_i is a vector including all moments at the i^{th} node, with at the tip $i = 0$ and at the root $i = n$, \vec{F}_j the forces in x, y, and z directions, and \vec{r} the position vector.

3.12.3. Structural Analysis

The boom idealization of the beam comes forth from the idealization of the two-force member. The two-force member is a geometry that is assumed to only carry axial loads. The stress in a two-force member is computed by Equation (3.102)

$$\sigma = \frac{F}{A} \quad (3.102)$$

where F is the axial load and A is the cross-sectional area of the two-force member.

The structural analysis of the beam was performed in accordance to Equations (3.103) and (3.104), for axial loading and bending respectively.

$$\sigma_y = \frac{F_y}{\sum B_i} \quad (3.103)$$

where F_y is the axial load and $\sum B_i$ is the sum of all boom areas.

$$\sigma_y = \frac{(M_x I_{zz} - M_z I_{xz})(z - \bar{z}) + (M_z I_{xx} - M_x I_{xz})(x - \bar{x})}{I_{xx} I_{zz} - I_{xz}^2} \quad (3.104)$$

where M_x and M_z are the internal moments. \bar{x} and \bar{z} are the neutral axes of the geometry, as calculated by Equation (3.105). I_{xx} , I_{zz} , I_{xz} are the moments of inertia and product of inertia calculated by Equation (3.106), respectively.

$$\bar{x} = \frac{\sum B_i x_i}{\sum B_i} \quad \bar{z} = \frac{\sum B_i z_i}{\sum B_i} \quad (3.105)$$

$$I_{xx} = \sum B_i (z_i - \bar{z})^2 \quad I_{zz} = \sum B_i (x_i - \bar{x})^2 \quad I_{xz} = \sum B_i (x_i - \bar{x})(z_i - \bar{z}) \quad (3.106)$$

where x_i and z_i the coordinates of the i^{th} boom, and B_i is the boom area as obtained by Equation (3.107).

$$B_i = \sum_{j=-1, j \neq i}^1 \frac{t_{skin} b}{6} \left(2 + \frac{\sigma_j}{\sigma_i} \right) \quad (3.107)$$

With the use of previously mentioned formulas and an initial guess for boom area and skin thickness, an iterative sizing process was started. The initial guess for boom areas followed from Equation (3.108), derived from thin-plate theory.

$$B_{initial} = \frac{l_c t_{min}}{n} \quad (3.108)$$

where l_c is the length of the circumference, t_{min} the minimum thickness that can be produced, and n the number of booms. The minimum thickness was used as the initial skin thickness, with a value of 1 mm.

Once the initial guesses for the boom areas were computed, the stresses were calculated, and in case any of the booms was carrying a stress greater than allowed, an iteration would begin where the boom areas would be increased and the moment of inertia and the stresses recomputed. The necessary skin thickness would then be calculated based on these boom areas after no stresses exceeded the allowable stress. The allowable stress was set to be the yield stress of the material, divided by a safety factor of 1.5. In the case of composites, however, the allowable stress was calculated to be a third of the compressive strength, divided by the same safety factor.

The shear stress was calculated using a combination of the shear force and torque throughout the beam. The shear flow for a boom idealization of a thin-walled structure can be found using Equation (3.109).

$$q_s = q_b + q_{s0} = - \frac{V_z I_{zz} - V_x I_{xz}}{I_{xx} I_{zz} - I_{xy}^2} \left[\sum_{i=1}^n B_i z_i \right] - \frac{V_x I_{xx} - V_z I_{xz}}{I_{xx} I_{zz} - I_{xy}^2} \left[\sum_{i=1}^n B_i x_i \right] + q_{s0} \quad (3.109)$$

where q_s is the total shear flow, q_b is the shear flow when a cut is made in the structure, and q_{s0} is the closed section shear flow. With the use of moment equivalence, the closed section shear flow can be computed by the use of Equation (3.110).

$$V_x \eta_0 - V_z \xi_0 = \sum_{i=1}^n p_i q_{b_i} s_i + 2A_m q_{s0} \quad (3.110)$$

where η_0 is the moment arm of the shear force in x -direction, ξ_i is the moment arm of the shear force in z -direction, p_i is the moment arm for the shear flow p_{b_i} and s the length of over which the shear flow acts, and A_m is the enclosed area. [63]

3.12.4. Failure modes Identification

With the structural analysis computed, failure modes can be identified. The failure modes of interest for the conceptual design were yielding, buckling, and vibrations. For some specific divisions, such as the blades of the rotor where the impact of martian dust was of interest.

Yield was evaluated following the von Mises yield criterion. Von Mises yield criterion is shown in Equation (3.111).

$$\sigma_v = \sqrt{\frac{1}{2} \left[(\sigma_x - \sigma_y)^2 + (\sigma_y - \sigma_z)^2 + (\sigma_x - \sigma_z)^2 \right] + 3(\tau_{xy}^2 + \tau_{yz}^2 + \tau_{xz}^2)} \quad (3.111)$$

For a idealized structure where the booms only carry axial loads, and the sheet only shear loads, Equation (3.111) simplifies to Equation (3.112) and Equation (3.113) for the boom and sheet respectively.

$$\sigma_{v,boom} = \sigma \quad (3.112)$$

$$\sigma_{v,sheet} = \sqrt{3}\tau \quad (3.113)$$

The structure was also evaluated for buckling and adequately designed for if buckling occurred in compression. The critical buckling stress was obtained by Equation (3.114).

$$\sigma_{cr} = C \frac{\pi^2 E}{12(1-\nu^2)} \left(\frac{t}{b} \right)^2 \quad (3.114)$$

where σ_{cr} is the critical stress above which buckling occurs, C is the buckling coefficient which is set to be 5.6, ν is the poisson ratio and is 0.32 for the considered materials as obtained from available software [64], t is the thickness of the plate, and b is the width of the plate. The structure was evaluated for buckling and if the stresses exceed the critical stress. In places where the stress exceeds the critical stress stringers and ribs are placed in the geometry while minimizing mass.

Lastly, the structure was evaluated for vibrations. The vibrational analysis is of importance for the rotors, the wing, and the tail boom. The blades and the wing are assumed to be distributed mass Euler beams, while the tail boom is assumed to be a spring-damper system with a lumped mass at the end.

The vibrations of the blades and the wing were assumed to be Euler beams with a distributed mass. The wing was clamped at both edges due to the brace clamping the wingtip. And the blades were assumed to be clamped at the root and free at the tip. The vibrational analysis on these two structures was performed by the use of the python package `vibration_toolbox`¹¹.

The tail boom is assumed to be a spring-damper system with an equivalent stiffness as shown in Equation (3.115), and an equivalent damping coefficient as seen in Equation (3.116)

$$k_{eq} = \left(\frac{3EI}{l^3} + \frac{3\pi}{l} q_{S_h} \right) \cdot m^{-1} \quad (3.115)$$

¹¹<https://vibrationtoolbox.github.io/>

where E is the Young's modulus of the tail boom, I the moment of inertia, l the length of the beam, q the dynamic pressure as experienced by the horizontal tail, S_h the surface area of the horizontal tail, and m the mass of both the tail boom and the empennage subsystem. For vibrations in z -direction the horizontal stabilizer is of interest and for vibrations in the y -direction the vertical stabilizer is of interest.

Aerodynamic damping was assumed to be present, as the surface area of the control surfaces move against the direction of flow. This caused a drag force that quadratically damps the system with an equivalent damping coefficient as shown in Equation (3.116).

$$c_{eq} = \frac{1}{2} \rho_0 S_h C_D m^{-1} \quad (3.116)$$

where ρ_0 is the air density, S_h is the surface area of the horizontal stabilizer, and C_D is the drag coefficient which is 1.28 for a flat surface.

The spring-damper system that was solved followed Equation (3.117)

$$\ddot{z} + c_{eq}\dot{z} + k_{eq}z = 0 \quad (3.117)$$

where \ddot{z} is the second time derivative of z , \dot{z} the time derivative of z , and z is the distance from equilibrium position.

3.12.5. Materials

For the design of structures, several materials were considered. The design of most components were strength-limited. In designing for strength, a selection was made based on the material index for specific strength. From this, the material chosen is Carbon Fiber Reinforced Polyetheretherketone (CF/PEEK) for its high strength and relatively low density when compared to aerospace alloys. In contrast to most components which were designed for strength, the blades and the tail beam were designed for stiffness, as they are exposed to vibrations and other aeroelastic effects. The material selection for these parts were driven by the material index for specific stiffness. The material chosen for stiffness is Carbon Fiber Reinforced Cyanate Ester (CF/Cy), for its high stiffness and high strength in relatively low density.

Regarding the use of metals, the vertical stabilizer needed to be made out of a conducting material for communication purposes. Since the strength required by this structure was not too much (as will be seen in Section 4.12), the material used in its design is Al518.0 which is a light aluminum alloy. Furthermore, titanium was used for the sizing of the rivets in the assembly that will be described in Section 9.4. All material properties can be attained from Ansys Granta Edupack [64].

Other considerations made, were their resistance to the harsh environment of Mars. The chosen materials show great resistance to ultraviolet radiation [65, 66] and are able to withstand the temperature range the aircraft needs to endure [64].

3.12.6. Limitations and future recommendations

Due to time constraints, several aspects of the structural analysis of the aircraft were not performed. Here, the limitations of the design are mentioned and formed into recommendations for future development, namely:

1. Load-bearing components
2. Aeroelastic phenomena
3. Design of joints and tilting mechanism
4. Buckling
5. Fiber orientation
6. Fatigue
7. Crashworthiness

Firstly, the only load-bearing component considered is the skin, even in the presence of stiffeners and other reinforcing structures. Future research could expand the code such that it iterated the stress calcu-

lation over the added structural components in order to more accurately size the structure, or even make the skin not load bearing in order to reduce its thickness.

Secondly, aeroelastic phenomena such as flutter was not investigated due to time constraints. Furthermore, the calculated natural frequencies were for an idealized structure, which will induce an error in the calculation. It is strongly recommended to use a more advanced FEM tool in order to perform an aeroelastic analysis on components such as the wing, rotor blades, and tail.

Thirdly, the design of most joints such as the point at which horizontal and vertical stabilizers intersect has currently been neglected, as has the design of the mechanism that would allow for the tilting of the rotors. Future research should pay special attention to these parts that will most likely need reinforcement due to stress concentrations.

Additionally, the buckling analysis should be developed further, as now the only buckling mode of failure considered is thin sheet buckling. Other forms of buckling such column buckling for the brace and the stringers on the sheets should be investigated in further analysis.

Furthermore, the composites were assumed to have a quasi-isentropic lay-up. Investigating the required loading directions could result in a more specific lay-up that reduces the thickness and saves mass.

Regarding EOL, fatigue loads were not investigated due to time constraints. This is an important aspect that future iterations should look into given the large operational life of the design and the lack of infrastructure on Mars to make repairs.

Finally, the undercarriage and crashworthiness of the design was not explored in this iteration. This aspect should be addressed in future iterations in order to reduce the risk of mission failure.

Subsystem Design Results

4.1. Wing Sizing Results

By Adrian Beño, Pedro Santos

Following the wing sizing methodology described in section 3.2, the defining wing and aileron parameters are presented in Table 4.1 and Table 4.2, respectively. The wing planform is shown in Figure 4.1. Although the global optimization methodology was unsuccessful, straight leading edge resulted in slightly increased lift performance in XFLR5 simulations. The chord of ailerons was required not to exceed 30% of the local chord as this would interfere with structural constraints of the wing, as well as quicken the flow separation. This is a problem for highly cambered airfoils, such as S1223 shown in Figure 4.2, and is described in detail in subsection 5.2.1.

Table 4.1: Wing design parameters

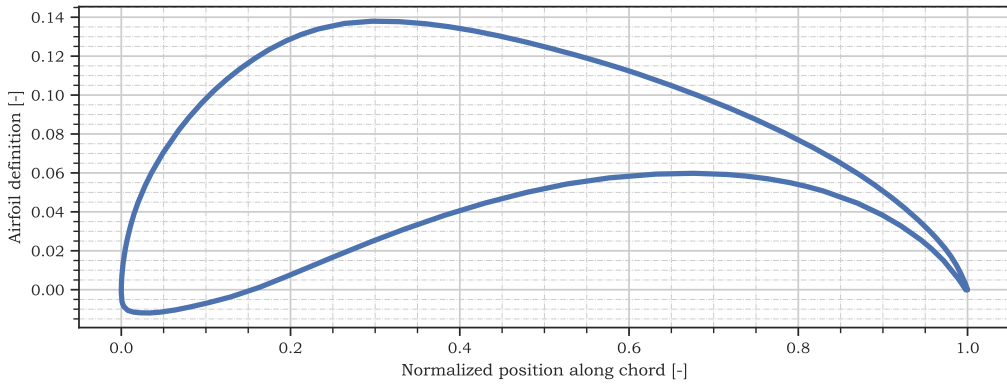
Parameter	Value	Parameter	Value
b [m]	44.75	c_{tip} [m]	1.99
S [m^2]	133.5	$V_{TAS_{cruise}}$ [m/s]	111.1
MAC [m]	3.09	M_{cruise} [-]	0.46
AR [-]	15	Re_{cruise} [-]	664'000
λ [-]	0.5	$C_{L_{cruise}}$ [-]	1.33
ϕ [deg]	0	$C_{D_{cruise}}$ [-]	0.045
Λ [deg]	0	α_{cruise} [deg]	1
Γ [deg]	0	Airfoil [-]	S1223
c_{root} [m]	3.98		

Table 4.2: Aileron design parameters

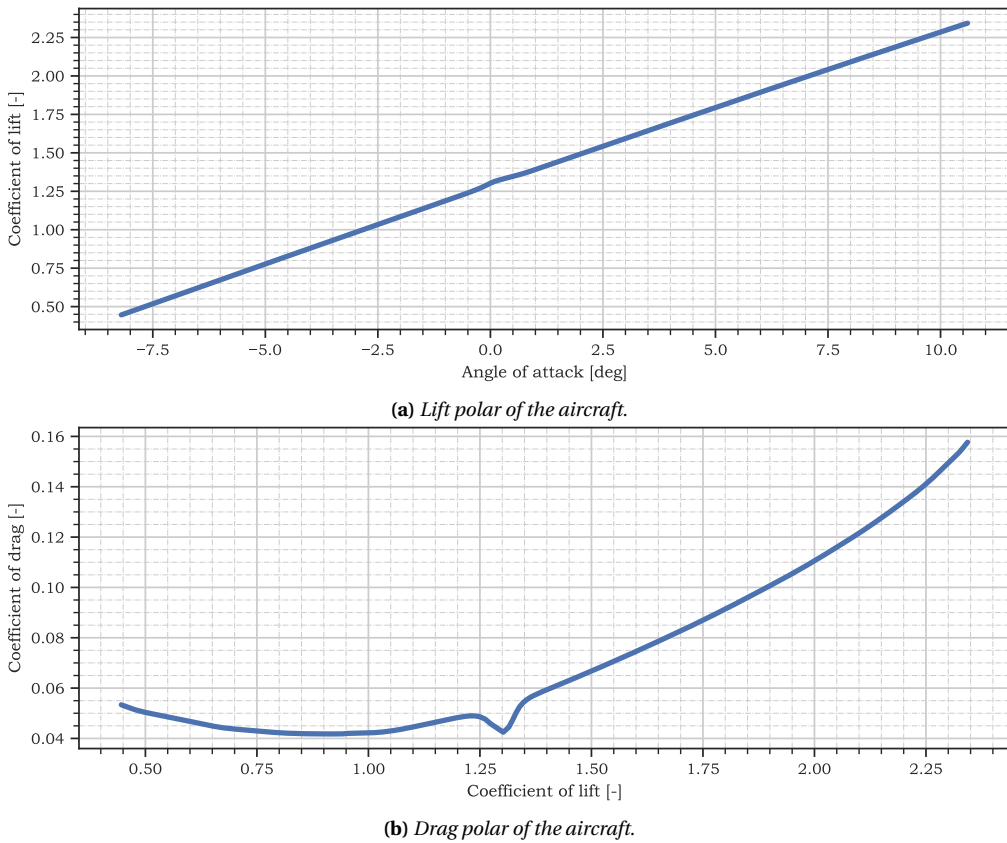
Parameter	Value	Parameter	Value
Aileron span (per aileron) [m]	11.19	Coefficient of rolling moment [-]	0.15
$MAC_{aileron}$ [m]	0.75	Hinge moment (full upwards deflection) [Nm]	400
δ [deg]	20	Hinge moment (full downwards deflection) [Nm]	150



Figure 4.1: Wing planform. Leading edge is straight.

**Figure 4.2:** The definition of the S1223 airfoil

The lift and drag polars of the aircraft are shown in Figure 4.3a and Figure 4.3b, respectively. The polars are results of XFLR5 simulations.

**Figure 4.3:** The lift and drag polars of the aircraft (including tail). Data from XFLR5 simulations.

The dip in the lift-drag polar in Figure 4.3b is just a computational artifact of XFLR5 and it does not represent physical aerodynamic phenomenon. It exists due to the interference of the panel behind the main wing, which is used to compute the downwash, with the panels on the tail, of the vortex lattice method. It is a numerical artifact of this panel method and shall be neglected when interpreting the graph. Similar but smaller upwards pointing dip can be seen in Figure 4.3a too.

4.2. Rotor Sizing Results

By Sebastian Harris

After following the steps in section 3.3, the values are modified in order to match the requirements better. Modifications to the chord, taper, and overall blade shape were made. The results can be summarized

in the exact breakdown as that of the methods section, starting with a summary of the previous work done in subsection 4.2.1. Next, the upper and lower rotor geometry and performance are given in subsection 4.2.2 and subsection 4.2.3. This leads to the description of the rotor performance in cruise, as seen in subsection 4.2.4 and finally with a description of the rotorwash in subsection 4.2.5

4.2.1. Previous findings

The previous report established a process for determining the number of rotors. This resulted in the following rotor dimensions:

Table 4.3: Rotor dimensions from the midterm report

Number of Blades	Radius	Chord	Thrust
6	10.4 [m]	0.52 [m]	2789.72 [N]

4.2.2. Upper Rotor

The upper rotor dimensions and performance, after being determined and iterated on, can be summarized in Table 4.4, with the additional mention that 8 blades are present on the rotor.

Table 4.4: Final upper rotor characteristics

Radius [m]	0.	0.9	1.4	1.8	2.7	3.6	4.6	5.5	6.4	7.3	8.2
Chord [m]	0	0	0.75	0.75	0.68	0.55	0.46	0.39	0.34	0.30	0.27
Twist [deg]	0	0	14.5	11.4	10.0	8.8	8.0	7.5	7.1	7.0	7.2
Hover Thrust [N]	3072										
Hover Torque [Nm]	249										
Hover Power [kW]	50										
Hover RPM [-]	233										

4.2.3. Lower Rotor

As the lower rotor performs in the wake of the first rotor, the twist and performance characteristics are modified to reflect this, leading to the geometry and performance of Table 4.5, with the additional mention that 8 blades are present per rotor. Namely, the downwash of the first rotor results in a wake with an axial velocity of 29.263 m/s and tangential velocity of 48.299 m/s which must be accounted for in the angle and rotation of the second rotor.

Table 4.5: Final lower rotor characteristics

Radius [m]	0.	0.9	1.4	1.8	2.7	3.6	4.6	5.5	6.4	7.3	8.2
Chord [m]	0	0	0.75	0.75	0.68	0.55	0.46	0.39	0.34	0.30	0.27
Twist [deg]	0	0	14.5	13.4	11.1	10.1	9.1	8.3	7.6	7.0	6.8
Hover Thrust [N]	2503										
Hover Torque [Nm]	356										
Hover Power [kW]	71										
Hover RPM [-]	175										

4.2.4. Cruise

In cruise, two main conditions are important: minimum thrust to sustain cruise and maximum thrust, given the power rating of the aircraft. These values are summarized in the following table.

Table 4.6: Configuration of the upper and lower rotors in cruise

	Minimum Power		Maximum Power	
	Upper Rotor	Lower Rotor	Upper Rotor	Lower Rotor
Thrust [N]	9.37	419.43	335.66	534.52
Power [kW]	10.68	47.45	47.45	103.87
RPM	1.03	10.35	26.90	20.69
Collective [deg]	68.41	43.74	19.08	22.158

4.2.5. Rotor Downwash

The downwash of the rotor during take-off will produce a dust cloud. This cloud can be defined by a set of distances as seen in Figure 4.4. In the case of the tiltrotor design in take-off, the following dimensions apply:

- $R_C = 27.29 \text{ m}$
- $R_V = 21.42 \text{ m}$
- $H_C = 12.81 \text{ m}$
- $l_v = 3.83 \text{ m}$

4.2.6. Unpowered Rotation

Considering the airfoil used for the blades, the maximum ratio of $\frac{c_L^3}{c_d^2}$ is of 67.95 and, with an average solidity factor of $\sigma = 0.159$, the difference in normalized velocities is of 0.096. Using Figure 4.5, the relationship leads to a maximum descent rate of 34.74 m/s.

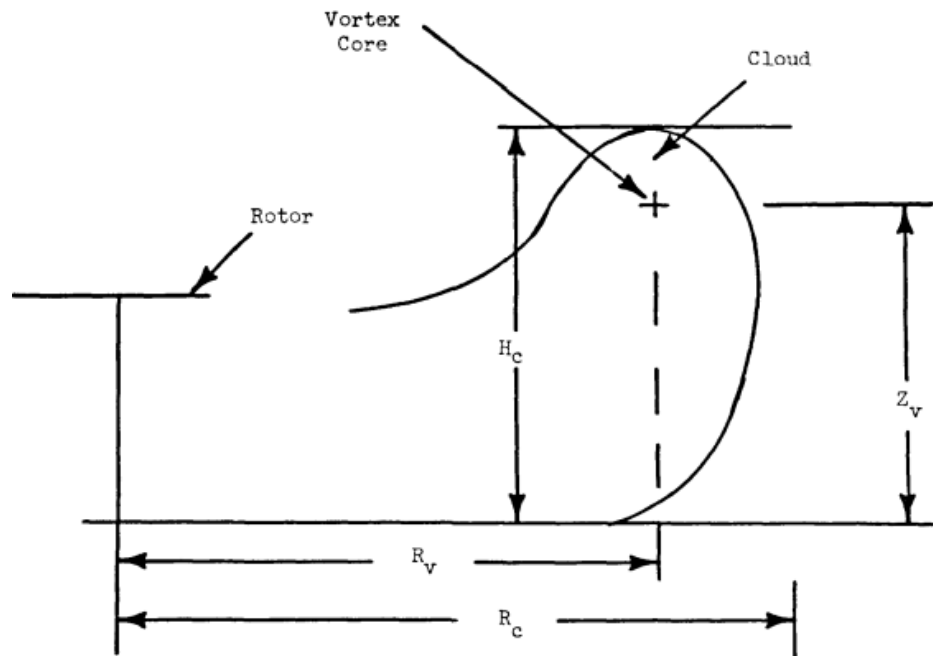


Figure 4.4: Rotor Particle cloud Geometry [23]

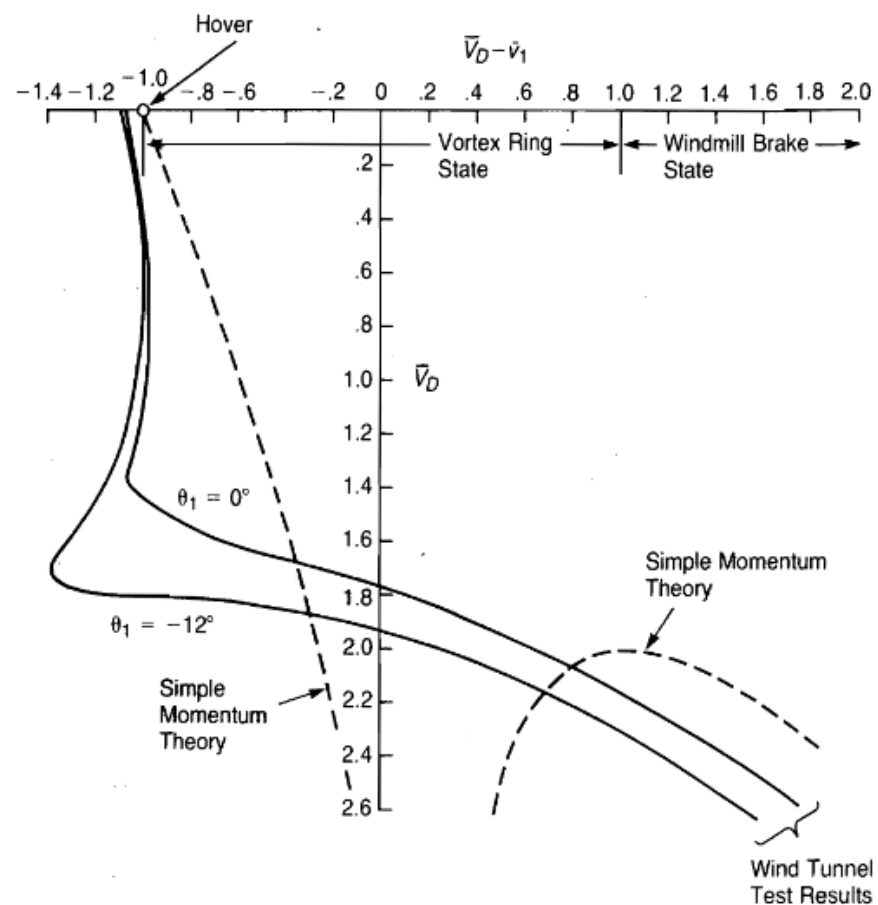


Figure 4.5: Nondimensional Velocities in Vertical Descent [20]

4.3. Control and Stability

By Patrick Kostelac, Thomas van de Pavoordt Control and stability is an important aspect of every design. Stability is necessary as it ensures a steady and safe flight, while control is necessary in order to arrive at the wanted destination. As a result control and stability have a large influence over the design in terms of the tail size and position as well as the control surfaces, whose design will be outlined in this chapter.

4.3.1. Static stability

By Patick Kostelac The first output of the static stability is the loading diagram which shows the possible range of CG values. The inputs for the loading diagram are shown in Table 4.7:

Table 4.7: Component mass and CG location

Variable	OEW	payload	crew
mass	2650	100	250
CG	0.34	0.94	-0.24

With these values the loading diagram in Figure 4.6 is constructed. From the loading diagram the most aft CG was found to be at 0.3645 x/c and the most forward CG was found to be at 0.2900 x/c.

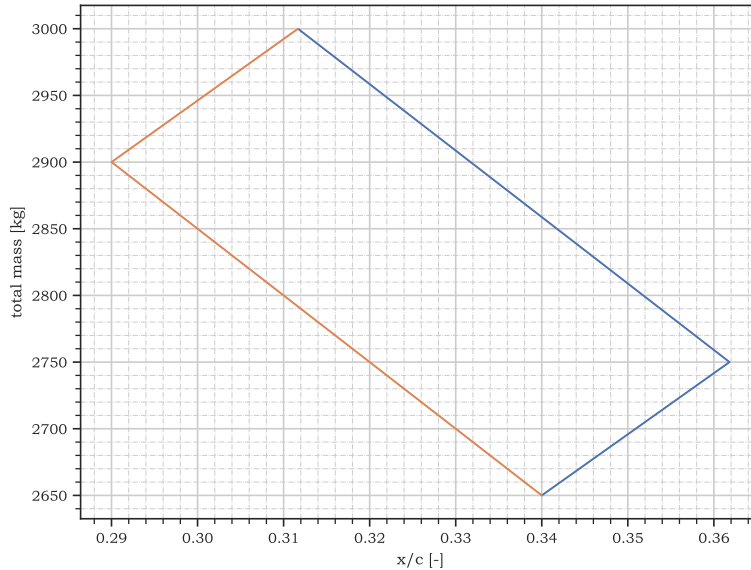


Figure 4.6: Loading diagram of the aircraft

Next, the scissor plot with the final values can be constructed. The final values of all the coefficients for stability and control can be seen in Table 4.8. With the X_{cg} being varied from 0 to 1. The scissor plot can be seen in Figure 4.7.

Table 4.8: Variable values

Variable	$C_{L_{ah}}$ [-]	$C_{L_{aA}}$ [-]	$\frac{de}{da}$ [-]	l_h [m]	c [m]	$\frac{V_h}{V}$ [-]	x_{ac} [m]	$C_{m_{acw}}$ [-]
value	6.283	5.271	0	13.00	3.978	1	0.25	-0.33

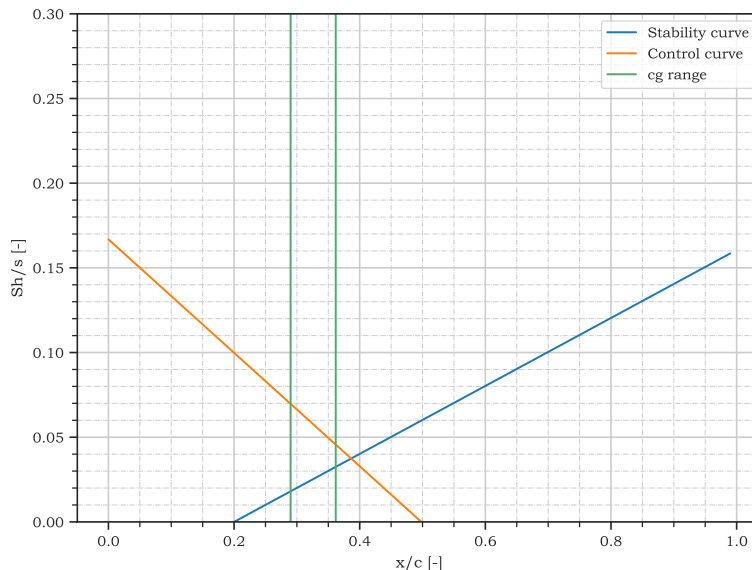


Figure 4.7: The scissor plot of the aircraft

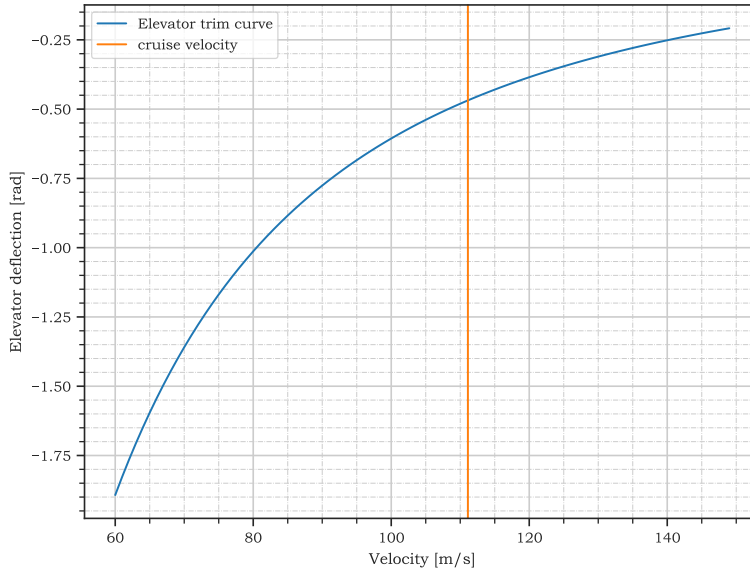
It can be seen that the minimum CG value constrains the controllability, while the maximum CG value constrains stability. From the scissor plot it is also clearly visible that it is important not to make the aircraft too stable as that would make it uncontrollable and vice versa. Controllability was found to be the driving requirement giving the final value of $Sh/S = 0.0635$.

Through the sum of forces in the body x direction the thrust for cruise was found to be 474 N. The optimum cruise C_{Lw} of the main wing was found to be 1.33 during wing sizing which meant that C_{Lh} can be calculated through the sum of forces in body z direction and was found to be 0.1635. The x location of the main wing aerodynamic center with respect to the CG is known to be 0.356 m from the loading diagram. The x location of the tail is then calculated through the sum of moments and was found to be 12.64 m behind the cg. Finally, through the iteration of AOA the C_{m_a} was calculated to be -0.1940, since C_{m_a} is negative, the aircraft is determined to be statically stable.

The neutral points of the aircraft have been determined to be 0.5664 x/c for the stick fixed condition and 0.5147 x/c for the stick free condition. The most aft location of the CG was determined to be 0.3645 x/c by the loading diagram. Since both of the neutral points are behind the most aft CG the aircraft is determined to be stable. With the neutral points known, the elevator trim curve was constructed. The final values of the coefficients used to create the elevator trim curve are presented in table Table 4.9 with the velocity being varied from the stall speed to 150 m/s which equates to mach 0.7 which was set as an upper limit of the cruise speed in the requirements. The elevator trim curve can be seen in Figure 4.8.

Table 4.9: Variable values

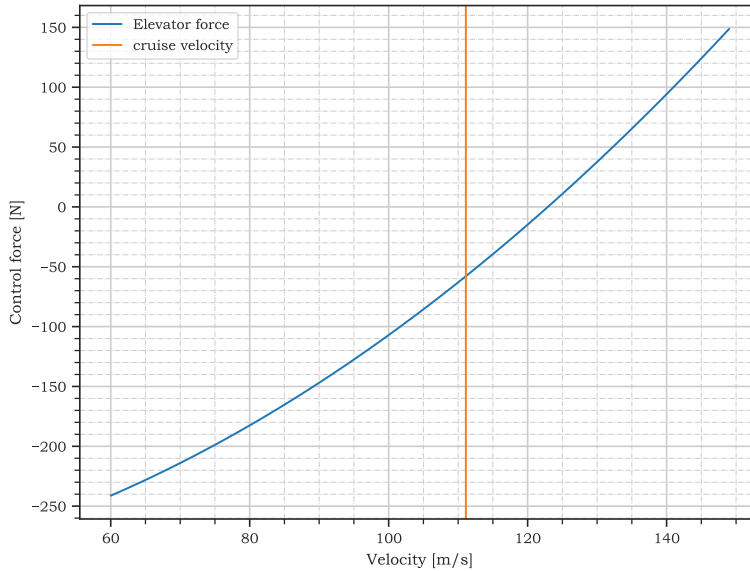
Variable	$C_{m_{\delta_e}}$ [-]	C_{m0} [-]	W [N]	ρ [kg/m ³]	S [m ²]	x_{cg}/c [-]	$x_{n_{fixed}}/c$ [-]
value	-0.279	-0.236	11130	0.01	133.5	0.2900	0.5664

**Figure 4.8:** Elevator trim curve

From the elevator trim curve it can be seen that at the cruise velocity of 111 m/s, the elevator deflection in order to trim the aircraft is -3.446° . The deflection of -3.091° produces a C_{Lh} of 0.3389 which is slightly higher than the predicted C_{Lh} of 0.1635 through the moment analysis. This discrepancy will be discussed later. The parameters used in the control force calculation that have not already been presented are shown in Table 4.10. The elevator control force curve is shown in Figure 4.9.

Table 4.10: Variable values

Variable	$\frac{d\delta_e}{dS_e}$ [-]	S_e [m^2]	c_e [m]	C_{h_δ} [-]	C_{m_δ} [-]	$x_{n_{free}}$ [x/c]	$C_{h_{\delta t}}$ [-]	$(\delta_{te} - \delta_{te0})$ [$^\circ$]
value	6.283	16.96	1.504	-0.2790	-0.6450	0.5147	-0.228	20.95

**Figure 4.9:** Elevator control force curve

Next, the trim stability criterion is checked. Trim stability is defined as the slope $\frac{d\delta_e}{dV}$ which needs to be positive for a stable aircraft. From the graph it is visible that the curve is positive for the entire range

of cruise speeds. Lastly the elevator control force stability $\left(\frac{dF_e}{dV}\right)_{F_e=0}$ is checked. This value needs to be positive in order to achieve stability and was calculated to be 3.248 Ns/m making the aircraft stable.

4.3.2. Vertical tail design

The minimum required vertical tail area for the cross wind condition was determined to be 10.93 m^2 for a cross wind of 15 m/s, while the minimum required vertical tail area for the one engine out condition was determined to be $S_v = 11.33 \text{ m}^2$. Thus the one engine out condition was determined to be critical. This allows for cruise with three out of the four engines still remaining operative. During a one engine out condition a horizontal landing will be performed. This will be done by turning off an additional engine and tilting the rotors at a 87.07° with respect to the body x axis. Allowing for an approach speed of 67.66 m/s with the two engines producing 267.52 N of thrust in the body x direction (horizontal) and 5232 N of thrust in the negative body z direction (vertical). Under this condition the aircraft can land horizontally without the blades getting damaged by the ground. This allows for a landing distance of 1371 m in the one engine out condition.

4.3.3. Empennage parameters

By Patrick Kostelac By combining all of the static stability results, the empennage design can be finalized. The scissor plot resulted in $Sh/S = 0.0635$ constraining the minimum horizontal tail size. The cross wing and one engine out condition constrained the minimum vertical tail size to 11.33 m^2 . Other than the minimum areas required, the static stability equations take additional parameters such as $C_{L_{ah}}$, $C_{m_{\delta_e}}$, $\frac{d\delta_e}{dS_e}$, S_e , c_e , C_{h_δ} , C_{m_δ} and $C_{h_{\delta_t}}$. S_e is determined by the scissor plot, C_e , the mean aerodynamic chord and b , the span were found through the optimum aspect ratio which according to [16] is half of the aspect ratio of the main wing. The root chord (C_r) and tip chord (C_t) were determined through the optimum taper ratio which was found according to [16]. The rest of the coefficients are all determined by choosing the airfoil for a horizontal tail and performing xflr5 analysis. The final airfoil chosen for the horizontal tail is NACA0012. One of the main reasons for choosing this airfoil was the need to generate both downforce and lift at different flight stages. The design of the vertical tail was simpler with the area determined by one engine out condition. The chord and span were determined by choosing an optimum aspect ratio which according to [16] was found to be two. The root chord and tip chord are again found through optimum taper ratio which was determined according to [16]. Lastly the $C_{y_{deflect}}$ and $C_{y_{side}}$ are determined from xflr5 analysis of the airfoil which was once again determined to be NACA0012 because of the need to generate side force in both direction. The final parameters for the horizontal tail is shown in Table 4.11 and the final parameters for the vertical tail are shown in Table 4.12.

Table 4.11: Horizontal tail parameters

Variable	$S [\text{m}^2]$	AR [-]	$b [\text{m}]$	taper ratio [-]	$C_r [\text{m}]$	$C_t [\text{m}]$	sweep [°]	$(X_h - X_{cg}) [\text{m}]$	
value	16.96	7.5	11.28	0.4		2.148	0.8592	4.899	12.64

Table 4.12: Vertical tail parameters

Variable	$S [\text{m}^2]$	AR [-]	$b [\text{m}]$	taper ratio [-]	$C_r [\text{m}]$	$C_t [\text{m}]$	sweep [°]	$(X_v - X_{cg}) [\text{m}]$	
value	11.33	2	4.760	0.4		3.400	1.360	17.82	12.64

4.3.4. Dynamic stability

By Thomas van de Pavoordt For dynamic stability, the wing, elevator, and rudder were modeled in XFLR5 according to the values described in Section 4.3.1 and Section 4.3.3. A stability analysis was performed, which resulted in 8 eigenvalues for the aircraft. XFLR5 defines 4 modes for both longitudinal and lateral. Longitudinal mode 1 and 2 represent the complex conjugates for the short-period motion, mode 3 and 4 represent the phugoid motion. Lateral mode 1 represents the a-periodic roll, mode 2 and 3 the Dutch roll and mode 4 represents the spiral. Results are shown in Table 4.13:

Table 4.13: Eigenvalues from XFLR5 stability analysis

Mode	Eigenvalue
Short-period	$-0.3156 \pm 1.0722i$
Phugoid	$-0.0018 \pm 0.1687i$
A-periodic roll	$-0.2171 \pm 0.0000i$
Dutch roll	$-0.1238 \pm 0.4037i$
Spiral	$+0.1236 \pm 0.0000i$

This shows that all eigenmodes except the spiral are stable and damped. The spiral eigenmode proved to be unstable. However, this is not a problem as most aircraft have an unstable spiral. The spiral eigenmode takes a long time to accelerate significantly and all pilots are trained to be able to exit the spiral in appropriate time.

4.3.5. Cruise control

By Patrick Kostelac During cruise the aircraft is controlled by the four aforementioned PID controllers, therefore the first output of the cruise control are the controllers themselves. The controller specifications can be seen in Table 4.14. The minimum and maximum force of the thrust controller was determined by the physical limitations of the rotors. The minimum and maximum force of the aileron and elevator controller was determined by the rate of roll and rate of pitch requirements issued by the Code of Federal Regulations section 23 [67] and rudder requirement was derived from the one engine out condition.

Table 4.14: Cruise controller parameters

Controller	Proportional gain	Integral gain	Derivative gain	Max Force	Min Force
Thrust	1000	5	0	870.2	0
Aileron	-4000	-1	-7500	853	-853
Rudder	15000	-50	-15000	731	-731
Elevator	25000	6000	5000	1227	-1227

With the controllers tuned and limited to the achievable values, they can be incorporated into the system. The cruise control takes an initial disturbance as input and produces the force required by each of the control surfaces and the thrust as output. The initial condition given to the system and the desired condition can be seen in Table 4.15. The change in state can be visible in Figure 4.10 while the forces provided by each control surface in order to reach the desired condition are visible in Figure 4.11.

Table 4.15: Initial and final states

State	Initial Value	Target Value
attitude [°]	(30, -5, 5)	(0,0,0)
linear velocity [m/s]	(100, 0, 0)	(111, 0, 0)
angular velocity [°/s]	(0, 11.45, 0)	(0,0,0)

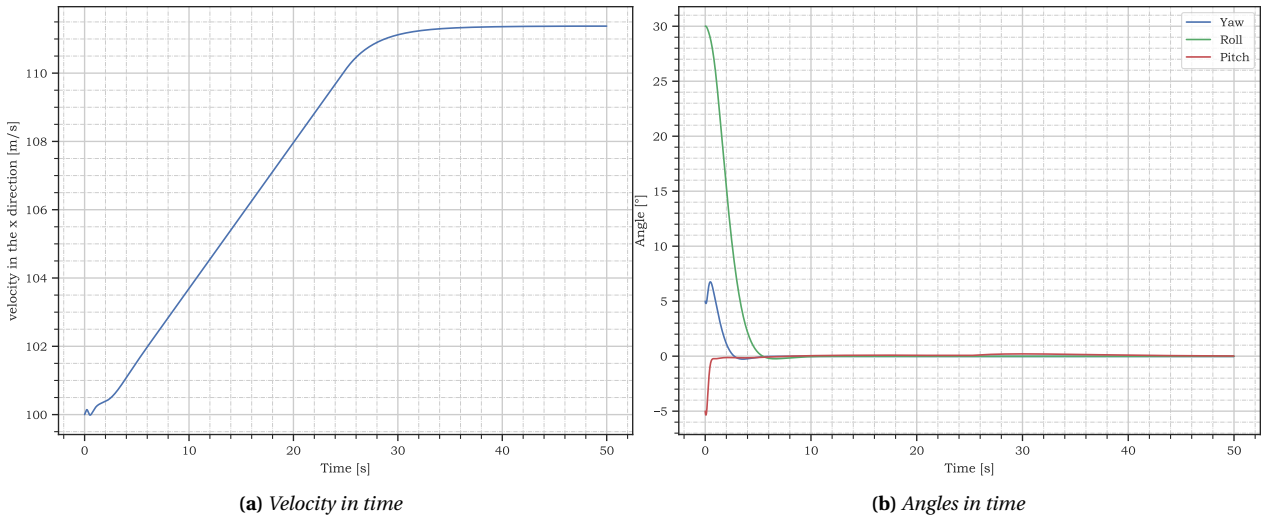


Figure 4.10: Aircraft state in time

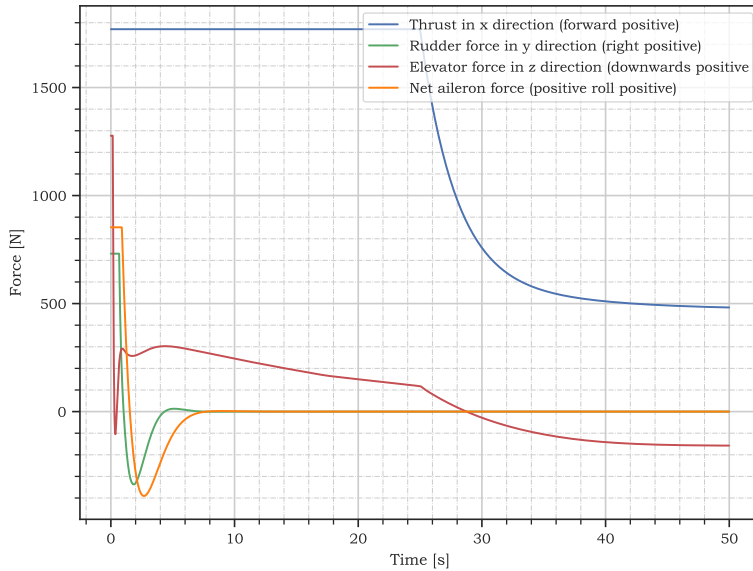
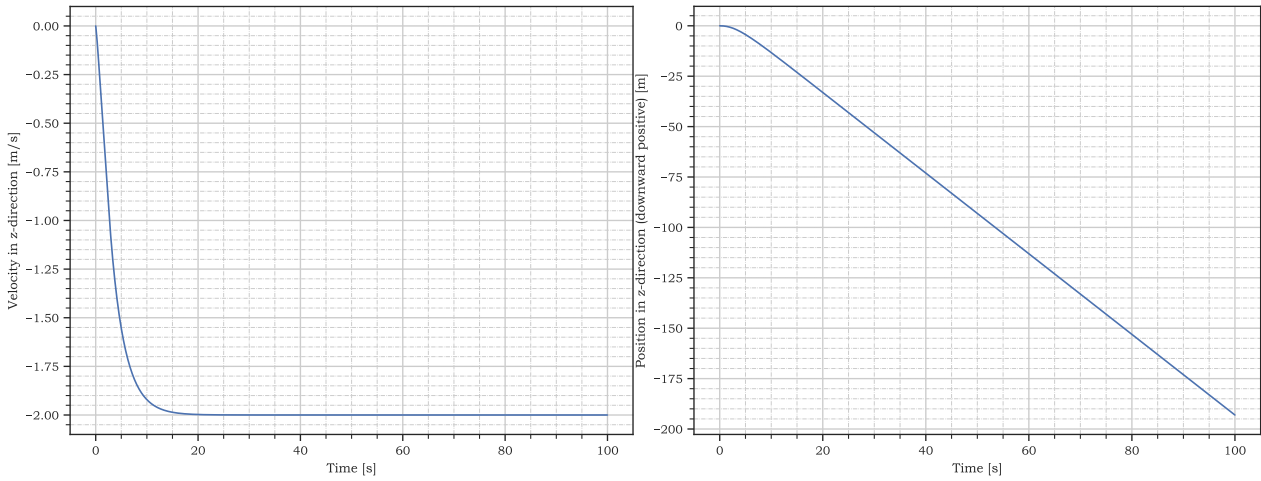


Figure 4.11: Thrust and control forces in time

4.3.6. Take-off, landing and transition control

By Thomas van de Pavoordt

For take-off (and in reverse thus landing), the controller utilizes the thrust to obtain the desired reference state of 2 m/s upward velocity with no change in Euler angles. The controller is tuned with 6000 proportional gain, 1000 derivative gain and 1600 integral gain. The controller for the attitude of the aircraft, or the slight pitching of the engines, is tuned with -25000 proportional gain, -25000 derivative gain and -5000 integral gain to quickly diminish any attitude disturbances. Figure 4.12 shows the velocity and position in z-direction of the aircraft during take-off, where it should be noted that downward velocity or position is considered positive, in line with the body reference frame of the tiltrotor.



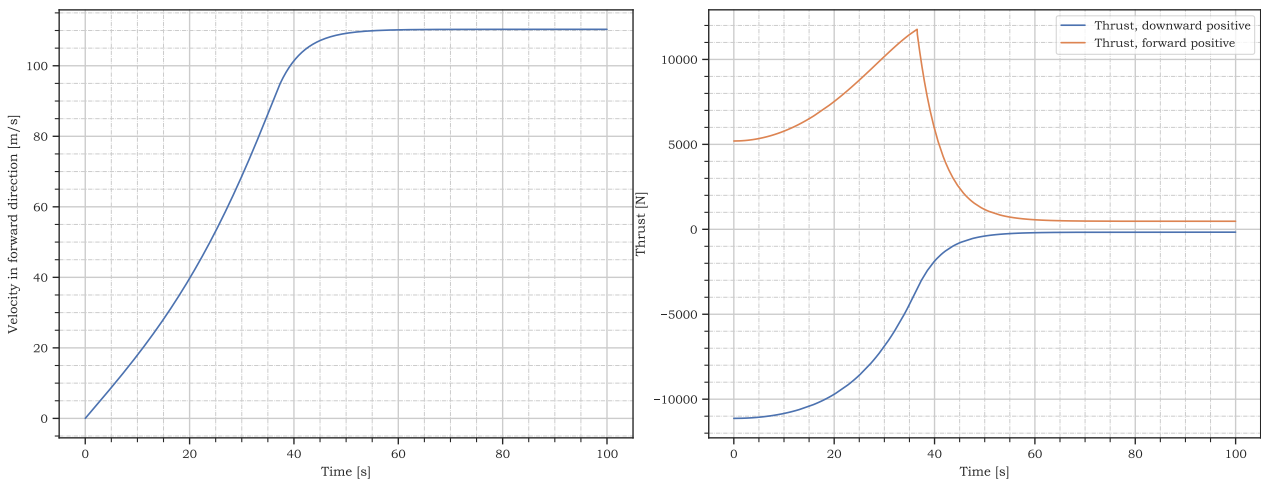
(a) Velocity in z-direction in time during take-off

(b) Position in z-direction in time during take-off

Figure 4.12: Aircraft state in time during take-off

Figure 4.12 shows that the tiltrotor achieves a constant upward velocity of 2 m/s after approximately 20 s. It gradually gains altitude and is at almost 200 m after 100 s.

During transition, a constant trade-off between thrust in upward direction, thrust in forward direction, lift in upward direction and drag in backward direction is happening. Two controllers will be employed in series. The first controller controls the thrust in a more coarse sense. It utilizes inputs to the thrust from secondary controllers and determines the maximum amount of thrust the rotors can actually produce and will then allocate that to both forward and upward thrust. Once the velocity increases enough, the second controller will take over to fine-tune towards the desired velocity of 400 km/h. The first controller is tuned with 1000 proportional gain, 2500 derivative gain and 100 integral gain. The second controller is tuned with 9 proportional gain, 6 derivative gain and 9 integral gain. Figure 4.13a shows the velocity in x-direction, where forward velocity is positive. Figure 4.13b displays the distribution of the thrust between thrust in x-direction (forward positive) and thrust in z-direction (downward positive).



(a) Velocity in x-direction in time during transition

(b) Thrust distribution in time during transition

Figure 4.13: Aircraft state in time during transition

It can clearly be seen in Figure 4.13a that the aircraft reaches the desired cruise speed. Figure 4.13b shows that the thrust in z-direction is decreased to 0, as speed and thus lift over the wing increases. Thrust in x-direction is first increased to achieve cruise speed as fast as possible and once the controller for finetuning kicks in, it can be gradually decreased until the thrust in x-direction only matches the amount of drag during cruise.

4.4. Undercarriage Sizing Results

By Sebastian Harris After the calculations of section 3.5, the undercarriage size is as follows. First, the main landing gear is 0.869 m in front of the center of gravity, whereas the tail landing gear is 10 m behind the center of gravity. Regarding the tip-over clearance, a distance of at least 0.5 m is required between the main landing gear and the center of gravity in the y-direction. However, due to the large span of the aircraft, the wing tip clearance requires an additional landing gear at a distance of 18.383 m from the central axis.

Furthermore, considering the crashworthiness of the landing gear, it is crucial to note that even in autorotation, a flare near the ground will reduce the descent speed and decrease kinetic energy. Nonetheless, in a total power blackout with no control of the blades or engines, the descent speed calculated in subsection 4.2.6 applies. Considering the current situation utilizing a total of 5 landing gear struts, split between one on the tail, two on the wings, and two on the fuselage, this energy is split between the 5 systems. This leads to an energy per strut of 724 kJ for which, considering an absorber stroke of 0.5 m, would require a force of 713 kN leading to a total induced acceleration of $129 g_{mars}$ or $48.6 g_{earth}$, equivalent to a car crash, with seatbelt at 50 km/h¹. Although these values are high, in the case of a crash landing these are more than survivable conditions. Thus, it was decided a crash-designed undercarriage is not sufficient.

4.5. Fuselage

By Pedro Santos

The final layout and dimensions of the fuselage can be seen in Figure 4.14, corresponding to a total wetted area of $31 m^2$. A rendering of the fuselage's interior can be seen in Figure 4.27.

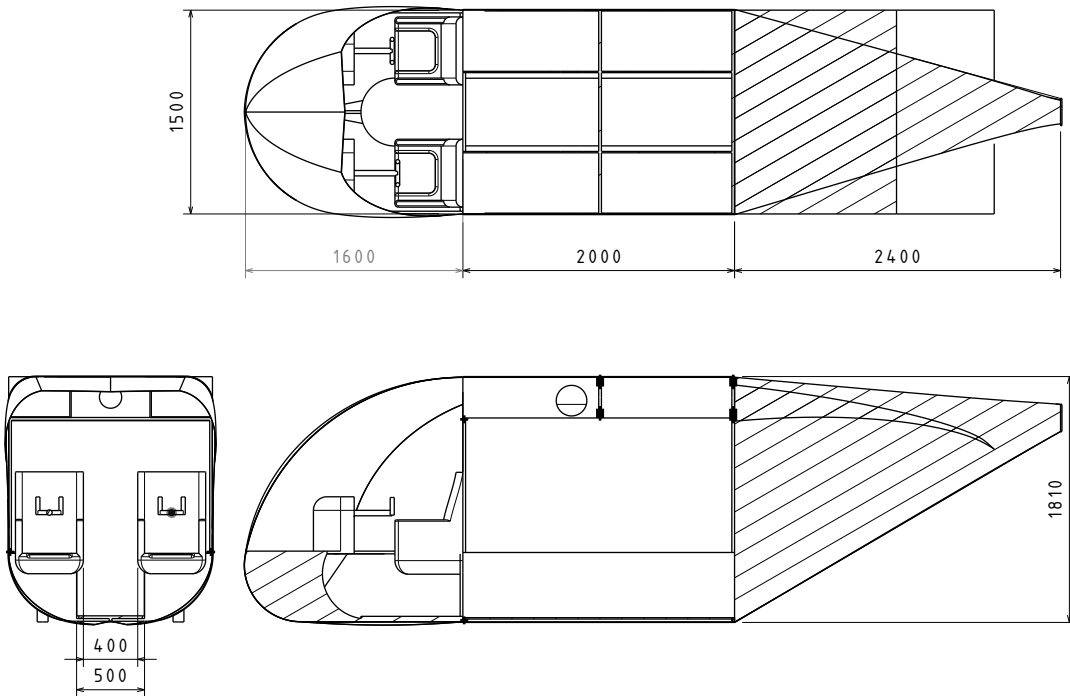


Figure 4.14: Internal layout of the fuselage.

Furthermore, using the formulas presented in section 3.6, the C_D obtained was 0.031 which due to the aircraft's wetted area of roughly $31 m^2$, lead to a total fuselage drag of about 59 N at a cruise speed of 111 m/s and an atmospheric density of $0.01 kg/m^3$.

¹URL: <https://www.wral.com/story/high-speed-car-crashes-exert-lethal-force/17903314/> [cited 2023-06-21]

4.6. Power Sizing Results

By Timo de Kemp

In this section power subsystem results will be presented, the method from Section 3.7 will be followed. Starting with the engine and gearbox sizing, battery sizing, and solar panel sizing.

4.6.1. Engine & gearbox sizing

As described in Section 3.7 the power the rotors need and the engine need to provide are different due to inefficiencies in the gearbox. These powers for both take-off and landing for the upper and lower rotors are shown in Table 4.16.

Table 4.16: Parameters for the upper and lower rotor for both take-off and cruise

	ω_{TO} [rpm]	P_{TO} [kW]	$P_{TO_{eng}}$ [kW]	ω_{cr} [rpm]	P_{cr} [kW]	$P_{cr_{eng}}$ [kW]
Upper rotor	232.9	52.65	55.94	22.47	51.71	54.94
Lower rotor	180.0	104.28	110.8	22.47	80.74	85.79

From Table 4.16 it is seen that the power differs significantly between the upper and lower rotor. Therefore five electric engines from Emrax are considered the main properties of these engines are shown in Table 4.17. Combining Table 4.16 and Table 4.17 engines can be selected for the upper and lower blades.

Table 4.17: Emrax engine specifications relevant for design

Engine type	$P_{cont_{max}}$ [kW]	ω @ max power[rpm]	$T_{cont_{max}}$ [Nm]	Mass[kg]
188 ²	37	6500	56	7.1-7.9
208 ³	56	6000	90	9.4-10.3
228 ⁴	75	5500	130	12.9-13.5
268 ⁵	117	4500	250	21.4-22.3
348 ⁶	210	4500	500	43.1-43.9

The engines are selected for which the max required power is lower than the possible required power of the engine, making sure to pick the closest one to limit the mass. From the power-rotational speed graphs presented in the technical data sheet and in Figure 4.15 the rotational speed for the required power is determined. With this rotational speed and the rotational speed of the rotors the required gear ratio is determined, rotational speeds and gear ratios are presented in Table 4.18.

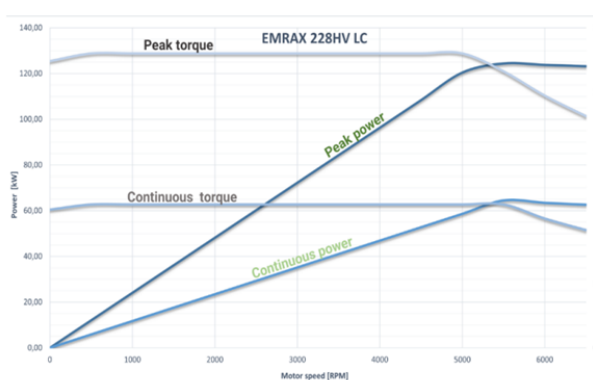


Figure 4.15: Power and torque versus the rotational speed for the 228 engine

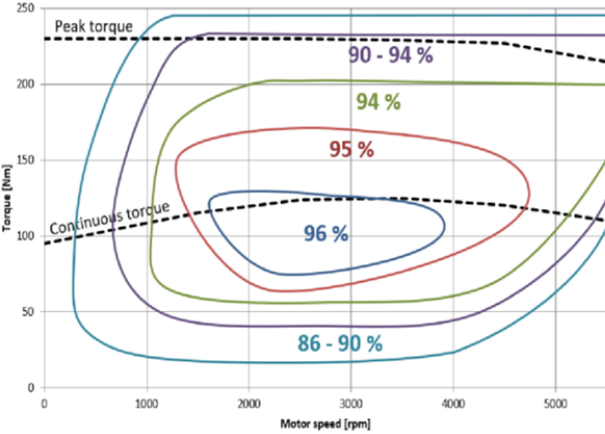


Figure 4.16: Efficiency map for the 228 engine

With this gear ratio the torque required by the rotors can be transferred to the torque the engine has to provide, taking also into account the gearbox efficiency. With the torque and the rotational speed the efficiency of the engine can be predicted for the setting using the efficiency map in Figure 4.16. The efficiencies found are also presented in Table 4.18.

Table 4.18: Upper and lower rotor, engine and gearbox parameters for take-off and landing

	Engine selected	ω_{TO}	Gear ratio TO[-]	Efficiency TO	ω_{cr}	gear ratio cruise[-]	Efficiency cruise
Engine upper rotor	228	5000	21.5	0.94	5000	222.5	0.94
Engine lower rotor	268	4500	25	0.86	4200	195	0.92

4.6.2. Battery sizing

To start the battery sizing an estimate of the power and energy needed has to be made. From all subsystems that require power the worst-case power has been taken into account. In Table 4.19 a summary of the subsystem is given including the powers required for flight.

Table 4.19: Power and energy required from the subsystems

	Power[kW]	Time used[hr]	Energy[kWh]
Take-off/Landing	354.53	0.167	59.21
Cruise	285.54	2.5	713.85
Flight computer	0.025	3	0.08
Communication	0.27	3	0.81
Sensors	0.09	3	0.27
Thermal	0.05	3	0.15
Avionics	1.275	2.5	3.18
Total			777.55

For the battery sizing first an estimate was made for the gravimetric energy density of future batteries. The current battery technology proved to make the design in feasible. Some research has been done to find current lab prototypes as well as prospects for the future, looking at both lithium ion as well as solid state battery technology. As the battery mass due to this undeveloped technologies is uncertain, the mass left on the budget was dedicated to the batteries.

The gravimetric energy density of batteries is an important parameter as this indicates how much energy is stored per unit of mass. Current available batteries have a gravimetric energy density of approximately 350 Wh/kg, while some Chinese researchers have found a 711 Wh/kg battery cell[68]. However to make the design work another increase is necessary while keeping the life cycle degradation similar to the current batteries.

While looking into the future of batteries the lithium ion batteries seem to be reaching its theoretical limit. A technology that has great opportunities for increasing the gravimetric energy density are Lithium air batteries, however the required oxygen also has to be stored as no oxygen is present in Martian atmosphere. Finally solid state batteries were looked into, these batteries have a significantly higher theoretical gravimetric energy density and are safer due to limited fire risks and reduced leak risk [69]. In an article estimation it was projected that solid state will be 2-2.5 more dense than current lithium-ion technology⁷, while it was presented by Goodenough to be 3 times more dense[70]. Therefore the solid state batteries should be able to have a gravimetric energy density of 700-1050 Wh/kg. The design was made assuming

⁷URL: <https://www.flashbattery.tech/en/how-solid-state-batteries-work/> [cited 2023-06-19]

a density of 875 Wh/kg. An added benefit is that current life cycle degradation for solid state batteries is more than 4x higher than lithium ion batteries⁸.

The amount of mass left for batteries on the Helios and Atlas variant are different as the Helios will have solar panels attached for autonomous recharging. While the Atlas has to rely on grid power to recharge. Due to the added mass of the solar panels, sized in Section 4.6.3, the Helios variant will have 903 kg and the Atlas 1057 kg available for Energy storage. Further information on the energy stored and range for both variants can be found in Table 4.20.

Table 4.20: Battery size for both variants and the associated range

	Battery mass[kg]	Energy stored[kWh]	Range[km]
Areon Helios	903	790.125	906
Areon Atlas	1057	924.875	1077

Finally as described in Section 3.7 the maximum power of the battery pack will be checked to the maximum power required in flight, which is at take-off. The power density of current lithium-ion batteries is used to determine the power of the battery pack. This is conservative as solid state will perform better than current lithium ion batteries according to Janek and Zeier[1]. With a power density of 1800 W/kg, the total power will be as presented in Table 4.21. A similar calculation is done for the volume the batteries take, with and energy density of 800 Wh/L, and presented in Table 4.21

Table 4.21: Power and volume of the battery systems and their requirements

	Power battery[kW]	Power required[kW]	Volume battery[m ²]	Max volume[m ²]
Areon Helios	1630.8	357	0.988	1.57
Areon Atlas	1902.6	357	1.16	1.57

4.6.3. Solar panel sizing

The solar panels will be sized for the Helios variant, the large surface area of the wings will be excellent for the placement of solar panels. From Rocketlab the IMM- α ⁹ is selected. The efficiency of this cell is 32% and its performance after the design life time will be 90% of begin of life performance. The solar panels will be on the wing the aileron giving an area of 116.82 m². The average of the sine between 0 and 180 degrees will be used for daylight operations. Finally the solar irradiance on Mars is 590 W/m²[71]. The generated power, its effect on range due to in flight recharging and between flight recharging time are documented in Table 4.22.

The mass of the panel is calculated as presented in Section 3.7 where the cell and glass mass per squared meter is gathered from the datasheet⁹ and are 0.49 and 0.83 respectively. The panel area is as given above, resulting in the mass presented in Table 4.22

Table 4.22: Integrated wing solar panels consequences for Helios variant

	Power[kW]	Range increase[km]	t _{recharge} [days]	m _{panel} [kg]
Wing solar panels	12.6	42	5	154

⁸URL: <https://www.asme.org/topics-resources/content/solid-state-batteries-drive-the-future-of-the-ev-market> [cited 2023-06-19]

⁹URL: <https://www.rocketlabusa.com/assets/Uploads/RL-SolAero-Data-Sheet-IMM-Alpha.pdf> [cited 2023-06-19]

4.7. Electrical block diagram

To show the dependencies between all electrical components, the block diagram shown in Figure 4.17 has been constructed. The block diagram shows the major components of the system as well as the needed transformers and converters to make sure the right voltage and currents are provided to the systems. To give a reference on the high and low voltages low voltages are in the range 8-48 V while the high voltage system operates around 700 V. The Storage unit is presented as one block however several independent battery packs will be stored in the final design to have redundancy and the accurate power.

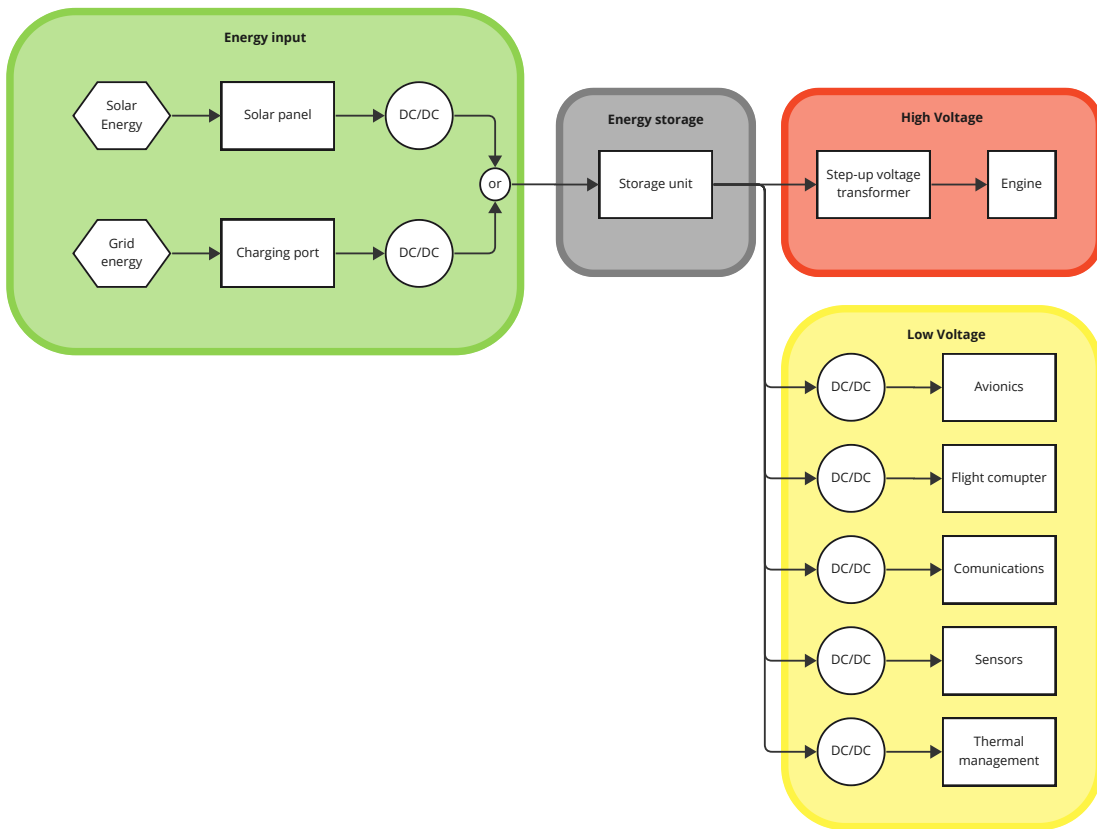


Figure 4.17: Electrical block diagram with the high, low voltage and energy supply systems.

4.8. Thermal Management System Results

By Joachim Bron

This section summarizes the key results of the TMS sizing following the method laid out in Section 3.8. To cool the engines and batteries, it was decided to add radiators around the batteries and around the engines. Active cooling, i.e. using pipes and pumps was mostly avoided due to the mass penalty the design would incur. The radiators were sized in such a way that both the equilibrium temperatures fall within the acceptable temperature range for both: 0-60 °C and 0-120 °C for the engines. The results of the calculations performed as well as the data used are given in Table 4.23, following the method and some of the data given by Quatrocchi et al. (2022) [27]. The last row shows the balance temperature for both the engines and batteries, for both the worst case hot and cold scenario. As detailed in the next two subsections, the final TMS was found to have a mass of 115 kg.

4.8.1. Batteries

In order to cool the batteries, the batteries were split into 7 parts stacked on top of each other, which allows air to flow through and dissipate more heat by convection. The 2 batteries are located under the "benches" of the fuselage and are approximately 2 m long, with a quarter circle extruded shape, as shown

in Figure 4.27. The batteries have a radius of approximately 0.4 m. The radiator consists of 5 quarter circular plates attached to the circular part of the battery, stacked on top of each other and separated by 10 mm. Each plate has a thickness of 1 mm and a length of 2 m. The material chosen was aluminium, which has a density of $\rho_{Al} = 2700 \text{ kg/m}^3$. This material was chosen as it has a relatively low density compared to other metals, while having good thermal conductivity. The mass of the radiator was calculated to be slightly less than 34 kg. Using this radiator, the battery has a temperature of 48.3 °C and 1.8 °C for the worst hot and cold condition, respectively. Note that slots (similar to fish gills) were added to the side of the fuselage to allows the airflow to enter, and that these can be opened or closed to restrict air flow or fully allow it. In the worst case cold condition, these slots are fully closed such that no convection occurs and such that no valuable heat is lost. A sketch of the radiator and battery cross section is provided on the right side of Figure 4.18 for visualization.

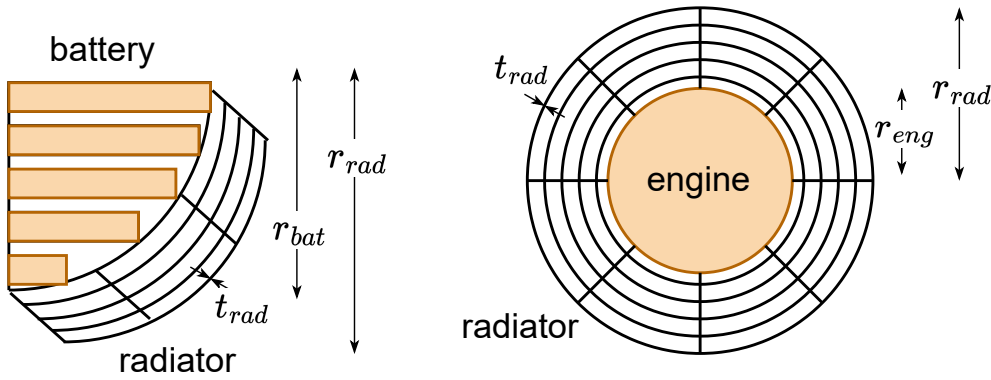


Figure 4.18: Sketch of cross sections of one of the two batteries and its radiator (left) and one of the engines and its radiator (right)

4.8.2. Engines

To cool the engines, a radiator was placed around each engine, as pictured in Figure 4.18. The radiator consists of 10 circular shells and 30 radial shells. This adds enough area such that the engines can be properly cooled. The walls have an average thickness of approximately 0.5 mm and a length of 1.99 m, and are made of aluminium. The radiators have an outer diameter of 0.4 m and an internal diameter of 0.2 m. With these dimensions, the mass of the radiator was found to be slightly less than 82 kg. Using this radiator, the engines have a temperature of 117.8 °C and 28.6 °C for the worst hot and cold condition, respectively.

To ensure a proper thermal transfer between the engines and their radiators, it is assumed the default selected engines undergoes a slight modification specifically for our design, in which a small pump is included. This pump moves a coolant from the engine to the radiator in a closed loop to assist in transferring the heat to the radiators. The coolant used is trichlorofluoromethane, also known as CFC-11 or "Freon". This coolant was chosen as it can operate in the wide range of hot and cold temperatures encountered on Mars, and because it has been chosen for other missions to Mars [72]. A sketch of the radiator and engine cross section is provided on the right side of Figure 4.18 for visualization.

4.9. Communications Sizing Results

By Dominik Stiller

This section present results for the communication subsystem, following the method outlined in Section 3.9. Only uplink (vehicle to base) results are shown, since the large transmitter power makes down-link (base to vehicle) less critical.

Table 4.24 summarizes key parameters and performance of the UHF and HF link. The links are also visualized in Figure 4.19. For skywave communication, which depends on the incidence angle, both edge cases are considered. All links are closed with a margin exceeding 3 dB. UHF requires much more transmitter power (25 W) to overcome the large free-space path loss. The hemispherical antenna has a

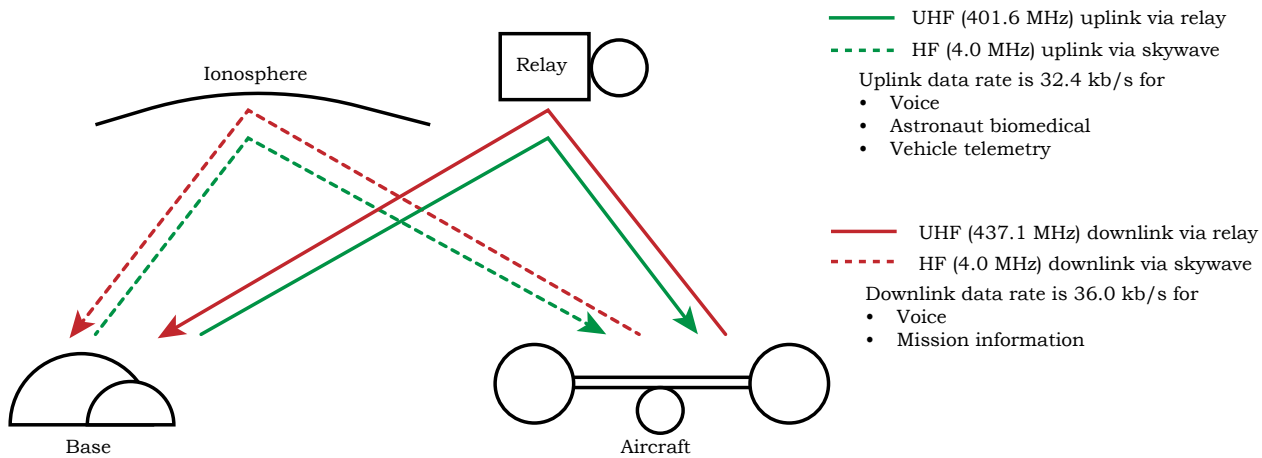


Figure 4.19: Communication Flow Diagram. Two redundant modes increase availability and reduce dependence on environment and infrastructure.

typical gain of 4 dBi [45] and an assumed pointing loss of 2 dB (low due to wide beamwidth). NVIS has high environmental attenuation due to the ionosphere, but a transmitter power of less than 1 W is still sufficient. The shunt antenna gain is unknown, therefore we assume no gain and a pointing loss of 3 dB.

The communications subsystem consists of the HF and UHF antennas, a transceiver, a coupler for the HF antenna, and cabling. The total mass is estimated to be 25 kg, and the peak power to be 88 W. The transceiver consuming these 88 W is assumed to be a modified version of NASA's Electra, capable of higher output powers. The tuner may need similar levels of power, but only when adjusting to a new frequency. The antennas are purely passive.

Note that the transmitter power of 25 W is much more than for current rovers, which use 5-10 W for omnidirectional UHF, since our relay is at 6000 km. Relays for the rovers orbit at 400 km, but only have very short relay passes, while the aircraft needs continuous communication [31].

4.10. Navigation and Instrumentation

By Dominik Stiller

This section summarizes the navigation and instrumentation subsystem, following the considerations from Section 3.10.

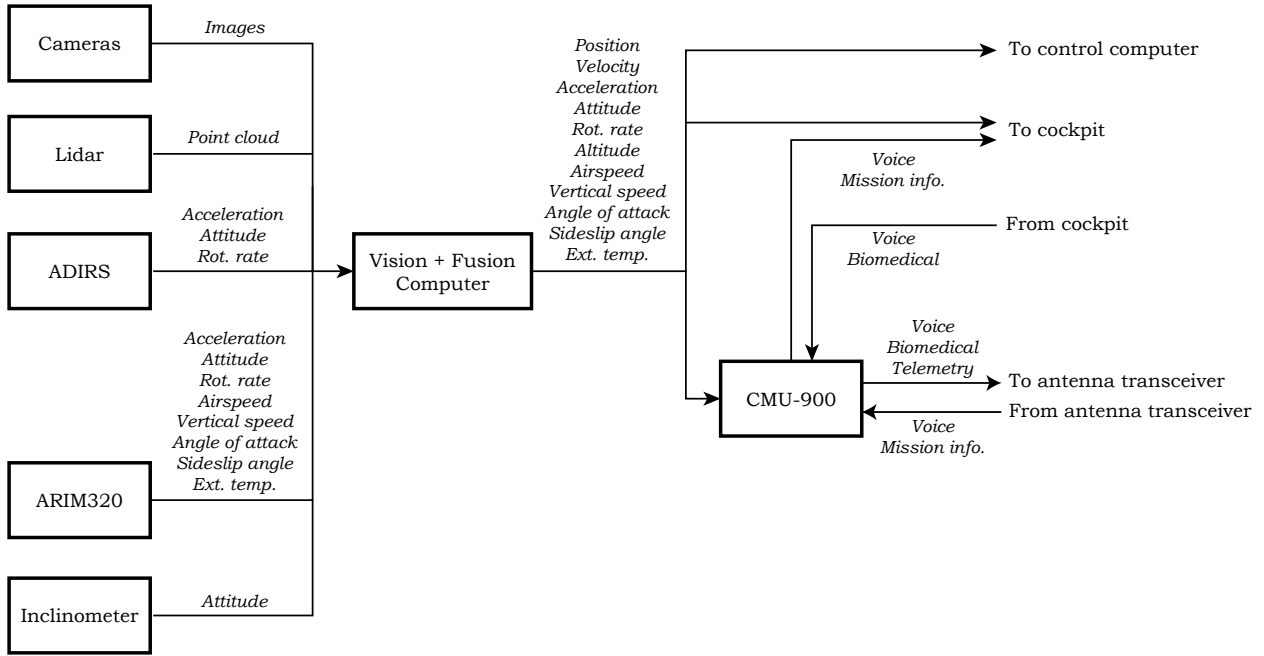
The aircraft will be equipped with the following sensors:

- Horizontally omnidirectional monoscopic color cameras ($3 \times 120^\circ$)
- Nadir-facing dust-penetrating lidar
- Honeywell Air Data Inertial Reference System (ADIRS) (flight computer with accelerometers and gyroscopes)
- Aventech ARIM320 (pitot-static system with accelerometers, gyroscopes, angle of attack/sideslip, and external temperature)
- Inclinometer

In addition, the following components are necessary for data handling:

- Vision/fusion computer
- Collins Aerospace CMU-900 Communication Management Unit

The processing of sensor information is handled by the vision and fusion computer containing a dedicated graphic processor. This computer collects all inputs and forwards them to the control computer, cockpit and the antenna transceiver. Internal and external communication is linked through the communication management unit. The data flow is visualized in Figure 4.20.

**Figure 4.20: Data Handling Diagram**

The quantities collected by the sensors for use by the flight control system and astronauts are summarized in Table 4.25. The inertial–visual navigation system is at the core, collecting position, velocity, attitude, and rotational rates. These are primarily based on data from cameras, fused together with accelerations and possibly satellite ranging/tracking. During take-off and landing, the lidar provides ground surveillance, including altimetry, topology, and obstacle detection. The lidar can also swivel forwards for vision in dust storms. Miscellaneous flight-relevant quantities are provided by the ADIRS and ARIM320, which are also fused for redundancy and increased accuracy.

The lidar operation during landing is intended as follows: after reaching the landing site, the aircraft maps the site from an altitude such that no dust is lifted. If the site is considered safe to land, the aircraft descends and continuously measures the altitude from the lidar. In case the dust is too opaque, the inertial sensors take over until the lidar can observe the ground again.

Table 4.23: Details and results of the TMS sizing, and balance temperatures of the batteries and engines for the hot and cold worst case scenario

			Battery		Engine	
	Symbol	Unit	Hot	Cold	Hot	Cold
Boundary conditions						
Ambient air temperature	T_{amb}	K	271	183	271	183
Air speed	v	m/s	2	111	2	111
External heat input						
<i>Direct solar radiation</i>						
Solar intensity	I_s	W/m ²	587	0	587	0
Absorptivity	α	-	0.2	0.2	0.2	0.2
View factor	$F_{s/v}$	-	1	1	1	1
Area	A_{solar}	m ²	0	0	0.8	0.8
Solar radiation power	\dot{Q}_{sun}	W	0	0	93.5	0
<i>Indirect solar radiation</i>						
Albedo factor	b	-	0.4	0.4	0.4	0.4
View factor	$F_{s/v}$	-	1	1	1	1
Area	A_{solar}	m ²	0	0	0.8	0.8
Albedo radiation power	\dot{Q}_{albedo}	W	0	0	37.4	0
<i>Planetary radiation</i>						
Radiation intensity	J_p	W/m ²	70.7	16.9	70.7	16.9
Area	A_{solar}	m ²	0	0	0.8	0.8
IR radiation power	\dot{Q}_{IR}	W	0	0	56.3	13.4
Internal heat input						
Power output	P_{out}	kW	368	303	312	265
Efficiency	η	-	0.95	0.95	0.847	0.875
Internal heat input	\dot{Q}_{int}^{in}	kW	19.4	15.9	56.3	37.8
Heat output						
<i>Convection radiation</i>						
Convection coefficient	h	W/m ² /K	0.269	2.157	0.269	2.157
Convection area	A_{conv}	m ²	72.8	0	62.9	62.9
Convection power	\dot{Q}_{conv}	kW	0.991	0	2.0	16.1
<i>Thermal radiation</i>						
View factor	F	-	1	1	1	1
Emissivity	ε	-	0.85	0.85	0.85	0.85
Radiating surface area	A_{out}	m ²	72.8	72.8	62.9	62.9
Radiation out power	\dot{Q}_{out}	kW	18.4	15.9	54.5	21.7
Balance temperature						
	T_{sub}	K	321.4	275.0	391.0	301.8
		°C	48.3	1.8	117.8	28.6

Table 4.24: Uplink performance summary for both modes. The transmitter power for UHF is significantly higher than for HF at a much lower margin. This is due to the large free-space path loss.

	Unit	UHF	HF	HF
		Relay	Skywave (1000 km hop)	Skywave (NVIS)
Frequency	MHz	401.6	4.0	4.0
Data rate	kb/s	32.4	32.4	32.4
Tx–Rx distance	km	8240	1050	320
Round-trip latency	ms	110	7	2
Transmitter power	W	25	0.1	0.1
Transmitter gain	dBi	4.0	0.0	0.0
Free-space path loss	dB	-162.8	-104.9	94.6
Environmental loss	dB	-0.5	-4.0	-40
Total pointing loss	dB	-3.0	-6.0	-6.0
Total line loss	dB	-2.0	-2.0	-2.0
Receiver gain	dB	2.0	0.0	0.0
E_b	db(J/bit)	-193.5	-172.0	-197.7
N_0	db(W/Hz)	198.6	206.2	206.2
Received E_b/N_0	dB	5.2	34.2	8.5
Required E_b/N_0	dB	1.0	1.0	1.0
Margin	dB	4.2	33	7.5

Table 4.25: Summary of measured quantities and corresponding sensors. All quantities except the external temperature are either collected by redundant sensors or fused with related measurements.

Quantity	Sensor(s)	Fused with...
Position	Camera, lidar, ranging	Velocity
Velocity	Camera, Doppler tracking	Acceleration, airspeed
Acceleration	ARIM320, ADIRS	
Attitude	Camera, ARIM320, ADIRS, inclinometer	Rotational rates
Rotational rates	Camera, ARIM320, ADIRS	
Altitude	Lidar	Velocity, position
Airspeed	ARIM320	Velocity
Vertical speed	ARIM320	Airspeed, attitude
Angle of attack	ARIM320	Airspeed, attitude
Sideslip angle	ARIM320	Airspeed, attitude
External temperature	ARIM320	

4.11. Life Support System (LSS)

By Joachim Bron

Following the method laid out in Section 3.11, the tanks were sized. Furthermore, the decision was made to go for multiple smaller tanks instead of one big tank to have a redundant system and not single points of failure. This does not negatively impact the mass, since it can analytically be shown that the mass is independent of the number of tanks used.

Solving the optimization problem for the oxygen tank leads to the plot shown in Figure 4.21. This figure shows the mass of the empty oxygen tank as function of diameter and thickness. The constraints are also visible: the dashed line represents the thin walled constraint, while the dotted line represents the minimum required diameter constraint for the tank to not yield under the pressure. Based on the optimization, a pressure of approximately 9.2 atm was found for each oxygen tank (for a diameter of 15 cm). This pressure will consequently be used in the sizing of the tanks.

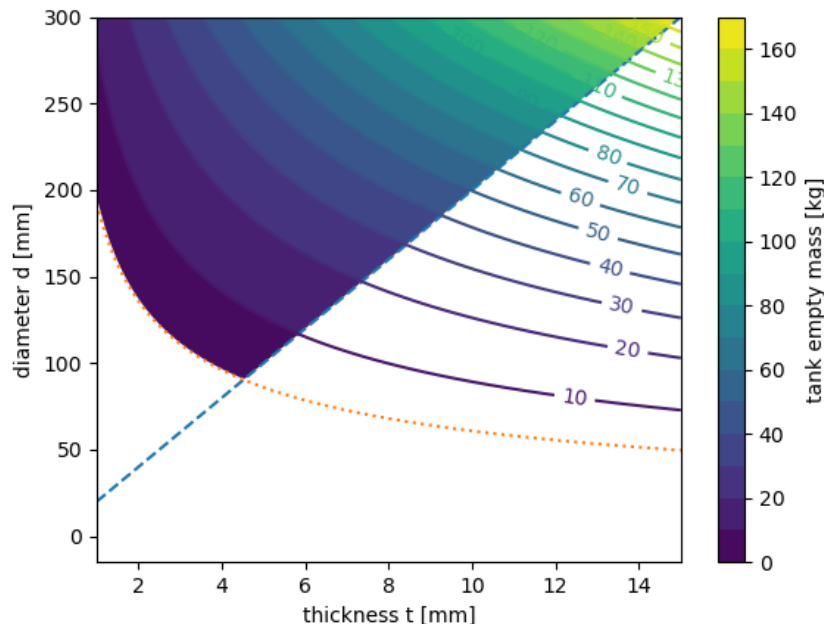


Figure 4.21: Empty oxygen tank mass as a function of diameter and thickness

The tanks were then sized for this mass-minimizing pressure, and the results are summarized in Table 4.26, which gives data on the general LSS and data on astronauts and their needs, and Table 4.27, which gives the data on the results for the oxygen and water tanks. The stresses in the liquid tank turned out to be much lower than the oxygen tank, and for manufacturing simplicity reasons the same thicknesses were used for the liquid tank as the oxygen tank even though this meant the water tanks were over-engineered.

As can be seen from the results given in Table 4.26 and Table 4.27, it was decided to go for 3 oxygen tanks and 2 water tanks. The oxygen tanks have a diameter of 15 cm (chosen for easy handling), and a length of 45.9 cm. The water tanks have a diameter of 12 cm and a length of 39.4 cm. Both have a spherical shell and cylindrical part thickness of 1.6 mm and 3.2 mm, respectively. The oxygen tanks have a mass per tank of 4.651 kg and the water tanks have a mass per tank of 3.232 kg, which with the mass of their contents are still easy to carry by the astronauts. The total mass of the LSS, i.e. the mass of the tanks with the contents, was found to be 29.445 kg. Note that the material used is steel, since it is a common material used for pressurized tanks, although it is heavier than composite based tanks. Also notice the fact that the leak-before-break criterion is met for both tanks, adding safety to the design.

Table 4.26: Summary table of the LSS: general (left) and astronaut (right) data

LSS		
Variable	Value	Unit
air_days_needed	1.500	-
air_leakage_rate	0.040	kg/day
empty_mass	20.42	kg
mass_per_tank_H2O	3.988	kg
mass_per_tank_O2	0.880	kg
num_astronauts	2.000	-
num_tanks_air	3.000	-
num_tanks_water	2.000	-
required_mass_air	2.640	kg
required_mass_water	7.976	kg
required_rate_air_LSS	1.760	kg/day
required_rate_water_LSS	7.976	l/day
total_mass	31.033	kg
water_days_needed	1.000	-

Astronauts		
Variable	Value	Units
required_rate_air	0.840	kg/day
required_rate_water	3.988	l/day
suit_pressure	2.00E+04	Pa

Table 4.27: Summary table of the LSS tanks: oxygen (left) and water (right) tank data

O2 tank			H2O tank		
Variable	Value	Unit	Variable	Value	Unit
Leak-before-break	True	-	Leak-before-break	True	-
SF	1.000	-	SF	1.000	-
SF_Leak-before-break	9.259	-	SF_Leak-before-break	7.32E+04	-
content	O2	-	content	H2O	-
content_mass	0.880	kg	content_mass	3.988	kg
content_pressure	9.21E+06	Pa	content_pressure	1.46E+03	Pa
content_rho	121.754	kg/m3	content_rho	997.000	kg/m3
content_temperature	291.150	K	content_temperature	291.150	K
d_over_t	46.688	-	d_over_t	37.360	-
diameter	0.150	m	diameter	0.120	m
empty_mass	4.651	kg	empty_mass	3.232	kg
gas_M	32.000	g/mol	length	0.394	m
gas_R	259.812	J/kg/K	material	Steel	-
length	0.459	m	material_E	1.93E+11	Pa
material	Steel	-	material_Kic	1.00E+08	Pa m1/2
material_E	1.93E+11	Pa	material_rho	8.00E+03	kg/m3
material_Kic	1.00E+08	Pa m1/2	material_sigma_y	2.15E+08	Pa
material_rho	8.00E+03	kg/m3	max_allow_crack	0.069	m
material_sigma_y	2.15E+08	Pa	shape	cylindrical	-
max_allow_crack	0.069	m	t_cyl	0.0032	m
shape	cylindrical	-	t_sph	0.0016	m
t_cyl	0.0032	m	thinwalled	True	-
t_sph	0.0016	m	volume	0.004	m3
thinwalled	True	-			
volume	0.007	m3			

4.12. Structures Results

By Javier Alonso García and Freek Braspenning

In this section the result that followed the method mentioned in Section 3.12. The results are presented for each of the structural systems.

4.12.1. Rotor blades

The rotor blades were sized for the loads in take-off since it is then where the loads would be greatest. These loads were modeled as a uniformly distributed load. This is possible due to the change in blade pitch along its span as described in Section 3.3.

Yield The calculated thrust for each rotor is of 3.072 kN, which yields a total of 384.0 N on each blade. Similarly, the torque required to spin the rotor is 250.7 Nm, which along a span of 7.31 m yields a drag of 34.30 N per blade. Furthermore, the centripetal force turned out to be 77.31 kN. The resultant internal loading of the rotor blades can be seen in Figure 4.22a. With this loading, the stress on 80 booms was evaluated at 421 positions along the span, yielding the stress distribution seen in Figure 4.22b.

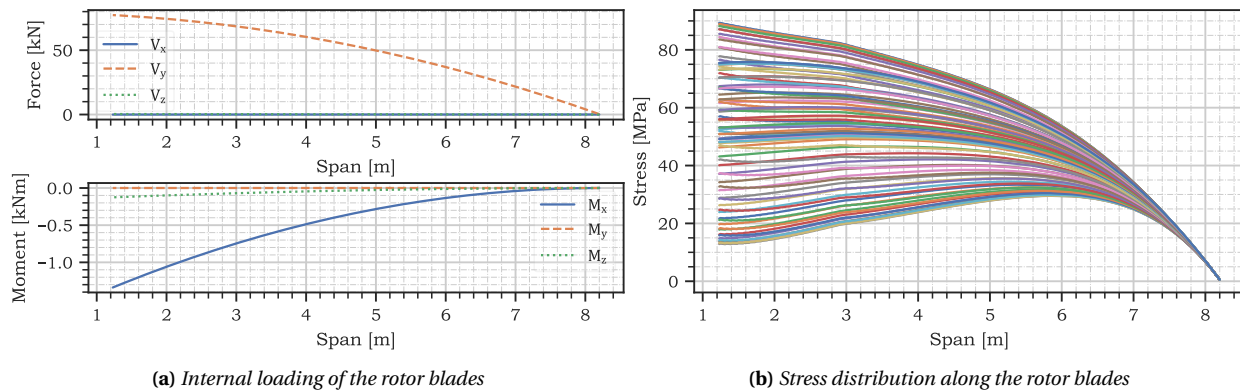


Figure 4.22: Loading case of the rotor blades and resultant stress distribution

The material chosen for the rotor blades was a cyanate ester polymer with carbon fiber reinforcement, whose maximum allowable stress is 672.5 MPa. Since the maximum stress in the structure is 55.91 MPa, no additional reinforcements are needed to avoid this failure mode.

Vibration Since the structure is purely in tension, buckling was not analyzed and vibrations were considered the next failure mode. The rotor blades were sized as an idealized Euler-Bernoulli beam, where the rear blades had a slightly higher natural frequency due to the higher twist near the root. In order to account for taper and the change in twist along the span, the average cross-sectional area and moment of inertia were used, as well as a constant length-wise density. These values, as well as the natural frequency of the first mode of vibration can be seen in Table 4.28.

Table 4.28: Parameters and natural frequencies of the rotor blades as Euler-Bernoulli beams with clamped-free boundary conditions [64]

Blade	L [m]	E [GPa]	I _{xx} [m ⁴]	A [m ²]	ρ [kg/m ³]	ω _n [Hz]
Front	8.2	337.5	3.202 E ⁻⁶	1.072 E ⁻³	1645	6.549
Rear	8.2	337.5	4.361 E ⁻⁶	1.072 E ⁻³	1645	7.643

As explained in Section 4.2, the frequency with which the blades will rotate is 3.87 Hz. This implies that the lowest natural frequency of the blades will be approximately 1.7 times higher than the frequency of oscillation; therefore, no reinforcements are deemed necessary for the moment, however, a margin of 2 kg per blade was left as a margin in case further research disproves this assessment.

Impact fracture During take-off and landing the aircraft will generate a dust cloud which could impact into the rotor blades. These dust particles will have an average radius of 1.8 cm^2 and an average mass of $3.796 \times 10^{-5} \text{ kg}$. Furthermore, their maximum speed relative to the blades will be 207.0 m/s , therefore, the total kinetic energy of the particles per square meter will be 799.0 J/m^2 . According to the Ansys GRANTA EduPack software [64], the energy per square meter required to notch the cyanate ester polymer is between 82 kJ/m^2 and 101 kJ/m^2 , therefore, no additional reinforcements were deemed necessary. Once again, however, a margin was applied in case further research disproves this assessment.

Final results The final dimensions and properties of the rotor blades can be seen in Table 4.29. Note that the change in material properties of the cyanate ester polymer due to a change in temperature was not evaluated, therefore, an additional 2 kg per blade were added as a margin in case further research reveals that reinforcements are needed.

Table 4.29: Final parameters of the rotor blades

Length	Skin thickness	Mass	Natural frequency
8.2 m	1 mm	14.28 kg	6.549 Hz and 7.643 Hz

Even if the stresses and natural frequencies were slightly different between the front and rear blades, the skin by itself provided enough structural integrity in both cases, therefore, the mass of both is the same. With a total of 4 rotors and 8 blades per rotor, the total mass of the blades will be 342.6 kg .

4.12.2. Wings

In order to size the wings, two loading cases were considered: take-off and cruise. Furthermore, the wing was modeled as a beam pinned at the root, such that the force induced by the brace will make M_x at the root equal to 0 in order to achieve equilibrium.

Yield The loading in take-off was modeled as a point load of 6.121 kN upwards representing the thrust and another point load of 768.6 N downwards representing the weights of the propellers and engines. With a length of 22.33 m and a fuselage height of 1.8 m , the wing-brace will be at an angle of 4.608 deg , therefore, it will exert a force of 66.63 kN in order to achieve equilibrium, resulting in a constant compressive force of 66.41 kN along the span, as seen in Figure 4.23a. Note that the moment represented in this graph has a magnitude of E^{-14} , therefore it can be attributed to a floating number error and assumed to be 0 all through the wing.

During cruise, on the other hand, a distributed load representing the lift and drag were inputted based on the output of XFLR5, resulting in the loading seen in Figure 4.23b. Note that these aerodynamic forces correspond to the ailerons-down configuration to satisfy the roll requirement. Here, a compressive force of 58.34 kN can be observed, as well as a maximum internal moment of 32.60 kNm .

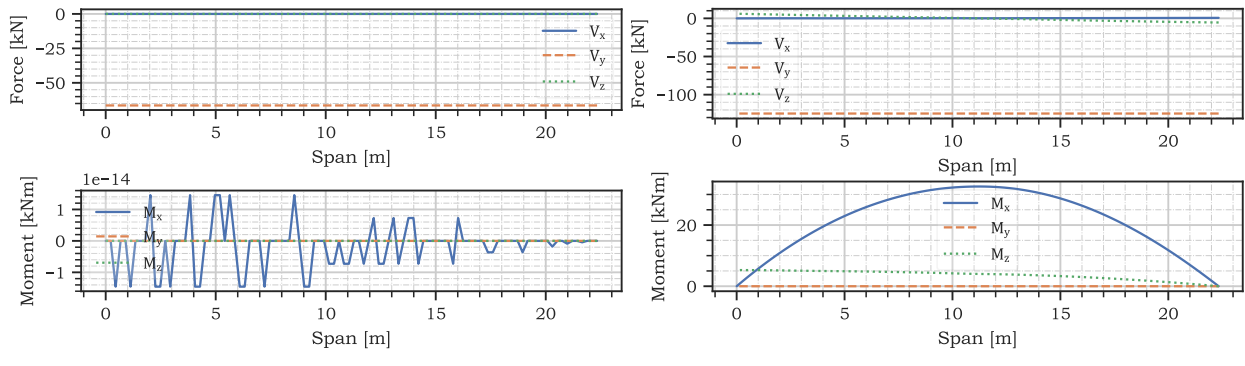


Figure 4.23: Internal loading of the wing in take-off and cruise

Seeing how the internal load during take-off is just a compressive force, the internal stress distribution can be analytically calculated, resulting in a maximum stress at the tip (where the wing is smaller) of approximately 16.0 MPa. The stress distribution during cruise, on the other hand, can be seen in Figure 4.24.

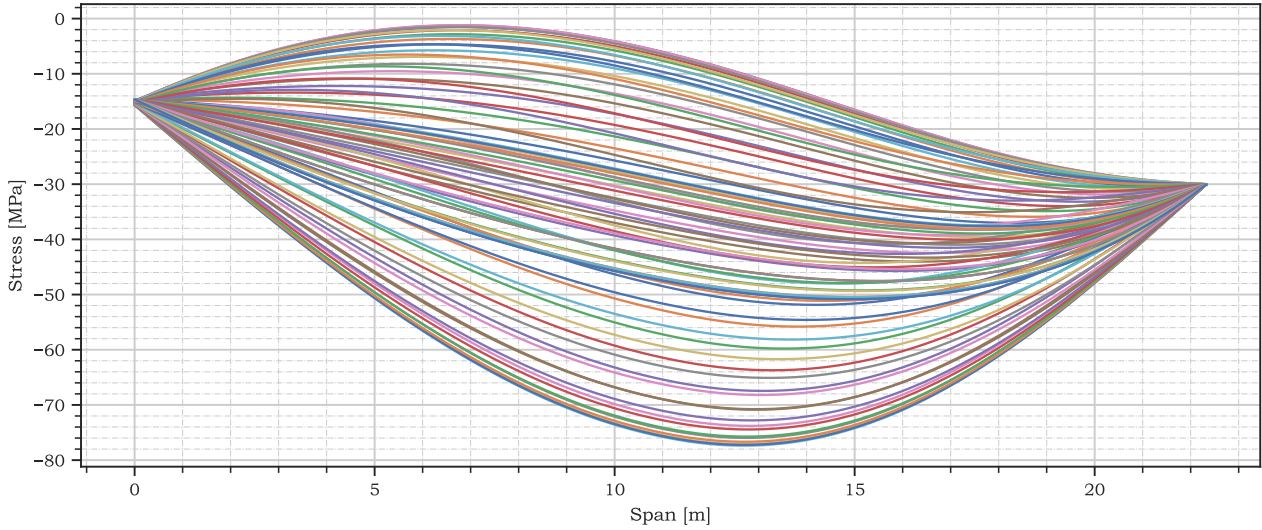


Figure 4.24: Axial stress distribution along the wing and each of the booms

In this figure we can see that the stress is maximum at half of the span, where the bending moment adds up with the compressive force, resulting in a maximum compressive stress of 46.72 MPa. This is still a factor of 5.102 beneath the allowable compressive stress, therefore, no additional reinforcements were considered for this failure mode.

Buckling Modeling each side of the wing as a thin plate and applying the methodology detailed in Section 3.12.4, the best rib and stringer configuration can be seen in Table 4.30, where Segment 1 is the segment the root and the first rib and Segment 5 is the segment between the last rib and the tip.

Table 4.30: Number of stringers in between each evenly-spaced rib for the top and bottom half of the wing

Section	Segment 1	Segment 2	Segment 3	Segment 4	Segment 5
Top	28	31	29	25	19
Bottom	30	33	31	27	20

This stringer distribution adds a total of 79.17 kg when made out of the same material as the wing.

Vibration Following the same approach as for the rotor blades, the natural frequency of the wings was calculated to be 10.43 Hz without accounting for the effect of the stiffeners and using clamped-pinned boundary conditions. Flutter speed was not calculated due to time constraints, however, the effects of the rotors should not be large enough to induce failure in the wing by themselves.

Final results With the geometry detailed in Section 4.1, a skin thickness of 1 mm and the stringer and rib distribution detailed in Table 4.30, the total mass of both wings will be 591.1 kg and will have a natural frequency greater than 10.43 Hz. Additionally, the brace will have to be a hollow cylinder of 1 mm in thickness and a radius of 4.45 cm, resulting in an additional weight of 9.75 kg.

4.12.3. Tail group

The tail group is made comprised by the horizontal and vertical stabilizers, and the tail pole that unites the tails to the fuselage. The loading on the tails was modeled as a uniformly distributed loading as no XFLR5 simulation was performed due to time constraints. This is, however, a conservative approximation since it will yield a moment at the root higher than one with a pseudo-elliptical distribution.

Yield The axial stress distribution of the horizontal and vertical stabilizers can be seen in Figure 4.25. Note that the axis of reference used to produce the plots is a local axis, therefore, the y-axis of the vertical stabilizer will correspond to the z-axis of the horizontal stabilizer and they will share the same x-axis.

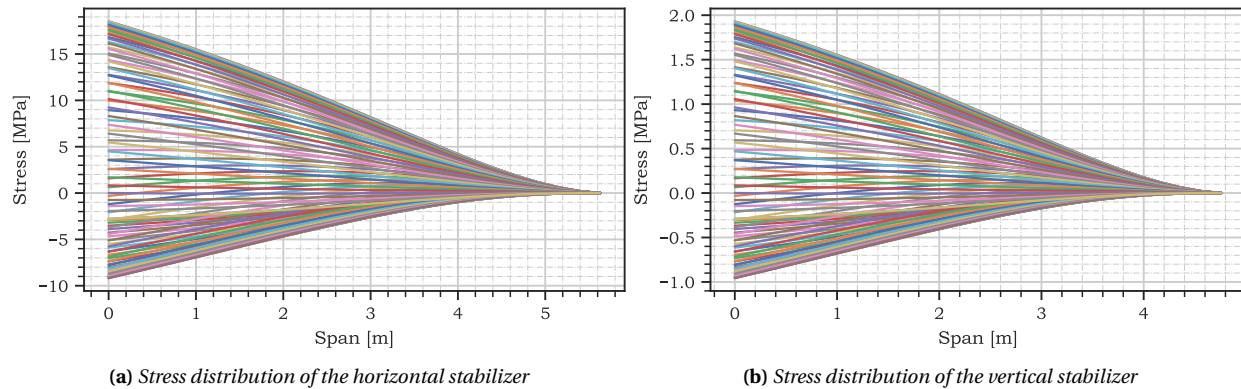


Figure 4.25: Axial stress distribution in the tail

Once again, since at no point in the structure did the axial stress reach the maximum allowable stress, no additional reinforcements were considered for this failure mode.

Buckling The horizontal stabilizer should have 2 ribs per side, therefore 4 in total, with the stringer distribution detailed in Table 4.31. The vertical stabilizer, on the other hand, would only need 1 rib.

Table 4.31: Stringer distribution in the vertical and horizontal stabilizers

Stabilizer type		Segment 1	Segment 2	Segment 3
Horizontal	Top	6	3	1
	Bottom	2	1	0
Vertical	Top	5	1	0
	Bottom	2	0	0

These reinforcements would add a total of 5.894 kg to the structure. Note that since the reinforcements are made out of the same material as the structure itself, the stringers and ribs of the vertical stabilizer are also considered to be made out of aluminum.

Vibration The vibrations of the tail were modeled in a different manner than those of the other structures. Since most of the mass is concentrated at the end of the tail pole, the system was modeled as a damped mass-spring system. The system is excited by a rudder input and an elevator input. The response of the system is shown in Figure 4.26. The results show that the system is stable, but the aerodynamic damping of the control surfaces is negligible. For a more damped system, it would be desirable to implement a damper. Furthermore, the magnitude of the deflection is undesirable but can be resolved by further developments, such as updating the tail-pole from a beam to a truss.

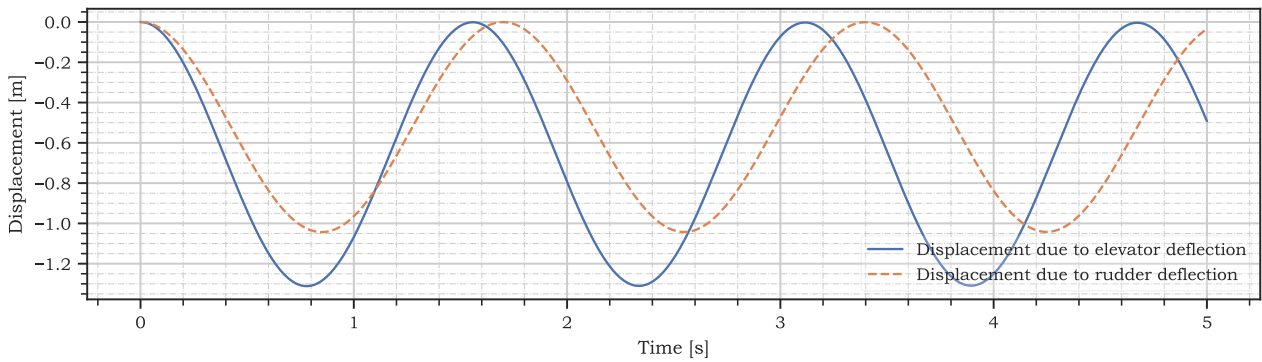


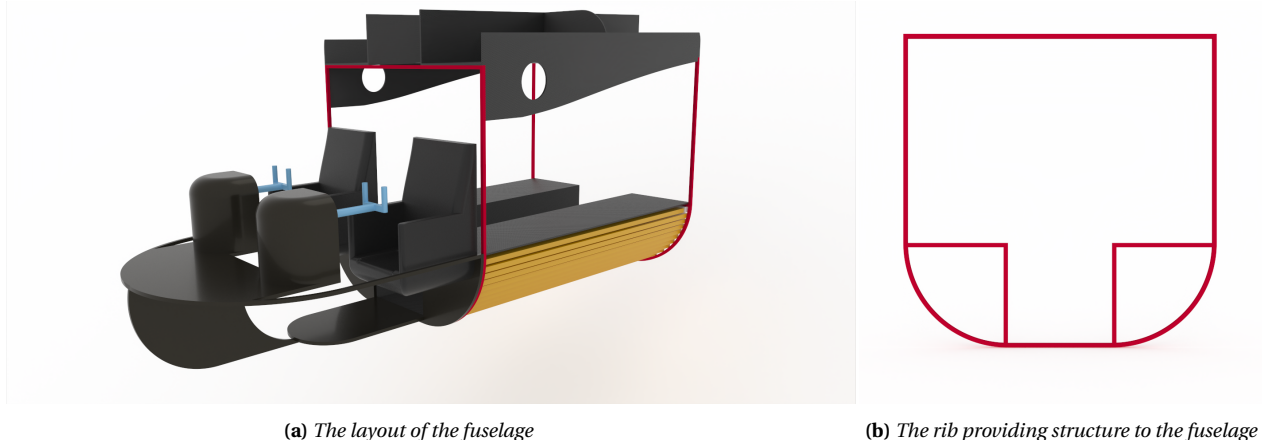
Figure 4.26: The vibrations of the tail due to a step input of the rudder and elevator

Final results With the geometry detailed in Section 4.3, a skin thickness of 1 mm, and the rib and stringer distribution detailed in Table 4.31, the total mass of the horizontal stabilizer is 112.0 kg, the vertical stabilizer's is 59.0 kg and the tail pole will have a total mass of 10.91 kg, making the total mass of the system 126.2 kg.

4.12.4. Fuselage

The internal structure of the fuselage has been sized in compliance with the layout as presented in Section 4.5. The sizing of the fuselage structure is limited by the time constraint. The preliminary sizing includes a proposal for further development which should include an in-depth structural analysis.

The load-carrying components of the fuselage are the ribs, as illustrated in Figure 4.27b. These ribs will transfer the loads of the wing and rotors into the landing gear during storage, and the weight of the fuselage with payload into the wing during flight, thus the ribs will be acting in both compression and tension. Preliminary calculations show no failure of the ribs, but these results are limited by the absence of column buckling calculations.



(a) The layout of the fuselage

(b) The rib providing structure to the fuselage

Figure 4.27: The internal layout fuselage and the structural components

Further development of the fuselage structure will include an in-depth design of the structural components, and also an in-depth analysis of the skin as a load-carrying sheet in shear. Furthermore, the fuselage includes the wingbox, to which the wings are attached, which is a critical component of the aircraft's structure and should be thoroughly analyzed.

Verification and Validation

5.1. Common Verification and Validation Procedures

By Adrian Beño

There are several verification and validation procedures that have been implemented by all subsystem design groups and these are listed in this overview. Verification or validation procedures specific to the individual subsystems are described in detail in section 5.2.

Common verification procedures

- **Unit tests:** All the programming was done in Python programming language, for which there is readily available unit test package `unittest`. This was implemented to test all of the code where applicable.
- **System tests:** Where applicable due to more complex code structure, such as implementation of polymorphism, inheritance or nested function calling, system tests were performed to ensure correct interface between the different classes or functions.
- **Analytical solution:** In case of any numerical solvers implemented to solve problems which in general do not have analytical solutions, there were comparisons made with analytical solution available to simpler problems, such as simpler problems where the geometry of the structure is less complex or the flow can be considered inviscid. This was to verify that the software solves the equations correctly, and also provides insight into the error analysis of the numerical solver, such as determination of the optimal step size of Forward Euler numerical discretization.
- **Analysis of proper functioning on simpler problems:** In case that no analytical solution exists, not even for simplified problems, the proper functioning was checked on simplified problems and verified purely based on the approximate expected outcome. For example, there exists expectation on controller's behavior applied to 2nd order system; the oscillations shall disappear and transient behavior shall be suppressed.

Common validation procedures

- **Literature comparison:** The validity of the underlying models behind the system and subsystem design was established by comparing the predictions of the developed models to currently existing designs. Such as predictions on weight, given certain design parameters, such as size. If the model predictions were similar enough (as defined per individual model), it can be concluded that there is enough confidence in the model within a certain domain of inputs. Any discrepancies between the model output and real-world values would be addressed in sensitivity analysis.
- **Expert discussions:** Multiple discussions with experts in the respective fields were actively conducted in case that there was no literature found on certain subsystem design or expert knowledge was required to establish validity of certain assumptions. This mainly applied in general to aerodynamics related modelling or design decisions.
- **Experimental validation:** Unfortunately, no experimental validation was done for any subsystems except for the wing subsystem. This was due to unavailability of resources, for example due to choice of technology which is still being developed and is not accessible off-shelf, or due to time constraints.

5.2. Model Verification and Validation and V&V Plan

5.2.1. Wing

By Adrian Beño, Pedro Santos

Validation

The design of the whole aircraft was mostly driven by the lift performance of the S1223 airfoil, and subsequently of the wing. Moreover, much of the analysis of the main wing was done in XFLR5, as well as

stability and controllability analysis. Hence, precise data on the behavior of the S1223 airfoil had to be obtained and validated experimentally. This was done in the open jet M wind tunnel at TU Delft using a 3D printed airfoil which spanned the entire flow section of the tunnel, so as to mimic the 2D infinite wing behavior. This is shown in Figure 5.1.



Figure 5.1: The 3D printed S1223 airfoil in front of the open jet wind tunnel.

The model airfoil had chord equal to $c = 0.23$ [m] and was dimensioned with respect to the available flow velocity in the wind tunnel so as to best match the Reynolds number of the aircraft during various flight conditions. The Reynolds number was varied by the flow speed $V_\infty \in \{5, 10, 13, 16, 20\}$ [m/s]. This resulted in Reynolds number of $Re \in \{0.75, 1.5, 2, 2.4, 3\} \cdot 10^5$, respectively. The highest Reynolds number corresponds to half of the value in cruise condition because higher Reynolds numbers could not be reached in the wind tunnel. Nonetheless, this already gives a good indication of the airfoil characteristics.

The raw data from the wind tunnel first had to be adjusted for the effects that the open-jet wind tunnel artificially introduces. This was done with the corrective factors suggested by T. Broertje, BSc., who was supervising the experiment. The first corrective factor accounts for the solid blockage for models spanning the tunnel. In other words, the induced velocity is smaller at the model position than in a closed tunnel. The velocity that the wing sees must be corrected by Equation 5.1, as defined in [73].

$$U_{true} = U_\infty + \Delta U_B \quad ; \quad \Delta U_B = U \epsilon_s = U \left[-\frac{\pi^2}{24} \left(\frac{c}{h} \right)^2 \left(\frac{t}{c} \right)^2 \lambda_2 \right] \quad (5.1)$$

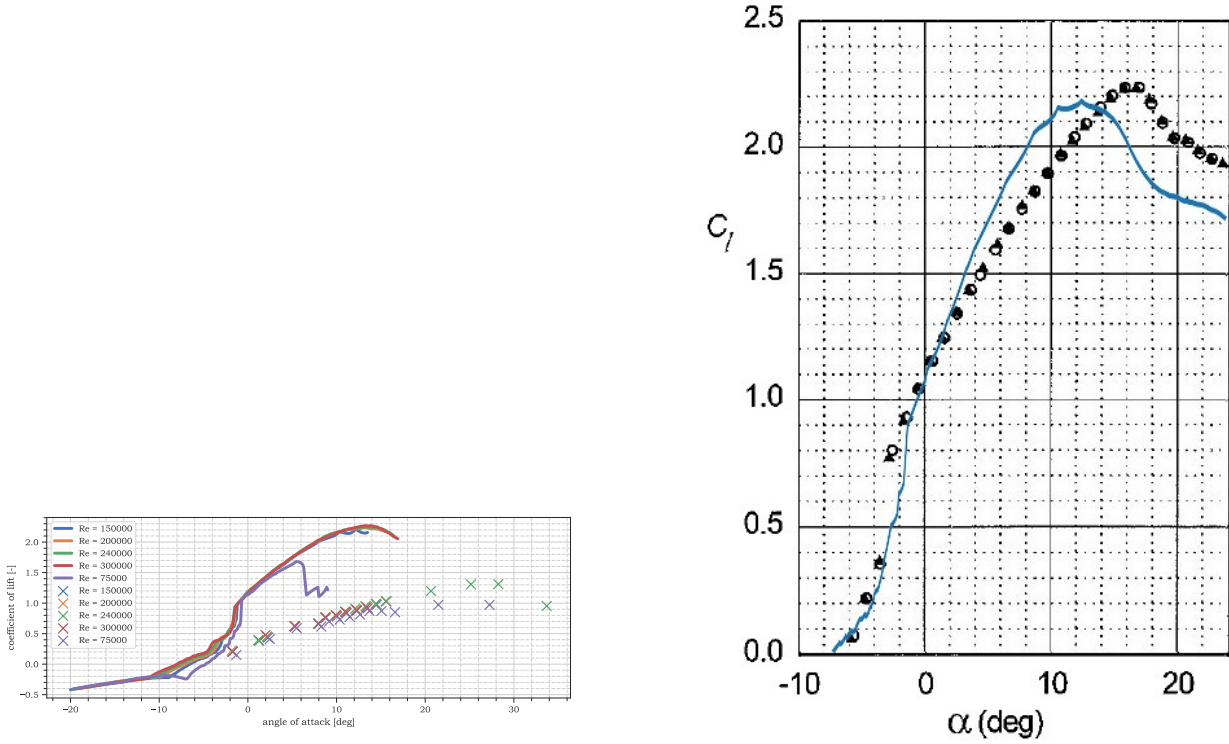
where U_{true} is the velocity that the wing in front of the wind tunnel sees, U_∞ is the freestream velocity, c is the chord length, h is the wind tunnel height and $\lambda_2 = 6.47$ is the shape factor. The second corrective factor accounts for the lift interference. The geometrical angle of attack and the measured coefficient of lift must be corrected by Equation 5.2 and Equation 5.3, respectively,

$$\alpha_{true} = \alpha + \Delta \alpha \quad ; \quad \Delta \alpha = -\frac{c C_l}{4h} \left[G_0 + \frac{\pi c}{\beta h} \left(\frac{1}{4} + \frac{C_m}{C_l} \right) G_1 \right] \quad (5.2)$$

$$C_{l_{true}} = C_l + \Delta C_l \quad ; \quad \Delta C_l = C_l \frac{\pi^2 G_1}{8} \left(\frac{c}{\beta h} \right)^2 \quad (5.3)$$

where C_l is the coefficient of lift already corrected by U_{true} , β is the Prandtl-Glauert compressibility factor, C_m is the coefficient of moment already corrected by U_{true} and $G_0 = 0.96$ and $G_1 = 0.33$ are corrective constants, as defined in [73]. The corrected measurements are presented in Figure 5.2, along with the predictions of XFLR5, which does assume a model on viscosity. For the completeness of the analysis,

we also provide predictions of XFLR5 as compared to the experimental measurements from [11] in Figure 5.2b.



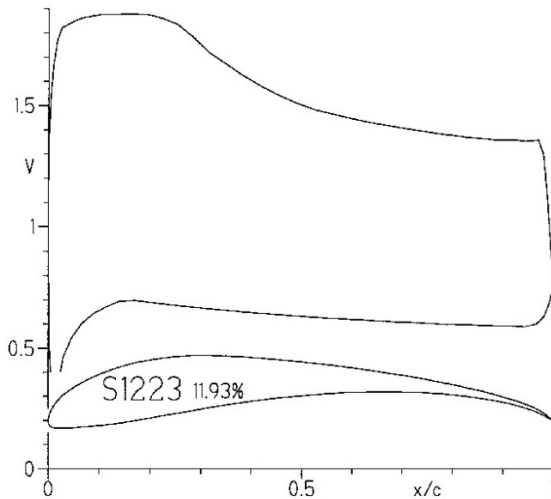
(a) Coefficient of lift C_l as function of angle of attack α . Continuous curves correspond to the data from XFLR5 simulations, crosses correspond to the experimentally measured values.

(b) Comparison of lift curves of airfoil S1223. The blue line corresponds to XFLR5 numerical simulation. Black dots correspond to experimentally given in [11]. Both at $Re = 2 \cdot 10^5$.

Figure 5.2: The lift and drag polars of the S1223 airfoil, as experimentally measured and theoretically predicted by simulations in XFLR5.

The polars reveal that the theoretical predictions of XFLR5 match the experimental measurements in [11] to accuracy of 11% in the maximum error. At the same time, in house made validation reveals significantly lower lift performance of the airfoil. At this point, it is concluded that the wind tunnel correction methodology provided by T. Broertje, BSc., is incorrect and must further be examined. This is because the suggested correction factors appear to yield erroneous results with respect to his own measurements performed on airfoils with well established lift polars. At the same time, the flow visualization and stall behavior is unaffected by this and is analyzed further.

As in the experimental results at $Re = 200'000$ in [11], our results also reveal smooth stall behavior. As can be seen from Figure 5.2a, the experimentally measured stall behavior is smooth unless tripping strips are used, as described later. This implies that weather conditions possibly leading to the aircraft stall do not pose life threatening situation due to sudden loss of lift and stall can be recovered. However, the theoretically predicted velocity distribution over the wing at the cruise angle of attack of $\alpha = 2.7$ [deg], given in Figure 5.3a, was not observed during the flow visualization, as given in Figure 5.3b.



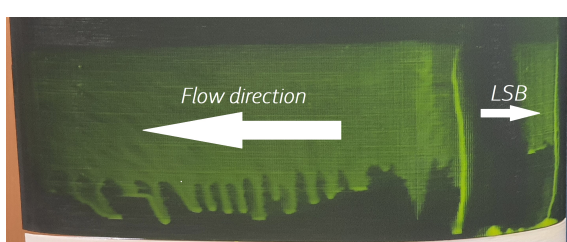
(a) The theoretically predicted inviscid velocity distribution over the S1223 airfoil [11].



(b) Experimentally conducted flow visualization using fluorescent oil.

Figure 5.3: The theoretically predicted velocity distribution over the S1223 airfoil in comparison to the experimentally conducted flow visualization. Both at $\alpha = 2.7$ [deg].

It is clear from Figure 5.3b that the oil is sliding down under gravity in the aft half of the airfoil, which indicates flow separation, whereas Figure 5.3a shows velocity distribution in the aft half which is higher than the freestream. In fact, the flow drastically loses speed already in the front part of the wing, because the oil is present and was not blown away. Hence, simulations regarding the pressure distribution over the wing should be completely disregarded. Moreover, laminar separation bubble (LSB) was observed, for nominal cruise angle of attack, as well as, for higher angles of attack, as can be seen in Figure 5.4. An attempt to resolve the laminar separation bubble (LSB) with tripping strip was attempted and indeed canceled it, but also resulted in sudden, very abrupt stall of the wing. The same procedure was conducted at lower angles of attack, and resulted in similar behavior. Hence, it is advised not to use tripping strips and rather investigate the influence of vortex generators in future research.



(a) Flow visualization at 37 [deg] angle of attack without tripping strip. LSB is visible just behind the leading edge of the airfoil.



(b) Flow visualization at 37 [deg] angle of attack with tripping strip. LSB is not present, but the wing is fully stalled.

Figure 5.4: Effect of LSB on stall characteristics of the airfoil.

To conclude, LSB should not be attempted to be removed with tripping strips as they results in complete stall of the wing and abrupt loss of all lift. Rather influence of vortex generators should be investigated to delay stall. Simple software, such as XFLR5, which only superimposes a model of viscosity on otherwise non-viscous flow, should not be trusted and is deemed invalid in predictions of velocity distribution over the wing. This is based on the discrepancy between the predicted velocity distribution and experimental flow visualization. Hence, further research must be done on aileron sizing, as this specifically assumes sufficient pressure over the ailerons. At the same time, there is enough confidence in the overall wing performance, as predicted by XFLR5, due to the similarity of results in Figure 5.2b and the 11% discrepancy can be mitigated by flying at slightly higher or lower angle of attack, as this would only introduce

negligible increase of drag.

5.2.2. Fuselage

By Pedro Santos

A drag calculator was written in python, for which verification was done by means of unit tests. They ensured that all calculations were being performed correctly.

For validating the drag results, data from literature was compared with the C_D value found by the calculator tool. Durgin's paper[74] mentions a fuselage C_D of 0.029 for a Cessna 172, and Figure 5.5 of Lai's paper[75] shows typical values of fuselage C_D 's to be between 0.025 and 0.035. This shows that the C_D of 0.031 found for this paper's aircraft's fuselage, inspired by the Cessna 172, is indeed within expected values.

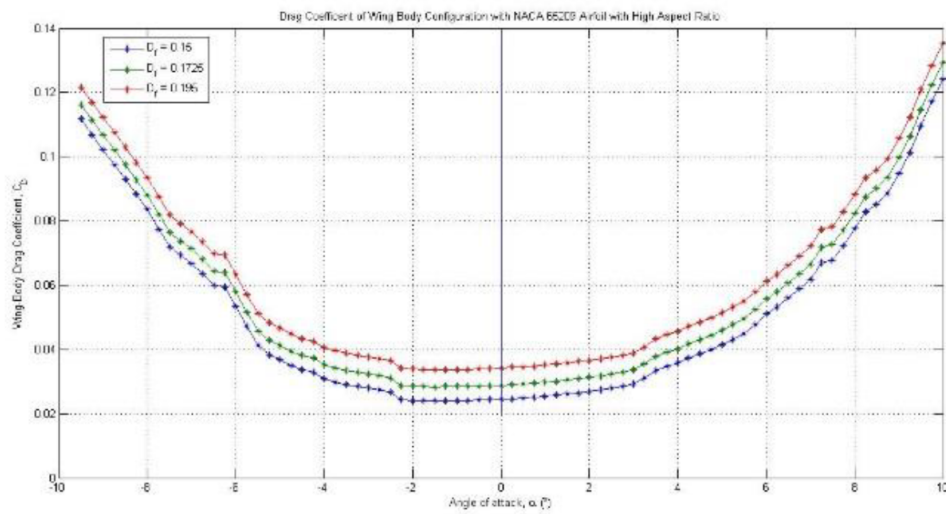


Figure 5.5: Drag coefficient of different fuselages accounting for wing interaction, for high aspect ratio aircraft[75].

5.2.3. Power

By Timo de Kemp

As the power system is depended heavily on the assumption of increasing the energy density of batteries significantly. As the current estimates of capabilities of solid state batteries are between 2-3 times more than current lithium-ion batteries. The mean is taken in the design to determine the battery capabilities.

To determine in what the possibility is that the Atlas variant will be able to reach the range requirement a uniform distribution between 2-3 times increase is taken. It can be calculated that for an increase of 2.33 the range for the Atlas configuration is 1000 km as required. Therefore in 67 % of the battery development the battery will be enough to meet the requirements. For the Helios configuration this probability is 37 %.

No validation was possible for the power subsystem due to the absence of the hardware and comparable system data. As the propulsion unit requires the most of the power a test could be performed, with just the battery, engine, gearbox, and blades to determine if the system is able to provide sufficient power and energy to the system.

5.2.4. Structures

By Javier Alonso García

Verification In order to verify the code used to size the structure of the aircraft a number of tests were performed. Firstly, the built-in functions of the class used to define the different geometries were tested

by comparing the output of those functions for simple beam geometries such as square beams against hand calculations.

Finally, the main code where the structure is sized was verified by comparing the results of hand-calculated natural frequencies to those outputted by the code and by ensuring that the stress in all structures was never larger than the allowable stress.

Validation Most of the equations used in the code have been developed and used extensively in the field, however, validation was still performed on the most critical parts and parts where big assumptions were made.

The first function to be validated was the one that calculated the internal loading within the beam since this is a critical function from which everything depends. This was done by comparing the output of the code to the results obtained during an experiment performed in 2015 by Abhishek et al. [76] when defining the same geometry. The results were within a 1% error margin.

The second function that was validated was the calculation of the natural frequency. This is of special importance since the value calculated was that of an approximate geometry and not of the actual elements, therefore, large errors may be present. An experiment carried out by Kemparaju and Samal [77] calculated the natural frequencies of 3 different beam geometries, each made out of 3 different materials for a clamped-free and clamped-clamped boundary conditions. They then compared the results to those obtained from analytical solutions for Euler-Bernoulli beams and FEM tools. Defining the same geometries and boundary conditions as they used and comparing the natural frequencies calculated resulted in an error of 19% for the clamped-free boundary condition and 25% for the free-free boundary condition. These errors are rather large, therefore, further analysis should be done on better methods of predicting the natural frequencies of the structure. On the other hand, the values obtained were in line with the analytical and FEM calculations performed by Kemparaju and Samal [77], therefore, it can be said that the model works as intended.

Finally, the last function validated was the one that calculated the critical stress for thin plate buckling. This was done based on the results of Roorda and Venkataramaiah [78], who analyzed buckling of thin steel plates for a wide range of thicknesses. In their analysis they concluded that Equation (5.4) could be used to conservatively predict buckling within a few percentage points of the experimental results with a C value of 5.58. Since that is the exact same formula used by the code except with a C value of 5.6, it was concluded that the results would be accurate within a reasonable margin.

$$\sigma_{cr} = \frac{5.58\pi^2 E}{12(1 - v^2)(b_w/t)^2} \quad (5.4)$$

5.2.5. Thermal Management System

By Joachim Bron

On top of basic unit tests, the TMS was also verified as a whole. First of all, the implementation of the convection coefficient calculation described in by Soria-Solinas et al. (2015) [28] was verified against the values which the authors obtain for their scenario (see figure 4 of [28]). The values were found to be the same with those calculated by the authors to be within less than 1% difference, supporting the claim that the calculation of h was correctly implemented.

Regarding validation, the convection coefficient h calculated at the 2 m/s condition was compared against the value found for NASA's Ingenuity drone and found to be within acceptable range [79]. The value calculated using our implementation was found to be around 0.3 for low values of windspeed (2 m/s), while the value found by Schmidt et al. (2018) [79]. Although there is a difference of around 30%, this still falls within the uncertainties associated with the calculation of h at these wind speeds. This is a good check to see if the h calculated at these low wind speeds is in the correct order of magnitude, as there is a lot of uncertainty in the calculation of this term.

The TMS sizing was performed according to the method outlined by Quattrochi et al. (2022) [27]. The authors in this paper apply their model to the case of NASA's curiosity rover. After the tool was built for our analysis, it was verified by using the inputs of this paper and checking if the outputs obtained using our implementation corresponded to the results stated in the paper. Once again, the values found were very close (difference of less than 1%) justifying the claim that the model is correctly implemented.

At this stage, no full validation of the model was performed due to the difficulty of performing tests and applying the model to our specific case. In the future to validate the TMS, a simple experimental setup could be built with just the battery and engines and their radiators. These tests, conducted in CO₂ gas at the right conditions, could help validate the model.

5.2.6. Communications

By Dominik Stiller

Next to some unit tests, the verification and validation of the communications subsystem was based on comparison with other link budgets. All comparisons are based on the resulting margin between received and required E_b/N_0 .

First, we implemented the link budget of an Earth-orbiting satellite, for which a detailed breakdown is published [80]. The results agree within 1 %.

Next, we implemented the link budget for the proposed relay network that we would be using [33]. The results agree within 1 dB. However, the system noise temperature is exceedingly high at 1410 K, while comparable systems have 550 K [39] or 630 K [40]. Also, the gain-to-temperature ratio is -21.5 dB/K, while typical values are around -27 dB/K [81]. Since the values for this scenario were taken from a plot with other inconsistencies, this validation may not be reliable.

Finally, we implemented the link budget for the Mars Cube One UHF surface-to-orbit link, for which a detailed breakdown is published [40]. The results agree within 0.3 dB, giving high confidence in the correctness of the UHF link sizing for our aircraft.

We also compared miscellaneous figures of merit. Martian UHF links typically have a gain-to-temperature radio around -27 dB/K [81]. For uplink and downlink we have -28 dB/K and -26 dB/K, respectively. Our effective isotropic radiated power is 46 dBm to 47 dBm, while typical values are around 40 dBm. This difference is to be expected, since our communications system is sized for relay at higher altitudes and uses a low-gain antenna. Also, our received power agrees with performance measurements for the Electra transceiver [39].

No validation was performed for the HF skywave link. This is because the performance depends heavily on environmental attenuation of skywaves on Mars, for which no reference exists. The Earth environment is too different for a useful comparison. However, the same link budget tool is used as for the UHF link, which increases the confidence somewhat.

5.2.7. Navigation and Instrumentation

By Dominik Stiller

No validation and verification was performed for the navigation and instrumentation subsystem since the sizing did not include any calculations. Only informed qualitative decisions were made based on literature. The performance will have to be verified in a testbed.

5.2.8. LSS

By Joachim Bron

On top of the usual unit tests, the implementation of the model was verified using external data. The model was applied to the case of one astronaut at Earth sea level conditions, and the value obtained for the required oxygen per person was found to be 659 liters. This falls within acceptable limits (17%) of

the value of 550 liters stated by a health website¹, and gives some confidence into the values used for the required oxygen rate. The model was applied to the case of the ISS², where similar values (to within 25%) were found. This discrepancy could be explained by the fact that our model does not include a COPV option, and full CFRP tanks were used instead for the verification.

At this stage, no validation was performed. In the future, it is recommended to perform a pressure test, in which the tanks are pressurized until failure to validate the model. It is also recommended to test for leakage and see at which pressure these occur, to validate the leak-before-break criterion.

5.2.9. Control and Stability system verification and validation

By Patrick Kostelac, Adrian Beňo

In order to verify the implementation of the PID controllers into the system, a verification on a simple system was performed. Instead of applying the controllers on the complex aircraft system, a simple damped second order system was created. It was then possible to apply the controllers to the simple system where the expected outcome can be easily predicted. By doing this, it was easy to verify whether the controllers are properly implemented. Once the appropriate implementation of the controllers was confirmed, they were again applied to the complex aircraft system. By doing this, when encountering an error, the possibility of that error being due to the controller implementation was then immediately eliminated.

In order to validate the control and stability section, a system validation based on a Cessna 172 parameters was performed.

During the static stability analysis, sets of formulas are used to estimate the horizontal and vertical tail properties are used. Those formulas take as input the information about the plane main wing and selected tail airfoil and produce as output the minimum size of the horizontal and vertical tail as well as the location of the tail and the change in moment coefficient due to the change in angle of attack. The values given for the Cessna were found in [82][83][74]. The comparison between the papers and the program output can be seen in Table 5.1.

Table 5.1: Comparison of the real values to program output

Parameter	Real Values	Program prediction	Difference %
$Sh/S [-]$	0.1705	0.202	-
$lb [m]$	3.928	4.03	2.531
$S_{rud} [m^2]$	0.584	0.690	-
$\frac{dC_m}{d\alpha} \frac{1}{rad}$	-0.895	-0.9772	8.032

The Sh/S and S_{rud} values indicated by the program are the minimum allowable values and are thus not directly comparable to the Cessna 172, but they are rather validated if they are found smaller than the real values. The distance between the main wing and the tail lb was calculated within 2.531% of the real value and is thus validated. The change in moment due to the change in angle of attack was calculated within 8.032% of the real values and are thus validated.

The formulas used in the static stability analysis have several different plane parameters used as inputs. Some of these parameters are easily found through airfoil analysis, but some other parameters are more obscure and harder to find which is why a sensitivity analysis was performed. Namely: $C_{N_{h\delta}}$, the change in normal coefficient of the tail due to the tail deflection, used in the computation of $C_{m\delta}$ and $C_{h\delta}$, C_{m0}

¹URL: <https://www.sharecare.com/health/air-quality/oxygen-person-consume-a-day> [cited 2023-06-21]

²URL: <https://www.nasa.gov/content/air-supply-high-pressure-tanks-ready-for-space-station> [cited 2023-06-21]

and $\frac{d\delta_e}{dS_e}$ which were all previously mentioned were not directly calculated. Thus their values estimated by comparing them to similar aircraft [84]. Because of that these values can not be considered accurate and a sensitivity analysis is performed to investigate their impact. The results of the sensitivity analysis can be seen in Table 5.2

Table 5.2: Comparison of the real values to program output

Parameter	$C_{N_{h\delta}}$	C_{h_α}	$C_{h\delta}$	C_{m0}	$\frac{d\delta_e}{dS_e}$
Value	2.43 [-]	-0.118 [-]	-0.279 [-]	0.0833 [-]	2.18 [rad/m ²]
Variation	(1.215-3.645)	(0.059-0.177)	(0.1395-0.4185)	(0.04165-0.12495)	(1.09-3.27)
Impact on result	32 %	1 %	11 %	9 %	14 %

From this table it can be seen that $C_{N_{h\delta}}$ has the largest impact on the design, where varying its value by 50% changes the area of the horizontal stabilizer by 32%, while C_{h_α} has minimum impact on the design. It is thus recommended that in the detailed design stage the most effort is put into investigating $C_{N_{h\delta}}$ and the least effort is put into investigating C_{h_α} .

5.3. Compliance Matrix

By Pedro Santos

In this section, the compliance matrix is presented. It shows whether the design requirements have been complied with or not, and how far the actual values are from the target values in case of non-compliance. Furthermore, a short rationale for non-compliance is also presented in the table. However, rationales which require extensive explanation, will be further clarified in section 5.4.

Table 5.3: Requirements Compliance Matrix

Identifier	Rationale for non-compliance	Compliance
REQ-USER-PERF-01		Complied
REQ-USER-PERF-02		Complied
REQ-USER-SARE-01		Complied
REQ-USER-SARE-02		Complied
REQ-USER-SUST-01		Complied
REQ-USER-ENGB-01		Complied
REQ-USER-ENGB-02		Complied
REQ-USER-ENGB-03		Complied
REQ-USER-OTHR-01		Complied
REQ-ASTR-SAFE-01		Complied
REQ-ASTR-SAFE-02		Complied
REQ-ASTR-SAFE-03		Complied
REQ-ASTR-SAFE-04		Complied
REQ-ASTR-SAFE-06		Complied

REQ-ASTR-SAFE-10		Complied
REQ-ASTR-CNTRL-01		Complied
REQ-ASTR-CNTRL-02		Complied
REQ-ASTR-CNTRL-03		Complied
REQ-ASTR-CNTRL-04		Complied
REQ-ASTR-CNTRL-05		Complied
REQ-ASTR-CMFRT-02		Complied
REQ-ASTR-CMFRT-03		Complied
REQ-MNFCT-COST-01		Complied
REQ-MNFCT-TXIC-01		Complied
REQ-MNFCT-TXIC-02		Complied
REQ-SCNCE-PAYL-01		Complied
REQ-SAG-INT-01		Complied
REQ-SAG-INT-02		Complied
REQ-SAG-INT-03		Complied
REQ-SAG-REUS-03		Complied
REQ-SAG-COMP-01		Complied
REQ-SAG-COMP-02		Complied
REQ-SAG-COMP-03		Complied
REQ-SAG-LIFE-01		Complied
REQ-SAG-OPE-02		Complied
REQ-SAG-OPE-03		Complied
REQ-SAG-OPE-04		Complied
REQ-SAG-OPE-05		Complied
REQ-SAG-OPE-06		Complied
REQ-LAU-01		Complied
REQ-LAU-02		Complied
REQ-LAU-03	Further testing is required	Not complied
REQ-LAU-04	Further testing is required	Not complied
REQ-CUST-FAST-01		Complied
REQ-CUST-INNO-02		Complied
REQ-CUST-COST-01		Complied
REQ-CUST-COST-02		Complied
REQ-CUST-COST-03		Complied

REQ-LCD-LVEH-SIZE-01		Complied
REQ-LCD-LVEH-SIZE-02		Complied
REQ-LCD-LVEH-SIZE-03		Complied
REQ-LCD-LVEH-SIZE-04		Complied
REQ-LCD-LNCH-LOAD-01		Complied
REQ-GOPS-ACT-ASS-01		Complied
REQ-GOPS-ACT-ASS-02		Complied
REQ-GOPS-ACT-ASS-03		Complied
REQ-GOPS-ACT-MAINT-02		Complied
REQ-GOPS-ACT-MAINT-03		Complied
REQ-AVNC-GNRL-01		Complied
REQ-AVNC-IFC-01		Complied
REQ-AVNC-IFC-02		Complied
REQ-AVNC-IFC-03		Complied
REQ-AVNC-IFC-07		Complied
REQ-AVNC-IFC-08		Complied
REQ-AVNC-IFC-09		Complied
REQ-AVNC-IFC-10		Complied
REQ-AVNC-IFC-11		Complied
REQ-AVNC-IFC-12		Complied
REQ-AVNC-IFC-13		Complied
REQ-AVNC-IFC-14		Complied
REQ-AVNC-NAV-01		Complied
REQ-AVNC-NAV-02	Replaced by lidar	Not complied
REQ-AVNC-NAV-03	Replaced by lidar	Not complied
REQ-AVNC-NAV-04		Complied
REQ-AVNC-NAV-05	Investigated in detailed design	Not complied
REQ-AVNC-NAV-07		Complied
REQ-AVNC-ICE-01	Investigated in detailed design	Not complied
REQ-AERO-LFT-01		Complied
REQ-AERO-LFT-02		Complied
REQ-AERO-LFT-03		Complied
REQ-AERO-LFT-04		Complied
REQ-AERO-LFT-05		Complied

REQ-AERO-LFT-06		Complied
REQ-AERO-LFT-07		Complied
REQ-THRM-01		Complied
REQ-THRM-INS-02		Complied
REQ-THRM-INS-03		Complied
REQ-THRM-HTCL-03		Complied
REQ-THRM-HTCL-04		Complied
REQ-THRM-DTCT-01		Complied
REQ-STG-PAY-01		Complied
REQ-STG-PAY-02		Complied
REQ-STG-PAY-04		Complied
REQ-STG-PAY-05		Complied
REQ-STG-PAY-06		Complied
REQ-LFSP-01		Complied
REQ-LFSP-AIR-01		Complied
REQ-LFSP-AIR-03		Complied
REQ-LFSP-WTR-01		Complied
REQ-STR-LD-01		Complied
REQ-STR-LD-02		Complied
REQ-STR-LD-03	Investigated in detailed design	Not complied
REQ-STR-ENV-01		Complied
REQ-STR-ENV-04		Complied
REQ-STR-THR-01		Complied
REQ-STR-THR-02		Complied
REQ-STR-THR-03		Complied
REQ-STR-FTG-01		Complied
REQ-CS-01		Complied
REQ-CS-02		Complied
REQ-CS-03		Complied
REQ-CS-04		Complied
REQ-CS-05		Complied
REQ-CS-06		Complied
REQ-CS-09		Complied
REQ-CS-10		Complied

REQ-GNC-APS-01		Complied
REQ-GNC-DGP-01		Complied
REQ-GNC-DGP-02		Complied
REQ-GNC-DGP-03		Complied
REQ-GNC-DGP-04		Complied
REQ-GNC-DV-01		Complied
REQ-GNC-DV-02		Complied
REQ-GNC-DA-01		Complied
REQ-GNC-DA-02		Complied
REQ-GNC-DDH-01		Complied
REQ-GNC-DDH-03		Complied
REQ-CDH-DAT-01		Complied
REQ-CDH-DAT-02		Complied
REQ-CDH-DAT-03		Complied
REQ-CDH-DAT-04	Payload is separated from system	Not complied
REQ-CDH-DAT-05		Complied
REQ-CDH-DAT-06		Complied
REQ-CDH-DAT-08		Complied
REQ-CDH-DAT-09		Complied
REQ-CDH-DAT-10		Complied
REQ-CDH-DAT-11		Complied
REQ-CDH-PRO-02		Complied
REQ-CDH-PRO-03		Complied
REQ-CDH-PRO-04		Complied
REQ-CDH-CMD-01		Complied
REQ-CDH-CMD-02		Complied
REQ-CDH-CMD-03		Complied
REQ-CDH-CMD-04		Complied
REQ-CDH-CMD-05		Complied
REQ-TTC-01		Complied
REQ-TTC-INT-02		Complied
REQ-TTC-EXT-02		Complied
REQ-TTC-EXT-03		Complied
REQ-TTC-EXT-04		Complied

REQ-TTC-EXT-05		Complied
REQ-TTC-EXT-06		Complied
REQ-TTC-EXT-07		Complied
REQ-TTC-EXT-08		Complied
REQ-TTC-EXT-09		Complied
REQ-TTC-EXT-10		Complied
REQ-TTC-PRO-02		Complied
REQ-TTC-PRO-04		Complied
REQ-THR-01		Complied
REQ-THR-02		Complied
REQ-THR-03		Complied
REQ-THR-04		Complied
REQ-THR-05		Complied
REQ-THR-07		Complied
REQ-PWR-01		Complied
REQ-PWR-ELEC-01		Complied
REQ-PWR-ELEC-02		Complied
REQ-PWR-ELEC-03		Complied
REQ-PWR-ELEC-04		Complied
REQ-PWR-ELEC-05		Complied
REQ-PWR-02		Complied
REQ-PWR-04		Complied
REQ-EOL-TRANSP-01		Complied
REQ-EOL-DISS-01		Complied
REQ-EOL-DISS-02		Complied
REQ-EOL-DISS-03		Complied
REQ-EOL-DISS-04		Complied
REQ-EOL-DISS-05		Complied
REQ-SAF-EMR-01	Controlled landing is possible in all situations	Not complied
REQ-SAF-EMR-02	Astronaut safety is prioritized over aircraft integrity	Not complied
REQ-SAF-ENV-01		Complied
REQ-SAF-ENV-02		Complied
REQ-SAF-ENV-03		Complied
REQ-ETHC-01		Complied

REQ-ETHC-02		Complied
REQ-ETHC-03		Complied
REQ-SUST-01		Complied
REQ-SUST-02		Complied
REQ-SUST-03		Complied
REQ-SUST-04		Complied
REQ-PPFO-EMB-01		Complied
REQ-PPFO-EMB-02		Complied
REQ-PPFO-LND-01		Complied
REQ-PPFO-LND-02		Complied
REQ-PPFO-LND-03		Complied
REQ-PPFO-LND-05		Complied
REQ-PPFO-MNT-01		Complied
REQ-PPFO-MNT-02		Complied
REQ-PPFO-MNT-03		Complied
REQ-PPFO-FRD-01		Complied
REQ-PPFO-FRD-02		Complied
REQ-PPFO-FRD-03		Complied
REQ-PPFO-FRD-04		Complied
REQ-PPFO-FRD-05		Complied
REQ-PPFO-ENS-01		Complied
REQ-TOFF-PPS-01		Complied
REQ-TOFF-PPS-02		Complied
REQ-TOFF-PPS-03		Complied
REQ-TOFF-CMCH-01		Complied
REQ-TOFF-CMCH-02	A conclusion has been reached that such system is not required	Not complied
REQ-TOFF-TOM-01	Deemed unnecessary	Not complied
REQ-TOFF-CTOFF-02		Complied
REQ-TOFF-CTOFF-03		Complied
REQ-CLMB-01		Complied
REQ-CLMB-04		Complied
REQ-CLMB-05	The landing gear has been decided to be static (fixed).	Not complied

REQ-MAN-01	Complied
REQ-MAN-02	Complied
REQ-MAN-03	Complied
REQ-MAN-04	Complied
REQ-MAN-05	Complied
REQ-MAN-06	Complied
REQ-MAN-07	Complied
REQ-MAN-08	Complied
REQ-MAN-09	Complied
REQ-MAN-10	Complied
REQ-MAN-11	Complied
REQ-CRUS-04	Complied
REQ-CRUS-05	Complied
REQ-CRUS-06	Complied
REQ-CRUS-07	Complied
REQ-CRUS-08	Complied
REQ-CRUS-09	Complied
REQ-DSCT-03	Complied
REQ-LDG-FAPP-01	Complied
REQ-LDG-FAPP-02	Complied
REQ-LDG-FAPP-03	Complied
REQ-LDG-TDWN-01	Complied
REQ-LDG-TDWN-02	Complied
REQ-LDG-TDWN-03	Complied
REQ-LDG-TDWN-04	Complied
REQ-LDG-DLRT-02	Complied
REQ-LDG-DLRT-04	Complied

5.4. Feasibility Analysis

By Sebastian Harris

Despite most requirements being met, it is clear from the table above that some requirements are not met. For most, these do not impact the feasibility of the product but rather limit it in some ways.

First, REQ-LAU-03 and REQ-LAU-04 depend on testing; as a launcher has not been selected, the loads induced into the disassembled design have not been quantified. In later phases of the design, these will be quantified, and any modifications required will be introduced to the design.

Regarding REQ-AVNG-NAV-02 and REQ-AVNG-NAV-03, the capabilities of the original instruments re-

quired were replaced by a lidar, which means the performance of the requirement is complied with despite the lack of instruments.

Considering REQ-AVNC-NAV-05 and REQ-AVNC-ICE-01, they will be investigated in further design phases and, as such, cannot be determined at this stage. This is the same case for REQ-STR-LD-03.

Considering the command and data handling system's requirement to communicate with the payload, this will not be the case as the payload of scientific instruments is independent of the designed system. Thus, despite REQ-CDH-DAT-04 not being complied with, it does not impact the feasibility of the design.

Regarding astronaut and aircraft safety, REQ-SAF-EMR-01 was not considered, as a controlled landing is possible in all situations and thus did not require an abort system. Meanwhile, the crashworthiness of the aircraft was determined to be sufficient despite the increase in impact loads due to the low probability of all engines failing. However, in case external authorities require this to be implemented, an additional crash system can be implemented through the use of airbags similar to those used in rover landings.

The impact of REQ-TOFF-CMCH-02 and REQ-TOFF-TOM-01 is also negligible despite the requirement not being complied with. Nonetheless, further investigation into including a de-icing mechanism will need to be performed to ensure the safety of the astronauts.

Regarding the retraction of the landing gear, REQ-CLMB-05 was not complied with due to the unfavorable results of retractable gear. The increase in drag from a fixed landing gear is more favorable than the increased weight of a retractable system.

Final Design

With the sizing of all subsystems finished, a summarizing look at the final design is in good order. It is also an excellent time to dive deep into the actual performance of the tiltrotor as well as the risks still associated with the design and more. This will allow for conclusions on the sensitivity of the design, the market for it and what the future holds for the tiltrotor.

6.1. Configuration

By Javier Alonso García

After sizing all the subsystems, the final parameters for the aircraft are known. Firstly, the geometry and mass of the aerodynamic surfaces can be seen in Table 6.1. The general layout of the aircraft can be seen in Figure 6.1.

Table 6.1: General geometry of the wing and tails.

	Span [m]	Root chord [m]	Tip chord [m]	Front sweep [deg]	Aft sweep [deg]	Mass [kg]
Wing	44.67	3.910	1.985	0	4.927	591.1
Horizontal stabilizer	11.26	2.144	0.857	12.87	0	112
Vertical stabilizer	4.760	3.400	1.360	23.20	0	59

Additionally, the propulsion system will consist of 2 sets of counter-rotating rotors, each with 8 blades of 8.6 m in length. These blades will be twisted such that the angle of attack is constant during take-off along the blade, thus producing the same thrust while reducing the loads on the structure. Each of these blades will have a mass of 14.28 kg including 2 kg for margin, amounting to a total of 342.6 kg.

Those rotor blades will be powered by 2 EMRAX228 engines for the front rotors and 2 EMRAX268 engines for the aft rotors. The different types of engines were selected based on the different power required by each rotor. In total, however, the total power required by the system was 354.5 kW during take-off and 285.5 kW during cruise. These engines will get their power from batteries stored in the lower half of the fuselage, which need a capacity of 777.5 kWh for a 1000 km flight. Current batteries do not have the energy density necessary to store that much energy and stay within the mass margin, therefore, future solid-state batteries were assumed to have an energy density of 875 Wh/kg and the same degradation as current batteries. Finally, depending on the configuration chosen (Helios/Atlas) and thus the presence or absence of solar panels, the available battery mass varied between 903 kg and 1057 kg, allowing for a range of 906 km and 1077 km respectively.

Additionally, the engines and batteries will need to be kept within a certain temperature range for them to stay operative, therefore, a thermal control subsystem was designed. These components will generate heat that will be exhausted via radiators to the exterior to prevent them from heating up beyond the maximum operative temperature.

Furthermore, the aircraft will need sensors for navigation and a communications subsystem. The communication subsystem will allow for two-way communications with the base and to transmit telemetry and astronaut biomedical information. Regarding navigation, the sensors will allow the aircraft to determine its position, velocity and attitude and provide landing guidance.

Finally, being a crewed aircraft implies that some life support systems need to be on board. It was decided

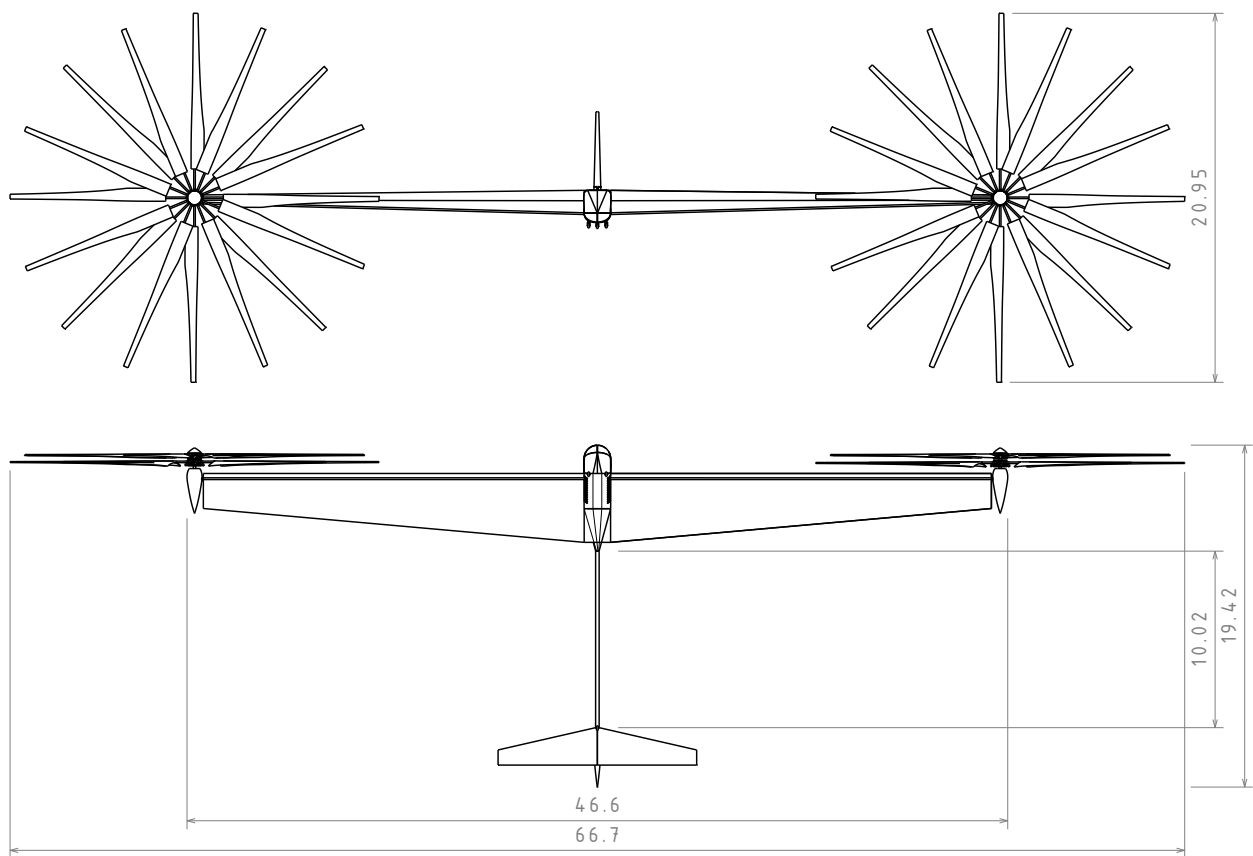


Figure 6.1: Aircraft's front and bottom view with some relevant dimensions in m

that the fuselage would not be pressurized since that would add too much weight to the structure, therefore, the astronauts will keep their suits on during the travel. The only tasks that the life-support subsystem will need to perform will be to provide oxygen and water to replenish that of the suits. Enough oxygen will be on board to sustain 2 astronauts for 36 h and enough water for 24 h without rationing.

6.2. Performance Analysis

By Javier Alonso García, Thomas van de Pavoordt

This section will analyse the flight profile of the tiltrotor in Section 6.2.1, whereafter the flight envelope will be explored in Section 6.2.2. Also, due to the large size and rotation speed of the propellers, a preliminary look is taken into the noise characteristics of the tiltrotor in Section 6.2.3.

6.2.1. Flight Profile

The tiltrotor has been designed to take off, cruise and land with batteries designed to deplete at End-Of-Life. The aircraft, therefore, does not have a flight profile which accounts for diversions or loiter, however, the risk of the astronauts not finding a suitable landing location is deemed so low that it is acceptable. The range in Atlas configuration is up to 1077 km at nominal cruise speed, or the endurance is approximately 2 hrs at continuous maximum power, during which plenty of opportunities for landing locations will arise. Also, with the possibilities of bases on the surface of Mars, together with the tiltrotor as means of transportation, the assumption is made that these bases will logically be placed within the range of the tiltrotor from each other.

For the take-off maneuver, the tiltrotor can achieve a Rate of Climb (ROC) of 2 m/s. As mentioned in Section 4.3.6, the tiltrotor can achieve an altitude of 200 m within 100 s. This can be extended to achieve a desired altitude, after which the transition maneuver of about 60 s will put the aircraft in cruise mode. During cruise, the tiltrotor can achieve a ROC of 65.2 m/s for altitude corrections or evasive maneuvers.

A very typical diagram for aircraft is the payload-range diagram, where a trade-off is performed between having more fuel (and thus a larger range) or more payload on board. This design, however, uses batteries to power the propellers, therefore there is no trade-off to make between fuel mass and payload mass. Using less batteries to allow for a larger payload capacity could be an option. However, the power required for take-off is quite large, and due to the lack of information about the power density of the batteries used for reference, doing this was discarded. An alternative diagram, however, is a density-range diagram which evaluates what the maximum range will be depending on the atmospheric density. This is relevant since all the data given up to now is assuming an atmospheric density of 0.01 kg/m^3 , which is the lower bound of the atmospheric density throughout the year. This value, however, can go up to 0.021 kg/m^3 as an average, which would increase the power required by the rotors in cruise but make them more efficient in take-off. This relationship can be seen in Figure 6.2.

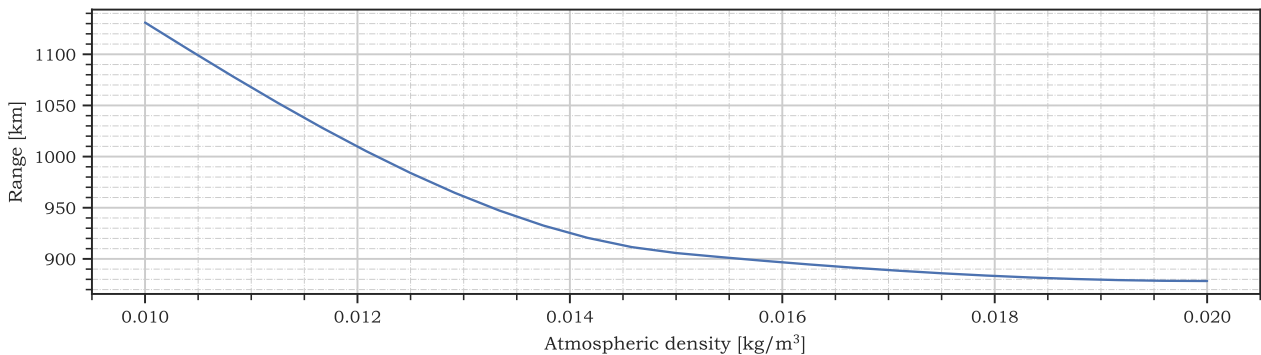


Figure 6.2: Power required by the rotors as a function of the atmospheric density

The range of the aircraft at its nominal payload can be kept almost constant by flying at a higher altitude where the atmospheric density was equal to 0.01 kg/m^3 . However, flying at higher densities would increase the maximum take-off force from the rotors, and thus, the maximum payload that the aircraft can carry.

6.2.2. V-n diagram

A V-n diagram is a useful way of representing the loads an aircraft is able to withstand at different speeds. Even though a velocity-load diagram is usually constructed with Earth-based certification of the aircraft in mind, which does not apply one-on-one to Martian aircraft, it was decided to create a V-n diagram for the tiltrotor as well, to indicate the extremes the aircraft can handle. In this diagram, the maximum allowable speed at which the aircraft can fly, or the dive speed, however, was derived from the Federal Airworthiness Regulations [?], which states that the dive speed should be no larger than 1.25 times the design cruise speed, V_{cr} , which is 400 km/s . [?] The structure was sized in order to withstand the roll constraint, which will induce an equivalent load factor of 2.2 on the structure as opposed to nominal cruise flight, therefore, that was taken as the maximum load factor of the aircraft. The minimum load factor of the aircraft is taken to be -1. The load factor is further computed according to Equation (6.1):

$$n = \frac{\frac{1}{2}\rho V^2 C_L}{W/S} \quad (6.1)$$

The gust diagram is computed with both Martian typical gusts in mind, the same for which the vertical tail was designed, and compared to Earth's typical gusts at different speeds. The regulations for Earth gusts stipulate at the design cruise speed, a gust speed of 56 ft/s occurs and at the dive speed these gusts are half this value.¹ Gust loads are further computed using Equation (6.2) and Equation (6.3):

$$n_{gust} = 1 \pm \Delta n \quad (6.2)$$

¹URL: <https://www.easa.europa.eu/en/document-library/easy-access-rules/online-publications/easy-access-rules-large-aeroplanes-cs-25> [cited 2023-06-20]

where

$$\Delta n = \frac{\frac{1}{2} \rho V C_{L_a} u}{W/S} \quad (6.3)$$

where u represents the gust speed the aircraft needs to withstand at a certain speed, V .

Figure 6.3 shows the results of the V-n diagram:

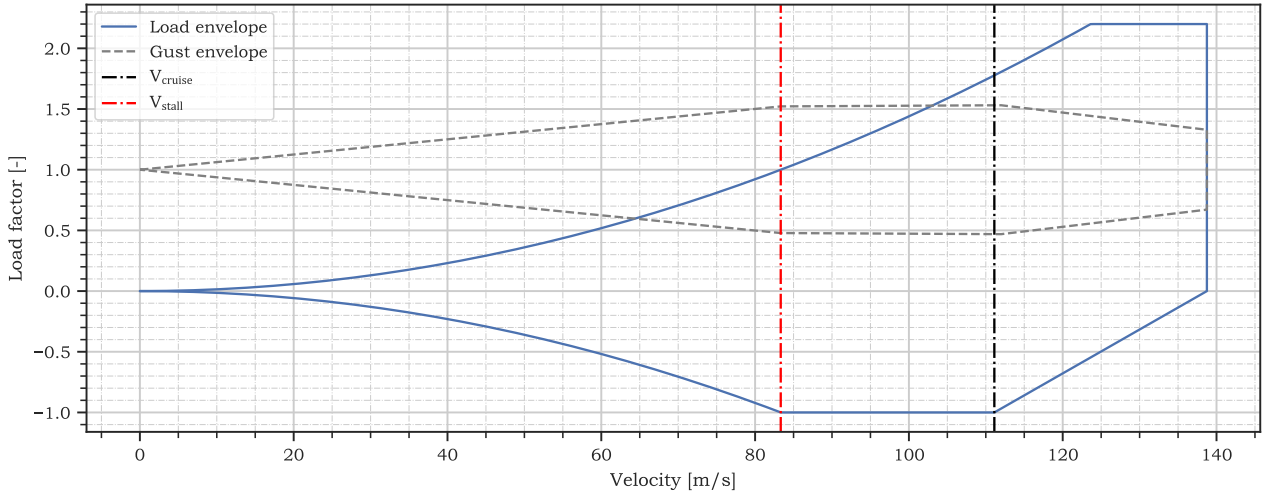


Figure 6.3: Tiltrotor's V-n diagram

As can be seen in Figure 6.3, the maximum load factor will be determined by the gust envelope between the stall speed and 100 m/s, the point after which the load envelope becomes critical. It demonstrates that the aircraft should, in normal conditions, not exceed the maximum allowable load factor.

6.2.3. Preliminary noise characteristics

During a helicopter flight, passengers must often wear headphones to protect them from the thundering sound of the rotors directly above them. Naturally, with such massive rotors on the tiltrotor, the question may arise whether their noise will cause a problem. Thankfully, the aircraft will not have to fly over densely populated areas with noise restrictions; in fact, the only people close to the aircraft are the two astronauts piloting it, since no ground crew (if present at all) will be required to be near the aircraft during take-off or landing. Therefore, the analysis of the noise emitted by the rotors will focus on the noise received by the astronauts sitting inside the cockpit, inside their suits.

To estimate the noise characteristics of the rotors, XRotor was used. The program was run after inputting the rotor geometry into the program and modifying the variables to match the Martian environment. As further input, the sound profile was calculated at a distance of 22.335 m along the wing axis and 1 m in the z-axis to provide an estimate of the location of the cockpit. This resulted in the sound profile in Figure 6.4. Note that this sound profile is only of the upper rotor and does not consider the acoustic interaction between blades or upper and lower rotors. Nonetheless, it provides a good first insight into the acoustic performance of the aircraft. Regarding intensity, the amplitude of the sound of 0.026 Pa leads to an equivalent strength of 62 dB assuming a reference pressure of 20 μPa . Where below 70 dB is considered good acoustic level for helicopter [85].

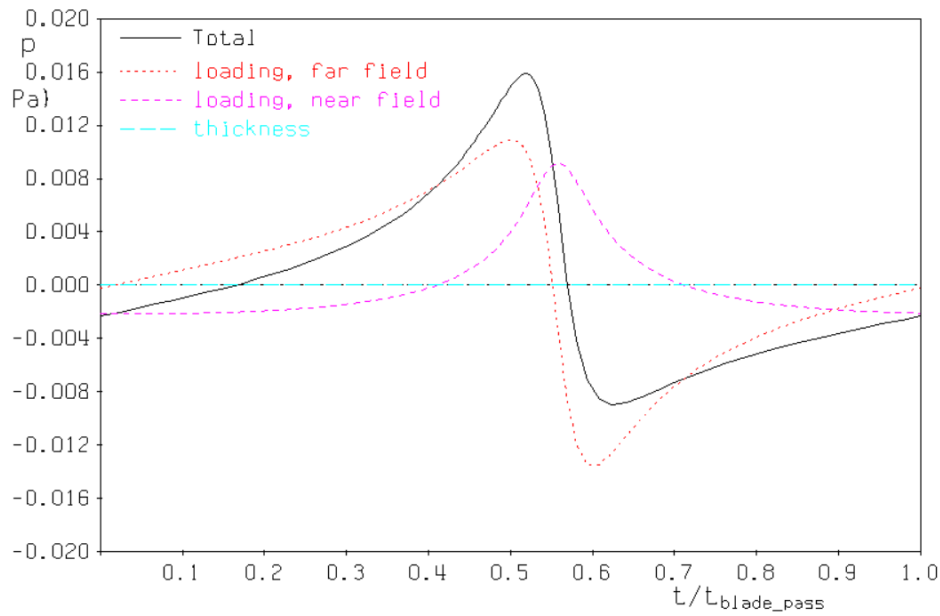


Figure 6.4: Pressure signature of a passing blade

6.3. Reliability, Availability, Maintainability and Safety

Despite the early stage of the design process in which this product was developed, the Reliability, subsection 6.3.1, Availability, subsection 6.3.2, Maintenance, subsection 6.3.3 and Safety, subsection 6.3.4, of the design can be determined.

6.3.1. Reliability

By Sebastian Harris

Determining the reliability of a system that is only produced once is complex. Not only is the dependency on the parts used much higher, as a single defective part could render the entire aircraft out of operation, but the uniqueness of certain parts does not allow for quantitative reliability estimation.

Structural frame

Due to the necessity to fit the product within the fairing of a rocket, the extensive use of joints and assembly required to prepare the tiltrotor for operations will be a failure unless proper measures are taken when further developing the aircraft's structure.

Engines

The engines are a critical part of the design, as their malfunction will lead to an inability to take off vertically. However, using electric engines reduces the number of moving parts and thus increases the reliability of the propulsion system [86]. Furthermore, the lack of combustion reduces the thermal load and limits the engine's vibrations.

Power supply

Due to the utilization of solid-state batteries, the reliability and subsequent safety of the power supply is far higher than in conventional battery arrays [87].

Avionics

The aircraft's avionics provide the pilot with vision during take-off, as the downwash of the rotors will produce a particle cloud that will either partially or fully limit their vision. The reliance on computer-assisted vision means any system failure will lead to additional danger to the astronauts. However, due to the terrain of Mars and the lack of structures that could pose a danger to such an aircraft, vertical take-off will not be too large of a risk to accept.

6.3.2. Availability

By Javier Alonso García

The aircraft was designed to be able to fly with an atmospheric density of 0.01 kg/m^3 and at an environmental temperature of -90° which are the most extreme conditions that one may encounter on the martian surface. Combined with its VTOL capabilities, the aircraft will be able to fly throughout the entire planet. Its availability, however, will be limited by the recharge time. In the Helios configuration, the aircraft will need approximately 60 h of sunlight in order to fully recharge, thus allowing for just one flight every 6 days. In the Atlas configuration, on the other hand, enough infrastructure to recharge the aircraft in 16 h is assumed, and since this can be done at night-time too, it would allow for one flight every 2 days.

Further environmental conditions such as prolonged dust-storms could also result in a reduced availability. As of now, the aircraft should be able to fly in the middle of a dust-storm provided that winds do not exceed those considered in Section 6.2.2.

6.3.3. Maintenance

By Javier Alonso García

The design should allow for maintenance with minimum equipment since the available infrastructure in Mars is uncertain. This has been met by the use of bolts and metal tightening rings (for more details see Section 9.4), both of which can be removed with minimal tooling to facilitate access to the structure's interior.

These activities will have to be done regularly in order to reduce the risk of failure, specially taking into account the limited number of spare parts that the astronauts will have at their disposal.

Given the low magnitude of the loads that will be induced in the structure, it was decided that both Aerion configurations should comply with the Light Aircraft Maintenance Schedule (LAMS), accounting for slight changes in the powerplant/engine revisions which should be adapted to those of an electrical engine as specified by the manufacturer [88]. Future research should focus on whether it is appropriate or not to reduce the inspection intervals in order to further reduce the risk of failure.

6.3.4. Safety

By Sebastian Harris

With Mars being inhospitable and posing a constant threat to the astronauts, the safety of the aircraft is critical to ensure the safety of the astronauts. The selection of a tiltrotor means that safety is included in the design from a concept level downwards.

First, using rotors for vertical take-off ensures that even with a loss of power, the aircraft can land using autorotation, which ensures a safe landing. In the event all engines fail, pilots are unresponsive, and the autopilot fails, the aircraft would descent at 38 m/s as mentioned in subsection 4.2.6. Such a value for descent would not be achievable in a conventional aircraft as the wing would be stalled and not generate sufficient lift to counteract the descent.

First, the life support system ensures astronauts can survive for 36 hours in the aircraft, vastly outlasting the length of a conventional mission.

6.4. Sensitivity Analysis

By Javier Alonso García

The aim of a sensitivity analysis is to check how dependent is the output of a code on certain inputs. As of the moment the way the software has been structured does not allow to perform a complete sensitivity analysis across subsystems, mainly due to the use of external software such as XFLR5. A small analysis, however, can be performed between the aerodynamics, structures and power subsystems.

This analysis will consist on changing the geometry of the wings (assuming the total lift does not change),

evaluate the change in mass of the wing, assume that the mass differential will be accounted for in the batteries and thus recalculate the aircraft's range. The results from this analysis can be seen in Table 6.2.

Table 6.2: Sobol indices relating the wing dimensions to the wing mass and aircraft range

Parameter	Wingspan	Root chord	Taper ratio
Wing mass	0.436	0.348	0.247
Range	0.436	0.348	0.247

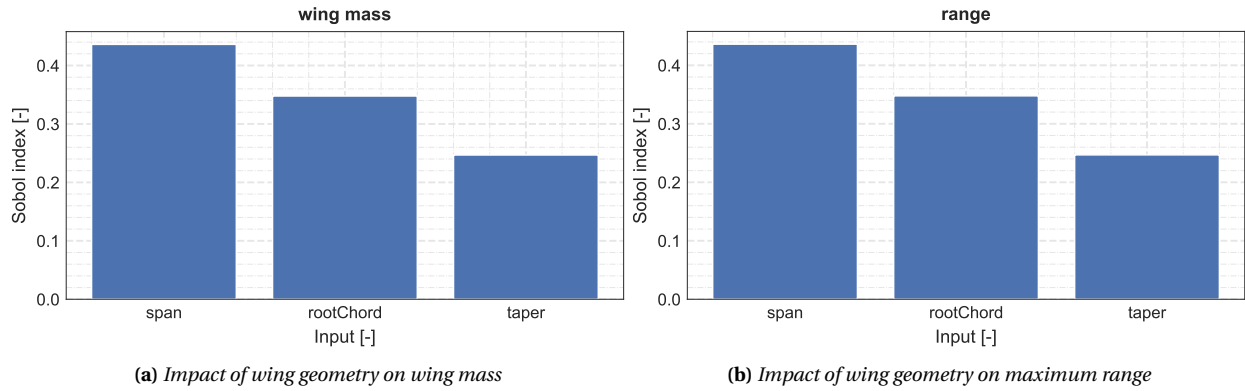


Figure 6.5: Sensitivity analysis of the wing geometry on wing mass and range

From these table and figures we can determine that the impact on both parameters is the same, and that both the span and the root chord will have a moderate impact on this value (a Sobol index of 0.4 indicates that the input is responsible for 30% of the variance in the output).

In future iterations this analysis could be extended to include different parts of the design that have not been tested such as the rotor blades or the fuselage design, or alternatively, the new aerodynamics could be computed.

Technical Risks

By Sebastian Harris

Technical risk assessment has been a continuous process throughout all phases of the project. This section describes the methodology (identical to midterm report), summarizes previously identified risks, and introduces new ones found after the detailed subsystem sizing.

7.1. Methodology

Within the risk assessment process, various methods are available to both size risks and their impact. In the context of this report, the scale in Table 7.1 is used.

Table 7.1: Score associated with probabilities and impacts of the risks

Scale	Probability	Impact
5	Very High ($p \geq 95\%$)	Catastrophic (Complete Mission Failure)
4	High($60\% \leq p < 95\%$)	Partial Mission Failure
3	Medium ($30\% \leq p < 60\%$)	Moderate performance reduction
2	Low ($1\% \leq p < 30\%$)	Small performance reduction
1	Very Low ($p < 1\%$)	Negligible

7.2. Risks identified in previous phases

The risks related to the design have mostly been already discovered in previous phases of the design. Nonetheless, they will be recalled in Table 7.2 to provide a significant overview of the risk assessment and mitigation process for the aircraft.

7.3. Risks identified in final phase

Detailed analysis and component selection for most subsystems has revealed new technical risks. These are summarized in Table 7.3. The mechanical failures can be mitigated by inspection during the pre-flight check.

Table 7.2: Technical risks identified in previous phases.

Risk ID	Description	Probability	Impact	Risk ID	Description	Probability	Impact
R-PREP-01	Imperfections in manufacturing	2	4	R-CR-04	Corrupted on-board computer	1	3
R-PREP-02	Damage during transport	2	4	R-CR-05	Structural failure	2	4
R-PREP-03	Errors in Assembly	2	4	R-CR-06	Strong turbulence	1	3
R-PREP-04	Missing items in package	2	4	R-LD-01	Engine failure	2	2
P-PREP-05	Launcher fails	1	5	R-LD-02	Dust clogs any air intake	3	3
R-STAT-01	Dust Storm leading to aircraft damage	3	3	R-LD-03	Control surface failure	2	4
R-STAT-02	Damage due to strong winds	3	3	R-LD-04	Non-functional landing gear	2	4
R-STAT-03	Damage due to Radiation	3	3	R-LD-05	Corrupted on-board computer	1	2
R-STAT-04	Incident when refueling/recharging	3	3	R-LD-06	Structural failure	2	3
R-STAT-05	Pre-flight procedures fail	3	3	R-LD-07	Need multiple approaches	3	2
R-STAT-06	Unable to refill energy storage	2	4	R-LD-08	Landing site is to small	3	3
R-STAT-07	Failure to assemble on sight	2	5	R-LD-09	Landing gear failure	2	4
R-OP-01	Life support failure	1	5	R-AR-01	Faulty batteries	1	5
R-OP-02	On-board fire	1	4	R-AR-02	Transmission failure [89]	1	4
R-OP-03	Compromised thermal insulation	2	3	R-AR-03	Gearbox Failure [89]	1	4
R-OP-04	Astronauts unable to operate the aircraft	2	5	R-AR-04	Hydraulic failure	1	4
R-OP-05	Power system failure	2	4	R-AR-05	Avionics failure[90]	1	3
R-OP-06	Improper maintenance	2	3	R-AR-06	Brownout [91]	4	3
R-TO-01	Engine failure	2	2	R-AR-07	Short-circuiting of electrical components	1	4
R-TO-02	Control surface failure	2	3	R-AR-08	Rotor failure	1	4
R-TO-03	Dust clogs any air intake	3	3	R-AR-09	Autopilot failure [89]	1	2
R-TO-04	Corrupted on-board computer	1	2	R-AR-10	Instrument failure [89]	1	3
R-TO-05	Structural failure	2	3	R-AR-11	Temperature control failure [92]	1	3
R-TO-06	Insufficient runway length	2	5	R-AR-12	Astronauts unresponsive [93]	1	5
R-TO-07	Insufficient lift produced	1	5	R-AR-13	Battery Ageing	5	3
R-CR-01	Engine failure	2	4	R-AR-14	Vortex Ring State	3	3
R-CR-02	Dust clogs any air intake	1	3	R-AR-15	Center of gravity shift	2	5
R-CR-03	Control surface failure	2	4				

Table 7.3: Technical risks identified in the final phase.

Risk ID	Description	Probability	Impact
R-OP-07	Cooling failure	2	4
R-OP-08	HF link failure	3	3
R-OP-09	UHF link failure	2	3
R-OP-10	Door failure	1	3
R-TO-08	Lidar failure	1	2
R-TO-09	Tilting mechanism failure	1	4
R-TO-10	Rotor collective failure	1	2
R-OP-07	Lidar failure	1	1
R-OP-08	Rotor collective failure	1	2
R-LD-10	Lidar failure	1	4
R-LD-11	Tilting mechanism failure	1	5
R-LD-12	Rotor collective failure	1	3

Financial Overview

The project's financial overview can be split into four main parts. First, the design's strengths, weaknesses, opportunities, and threats are analyzed in section 8.1. Next, the market is estimated through a process described in section 8.2. Initial cost estimates regarding the development, manufacture, and launch of the project can be found in section 8.3. Finally, the project's return on investment is analyzed in section 8.4.

8.1. SWOT Analysis

By Sebastian Harris

The first step in a market analysis is determining the combination of strengths, weaknesses, threats, and opportunities that make a design unique. The combination of these factors will, in part, dictate the performance and track to follow to lead to market such a product successfully. In the case of this design, the above characteristics can be summarized in a table through a SWOT analysis.

Table 8.1: SWOT Analysis of the final design

	Helpful	Harmful
Internal	Vertical Take-off	Large wingspan limits maneuvering
	Electric Propulsion is proven	Can't sustain long-term manned missions
	Can operate in dust storms	
	Can operate autonomously	
External	No similar competitors	Vulnerable to storm-induced power black-out
	Recently proven concept through Ingenuity	Dependent on future development of batteries
	Large interest in solid-state batteries will push their development	

8.2. Market Size Estimation

By Sebastian Harris

As interest in Mars has grown, the financial commitments of various space agencies have also increased. Despite no clear competitors present, it is nonetheless possible to compare the various proposed projects and concepts that, in theory, are available for these space agencies to choose from.

The concepts available for these agencies can be split between rover-based designs and aerial designs. These concepts can be summarized in Table 8.2.

Table 8.2: Concepts for Mars

Concept Name	Concept Type	Crew Size	Range [km]	Max Speed [km/h]	System Mass [kg]
Hoffman 1997 [1]	Rover	2	500	10	16500
Morphlab [1]	Rover	4	1000	NA	3700
Raymer [2]	Aircraft	2	482	278	2721.5

Estimates of the costs of manned Martian missions have varied significantly, but all values remain important financial commitments despite this. These costs for the first Mars mission varied between 42 and 517 billion USD FY2016 [94], with the most recent estimates projecting a total cost of 500 billion USD FY2016. When comparing the costs of transport vehicles in the context of a larger mission, a similar relationship could be found for the available budget for a Martian vehicle.

As the only extraterrestrial manned transport vehicle used to date, the lunar roving vehicle (LRV) was used on the Apollo 15, 16, and 17 missions. With a cost nearing 38 million USD in 1971, the LRV represented around 8.5% of the total 445 million USD for Apollo 15¹². Adjusted for inflation, these numbers become 285.35 million and 3.341 billion USD. Thus, assuming a consistent relative cost, the expected investment into astronaut transportation for a Manned Martian Mission would be between 4.44 and 53.8 billion USD FY2023.

Thus, the market, although yet to be defined, has a potential valuation in the tens of billions of dollars. Furthermore, the competition between various countries to land on Mars will further increase this market space as the above number only considers the plans of NASA.

8.3. Cost Breakdown

By Sebastian Harris

The costs of the final design can be traced to two main sources. The first is the manufacturing and development of the product, which entails the material costs of the product, as seen in subsection 8.3.2, followed by the costs of the power subsystem, in subsection 8.3.3

8.3.1. Personnel Costs

Despite the early stages of the design, it is nonetheless possible to have some estimates of the development and production costs based on historical aircraft development costs. As the design is still in the early phases, this process is done through initial estimates as follows:

$$H_E = e^{3.08} W_e^{0.588} V^{0.962} Q^{0.236} E^{0.018} \quad [95] \quad (8.1)$$

Where W_e is the mass of the aircraft in kg, V is the maximum speed of the aircraft in km/h , Q is the number of units produced, and E is the efficiency index assumed to be 0.75. Next, the processing equipment hours are calculated with

$$H_T = e^{10.25} W_e^{0.324} V^{0.039} Q^{0.4} E^{0.074} \quad [95] \quad (8.2)$$

Which is followed by the manufacturing hours calculated as

$$H_M = e^{11.8} W_e^{0.063} V^{0.022} Q^{0.627} E^{0.432} \quad [95] \quad (8.3)$$

From which the quality control hours are calculated as being 13.3% of the above number. Finally, the development support costs are calculated as

$$C_D = e^{9.32} W_e^{0.084} V^{1.13} E^{0.186} \quad [95] \quad (8.4)$$

These calculations can be summarized by Table 8.3.

¹URL: https://nssdc.gsfc.nasa.gov/planetary/lunar/apollo_lrv.html [cited 2023-06-19]

²URL: <https://www.statista.com/statistics/1028322/total-cost-apollo-missions/> [cited 2023-06-19]

Table 8.3: Research and Development Costs breakdown

Component	Per unit cost	Units	Cost
Engineering Hours	90 USD FY23 ³	946 055	85.1 MUSD FY23
Processing Hours	40 USD FY23 ⁴	472 175	18.9 MUSD FY23
Manufacturing Hours	50 USD FY23 ⁴	223 423	11.2 MUSD FY23
Quality Control Hours	45 USD FY23 ⁴	29 715	1.34 MUSD FY23
Development support costs	NA	NA	23.2 MUSD FY23
Sub-total			139.74 MUSD FY23

8.3.2. Material cost

The material costs of the aircraft can be seen in Table 8.4. Note that this only includes the wings, tail, rotor blades, wing brace, and tail-pole mass.

Table 8.4: Material cost breakdown

Material	Cost per unit	Unit [kg]	Total cost
CF/PEEK	95.9 USD FY22 [64]	709.15	68 942.51 USD FY22
CF/Cy	189.5 USD FY22 [64]	342.63	64 928.385 USD FY22
Al 518.0	1.82 USD FY22 [64]	59	107.38 USD FY22
Sub-total	146 833 USD FY23		

However, It is crucial to remember that the costs listed in Table 8.4 are for high-volume purchases, and since only one or two units will be produced, the prices may rise.

8.3.3. Power System Cost

The power system cost is mainly dictated by the batteries used, engines, and electrical cabling. These costs can be summarized by

Table 8.5: Breakdown of Power subsystem costs

Component	Cost per unit	Units required	Cost
Solid-state batteries	75 USD FY22/kWh ⁵	777.55 kWh	58 316.25 USD FY22
Emrax 228	2790 Euro FY22 ⁶	2	5580 Euro FY22
Emrax 268	6190 Euro FY22 ⁷	2	12380 Euro FY22
Sub-total	81 055 USD FY23		

³URL: <https://www.zippia.com/engineer-jobs/salary/> [cited 2023-06-20]

⁴URL: <https://www.avjobs.com/salaries-wages-pay/index.asp?c=manufacturing> [cited 2023-06-20]

⁷URL: <https://insideevs.com/news/551144/nissan-proprietary-solid-state-batteries/> [cited 2023-06-20]

8.3.4. Avionics Costs

Next, the avionics and their cost can be collected and added to the ongoing cost analysis. However, some components are missing as their costs could not be determined, for which a margin of 2 was added to the avionics components. This is mainly the case for both the HF and UHF antennas. Nonetheless, the components whose value could be determined still show the important of this subsystem relative to cost. As such, the breakdown of these components and their costs can be seen in Table 8.6

Table 8.6: Breakdown of Avionics subsystem costs

Component	Cost per unit	Units required	Cost
Coupler	4250 USD FY22 ⁸	1	4420 USD FY23
Pitot-Static	25000 USD FY20 ⁹	1	29500 USD FY23
Fisheye color camera	39000 USD FY20 ¹⁰	3	138060 USD FY23
LIDAR	165000 USD FY17 ¹¹	1	204600 USD FY23
Air data computer	255000 USD FY09 ¹²	1	362100 USD FY23
Graphic processing computer	2000 USD FY22 ¹³	1	2080 USD FY23
Data link	64412 USD FY11 ¹⁴	1	86956 USD FY23
Sub-total			1655 kUSD FY23

8.3.5. Summary of Costs

The launch costs must be determined before collecting all these costs and determining an initial overview of the cost of the development, manufacturing, and transportation of this design. Comparing past data on launch costs can give an indication of what these costs could look like in the future. Starting with Perseverance, coming in at a cost of 243 MUSD FY2020 for a total rover weight of 1025kg. Compared to the current project, this leads to an initial estimation of 839 MUSD FY2023. Finally, all these costs can be summarized in the final table of Table 8.7.

⁸URL: <https://www.seaerospace.com/sales/product/BendixKing/KAC-952/064-1017-11> [cited 2023-06-20]

⁹URL: <https://nts-info.com/product/ref-1146-aimms-20-aircraft-weather-probe/> [cited 2023-06-20]

¹⁰URL: <https://www.dpreview.com/news/4034995669/c-4-precision-optics-4-9mm-f3-5-hyper-fisheye-lens-for-sony-e-mount> [cited 2023-06-20]

¹¹URL: <https://newprovideo.com/equipment/product/cameras-camcorders/phoenix-lidar-camera-system> [cited 2023-06-20]

¹²URL: <https://aeroval.com/ref/1776446/HG2030BE02/> [cited 2023-06-20]

¹³URL: <https://www.arrow.com/en/products/945-13730-0055-000/nvidia> [cited 2023-06-20]

¹⁴URL: <https://aeroval.com/ref/293455/822-1239-151/> [cited 2023-06-20]

Table 8.7: Summary of costs

Section	Cost
Personnel	139.7 MUSD FY23
Material	146 833 USD FY23
Power System	81 055 USD FY23
Avionics	1 655 000 USD FY23
Product Total	141.6 MUSD FY23
Launch Costs	839 000 000 USD FY23
Carbon Offsets	630 000 USD FY23
Total Costs	981.23 MUSD FY23

8.4. Return on Investment

By Sebastian Harris

The return on investment of a scientific mission is difficult to measure. However, certain metrics can still be used to determine the impact of a manned Martian aircraft.

8.4.1. Economic impact on Earth

According to NASA, the agency generates over 69000 jobs, 14 billion USD FY22 in economic output, and 1.5 billion USD FY22 in tax revenue solely through its Moon to Mars initiative. Furthermore, the agency regularly develops spinoff technologies, which join the consumer market and improve the everyday lives of everyone in the united states. According to research, every dollar allocated to NASA results in between 7 and 14 USD FY22 of an economic boost. Thus, the ROI of investing around 1 billion USD FY23 would result in an economic boost of up to 14 billion USD FY23.

8.4.2. Avoided Cost

Although direct comparison with other transportation options on Mars is not possible, the performance comparison is directly related to cost by looking at the concepts developed in Table 8.2. Considering the cost of life support on Mars will cost around 41 million USD FY16 per year[94], maximizing the distance covered by a scientific mission decreases the total cost to the agency. Considering other missions have lower ranges and speeds, they will require more missions, lasting longer and ultimately costing more money.

Project Future

In this chapter the future of this project will be explained. Starting with the design and development logic in Section 9.1 showing what needs to be done for the design to be completed, this is also shown in time in Section 9.2 by presenting a Gantt chart. From this the logistics and operations for the production and operational phase will be presented in Section 9.3. Finally the production plan both for on Earth and Mars manufacturing will be presented in Section 9.4.

9.1. Project design and development logic

By Timo de Kemp

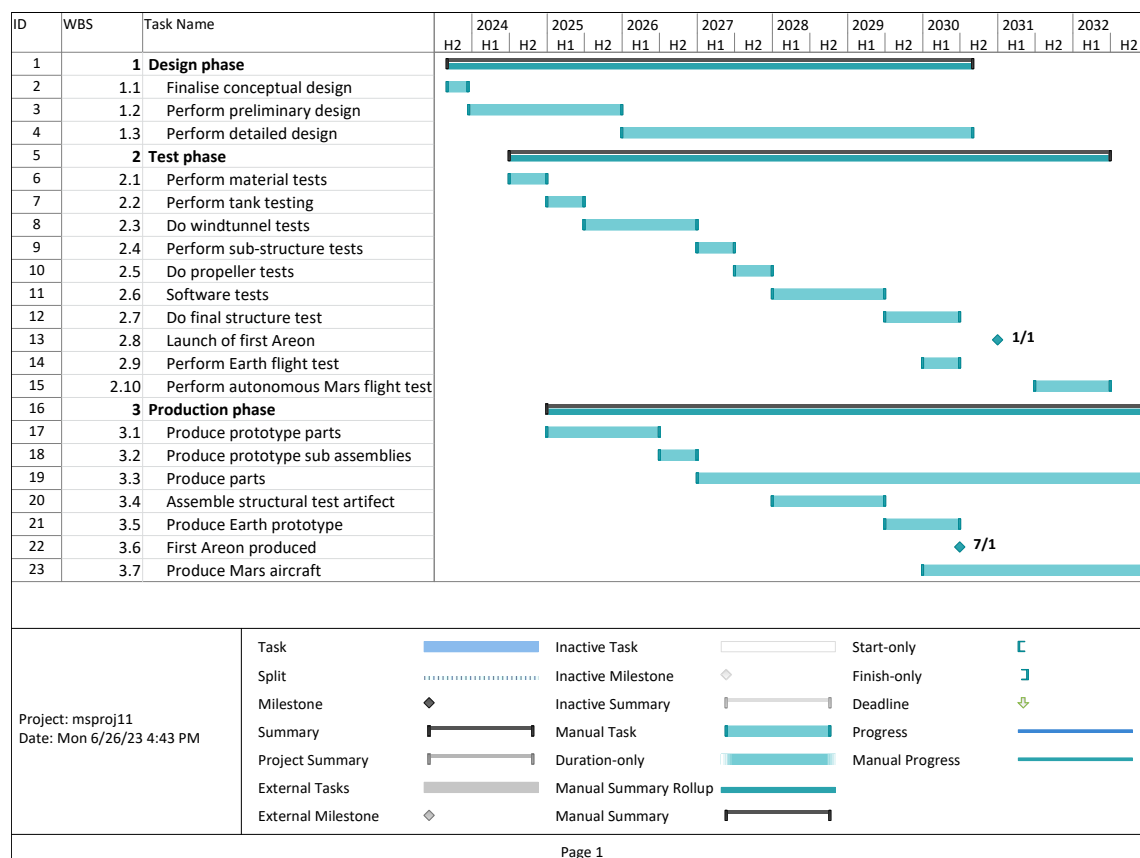
In this part the project design and development will be looked into, this investigation makes sure that a general time line from this preliminary design until the first operations is provided. The following list provides some future actions that have to be definitely done in the preliminary design, this is not ordered in time.

- Certify all off-the-shelf components for Mars usage
- Invest/develop battery technology
- Global optimization of wing parameters
- Investigate non-linear effects of prop-prop and prop-wing interactions
- Investigate vortex generator effects on lift capabilities
- Aileron design validation
- Investigate the 3D wing effects on the lift
- Do more high fidelity drag estimation of the fuselage
- Perform detailed cockpit design, placement of controls displays etc.
- Payload fastening methods need exploration and design
- Pilot seat design taking into account the space suit and life support connections
- Determine the in cabin radiation
- Investigate control lay-out for take-off and transition
- Determine aerodynamic coefficients, specifically C_{n_h} to construct more realistic state space model
- Lobby with space agencies for a constellation of relay orbiters for communication and positioning (GNSS)
- Perform detailed simulations of skywave propagation and availability on Mars
- Test radiation response of instrumentation sensors and flight computers
- Research the possibility of supersonic blades and its effect
- Size the wing and blade structure for aerelastic behaviour
- Investigate fatigue influences on structure and material
- Design the joints for the sub-assembly

9.2. Gantt chart

By Timo de Kemp

In Figure 9.1 the planning of the future of design, testing, and production is shown. The development of this aircraft will take 10 years which is slightly longer than the aircraft development for Earth this is due to the more limited access to Martian conditions and unknowns. Since the next ideal launch window opens in 2033, and transfer to Mars and assembly will take about one year, Areon will be able to start operating as soon as 2034.



Page 1

Figure 9.1: Gantt chart showing the future development of Areon

9.3. Operations and logistics

By Timo de Kemp

In this section the operations and logistic concept for the logistics for production and operation phase of the aircraft will be discussed. As can be seen in Figure 9.2, the flowchart starts from semi-finished materials i.e. processed metal or plastic pallets. These have to be transported to the manufacturing facility and manufactured into the sub-assemblies. The sub-assemblies will be transported to Mars. As little infrastructure is assumed on Mars, therefore only the final assembly will be done on Mars. The shipment of the equipment is also included to be complete, as well as possible resupply mission, with back-up or replacement parts for the aircraft. To keep the aircraft flying for a long time regular checkouts have to be done and maintenance when necessary to keep the aircraft from the end of its life.

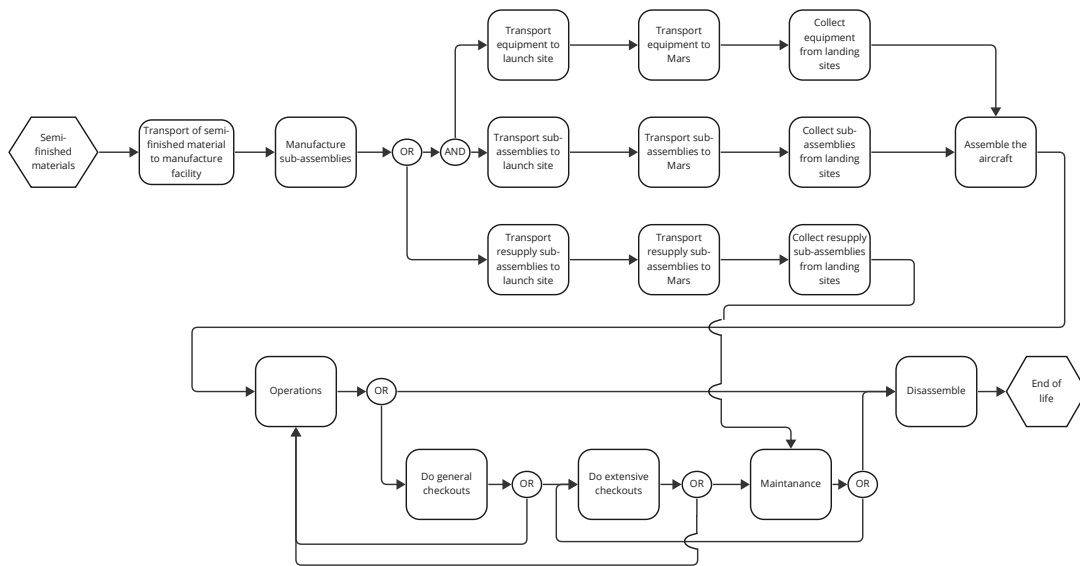


Figure 9.2: Flow chart which describes the operations and logistics for the production and operation phase.

9.3.1. Pre-operations

The pre-operations phase consists of an Earth production phase, a transportation phase, and a Mars assembly phase. In the Earth phase sub-assemblies will be manufactured on Earth, the production plan in Section 9.4 will give more detail on the manufacturing processes and size of sub-assemblies. The transportation phase includes the transportation from manufacturing facilities to Mars, and will be carried the majority of the way by SpaceX's Starship. The final pre-operations phase will be the Mars phase, where the sub-assemblies have to be assembled into the final product. The equipment and procedures for this assembly is also expanded in Section 9.4.

9.3.2. Operations

The operations are split into ground operations and in-flight operations. Ground operations describe the processes necessary for successful flight, before and after the aircraft is in the air. While the in-flight operations will describe the processes going on while flying, to keep the pilots updated as well as the ground station. The general mission consists of the ground operations stated in ground operations. After taxiing to a remote enough location for take-off, take-off is performed. After initial vertical climb the aircraft transitions to horizontal flight, after which it climbs to the desired altitude in this configuration. The aircraft descends to the transition altitude near the landing site, after which it performs transition and vertically lands. The mission at location is performed after which the aircraft returns in similar fashion. Once landed back at the base the aircraft will taxi to its final location to be recharged for the next flight.

Ground operations

After landing near the base, the following eleven steps have to be taken to have a safe next flight. The final weather checks have to be performed for the take-off site as well as down range. The weather requirements are given on the right. Dust storm are allowable, however the crosswind constraints may be violated in this case. Therefore, the local weather forecast should be checked before operations.

1. Taxi to base
 2. Secure the aircraft
 3. Disembark from aircraft
 4. Unload payload from the aircraft
 5. Check aircraft for damage
 6. Recharge the aircraft
 7. Plan the next flight
 8. Check weather forecast
 9. Load payload into the aircraft
 10. Embark into the aircraft
 11. Perform pre-flight checks
 12. Taxi to take-off position
- Airborne dust is acceptable
 - Temperature between -80 and 5 °C
 - Crosswind < 15 m/s
 - Vertical gusts < 15 m/s

The recharging as explained in Section 4.6 for the Helios variant will be done using solar panels and take 5 days. The charging for the Atlas variant will be depended on the charging power available. To make an estimate on the power available for charging on a base, it was decided to make this equal to the power consumed by two astronauts. The astronauts will be using 25 kW each according to Pombo [96], therefore the charging power for the Areon Atlas will be 50 kW resulting into a fifteen hour recharge period.

In-flight operations

Form the functions described in Section 2.5 have to be performed. The functions in take-off and cruise configurations are similar however they might have a different method of reaching these functions. As during take-off the thrust of the blades will be used to create the required lift, while during cruise the lift is created by the wings.

During flight operations the power to all subsystems will be provided by the batteries. This is crucial to the mission as the batteries not only provide power to the blades for lift/thrust, but also to the flight computer which keeps the aircraft dynamically stable. Power is also provided to the communications and navigation subsystem, which will ensure the astronauts will not get lost on Mars and keep in touch with base camp if something goes wrong.

9.3.3. End of life

After the operational life of 10 years the design is over it will enter the end of life stage. In this stage the aircraft will be recycled for use on Mars. The batteries can be used for base energy storage. The engines can be used to drive a rover or for on base purposes. The body of the design can be used as a shed for environmental pressurized storage. Finally the wings and blades could be used as beams in the construction of the base. Other parts of the aircraft will also have their purpose in the base on Mars.

9.4. Production plan

By Javier Alonso García

The aircraft needs to be transported to Mars in as few parts as possible, in order to facilitate the assembly by the astronauts. Starship was selected as the launcher for which the different parts would be sized since it is the largest launcher currently available. According to its user manual [97], the payload bay has a width of 8 m in diameter up to an altitude of 8 m, point at which the diameter starts to decrease up to 3.6 m at an altitude of 17.24 m. Given how the root-chord of the aircraft is 3.91 m, a maximum altitude per part of 15 m was imposed, where Starship's payload bay has a diameter of 5 m [97].

Assembly The aircraft will thus be disassembled into four groups: the fuselage, the tail, the wing and the rotor-blades, as seen in Figure 9.3. The fuselage would fit entirely into the payload bay, therefore, it will be entirely assembled on Earth. Similarly, each rotor blade will be manufactured on Earth stored separately

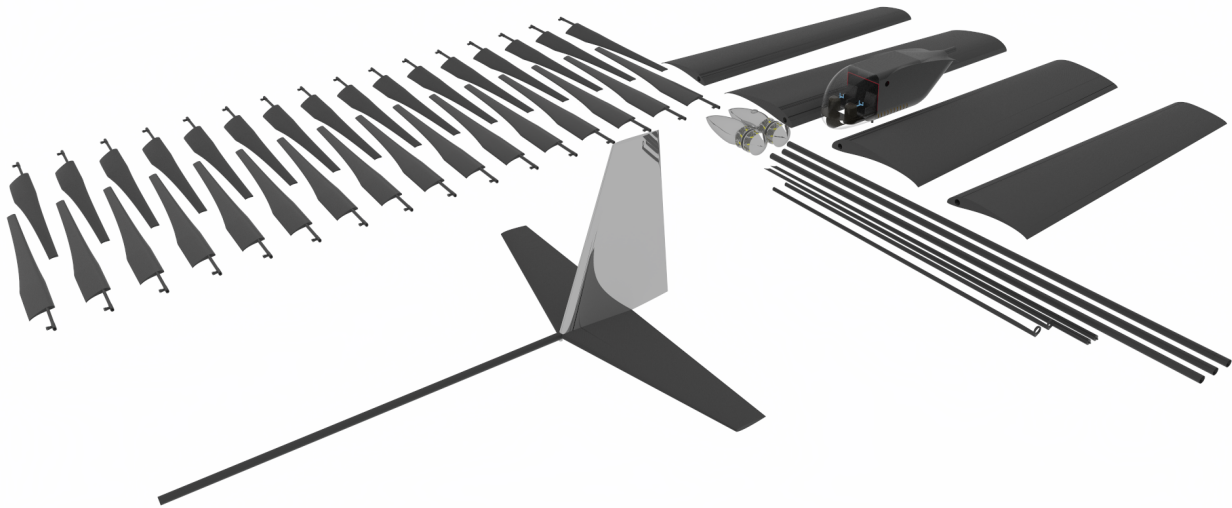


Figure 9.3: Disassembled view of the Areon

in order for them to be assembled on Mars. Thirdly, the tail was already sized keeping in mind the size constraint, thus, it will be manufactured on our planet and assembled on Mars. The wing on the other hand, have a span of 42.69 m tip to tip, therefore it would need to be divided into at least three parts. It was however decided to split it into 4 parts since having the wings already attached to the fuselage during transport would require a lot of space that could be needed for other aspects of the mission while offering few to no advantages.

The wing and the brace that supports it will thus be split into four equally-long parts, which will be assembled by the use of titanium hi-lok fasteners. The span-wise loading and the moment around the x-axis were analyzed for the worst-case loading scenario. For simplicity, the same number of fasteners was assumed at the top and bottom of the structure. The analysis revealed that the lightest option was to have 2 rows of 11 fasteners of 25 mm in diameter, both at mid-wing and the root. The braces and the tube that will go through the wing (used for holding the cables and similar purposes) will be assembled by means of a metal tightening ring. Note that in order to avoid overlapping of the joints, the tube within the wings was split into three parts instead of four.

In order to perform this assembly process, the astronauts will need access to wrench and drive tools and an assembly jig (or the materials and tools to assemble one) in order to mount the wings and tail into the fuselage. An electric pallet jack could also be useful in order to lift the structures onto their required position. However, the mass of each wing segment will be at most 133.7 kg which accounting for the ratio of Earth and Mars gravities would be equivalent to 50.57 kg on Earth, which can be lifted by 2 people with relative ease and placed on top of a supporting structure.

Production The first element considered is the rotor blades. The currently considered material is CF/Cy, which uses a thermoset as a matrix. This allows for the use of vacuum-infusion in order to extend the polymer along the carbon-fiber. Aircraft already in use such as the Boeing 787 or the Airbus A350 use this technique to produce fuselage and wing structures¹, so it is a proven method for doing so.

The wing, on the other hand, is made out of CF/PEEK, which has a thermoplastic as a base, therefore not allowing for the use of the vacuum-infusion technique. Combining this with their large size, the recommended process for the production of this part is tape lay-up, which is another proven method in the aerospace industry. This same method can be used for the production of the horizontal tail, tail-pole,

¹URL: <https://www.compositesone.com/composite-wings-are-easier-to-produce-with-vacuum-infusion/> [cited 2023-06-20]

wing-brace and fuselage.

All of these composite parts need to be placed in an autoclave. In the case of CF/Cy, the curing process takes place at a temperature of 180 °C and a pressure of 6.9 Bar, whereas the curing of CF/PEEK occurs at a temperature of 380 °C and a pressure of 4 Bar. Finally, the autoclave should have enough capacity for one of the four wing segments, which has a length of 10.67 m and a maximum width of slightly less than 4 m. These conditions are feasible since there is already an existing autoclave produced by ASC Process Systems for the Boeing 787 Dreamliner² with a length of 22.86 m, a width of 9.144 m and at a maximum pressure of 10.2 Bar. The maximum temperature of this autoclave is only 232 °C, however, studies have been done that show little to no change in the mechanical properties of CF/PEEK when cured for longer periods of time at lower temperatures if blended with other materials [98]. Alternatively, another autoclave supporting higher temperatures could be built, which can then later be used for the construction of aircraft on Earth.

Finally, the vertical stabilizer, made out of Al518.0 could be manufactured through bending of a thin-sheet and welding in order to achieve the desired shape.

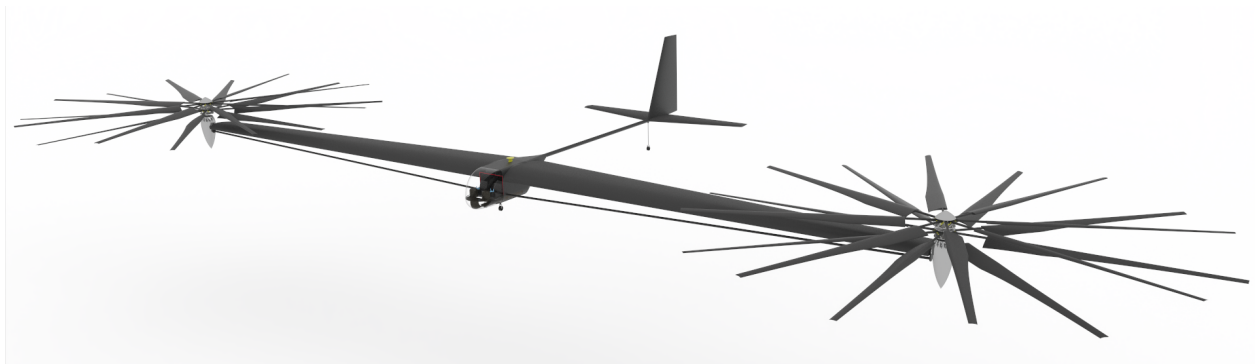
²URL: <https://www.reliableplant.com/Read/2451/world's-largest-autoclave-built-for-boeing-dreamliner>
[cited 2023-06-20]

Conclusion

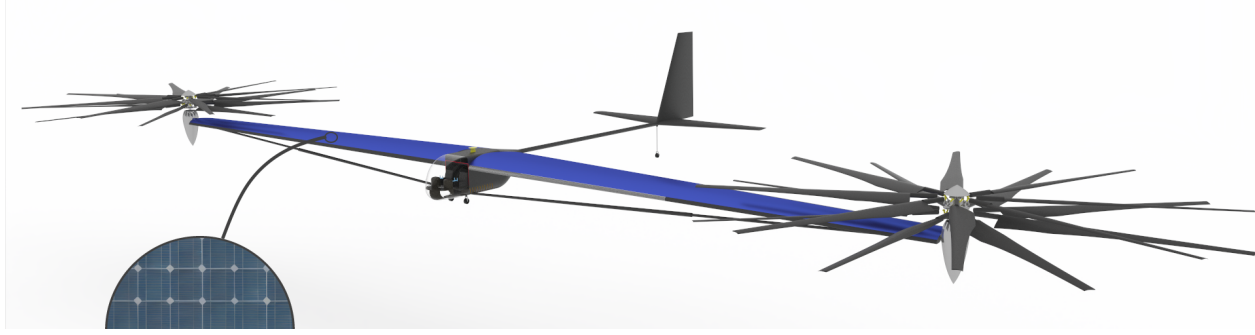
By Dominik Stiller

Rapid crewed transportation on Mars over long distances will become increasingly important as astronauts need to travel to remote exploration sites and travel between bases. This report concludes the conceptual design phase of Areon, an electric tiltrotor aircraft capable of transporting two astronauts and 100 kg of payload. Areon and its subsystems were sized for a range of 1000 km and a cruise speed of 400 km/h. The total cost was estimated to be 921 million USD FY23, which includes development and launch. Areon will be able to start operating on Mars as soon as 2034.

Areon deals with the rugged terrain and thin atmosphere of Mars by combining Vertical Take-Off and Landing with large wings. After lifting off the ground, the helicopter-like coaxial rotors tilt forwards to become propellers for efficient fixed-wing cruise. During cruise, Areon is controlled using traditional aerodynamic control surfaces and can navigate visually. The key design challenges for the preliminary and detailed design phases are (1) increasing the battery energy density, (2) modeling and controlling the transition maneuver, and (3) designing joints for easy assembly.



(a) Areon Atlas



(b) Areon Helios

Figure 10.1: Areon comes in two configurations: Atlas has higher range, while Helios provides autonomy through solar cells.

Areon comes in two configurations (Figure 10.1). Areon Atlas is the baseline version with a range of 1077 km and can recharge from the grid in 16 h. Areon Helios sacrifices 170 km of range to carry solar cells, which allow recharging without infrastructure in 5 sols. Better range performance is expected in practice since the aircraft was sized for worst case density. Given the range and speed, Areon is expected to set the precedent for future transportation on Mars.

Bibliography

- [1] Zakrajsek, J., McKissock, D., Woytach, J., Zakrajsek, J., Oswald, F., McEntire, K., Hill, G., Abel, P., Eichenberg, D., and Goodnight, T., "Exploration Rover Concepts and Development Challenges," *1st Space Exploration Conference: Continuing the Voyage of Discovery*, American Institute of Aeronautics and Astronautics, Orlando, Florida, 2005. doi:10.2514/6.2005-2525.
- [2] Raymer, D. P., French, J., Finger, D. F., Gomez, A., Singh, J., Pillai, R. G., Monjon, M. M., Marcos De Souza, J., and Levy, A., "The Raymer Manned Mars Airplane: A Conceptual Design and Feasibility Study," *AIAA Scitech 2021 Forum*, American Institute of Aeronautics and Astronautics, VIRTUAL EVENT, 2021. doi:10.2514/6.2021-1187.
- [3] Group 15, "Midterm Report – Design Synthesis Exercise," , May 2023.
- [4] Torenbeek, E., *Synthesis of subsonic airplane design: an introduction to the preliminary design, of subsonic general aviation and transport aircraft, with emphasis on layout, aerodynamic design, propulsion, and performance*, Delft University Press ; Nijhoff ; Sold and distributed in the U.S. and Canada by Kluwer Boston, Delft : The Hague : Hingham, MA, 1982.
- [5] Brundtland, G. H., "Our common future—Call for action," *Environmental conservation*, Vol. 14, No. 4, 1987, pp. 291–294. Publisher: Cambridge University Press.
- [6] Howarth, J., Mareddy, S. S., and Mativenga, P. T., "Energy intensity and environmental analysis of mechanical recycling of carbon fibre composite," *Journal of Cleaner Production*, Vol. 81, 2014, pp. 46–50. doi:10.1016/j.jclepro.2014.06.023.
- [7] Sakai, A., Kurniawan, W., and Kubouchi, M., "Recycled Carbon Fibers with Improved Physical Properties Recovered from CFRP by Nitric Acid," *Applied Sciences*, Vol. 13, No. 6, 2023, p. 3957. doi: 10.3390/app13063957.
- [8] Mandade, P., Weil, M., Baumann, M., and Wei, Z., "Environmental life cycle assessment of emerging solid-state batteries: A review," *Chemical Engineering Journal Advances*, Vol. 13, 2023, p. 100439. doi: 10.1016/j.cej.2022.100439.
- [9] Forget, F., Hourdin, F., Fournier, R., Hourdin, C., Talagrand, O., Collins, M., Lewis, S. R., Read, P. L., and Huot, J.-P., "Improved general circulation models of the Martian atmosphere from the surface to above 80 km," *Journal of Geophysical Research: Planets*, Vol. 104, No. E10, 1999, pp. 24155–24175. doi:10.1029/1999JE001025.
- [10] Millour, E., Forget, F., Spiga, A., Vals, M., Zakharov, V., Navarro, T., Montabone, L., Lefevre, F., Montmessin, F., Chaufray, J.-Y., Lopez-Valverde, M., Gonzalez-Galindo, F., Lewis, S., Read, P., Desjean, M.-C., and MCD/GCM Development Team, "The Mars Climate Database (MCD version 5.3)," *EGU General Assembly Conference Abstracts*, 2017, p. 12247.
- [11] Selig, M. S., and Guglielmo, J. J., "High-Lift Low Reynolds Number Airfoil Design," *Journal of Aircraft*, Vol. 34, No. 1, 1997, pp. 72–79. doi:10.2514/2.2137.
- [12] Somerville, A., Marino, M., Baxter, G., and Wild, G., "Understanding box wing aircraft: essential technology to improve sustainability in the aviation industry," *Aviation*, Vol. 20, No. 3, 2016. doi: 10.3846/16487788.2016.1195076.
- [13] Aloor, J. J., Wadhwa, G., Gurung, B., Singh, M., and Saha, S., "A Comparative Study of the Aerodynamic Performance of Box-wings and Mono-wings at Low Reynolds Number," 2021. doi:10.48550/ARXIV.2112.02872.
- [14] De Fezza, G., and Barber, S., "Parameter analysis of a multi-element airfoil for application to airborne wind energy," *Wind Energy Science*, Vol. 7, No. 4, 2022, pp. 1627–1640. doi:10.5194/wes-7-1627-2022.

- [15] Traub, L. W., Botero, E., Waghela, R., Callahan, R., and Watson, A., "Effect of Taper Ratio at Low Reynolds Number," *JOURNAL OF AIRCRAFT*, Vol. 52, No. 3, 2015. doi:10.2514/1.C032559.
- [16] Traub, L. W., "Aerodynamic Impact of Aspect Ratio at Low Reynolds Number," *Journal of Aircraft*, Vol. 50, No. 2, 2013, pp. 626–634. doi:10.2514/1.C031980.
- [17] Gross, J., and Traub, L. W., "Experimental and Theoretical Investigation of Ground Effect at Low Reynolds Numbers," *JOURNAL OF AIRCRAFT*, Vol. 49, No. 2, 2012. doi:10.2514/1.C031595.
- [18] Viúdez-Moreiras, D., Gómez-Elvira, J., Newman, C., Navarro, S., Marin, M., Torres, J., and De La Torre-Juárez, M., "Gale surface wind characterization based on the Mars Science Laboratory REMS dataset. Part II: Wind probability distributions," *Icarus*, Vol. 319, 2019, pp. 645–656. doi:10.1016/j.icarus.2018.10.010.
- [19] Newman, C. E., Hueso, R., Lemmon, M. T., Munguira, A., Vicente-Retortillo, , Apestigue, V., Martínez, G. M., Toledo, D., Sullivan, R., Herkenhoff, K. E., De La Torre Juárez, M., Richardson, M. I., Stott, A. E., Murdoch, N., Sanchez-Lavega, A., Wolff, M. J., Arruego, I., Sebastián, E., Navarro, S., Gómez-Elvira, J., Tamppari, L., Smith, M. D., Lepinette, A., Viúdez-Moreiras, D., Harri, A.-M., Genzer, M., Hieta, M., Lorenz, R. D., Conrad, P., Gómez, F., McConnochie, T. H., Mimoun, D., Tate, C., Bertrand, T., Bell, J. F., Maki, J. N., Rodriguez-Manfredi, J. A., Wiens, R. C., Chide, B., Maurice, S., Zorzano, M.-P., Mora, L., Baker, M. M., Banfield, D., Pla-Garcia, J., Beyssac, O., Brown, A., Clark, B., Montmessin, F., Fischer, E., Patel, P., Del Río-Gaztelurrutia, T., Fouchet, T., Francis, R., and Guzewich, S. D., "The dynamic atmospheric and aeolian environment of Jezero crater, Mars," *Science Advances*, Vol. 8, No. 21, 2022, p. eabn3783. doi:10.1126/sciadv.abn3783.
- [20] Prouty, R. W., *Helicopter performance, stability, and control*, R.E. Krieger Pub. Co, Malabar, Fla, 1990.
- [21] Singh Chauhan, S., "A simple method for estimating propeller-induced tangential velocities," , Aug. 2021.
- [22] Spera, D., "Models of Lift and Drag Coefficients of Stalled and Unstalled Airfoils in Wind Turbines and Wind Tunnels," , 2008.
- [23] Ferguson, S. W., "Evaluation of Rotorwash Characteristics for Tiltrotor and Tiltwing Aircraft in Hovering Flight," Tech. rep., Dec. 1990.
- [24] Smeur, E., "Incremental Control of Hybrid Micro Air Vehicles," Ph.D. thesis, Delft University of technology, 2018. doi:10.4233/UUID:23C338A1-8B34-40A6-89E9-997ADBDAFD75.
- [25] Anderson, N., and Loewenthal, S., "Comparison of Spur Gear Efficiency Prediction Methods," Tech. rep., NASA, Cleveland, ????
- [26] Colozza, A. J., "Comparison of Mars Aircraft Propulsion Systems," *NASA/CR*, Vol. 2003, No. 212350, 2003.
- [27] Quattrocchi, G., Pittari, A., Vedova, M. D. L. d., and Maggiore, P., "The thermal control system of NASA's Curiosity rover: a case study," *IOP Conference Series: Materials Science and Engineering*, Vol. 1226, No. 1, 2022, p. 012113. doi:10.1088/1757-899X/1226/1/012113.
- [28] Soria-Salinas, , Zorzano, M.-P., and Martín-Torres, F. J., "Convective Heat Transfer Measurements at the Martian Surface," 2015.
- [29] Bardera, R., Sor, S., and García-Magariño, A., *Aerodynamics of Mars 2020 Rover Wind Sensors*, IntechOpen, 2020. doi:10.5772/intechopen.90912.
- [30] Transport Canada, "COM—COMMUNICATIONS, NAVIGATION AND SURVEILLANCE," Aeronautical Information Manual TP 14371E, Mar. 2023.

- [31] Interagency Operations Advisory Group – Mars and Beyond Communications Architecture Working Group, “The Future Mars Communications Architecture – Volume 1,” , Feb. 2022.
- [32] Balaram, B., Canham, T., Duncan, C., Grip, H. F., Johnson, W., Maki, J., Quon, A., Stern, R., and Zhu, D., “Mars Helicopter Technology Demonstrator,” *2018 AIAA Atmospheric Flight Mechanics Conference*, American Institute of Aeronautics and Astronautics, Kissimmee, Florida, 2018. doi: 10.2514/6.2018-0023.
- [33] Gladden, R. E., Lee, C. H., Edwards, C. D., Viotti, M. A., and Davis, R. M., “A Dedicated Relay Network to Enable the Future of Mars Exploration,” *2021 IEEE Aerospace Conference (50100)*, IEEE, Big Sky, MT, USA, 2021, pp. 1–14. doi:10.1109/AERO50100.2021.9438420.
- [34] Ho, C., Golshan, N., and Kliore, A., “Radio wave propagation handbook for communication on and around mars,” Tech. Rep. JPL-Publ-02-5, 2002.
- [35] Ho, C., Slobin, S., Sue, M., and Njoku, E., “Mars background noise temperatures received by space-craft antennas,” *The Interplanetary Network Progress Report*, Vol. 42, No. 149, 2002.
- [36] Wertz, J. R., and Larson, W. J. (eds.), *Space mission analysis and design*, Space technology library, Kluwer Academic, Dordrecht ; Boston, 1991.
- [37] CCSDS, “VOICE AND AUDIO COMMUNICATIONS,” Blue Book CCSDS 766.2-B-1, Nov. 2017.
- [38] Cheung, K., “The role of margin in link design and optimization,” *2015 IEEE Aerospace Conference*, IEEE, Big Sky, MT, 2015, pp. 1–11. doi:10.1109/AERO.2015.7119220.
- [39] Edwards, C. D., “The Electra Proximity Link Payload for Mars Relay Telecommunications and Navigation,” *54th International Astronautical Congress of the International Astronautical Federation, the International Academy of Astronautics, and the International Institute of Space Law*, American Institute of Aeronautics and Astronautics, Bremen, Germany, 2003. doi:10.2514/6.IAC-03-Q.3.a.06.
- [40] Kobayashi, M. M., Shihabi, M., and Taylor, J., “Mars Cube One Telecommunications Subsystem Design,” *DESCANSO Design and Performance Summary Series*, Vol. 18, 2021.
- [41] Nielsen, E., Morgan, D., Kirchner, D., Plaut, J., and Picardi, G., “Absorption and reflection of radio waves in the Martian ionosphere,” *Planetary and Space Science*, Vol. 55, No. 7-8, 2007, pp. 864–870. doi:10.1016/j.pss.2006.10.005.
- [42] CCSDS, “PROXIMITY-1 SPACE LINK PROTOCOL— PHYSICAL LAYER,” Blue Book CCSDS 211.1-B-4, Dec. 2013.
- [43] CCSDS, “PROXIMITY-1 SPACE LINK PROTOCOL—CODING AND SYNCHRONIZATION SUB-LAYER,” Blue Book 211.2-B-3, Oct. 2019.
- [44] CCSDS, “TM SYNCHRONIZATION AND CHANNEL CODING— SUMMARY OF CONCEPT AND RATIONALE,” Green Book CCSDS 130.1-G-3, Jun. 2020.
- [45] Cobham Antenna Systems, “Type 19-430-10 UHF SatCOM Antenna,” , 2010.
- [46] Taylor, J., Lee, D. K., and Shambayati, S., “Mars reconnaissance orbiter telecommunications,” *DESCANSO Design and Performance Summary Series*, Vol. 12, 2006.
- [47] Gonzalez, F. J. J., Gil, E. P., Pinon, R. R., and Moreno, J. A. R., “Integrated HF antenna for vertical tail plane using virtual prototyping,” *The 8th European Conference on Antennas and Propagation (EuCAP 2014)*, IEEE, The Hague, Netherlands, 2014, pp. 1365–1369. doi:10.1109/EuCAP.2014.6902032.
- [48] McNutt, D. K., “Shunt antenna for aircraft,” , Mar. 2009.
- [49] Johnson, E. E. (ed.), *Third-generation and wideband HF radio communications*, Artech House mobile communications series, Artech House, Boston ; London, 2013. OCLC: ocn821731862.

- [50] Maki, J. N., Gruel, D., McKinney, C., Ravine, M. A., Morales, M., Lee, D., Willson, R., Copley-Woods, D., Valvo, M., Goodsall, T., McGuire, J., Sellar, R. G., Schaffner, J. A., Caplinger, M. A., Shamah, J. M., Johnson, A. E., Ansari, H., Singh, K., Litwin, T., Deen, R., Culver, A., Ruoff, N., Petrizzo, D., Kessler, D., Bassett, C., Estlin, T., Alibay, F., Nelessen, A., and Algermissen, S., "The Mars 2020 Engineering Cameras and Microphone on the Perseverance Rover: A Next-Generation Imaging System for Mars Exploration," *Space Science Reviews*, Vol. 216, No. 8, 2020, p. 137. doi:10.1007/s11214-020-00765-9.
- [51] Bell, D., Cesarone, R., Ely, T., Edwards, C., and Townes, S., "Mars network: a Mars orbiting communications and navigation satellite constellation," *2000 IEEE Aerospace Conference. Proceedings (Cat. No.00TH8484)*, Vol. 7, IEEE, Big Sky, MT, USA, 2000, pp. 75–88. doi:10.1109/AERO.2000.879277.
- [52] Liu, H., "Autonomous Navigation for Mars Exploration," *Mars Exploration - a Step Forward*, edited by G. Pezzella and A. Viviani, IntechOpen, 2020. doi:10.5772/intechopen.92093.
- [53] Yasuda, Y. D. V., Martins, L. E. G., and Cappabianco, F. A. M., "Autonomous Visual Navigation for Mobile Robots: A Systematic Literature Review," *ACM Computing Surveys*, Vol. 53, No. 1, 2021, pp. 1–34. doi:10.1145/3368961.
- [54] Arafat, M. Y., Alam, M. M., and Moh, S., "Vision-Based Navigation Techniques for Unmanned Aerial Vehicles: Review and Challenges," *Drones*, Vol. 7, No. 2, 2023, p. 89. doi:10.3390/drones7020089.
- [55] Phillips, T. G., Guenther, N., and McAree, P. R., "When the Dust Settles: The Four Behaviors of LiDAR in the Presence of Fine Airborne Particulates: When the Dust Settles: The Four Behaviors of LiDAR in the Presence of Fine Airborne Particulates," *Journal of Field Robotics*, Vol. 34, No. 5, 2017, pp. 985–1009. doi:10.1002/rob.21701.
- [56] Trickey, E., Church, P., and Cao, X., "Characterization of the OPAL obscurant penetrating LiDAR in various degraded visual environments," Baltimore, Maryland, USA, 2013, p. 87370E. doi:10.1117/12.2015259.
- [57] Laux, T. E., and Chen, C.-I., "3D flash LIDAR vision systems for imaging in degraded visual environments," Baltimore, Maryland, USA, 2014, p. 908704. doi:10.1117/12.2068339.
- [58] Federal Aviation Administration, "14 CFR § 25-59 - Aircraft.", May 2023.
- [59] Goldberg, S., Maimone, M., and Matthies, L., "Stereo vision and rover navigation software for planetary exploration," *Proceedings, IEEE Aerospace Conference*, Vol. 5, IEEE, Big Sky, MT, USA, 2002, pp. 5–2025–5–2036. doi:10.1109/AERO.2002.1035370.
- [60] Charles, W., and Lloyd, S., "Space Radiation," *NASA Human Research Program Engagement*, 2016.
- [61] Hassler, D. M., Zeitlin, C., Wimmer-Schweingruber, R. F., Ehresmann, B., Rafkin, S., Eigenbrode, J. L., Brinza, D. E., Weigle, G., Böttcher, S., Böhm, E., and others, "Mars' surface radiation environment measured with the Mars Science Laboratory's Curiosity rover," *Science*, Vol. 343, No. 6169, 2014, p. 1244797. Publisher: American Association for the Advancement of Science.
- [62] Wilson, A., *Supporting life: environmental control and life support for the multi-purpose logistics module (MPLM) of the International Space Station*, 1999.
- [63] Megson, T. H. G., *Aircraft structures for engineering students*, sixth edition ed., Elsevier aerospace engineering series, Butterworth-Heinemann is an imprint of Elsevier, Amsterdam ; Boston, 2017. OCLC: ocn954224012.
- [64] "Ansys GRANTA EduPack software," , 2022.
- [65] White, I. I., Tandon, R., Serna, L. M., Celina, M. C., and Bernstein, R., "An Overview of Basic Radiation Effects on Polymers and Glasses." Tech. Rep. SAND2013-8003P, Sandia National Lab. (SNL-NM), Albuquerque, NM (United States), Sep. 2013.

- [66] Naito, M., Kodaira, S., Ogawara, R., Tobita, K., Someya, Y., Kusumoto, T., Kusano, H., Kitamura, H., Koike, M., Uchihori, Y., Yamanaka, M., Mikoshiba, R., Endo, T., Kiyono, N., Hagiwara, Y., Kodama, H., Matsuo, S., Takami, Y., Sato, T., and Orimo, S.-i., "Investigation of shielding material properties for effective space radiation protection," *Life Sciences in Space Research*, Vol. 26, 2020, pp. 69–76. doi:10.1016/j.lssr.2020.05.001.
- [67] Federal Aviation Administration, "14 CFR § 23.157 - Rate of roll.", May 2023.
- [68] Li, Q., Yang, Y., Yu, X., and Li, H., "A 700 Whkg⁻¹ Rechargeable Pouch Type Lithium Battery," *Chinese Physics Letters*, Vol. 40, No. 4, 2023, p. 048201. doi:10.1088/0256-307X/40/4/048201.
- [69] "Comparision of solid state battery vs lithium - which is better," , Jul. 2022.
- [70] "Lithium-Ion Battery Inventor Introduces New Technology for Fast-Charging, Noncombustible Batteries," , Feb. 2017.
- [71] Appelbaum, J., and Flood, D., "Solar Radiation on Mars," , Aug. 1989.
- [72] Birur, G. C., Bhandari, P., Prina, M., Bame, D. P., Yavrouian, A. H., and Plett, G. A., "Mechanically Pumped Fluid Loop Technologies for Thermal Control of Future Mars Rovers," *SAE Transactions*, Vol. 115, 2006, pp. 95–103. Publisher: SAE International.
- [73] Garner, H. C., Rogers, E. W. E., Acum, W. E. A., and Maskell, E. C., "Subsonic wind tunnel wall corrections," technical AGARD-AG-109, NATO, Jan. 1966.
- [74] Kim, C.-w., "Scale modeling of Cessna 172," *Aerospace Engineering*, 2011.
- [75] Lai, H. C., and Kamaruddin, N. M., "Effect of fuselage diameter on aerodynamic characteristics for straight wing at low and high aspect ratio," *IOP Conference Series: Materials Science and Engineering*, Vol. 370, 2018, p. 012055. doi:10.1088/1757-899X/370/1/012055.
- [76] Abhishek, Anusha, Lionel, Kavish, Rujub, and Saif, "Shearing Force in Beams Experiment," 2015.
- [77] Kemparaju, H., and Samal, P. K., "Experimental Investigations On Free Vibration Of Beams," 2019. doi:10.5281/ZENODO.3374467.
- [78] Roorda, J., and Venkataramaiah, K., "Analysis of Local Plate Buckling Experimental Data," *CCFSS Proceedings of International Specialty Conference on Cold-Formed Steel Structures (1971 - 2018)*, 1982.
- [79] Schmidt, T., Cappucci, S., Miller, J., Wagner, M., Bhandari, P., and Pauken, M., "Thermal design of a Mars helicopter technology demonstration concept," 48th International Conference on Environmental Systems, 2018.
- [80] Speretta, S., "Lecture Notes AE2111-II – Spacecraft Telecommunications," , Sep. 2021.
- [81] Hansen, D., Sue, M., Peng, T., and Manshadi, F., "Frequencies for Mars Local High-Rate Links," *The Interplanetary Network Progress Report*, Vol. 42-153, 2003, pp. 1–10.
- [82] Nurohman, C., Arifianto, O., and Barecasco, A., "Hinge Moment Coefficient Prediction Tool and Control Force Analysis of Extra-300 Aerobatic Aircraft," *Journal of Physics: Conference Series*, Vol. 1005, 2018, p. 012020. doi:10.1088/1742-6596/1005/1/012020.
- [83] McIver, J., "Cessna Skyhawk II / 100 Performance Assessment," , Jan. 2003.
- [84] Muhammad, H., "Calculated static longitudinal stability and control characteristics of the Casa-Nurtanio 212 and Casa-Nurtanio 235 airplanes," *Delft University of Technology, Department of Aerospace Engineering, memorandum m-490*, 1983.

- [85] Deaconu, M., Cican, G., Toma, A.-C., and Drăgășanu, L. I., "Helicopter Inside Cabin Acoustic Evaluation: A Case Study—IAR PUMA 330," *International Journal of Environmental Research and Public Health*, Vol. 18, No. 18, 2021, p. 9716. doi:10.3390/ijerph18189716.
- [86] D'Urso, D., Chiacchio, F., Borrometi, D., Costa, A., and Compagno, L., "Dynamic failure rate model of an electric motor comparing the Military Standard and Svenska Kullagerfabriken (SKF) methods," *Procedia Computer Science*, Vol. 180, 2021, pp. 456–465. doi:10.1016/j.procs.2021.01.262.
- [87] Wang, C., and Sun, X., "The Promise of Solid-State Batteries for Safe and Reliable Energy Storage," *Engineering*, Vol. 21, 2023, pp. 32–35. doi:10.1016/j.eng.2022.10.008.
- [88] Lewis, D., "AEROPLANES & HELICOPTERS (PISTON ENGINED) NOT EXCEEDING 2730 KG MTWA LIGHT AIRCRAFT MAINTENANCE SCHEDULE (LAMS)," , May 2005.
- [89] Burroughs, L. R., "Study of helicopter transmission system development testing," Tech. rep., Jun. 1968.
- [90] Keonian, E., Sumerlin, W., Tall, M., Bussolini, J., and Baker, B., "Reliability of Avionics Systems." Tech. rep., Jul. 1971.
- [91] Leishman, J., "Rotorcraft Brownout Advanced Understanding, Control, and Mitigation," Tech. rep., Oct. 2014.
- [92] Eshima, S., and Nabity, J., "Failure Mode and Effects Analysis for Environmental Control and Life Support System Self-Awareness," 2020.
- [93] Dejogn, C., Wolbrink, A., and Larcher, J., "In-flight medical incapacitation and impairment of airline pilots." *Aviation, Space and Environmental Medicine*, Vol. 77, 2006, pp. 1077–9.
- [94] Jones, H. W., "Humans to Mars Will Cost About "Half a Trillion Dollars" and Life Support Roughly Two Billion Dollars," 2016.
- [95] Zhaodong, H., Rongxuan, L., and Jing, J., "Development and Production Costs Estimating for Aviation Equipment Based on Uncertainty Design," *Procedia Engineering*, Vol. 99, 2015, pp. 143–149. doi:10.1016/j.proeng.2014.12.518.
- [96] Pombo, D. V., "A Hybrid Power System for a Permanent Colony on Mars," *Space: Science & Technology*, Vol. 2021, 2021, p. 2021/9820546. doi:10.34133/2021/9820546.
- [97] SpaceX, "Starship Users Guide," , Mar. 2020.
- [98] Francis, B., Poel, G. V., Posada, F., Groeninckx, G., Lakshmana Rao, V., Ramaswamy, R., and Thomas, S., "Cure kinetics and morphology of blends of epoxy resin with poly (ether ether ketone) containing pendant tertiary butyl groups," *Polymer*, Vol. 44, No. 13, 2003, pp. 3687–3699. doi:10.1016/S0032-3861(03)00296-9.